10-1-2019 9:45 AM

Methodologies for Metal Functionalization of Phosphorus Based Photopolymer Networks

Vanessa Béland
The University of Western Ontario

Supervisor
Ragogna, Paul J.
The University of Western Ontario

Graduate Program in Chemistry
A thesis submitted in partial fulfillment of the requirements for the degree in Doctor of Philosophy

Recommended Citation

Béland, Vanessa, "Methodologies for Metal Functionalization of Phosphorus Based Photopolymer Networks" (2019). *Electronic Thesis and Dissertation Repository*. 6572.
https://ir.lib.uwo.ca/etd/6572

Summary

We live in an age with a constant demand for more out of less. For example, the growing use of digital electronic devices has fostered an expectation of perpetually faster, higher performing yet smaller device components. With growing concern for the environment, consumers expect green vehicles that can travel farther on less or alternative fuel than older models. While these tasks are daunting, scientists have discovered materials that show promise in accomplishing them. These materials are called ceramics. Ceramics can be composed of elements spanning the periodic table and can occur in many different forms. Some ceramics can be easily synthesized, while others can be difficult to access, especially in the context of using them in applications which have specific requirements. The research in this dissertation is targeted towards developing general methods for making ceramics. The work is based in using specialized plastic as a precursor. Throughout the thesis different types of plastic, with different chemical functionality, are explored for their ability to be functionalized with a diverse range of elements. Interestingly, if the element-containing plastic is pyrolyzed, it will leave an imprint of itself in the form of element-containing ceramic. While this research is targeted towards improving the production of useful ceramics, the focus in this early stage of the work is on understanding the fundamental structure and bonding in the new element-containing plastic and ultimately the effects that they have on the resulting ceramic materials.

Technical Abstract

In light of the above discussion, photopolymer networks with phosphonium cation, alkyl phosphine and olefin functionality were designed, synthesized and functionalized with metals by metathesis, coordination and hydrometallation reactions, respectively. The materials were strategically designed so that the metal functionalization step could be monitored and quantified. In some cases, this involved characterization by IR, NMR, or X-ray spectroscopic techniques, or by comparison to molecular analogues. It was found that by using a bi-functional photopolymer network, the material could be bi-metallized by orthogonal mechanisms. All metallized polymer networks were tested for their suitability as precursors to metal-containing ceramics. The polymers were pyrolyzed, and on analysis it was found that this methodology mostly favors metal oxides, but metal phosphates and phosphides can also be achieved. Further findings showed that tuning the amount of metal in the polymer precursor has the effect of controlling the amount of metal in the ceramics after pyrolysis. Selected polymer networks were patterned before being metallized and pyrolyzed and this was found to be an effective way of forming patterned ceramics.

Keywords

Phosphorus
Phosphonium
Phosphine
Phosphane-ene
Polymer Network
Metathesis
Coordination
Main Group
p-block
Donor
Acceptor
XANES
Hydrometallation
Orthogonal Functionalization

Co-Authorship Statement

This thesis includes work from three previously published manuscripts in chapters two, three and four. The article presented in chapter two was coauthored by: V. A. Béland, M. A. S. Ross, M. J. Coady, R. Guterman and P. J. Ragogna (*Chem. Mater.*, **2017**, *29*, 8884-8891). MASR performed formulation optimization, while MJC was responsible for electron beam lithography. RG mentored VAB in the early stages of the project. VAB performed the majority of experimental work and wrote the manuscript. PJR heavily edited the manuscript.

The work described in chapter three was coauthored by: V. A. Béland, Z. Wang, C. L. B. Macdonald, T. K. Sham and P. J. Ragogna (*Chem. Eur. J.* **2019**, Accepted.). ZW was responsible for performing XANES experiments. VAB was the major experimentalist in synthesizing and characterizing all compounds, including crystallographic solution and refinement and interpretation of XANES results. CLBM did the theoretical work and wrote the corresponding section in the manuscript. VAB wrote the remaining sections and assembled the manuscript. TKS and PJR edited the manuscript.

The work described in chapter four was coauthored by: V. A. Béland, Z. Wang, T. K. Sham and P. J. Ragogna (*Angew. Chem. Int. Ed.*, **2018**, *57*, 13252-13256). VAB was the sole experimentalist for this publication, synthesized and characterized polymer networks, including XANES measurements at the Canadian Light Source as well as data processing and interpretation. ZW and TKS were consulted on the data interpretation and helped to edit the manuscript. PJR edited the entire manuscript.

Acknowledgments

In my time at Western I had a lot of fun working at the bench, but I never came up with any good ideas there. I owe any creative troubleshooting that went into compiling this document to the people who took care of me, making sure that I didn't work too hard. Thanks to my rowing friends Scott, Jim, Smitty, Mark, Peter, Tiff, Liz, Jen and Renee for welcoming me back to the lake every time after a long hiatus… For understanding that I have a life outside of rowing, but also for giving me just the right amount of shit for not making the time to take care of myself. Thanks to my yoga friends Dianne, Liv, Mel, Dawn, Janice, Annie, Kat and Vanessa for the hugs and unconditional kindness. Thanks to Audra for the dance parties. Thanks to Jen, Camilla and Bill for the friendliest lunch time conversations. Thanks to Dwayne, Rob and Jay of Nasty Alex, and all the Rockaoke regulars, especially the three tenors: Mike "*Dr. Phil*," "*what if*" Rod "*was one of us*" and T-Wolf "*Tim*" of London, Rhonda Mac, Tamara, Sue, *Angel*-Steve, Dani, Chillvis, "*singing with*" Mark "*this could be our last mistake*," *Young* Phil, Willy V, Alex *the cat*, Carrie, Rowan, Kay, Hardee, *Rebel*-Yael, Aaron and *the lovely* Val, Mel, and Chris, for being my Thursday night family and the closest thing I have to a culture. Thanks to Geoff, Ryan and Ward for keeping the party going when it seemed like the show might not go on, and to Gavin for sound. Thanks to my best friend Claudia for the phone calls, the crazy adventures and for being the *Renaissance Girl* to my *Pyromaniac*! Thanks to the rest of the Blandford clan for including me.

Thanks to all the members of my family who I should see more often, but always manage to remind me that I come from somewhere. Thanks to Noreen, Steven, Sylvia, Bernd, Heather and Joe for taking me in as family. Thanks to Auntie Susan for being silly with me and listening to me. Thanks to Uncle Pat for teaching me about *OSOKNE*, about using Irish cream and teaching me to drive stick, and to Grandma for supporting our antics. Thanks to Justin for bringing cats into my life. Thanks to my dad for teaching me how to *really* laugh and to my mom for being my guardian angel.

I feel very lucky to have had the opportunity to work with the great people in the chemistry department. I need to thank Monica Chirigel, Yuhua Chen, Marylou Hart, Jon Aukema, John Vanstone, Barakat Misk, Mat Willans, Anita Borecki, Paul Boyle, Doug Hairsine, Todd Simpson, Tim Goldhawk, Debra Martin, Delroy and Steve. Not only for their

help, but for all of the smiles and hallway high fives that made it easy to come into work every day. A special thank you to Marilyn Steinberg for helping me improve on my communication skills and confidence. Thank you to my examiners for taking the time to read my thesis.

I had the pleasure of collaborating with Dr. TK Sham and Dr. Zhiqiang Wang who taught me everything I know about synchrotron experiments from sample preparation to data processing and interpretation. I am grateful to the entire Sham group for welcoming me to their office, group meetings and group outings and for making me feel like part of the team. Thanks to Dr. Matt Ward, Dr. Mohammad Banis, Dr. Jun Li and Jiatang Chen for using their expertise to help me acquire synchrotron data. Thanks to Dr. Chuck Macdonald for his quick turnaround of computational calculations.

Thanks to Keith Huynh and Scott Laneman for giving me the opportunity to gain industrial experience during my degree. Thanks to Ravi for telling me to shine. Thanks to the R&D team at Digital Specialty Chemicals, Dan, Chris, Adrian, Hitendra and Jonathan for enhancing my skill and spirit, especially Renan not only for his boundless patience with me, but for being such a great role model. You know you have a solid team when inventory count is fun.

Thanks to the friends in my cohort, Brooke, Rebecca, Lauren, Matt P., Ava, Madalena, Daisy, Ryan, Axie, Charmainne, Daniella, Trent and members of the W[O O]N Pyrolysis Team Joe and Amir for buying into the silliness and for blowing off steam with me in one way or another, whether it was through Beer O'Clock, a dance floor, or a simple conversation. Thanks to Mike, B-ryan, Cory, Huck, Mark and Jonathan for making me feel like I fit in somewhere. Thanks to Poly, Joanne, Tulio and Kitty for making sure that I ate dinner in good company on a regular basis, for somehow knowing when I need to take a break even when I don't and for being my lifeline in London.

Thanks to the members of the Ragogna group past and present for shaping my experience in the department. In particular, thanks to Jackie, Eleanor and Mahboubeh for taking me under their wings from day one and checking in on me to this day. Thanks to Benjamin for all of the puns and for lifting me up. Thanks to Matt for the long chats and office beers. Thanks to Tristan for keeping the silliness alive and for rallying the troups for lunch. Thanks to Soheil for the lesson in Krav Maga. Thanks to Ghazale for telling me to take breaks. Thanks to Yuqing for being the kind silent type and for showing me how to set up a RAFT polymerization. Thanks to Yuqing's wife, Irene, for tidying my desk (and his) when we weren't looking. Thanks to Kelly for kicking the can with me one last time. Thanks to Ryan for encouraging me to be creative. I've already mentioned Jonathan twice, but I can't thank him enough not only for showing me the ropes and teaching me about the mindset of working here, but for being such a great friend. Thanks to my supervisor Dr. Paul Ragogna for giving me the chance to work in his lab and for the guidance along the way. Paul, I am very sad to leave this strange place of yours that has become my home over the past six years, where there are No Rules on Friday (except for all of the rules) and anything is possible. Thanks to everyone for the crazy stories and for cheering me on.

Dedication

To a lady named Kathy Brown
who used to live Downtown.

Epigraph

But nothing worth having comes without some kind of fight
Got to kick at the darkness 'til it bleeds daylight

~Bruce Cockburn.

Table of Contents

List of Tables

List of Figures

List of Schemes

List of Abbreviations

3D	Three Dimensional
AIBN	azobisisobutyronitrile
APS	Advanced Photon Source
ASN	5-azasprio[4,4]nona-2,7-dienium
ATR-IR	Attenuated Total Reflectance Infrared
ATRP	Atom Transfer Radical Polymerization
BCPs	Bond Critical Points
br	broad
CLS	Canadian Light Source
CRP	Controlled Radical Polymerization
d	Doublet
DCTB	Trans-2-[3-(4-tert-butylphenyl)-2-methyl-2-propenylidene]malononitrile
DFT	Density Functional Theory
D.I.	Deionized
DMPA	2,2-dimethoxy-2-phenylacetophenone
dppe	1,2-bis(diphenylphosphino)ethane
dppp	1,3-bis(diphenylphosphino)propane
DSC	Differential Scanning Calorimetry

E	Element
E_0	Absorption Threshold Energy
EBL	Electron Beam Lithography
EDG	Electron Withdrawing Group
EDX	Energy Dispersive X-Ray
Et_2O	Diethylether
EV	Electric Vehicle
EWG	Electron Withdrawing Group
F-IPN	Full-Interpenetrating Polymer Network
FRP	Free Radical Polymerization
FSF	Free Standing Film
FT-IR	Fourrier Transform Infrared
FT-Raman	Fourrier Transform Raman
GOF	Goodness of Fit
HEA	2-hydroxyethyl acrylate
HER	Hydrogen Evolution Reaction
HOMO	Highest Occupied Molecular Orbital
HTC	High Technology Ceramics
ICSD	Inorganic Crystal Structure Database
IPN	Interpenetrating Polymer Network

IR	Infrared
IT	Information Technology
K-S	Kohn-Sham
LUMO	Lowest Unoccupied Molecular Orbital
m	Multiplet
MALDI-MS	Matrix Assisted Laser Desorption Ionization-Mass Spectrometry
MeCN	Acetonitrile
MO	Molecular Orbital
MOFs	Metal Organic Frameworks
mp	Melting Point
NBO	Natural Bond Orbital
NHC	N-Heterocyclic Carbene
NMP	Nitroxide Mediated Polymerization
NMR	Nuclear Magnetic Resonance
OER	Oxygen Evolution Reaction
OMRP	Organometallic Mediated Radical Polymerization
ORR	Oxygen Reduction Reaction
$[OTf]^-$	Triflate anion
PFS	Polyferrocenylsilane

PTFE	Polytetrafluoroethylene
PXRD	Powder X-Ray Diffraction
q	Quartet
QT-AIM	Quantum Theory of Atoms in Molecules
R_1	R-value
R^2	Coefficient of Determination
RAFT	Reversible Addition Fragmentation Chain Transfer
s	Singlet
SEM	Scanning Electron Microscopy
S-IPN	Semi-Interpenetrating Polymer Network
SS NMR	Solid state nuclear magnetic resonance
SXRMB	Soft X-ray Microcharacterization Beamline
t	Triplet
TEGDA	Tetraethyleneglycol diacrylate
TEGDAE	Tetraethyleneglycol diallylether
T_g	Glass Transition Temperature
TGA	Thermogravimetric Analysis
THF	Tetrahydrofuran
T_m	Melting Temperature measured by DSC

TM	Transition Metal
tmeda	Tetramethylethylenediamine
TPC	Tokyo Police Club
TTT	1,3,5-triallyl-1,3,5-triazine-2,4,6(1H,3H,5H)-trione
UV	Ultraviolet
UVA	Ultraviolet A (λ = 315-400 nm)
UVB	Ultraviolet B (λ = 280-315 nm)
UVC	Ultraviolet C (λ = 100-280 nm)
UVV	Ultraviolet V (λ = 400-450 nm)
V	Volume
WL	Whiteline
XANES	X-Ray Absorption Near Edge Structure
XPS	X-Ray Photoelectron Spectroscopy
Z	Number of Molecules in Asymmetric Unit

Chapter 1

1 Introduction

1.1 Synthetic Plastic: Applications from Fundamental Understanding

From cooking breakfast in the morning to calling a friend on the phone, plastic – ever since its commercialization during World War II – has found a way to embed itself into every aspect of our lives.[1] Its use has been an economic solution in preserving food, improving safety and is central to modern medicine, amongst many other application outlets .[1] The problem is that when plastic is discarded at the end of its life cycle, it ends up in the environment, where the majority does not break down. With plastic islands and microplastics building up in our oceans and lakes, this has become a global issue in material science, supply chain, culture, public policy and psychology.[2,3] The work of the material scientist is to understand as much as possible about plastic, from finding better, more sustainable ways of creating it, to how to deal with the plastic that we already have.[3–5] Past innovations in the area have always come from understanding the fundamental aspects of structure and bonding in the material. With this in mind, it is important to continue exploratory research in the area as it can lead to new, unprecedented understanding and opportunities.[6]

1.2 Polymer Synthesis

All plastics are polymers which are macromolecules composed of repeating units of the same chemical composition and structure. They can be synthesized by condensation or addition reactions of one or more monomers, which will ultimately make up the backbone of the polymer by anionic, cationic, olefin metathesis or radical mechanisms.

The most widely used method for creating polymers industrially is via free radical polymerization (FRP), which involves the catenation of the unsaturated units in olefins. FRP is typically classified as a chain growth polymerization, where there are three key reactions that occur in the transformation of monomer to polymer. These are initiation, propagation and termination. As outlined in Scheme 1.1, FRP begins with the thermal or photochemical cleavage of a radical initiator, which goes on to react with the monomer. This radical addition to monomers continues throughout the propagation step and allows the polymer chains to grow. As the concentration of monomer decreases, termination reactions become more likely than continued propagation. Termination can either arise from radical chains reacting with each other in combination or disproportionation reactions, or from radical chains reacting with solvent or impurities. The process of combination versus disproportionation results in polymer chains with vastly different molecular weights. While these termination steps become more likely as the concentration of monomer decreases, that does not mean they do not occur earlier on in the reaction. The polymer chains can be terminated at different times and in different ways, resulting in a broad distribution of molecular weights.[1]

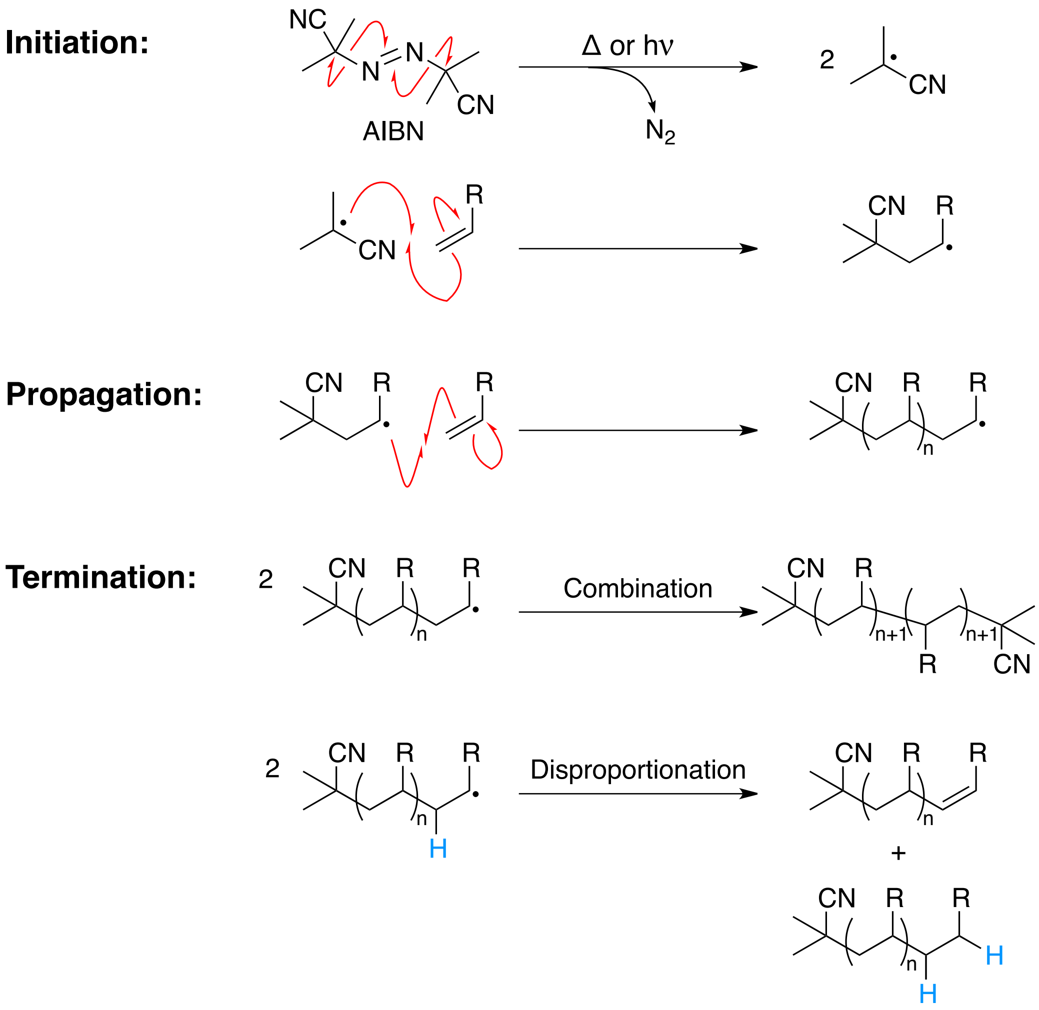

Scheme 1.1: Initiation using azobisisobutyronitrile (AIBN) as an example initiator, propagation and termination steps in FRP.

Polymers with narrow molecular weight distributions are desired for applications that require well-defined physical properties, and so polymer chemists sought to develop methods of mitigating undesired termination reactions to create what is known as living or controlled radical polymerization (CRP).[1] There are several methods of CRP that have been develop since the mid-1980s which include, nitroxide mediated polymerization (NMP), organometallic mediated radical polymerization (OMRP), atom transfer radical polymerization (ATRP) and reversible addition fragmentation chain transfer (RAFT) polymerization (Scheme 1.2). While these all involve unique reagents and mechanisms, the general idea of CRP is to decrease the concentration of propagating polymer chains by reversibly quenching them in order to mitigate termination steps.[7] An advantage of the living polymer chain ends is that they can be used to later continue the polymerization with a different monomer to make a block-copolymer. These methods have proven effective and have allowed polymers to enter the arena of synthetic precision that was previously reserved for molecular species.[8]

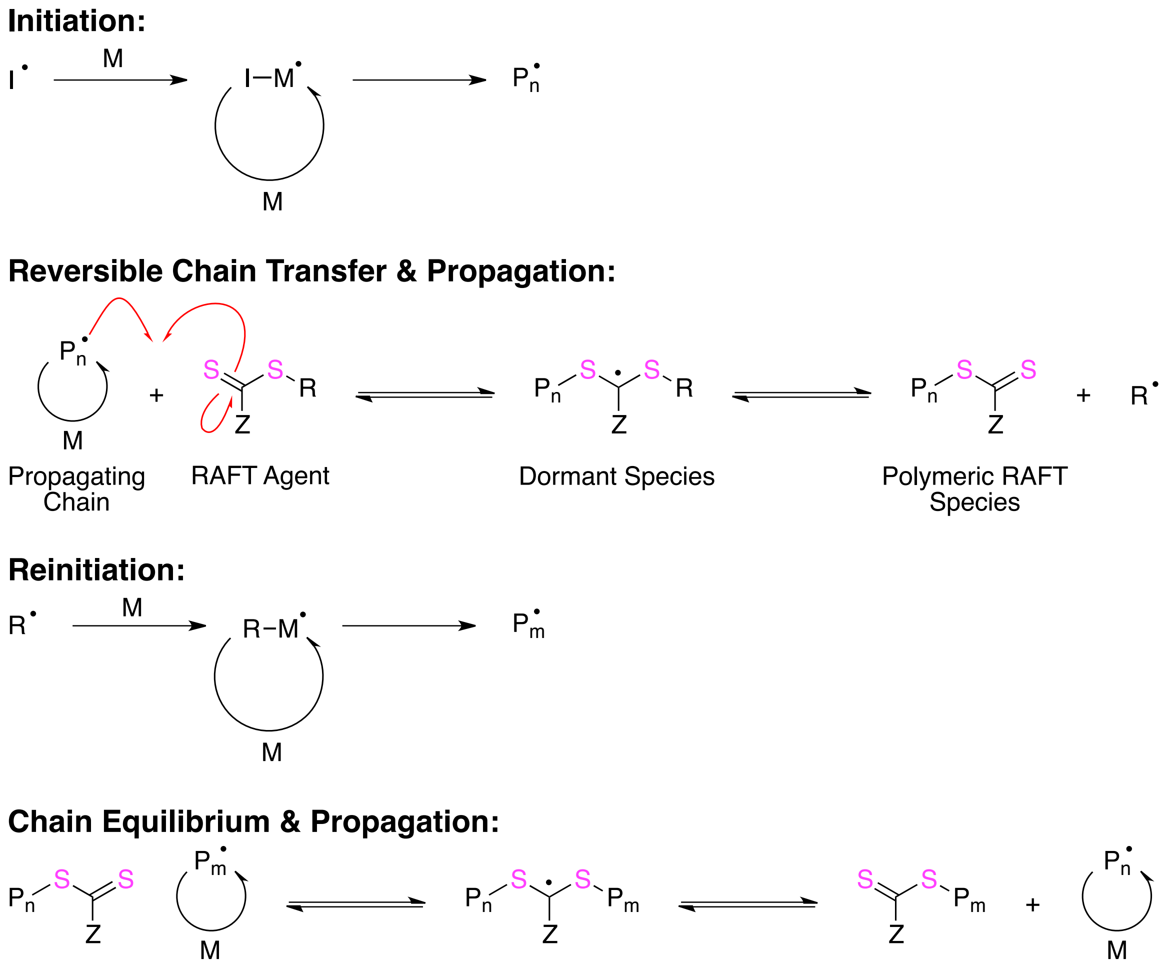

Scheme 1.2: Steps and mechanisms in RAFT polymerization featuring reversible reactivity of the growing polymer chains with the thiocarbonyl RAFT agent to create a dormant species. I ≡ radical initiator; M ≡ olefin monomer; P_n and P_m ≡ growing polymer chains.[9] Radical propagation is denoted by the circular fishhook arrow.

1.2.1 Photopolymerization

Chemists originally pursued photochemical approaches to polymer synthesis in search of a method to perform polymerizations at ambient temperature.[10] Photopolymers can be synthesized by cationic, anionic, FRP and CRP mechanisms.[11,12] Using light as the polymerization stimulus adds the potential for spatial control which can be leveraged in selective surface chemistry by masking techniques and 3D printing.[10,13–16]

Polymers can be synthesized photochemically by irradiating a combination of monomers and light-absorbing compounds called photoinitiators. There are cationic, anionic and radical photoinitiators and amongst them, they can absorb in the UV, visible or near IR range. There are even some that absorb specific wavelengths and provide selectivity over product formation.[10,11] Of the UV-absorbing initiators, there are Type I initiators, which cleave to generate radicals that initiate polymerization, and Type II initiators, which consist of electron and proton transfer between a light-absorbing molecule and a co-initiating species to generate radicals (Scheme 1.3).[11]

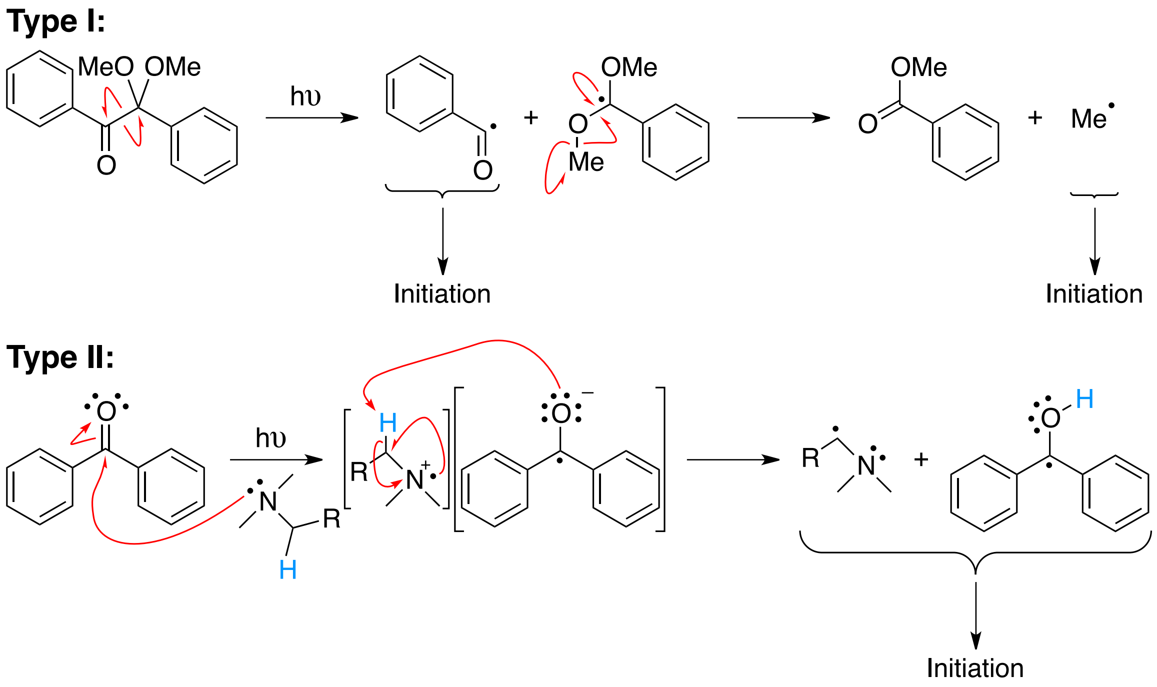

Scheme 1.3: Examples of Type I and Type II photoinitiation mechanisms. Top: radical cleavage of 2,2-dimethoxy-2-phenylacetophenone (DMPA); bottom: photo-induced electron and proton transfer between benzophenone and a tertiary amine.[11]

On irradiation of the photoinitiator, an electron is promoted from a filled bonding molecular orbital (MO) to an unfilled antibonding MO in a process called photoexcitation. From the excited state, the electron can relax back down to the ground state through internal conversion and fluorescence processes or can undergo intersystem crossing from the S_1 to the T_1 excited state. From the long-lived T_1 state, the electron can relax to the ground state by phosphorescence, or the molecule can dissociate into radicals that can be used to initiate polymerization (Figure 1.1).[17]

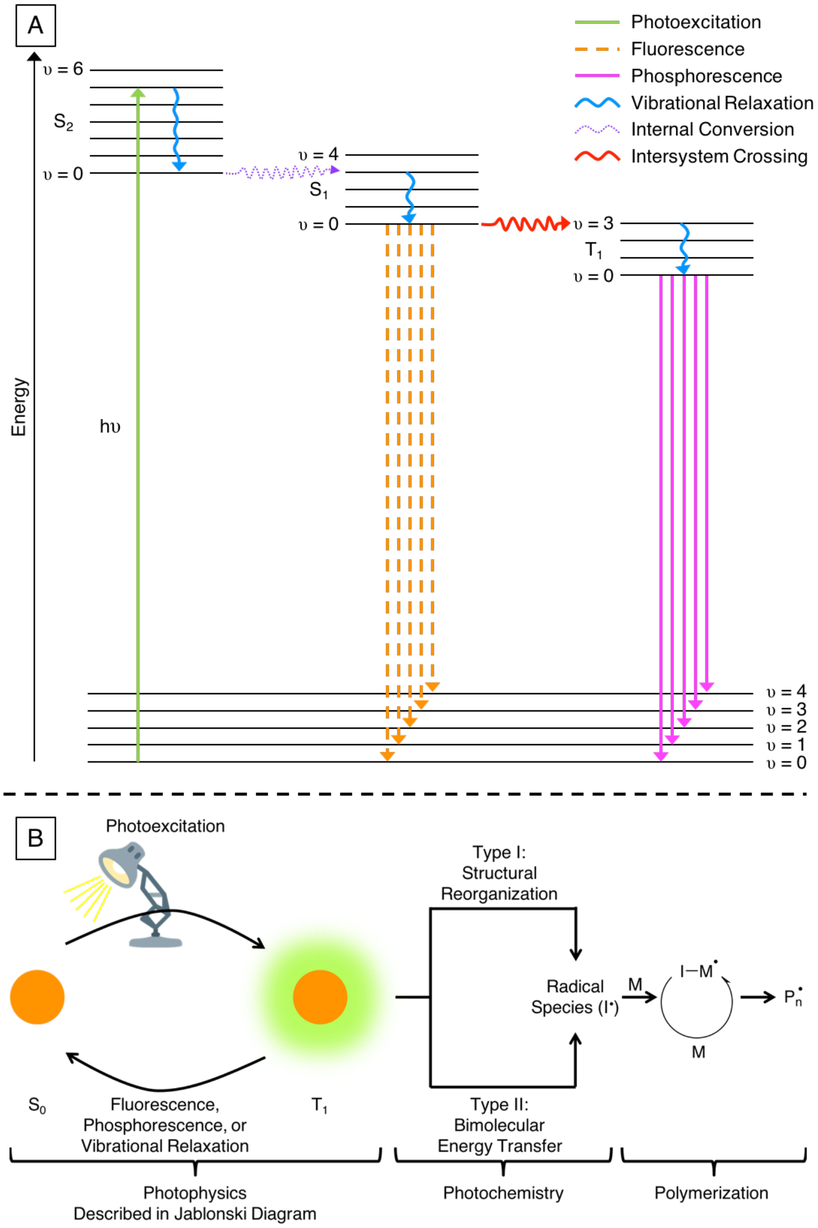

Figure 1.1: A: Jablonski diagram; B: diagram depicting the photophysical and chemical pathways a molecule can undergo from the excited state. I ≡ radical initiator; M ≡ olefin monomer; P_n ≡ growing polymer chains.[10,17]

1.2.2 Polymer Networks

Monomers can have more than one polymerizable functional group. While those that have one polymerizable group can form linear polymers, monomers with higher functionality can be used to prepare branched, or crosslinked polymer networks, where polymer chains are covalently connected to each other by bridging chains in 3-dimensions (Scheme 1.4). The degree of crosslinking can be controlled by the degree of functionality in the monomer, or by co-polymerizing monomers of different functionality. Crosslinking can be used to increase the rigidity of a polymer and often has the effect of decreasing its solubility.[1] Although polymer networks are generally insoluble, some of them have an ability to be swelled by solvent, which makes them susceptible to solution-like chemistry and characterization.[18–24]

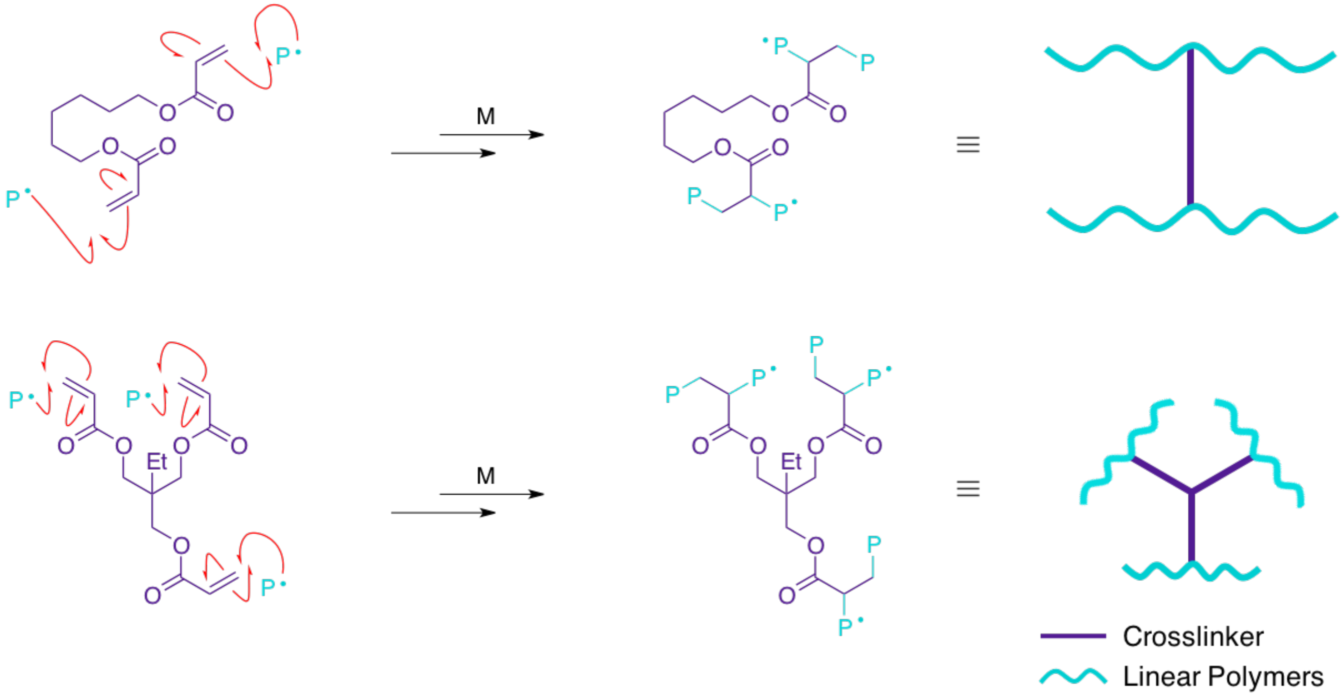

Scheme 1.4: Crosslinking using examples of di- and tri-functional acrylates. M ≡ olefin monomer; P ≡ polymer chains.

1.2.3 Shaping of Photopolymer Networks

The most general photopolymer network formulation must contain a multifunctional monomer and a photoinitiator. The reaction can be performed neat, or in the presence of solvent, and can consist of other additives, all of which will influence the properties of the resulting photopolymer network. The most common photopolymer formulations are acrylate-based and follow a FRP mechanism, but other systems are also known.[25] Because light is used as the reaction stimulus, photopolymer networks can be physically shaped at any step along the preparative pathway (Scheme 1.5).

The first option for shaping is by casting the liquid formulation into a mold or thin film, by conveyor or spin coating techniques. The liquid easily takes on the shape of the mold and forms a solid in place after being irradiated. A common application of this technique is in dental fillings, where the use of photopolymer networks have nearly completely replaced amalgam fillings.[25,26] Due to the fast curing time, photopolymerization can be integrated at the industrial scale to make polymer networks in roll-to-roll production methods, such as in the coating of optical fiber at a rate of 1524 m/min.[25,27]

Photomasking techniques can be used to cover the formulation during irradiation to selectively form photopolymers on a surface.[28,29] With recent advances in photolithography, this can be accomplished on millimeter to nano-length scales.[30–33] Finally, the solid material can be shaped by selectively degrading the solid product using techniques such as electron beam lithography (EBL), which has proven to be a useful method in creating prototypes in the information technology (IT) industry.[34]

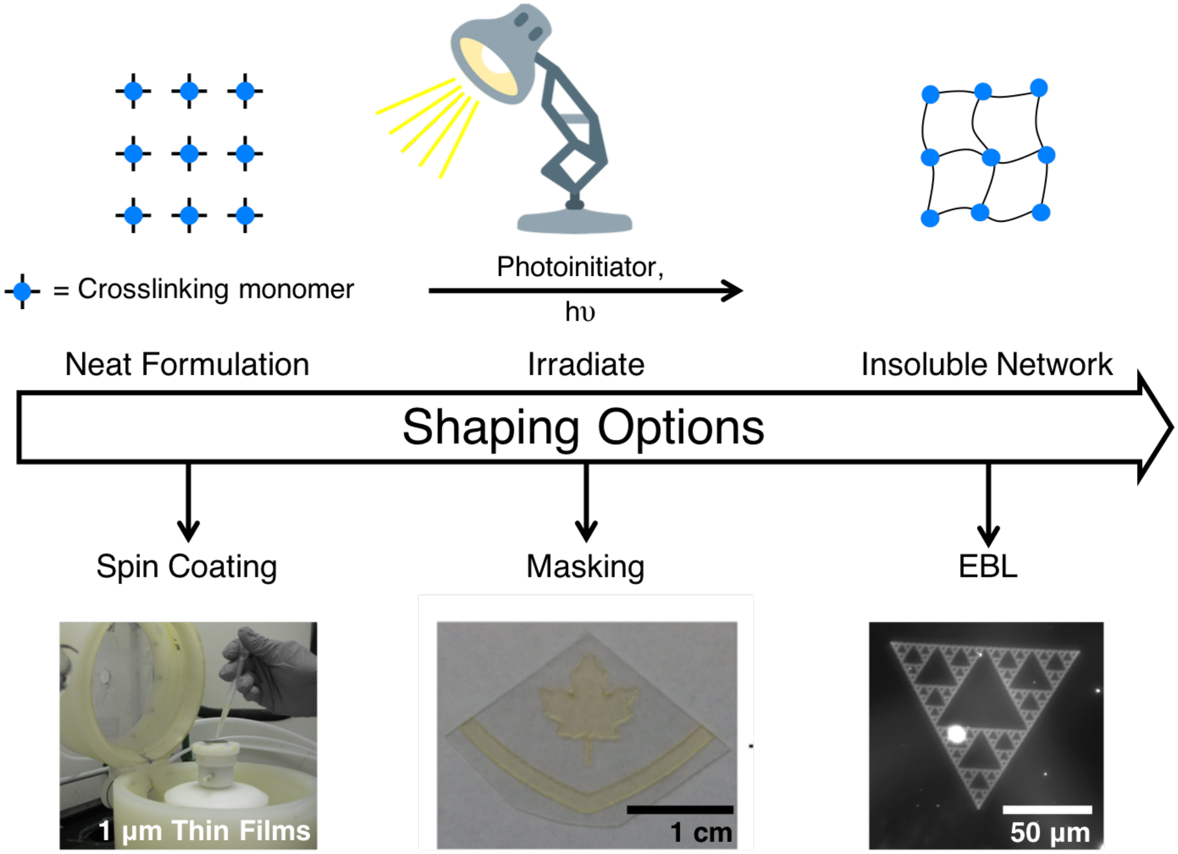

Scheme 1.5: General preparation of a photopolymer network showing options to shape the material along the different synthetic steps.[28,35]

1.2.4 Photo-Click Networks

Click reactions are those that are highly selective, quantitative, inert towards other functional groups, do not produce by-products and can be done under mild conditions.[36] The term was coined by Sharpless and coworkers in 2001, but the first reported click reaction was the cycloaddition between dienes and dienophiles discovered in 1928 by Otto Diels and Kirk Alder (Figure 1.2). A variety of cycloadditions are classified as click reactions, of particular note is the alkyne azide click reaction of strained alkynes which can be performed photochemically with no catalyst (Figure 1.2). Click chemistry is not exclusive to cycloadditions, for example, the radical photochemical initiation of thiol-ene and thiol-yne reactions also fall under the umbrella of click chemistry.[37] These reactions involve the addition of an S-H functionality across an alkene or alkyne to make thioether linkages (Figure 1.2). Analogous chemistry can be achieved by adding P-H functionality across olefins to generate alkyl phosphine environments. In the presence of a radical initiator, hydrogen abstraction from either the thiol or phosphine results in thiyl and phosphinyl radicals, which react with the olefin to give an alkyl radical; these subsequently abstract a hydrogen from a thiol or phosphine and can therefore propagate (Figure 1.2).[38] These kinds of reactions have been used to click functional units to nanoparticles in biomolecular labeling and drug delivery applications and of course, to make photopolymer networks.[38–42]

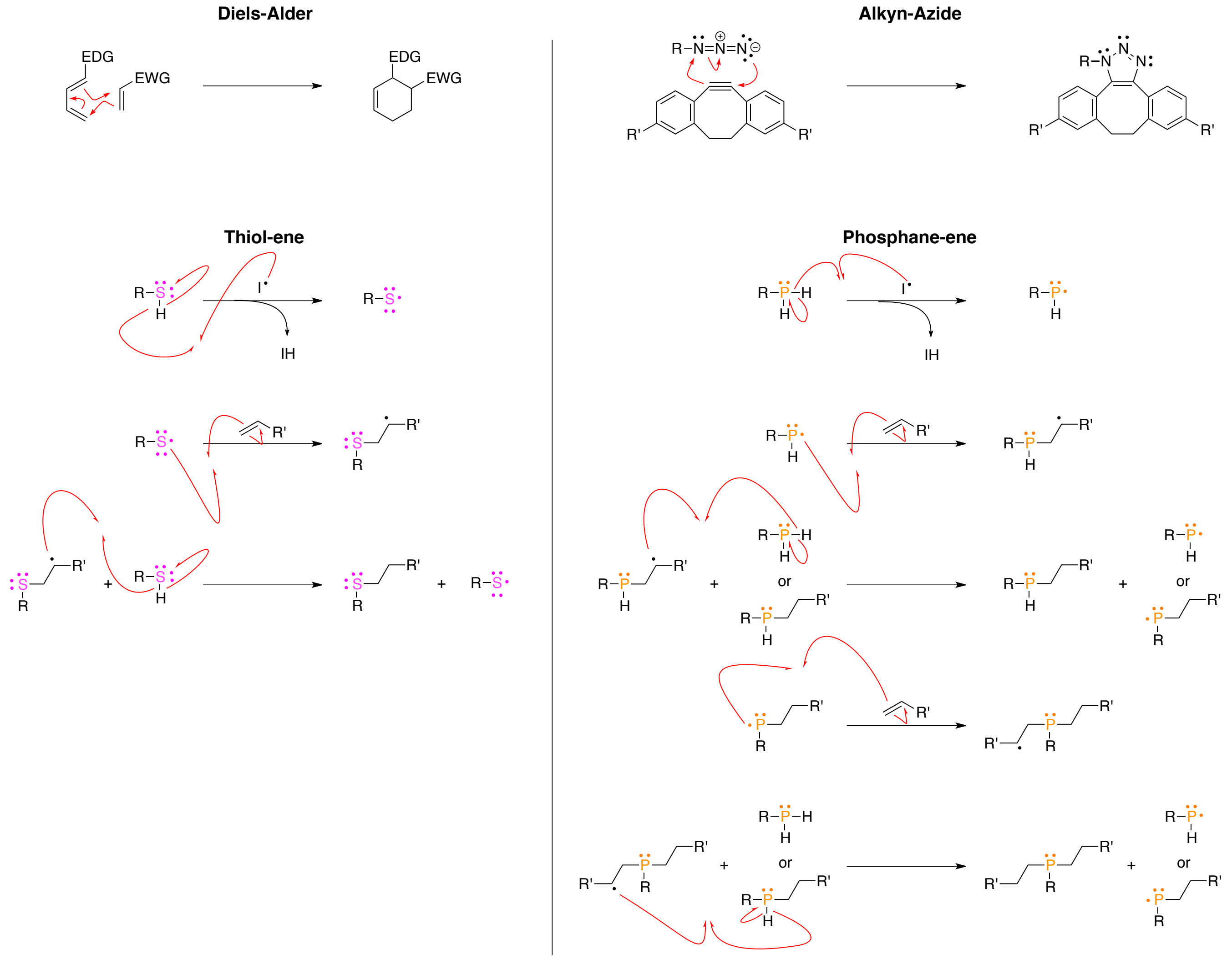

Figure 1.2: Diels-Alder, alkyne-azide, thiol-ene and phosphane-ene mechanisms.[38] EDG = electron donating group; EWG = electron withdrawing group.

Polymers and polymer networks can be generated by click chemistry. Since click chemistry is dependent on the addition of two different functional groups, the required degree of functionality in the monomer to make a linear polymer is two, while a functionality of at least three in at least one of the monomers is required to make polymer networks (Scheme 1.6). Photopolymer networks formed by the thiol-ene reaction have been established for some time, but in 2015 the analogous molecular phosphane-ene chemistry was applied to form alkyl phosphine based photopolymer networks (Figure 1.2).[38,41–43]

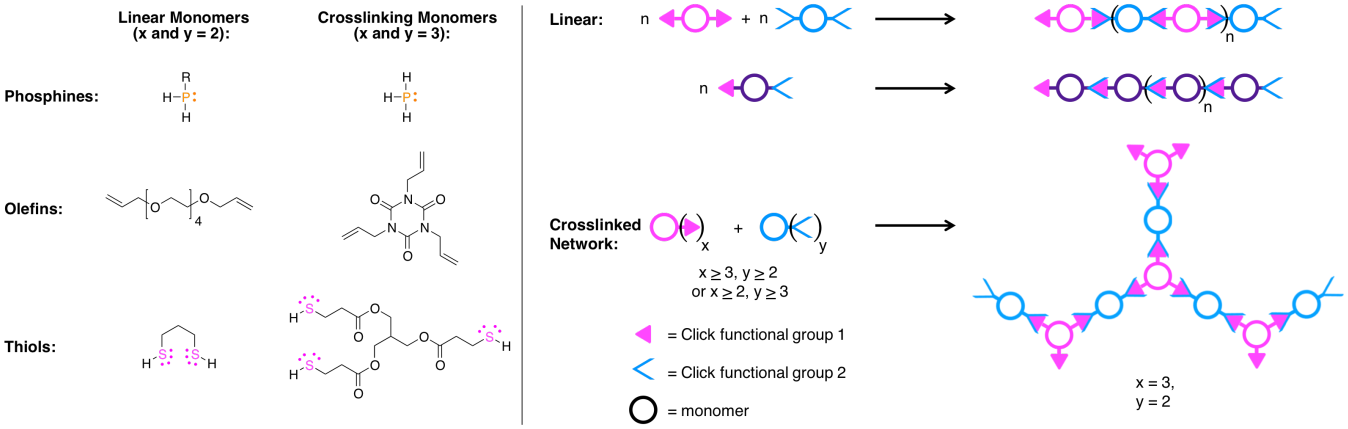

Scheme 1.6: Left: Examples of linear and crosslinking monomers for thiol-ene and phosphane-ene chemistry; right: monomer functionality requirements for linear and network photo-click polymers.

1.3 Functional Polymers

Functional polymers are those that possess desired physical or chemical properties. These properties are dictated by the structure and chemistry of the repeating units. For example, the strength of the C-F bonds in polytetrafluoroethylene (PTFE) make it a robust material, while the sterics of the fluorine atoms prevent reactivity and solvent interactions with the polymer backbone, making the polymer hydrophobic (Scheme 1.7).[6] Because of these properties, PTFE has found its way into countless applications with some examples in gas filtration, medicine, fishing lines and waterproof apparel.[6] Conjugated polymers are a good example of reactive functional polymers as their flexibility and ability to be either oxidized (positively (p)-doped) or reduced (negatively (n)-doped) has made them key players in the development of sensors, electrochemical devices, organic photovoltaics, organic light-emitting diodes, field effect transistors and stretchable electronics (Scheme 1.7).[44,45]

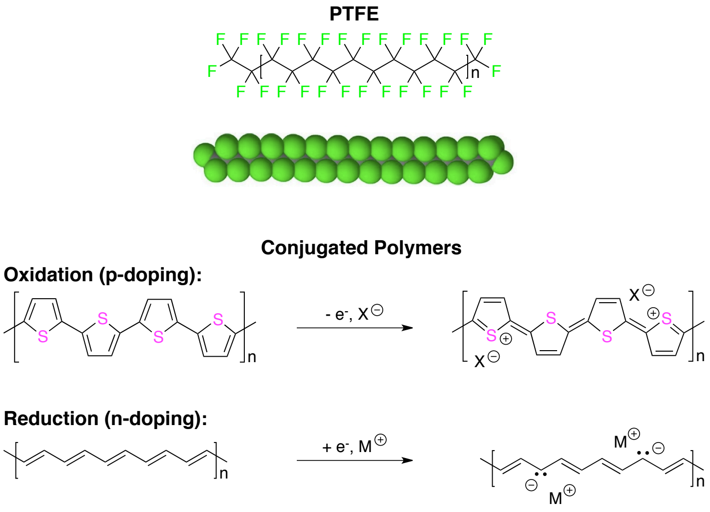

Scheme 1.7: Chemical and space-filling structures of PTFE.[46] Examples of p- and n-doping of polythiophene and polyacetylene, respectively.[44]

Polyphosphonium cations are particularly interesting functional polymers, not only for their favorable antifouling properties, but also for their potential to be further functionalized by metathesis of their labile counterions.[47] Polyphosphonium cations can be synthesized from phosphonium salts that are functionalized with a polymerizable group such as styrene, or acrylate (Scheme 1.8).[48–50]

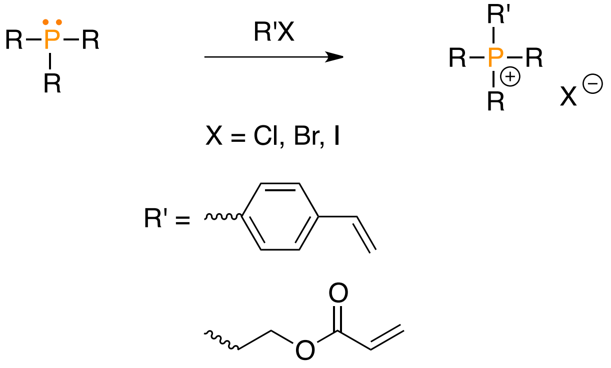

Scheme 1.8: General phosphonium salt monomer synthesis, demonstrating quaternization of a tertiary phosphine with a polymerizable group.

1.3.1 Functional Polymer Networks

In many applications, it is favorable for functional polymers to be insoluble so that they do not wash away. Functional polymer networks are useful in this way because while they are insoluble, they can be swelled by solvent, allowing for solution-like chemistry, which can be leveraged to tune the properties of the material. For example, matrixes of crosslinked polyferrocenylsilane (PFS) and ordered silica spheres have been leveraged in the commercialization of photonic ink. The polymer network can be swelled by solvent and undergo redox chemistry, reducing its swellability, resulting in contraction of the material. As the polymer matrix changes in size, so does the d-spacing between the opal spheres and the perceived colour of the material (Figure 1.3).[51]

Although chemically useful, not all functional polymers can be easily crosslinked.[52] In order to tune the physical properties, the functional polymer can be incorporated in an interpenetrating polymer network (IPN). There are two types of IPN, full-IPN (F-IPN), which involves two intertwined polymer networks, and semi-IPN (S-IPN), composed of a linear polymer entangled in a network. These materials can be synthesized by polymerization of a mixture of monomers that react by orthogonal mechanisms. Alternatively, S-IPN can be generated by incorporating a linear polymer into a polymer network formulation (Scheme 1.9).[53] These methods have been used in making hydrophobic and antibacterial surfaces as well as tissue mimetic materials.[54–56]

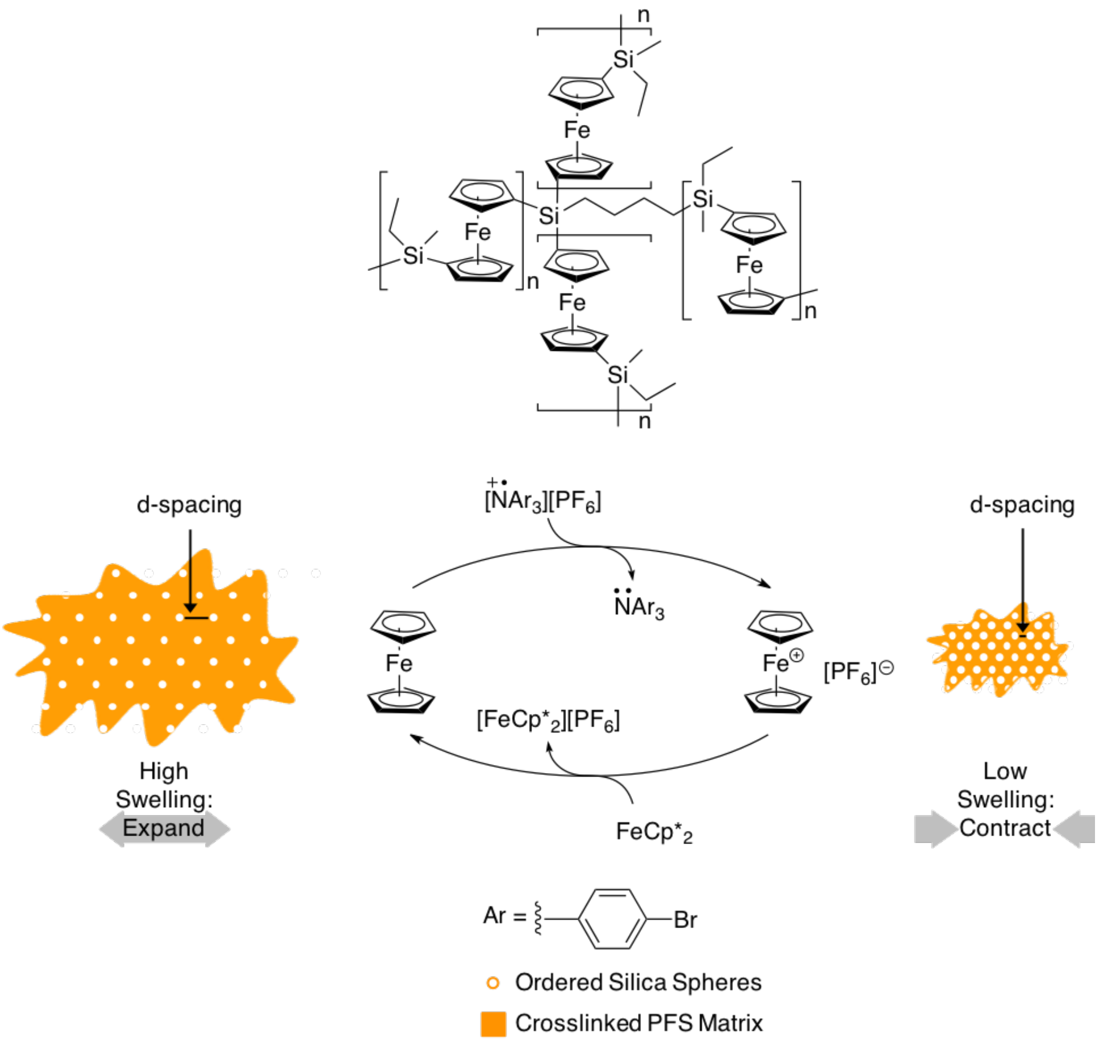

Figure 1.3: Structure of crosslinked PFS; middle: redox chemistry of the functional ferrocene moieties in the polymer and effect of polymer expansion and contraction on d-spacing of the silica spheres.[51]

When polyphosphonium cations have been incorporated into IPNs, they have shown an ability to be further functionalized by metathesis reactions to give metallized polymer networks.[57] Of particular interest has been an ability to selectively chemically functionalize surfaces of this kind by stamping and masking techniques.[28,58] As long as the materials are susceptible to solution chemistry, the functionalization of polymer networks is mainly governed by the types of functionality they possess. For example, thiol-ene and phosphane-ene polymers contain thioether and alkyl phosphine functionality, respectively, which can potentially be leveraged in coordination reactions.[59]

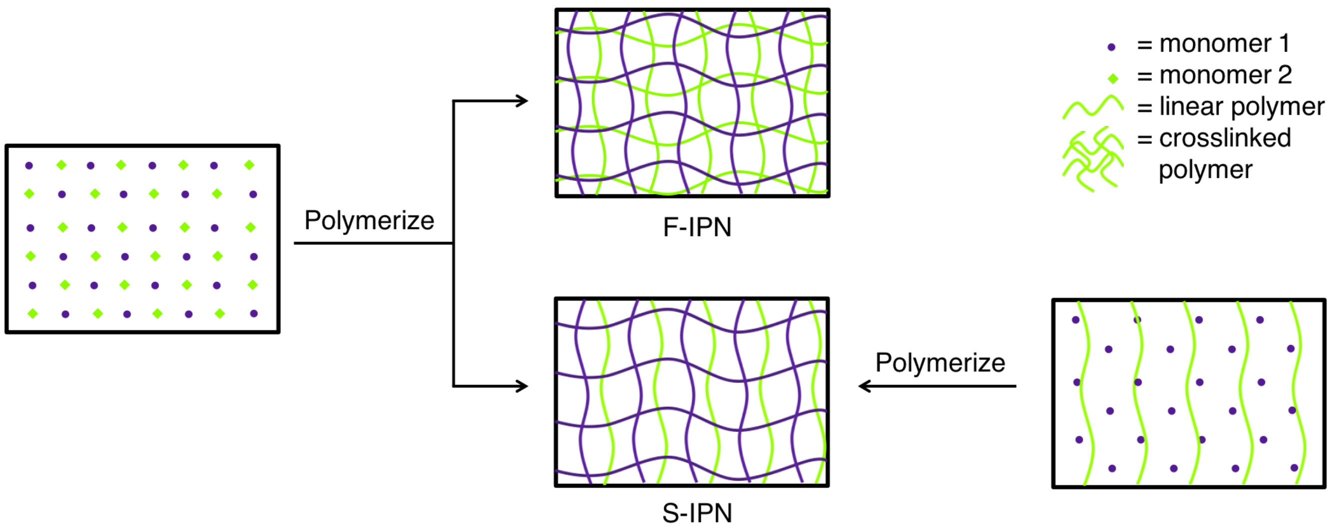

Scheme 1.9: General synthesis of F-IPN and S-IPN.

1.4 Metal-Containing Polymers & Polymer Derived Ceramics

Metallopolymers are structurally diverse and have found a role in numerous applications,[60,61] one in particular is their role as precursors to prepare polymer-derived ceramics.[62–65] Metal-containing ceramics have recently been investigated for a vast array of applications in the fields of electrochemistry, electrocatalysis and IT. In a quest to lower the carbon footprint of vehicles, chemists are striving to improve battery performance and develop efficient fuel cells for the clean generation of hydrogen as an alternative to fossil fuels.[66–68] Meanwhile, with the faltering of Moore's law, IT engineers are looking to room temperature ferromagnetic semiconductors that can be used to innovate the industry.[69–73] Different types of metal-containing ceramics can be found at the forefront of the above innovations and metal-containing polymers can be a convenient way of accessing them.

1.4.1 The Rise of Electric Vehicles

There are currently many initiatives towards clean and cheap transportation in the form of electric vehicles (EV). The green vehicle market has come a long way since the release of the Toyota Prius hybrid in 1997 to the new and sleek, fully battery powered 2019 Tesla models. Despite the innovation in the field in the past twenty years, there is still room to improve the low power output in cold weather, high cost of the current market batteries and overall efficiency of the batteries themselves.

The alternative to fully battery powered vehicles is to use a clean fuel source such as molecular hydrogen (H_2). H_2 itself is considered a clean fuel because in the context of the hydrogen evolution reaction (HER), the only emission is water. However, the two major industrial pathways in the *formation* of H_2 – steam methane reforming and coal gasification – use non-renewable resources and produce CO and CO_2 as byproducts (Scheme 1.10).[74,75] The electrolysis of water is considered a clean pathway to H_2, but currently only accounts for 4% of industrial production. This accounts for one main obstacle that must be overcome in order for H_2 to be considered a viable and sustainable fuel. Fuel cells that can replace the high emission and energy intensive methods for H_2 production must be developed.[66]

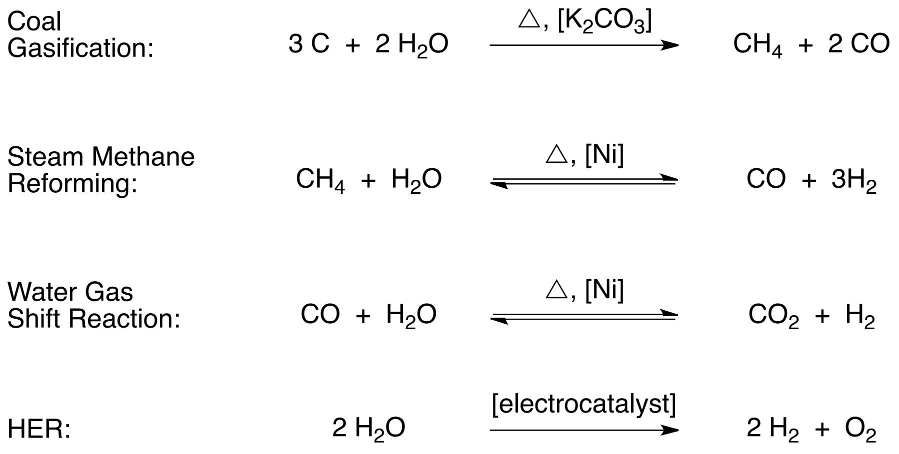

Scheme 1.10: Industrial pathways in H_2 production. Both coal gasification and steam methane reforming produce CO as a byproduct, which can be used in the water gas shift reaction to produce additional H_2 and CO_2.[66,74,75]

1.4.2 Ceramics in Batteries

Li-ion batteries are currently the leaders in the field and are used in commercial electric vehicles that can travel 565 km without recharging. The industry is targeting electric vehicles with travel range up to 800 km, while Li-ion batteries are approaching their performance limit, so new battery technologies must be investigated and developed.[76]

Despite approaching their performance limit, Li-ion batteries far outpace other types of batteries for being the leaders in the field of EVs. Recent work in this area has been focused on improving the electric conductivity of $LiFePO_4$ in battery cathodes by doping with other transition metals, which has the effect of lowering the calculated energy of the conduction band towards the Fermi level (0.05 – 0.07 eV lower than $LiFePO_4$; Figure 1.4).[67,68] In terms of the anode, both transition metal and main group oxides, mixed metal oxides and metal alloys have been investigated as cheaper alternatives to the platinum standard.[77]

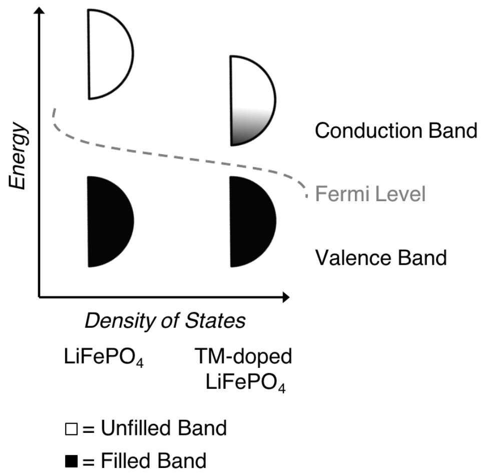

Figure 1.4: Band structure of $LiFePO_4$ versus transition metal (TM) doped $LiFePO_4$.

Metal air batteries consist of a metal anode and use ambient oxygen as the cathode. The cell is constructed so that the anode and electrolyte are encased in an O_2-permeable hydrophobic membrane (Figure 1.5). Since the oxygen reduction reaction (ORR) is slow, the membrane must be functionalized with an electrocatalyst. In order for metal air batteries to be rechargeable, they also need to be able to undergo the oxygen evolution reaction (OER) and possess either a bifunctional electrocatalyst, or a combination of both ORR and OER electrocatalysts.[76] With the incentive of moving away from precious metal electrocatalysts, there is an effort to improve the activity of metal oxides and carbonaceous materials.[76] In metal-air battery applications, the catalytic surface of platinum becomes saturated with $[OH]^-$ adspecies, which decreases its activity. This has inspired the investigation of nonprecious metal materials including manganese oxide and cobalt oxide which have promising electrocatalytic activity, while nickel and iron hydroxide have superior electrocatalytic activity to that of platinum.[76] Mixed metal spinel oxides including $Co_xMn_{3-x}O_4$, $MnCo_2O_4$, $Cu_xCo_{3-x}O_4$ and $NiCo_2O_4$ as well as $CuCo_2O_4$ and carbon nanotubes doped with Co_3O_4 have even shown promise in the bi-functional electrocatalysis of both the ORR and OER.[76,78–81]

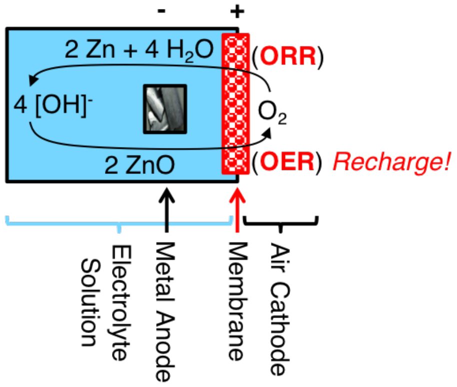

Figure 1.5: Diagram of a metal air battery.[76]

1.4.3 Ceramics in Fuel Cells

Several types of materials have emerged as promising low-cost electrocatalysts for HER.[66] Metal phosphides have garnered attention in particular because of their hydride and proton acceptor sites on the metal and phosphide sites, respectively.[66,82–84] From this analogy, phosphides of Fe, Co, Ni, Cu, Mo and W have been found to be active HER catalysts.[84] The HER activity of metal phosphides can be tuned by varying the metal to phosphorus ratio in nickel phosphide. The results show that a higher phosphorus content results in higher catalytic activity, but a material with low conductivity and so a balance between the two is desired.[84] Another way of tuning HER activity is through using mixed metal phosphides, which has the effect of reducing the free energy of H_2 adsorption to the catalyst surface (0.124 eV in Co_2P to -0.148 eV in $(Co_{0.4}Fe_{0.6})_2P$), thus expediting the turnover.[85,86]

1.4.4 General Structure and Electronic Requirements

Despite their desired electrochemical properties, a major drawback of the above-mentioned ceramics in the context of batteries or fuel cells is that they lack conductivity. In either field there has been an effort to improve the electrochemical activity of these materials by incorporating them into carbon. Carbon has the advantage of being conductive, and it is a substrate that can be doped with heteroatoms to further enhance the inherent conductivity.[66,77,87] A challenge in this field is finding a way to uniformly dope the carbon support with the active materials.[88] This can be accomplished using different templating techniques and recent work in the pyrolysis of metal organic frameworks (MOFs) has been geared towards streamlining the process.[77,89,90] MOFs possess advantageous characteristics such as high porosity and being homogenously functionalized with metals, which manifest in the resulting ceramics after pyrolysis. While MOFs provide a streamlined synthetic route to metal doped carbons, scalability remains a challenge that makes industrial implementation difficult.[91] In this context, metal-functionalized photopolymer networks may be a reasonable technology to develop as ceramic precursors because scalability has already been proven.[27]

1.4.5 Patterned Ceramics in Upcoming Technology

Moore's law has governed the information technology (IT) industry since 1975 when Gordon Moore, cofounder of Intel Corporation, made the prediction. The law, which is more aptly a business model, states that the number of transistors in a microchip will double every two years. The IT industry has been able to maintain this demand of supplying faster devices but is on the threshold of reaching its limit. In a 2015 review, through his own commentary and interviews with industry experts, Mitchell Waldrop clearly pinpoints the issues with Moore's law and the direction the industry is headed. More transistors on a given chip mean detrimental heat buildup, and the electronic behaviour of transistors changes for the worse once the space between them reaches the atomic scale. Chip speed reached its limit in 2004, and IT engineers were able to meet performance demands by using more chips, but this modification is also now approaching its progress limit.[69]

In order to continue innovation in the field, IT engineers are considering a move away from transistor-based devices toward those based on spintronics. Spintronic materials take advantage of different fundamental properties of the electron; charge and spin, respectively. Transistors are semiconductor materials that power digital computing by switching electron currents on and off to give binary 1's and 0's, respectively. Spintronic devices are being developed so that the spin ("up" or "down") of the material can be controlled and harnessed into binary code. There are two main types of spintronic materials; the traditional metallic ferromagnetic materials, which are applied to memory storage, and those made from ferromagnetic semiconductors, which have the potential to reduce energy consumption in transistors and revolutionize the way that they function.[70–73]

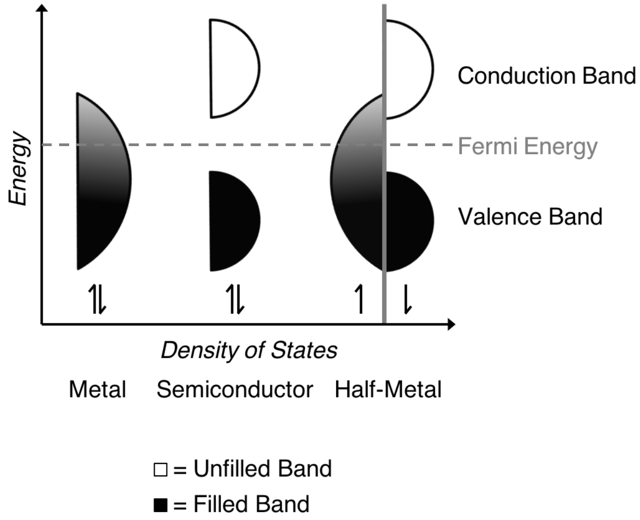

Figure 1.6: Band structures of a metal, semiconductor and half-metal. Half-metals are compounds that are selectively conductors to one spin, but insulators or semiconductors towards the opposite spin.[92]

The search for spintronic semiconductor materials that are ferromagnetic at room temperature is ongoing and a broad range of materials are being investigated from organic semiconductors, to half-metals, to doped ceramics that make use of elements spanning the periodic table (Figure 1.6).[93–105] In order for these spintronic materials to function in a device, not only do they need to be composed of the right material, they must also take on a specific shape. It has been found that nanowires display superior spintronic properties to the same bulk materials. The main barrier to research on nanoscale spintronic materials has been that it is difficult to fabricate the desired materials into the appropriate shapes on an appropriate scale for testing. Further, for doped materials, it is difficult to achieve uniform doping in small scale features.[106] Since research on composition of these ferromagnetic semiconductors is ongoing and shaping them is a challenge, it would be wise to develop a method that can pattern a wide range of materials on nano- to micro-length scales.[34,73]

1.4.6 Pyrolysis & shape retention of metal-containing polymers

Amphiphilic block copolymers have an ability to self-assemble into nano-domains. Combining polymer derived ceramics with metallopolymer lithography and block copolymer self assembly has been an innovative approach to achieve spacial control on the nano scale.[107–113] By pyrolyzing these assemblies, organic matter is volatilized, with the metal-containing ceramics occupying the same well-defined regions that were predetermined by the block copolymer assembly (Scheme 1.11). This approach to patterned metal containing ceramics is underscored by the pyrolysis of a range of different elements including main group polymers, PFS and cobalt-containing block copolymers, mainly targeting bit patterned media, which is applicable to data storage.[111,112,114]

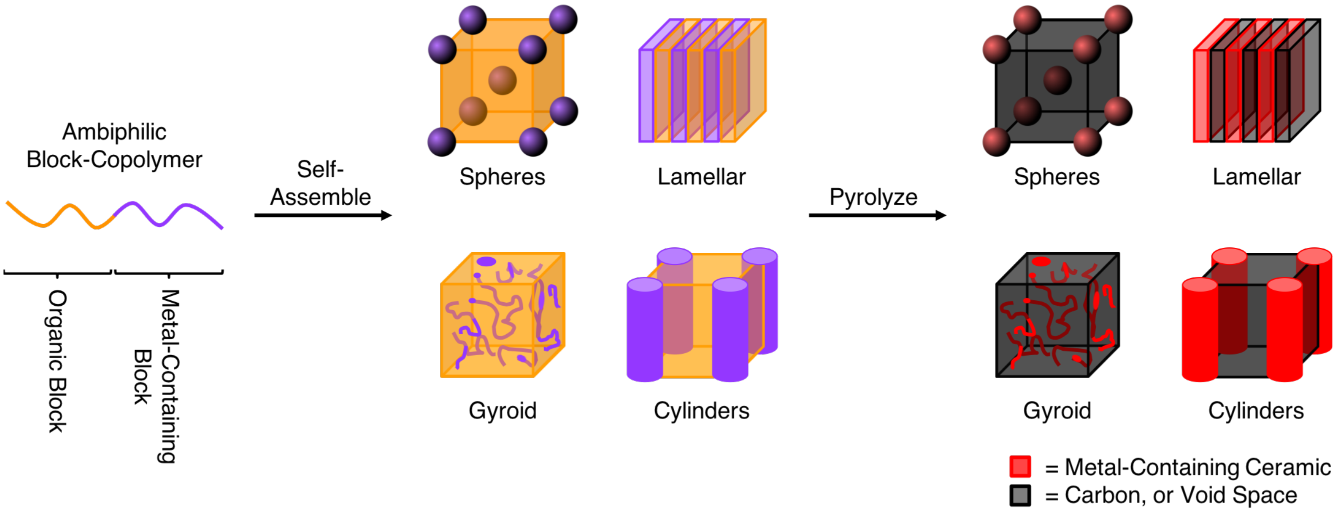

Scheme 1.11: Self-assembly of metal-containing ambiphilic block-copolymers and shape retention on pyrolysis. The morphology of the self-assembled nano-domains is dependent on the degree of incompatibility between the different blocks, the number of repeating units and the molecular weight of each block.[115]

The disadvantage to block copolymer lithography in the context of forming patterned ceramics is that it requires precise polymerization techniques that require a skilled hand and the process is difficult to scale. While it is possible to synthesize new monomers for polymerization, incorporating elemental diversity and density into the polymer also remains a challenge using this method. There are countless molecular precursors with well-defined stoichiometric ratios of a wide range of element types, which in principle could be leveraged for obtaining precise control over ceramic composition. All that is required for post-polymerization functionalization is a mechanism of binding these molecular precursors to the polymer scaffold. Coordination chemistry and ion exchange are the mechanisms that have been explored the most (Scheme 1.12).[59,63,65,108,109,114,116–118]

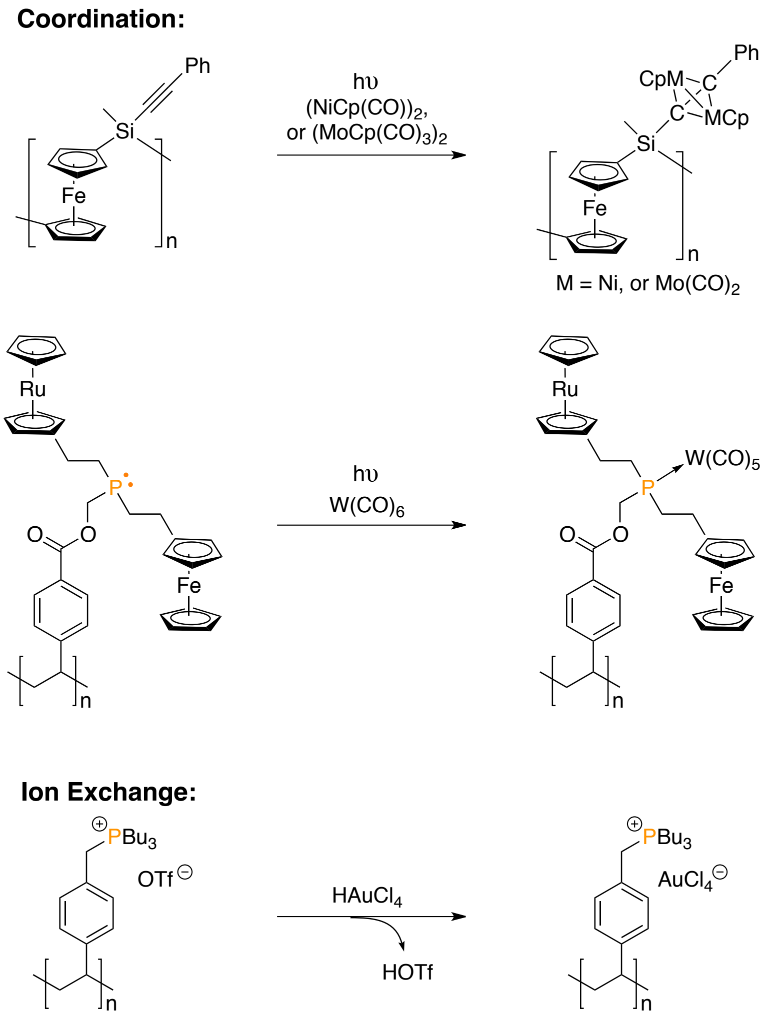

Scheme 1.12: Recent examples of metal functionalization of polymers by coordination chemistry and ion exchange.[109,116,118]

An underexplored area of metallopolymer chemistry has been metal functionalization of photopolymer networks. If polymer networks could be functionalized with inorganic elements, then they would be promising candidates to act as high technology ceramic precursors not only because of their enrichment with desired inorganic elements, but because of their ability to be shaped.

1.5 Scope of Thesis

In light of the above discussion, the work presented in this dissertation targets new methodologies for functionalizing photopolymer networks with metals so that they can act as polymer precursors for highly sought-after metal containing ceramics. Since these methodologies are in their infancy, the main focus of the work is on the synthesis and comprehensive characterization of the polymeric materials.

The idea being that control and understanding of the precursor will translate into control over the composition of the resulting ceramics.

In Chapter 2, a phosphonium-functionalized interpenetrating polymer network was functionalized with an anionic molybdenum carbonyl complex by metathesis. The native polymer network was cast into thin films and patterned on the micron-scale. These patterns were shown to retain their shape after functionalization with metal and subsequent pyrolysis (Figure 1.7).

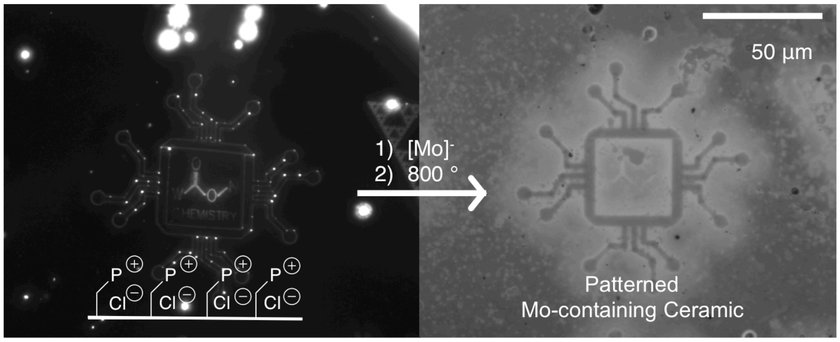

Figure 1.7: Left: confocal microscope image of a patterned phosphonium-functionalized S-IPN thin film. Right: Scanning electron micrograph of molybdenum-containing ceramic, showing shape retention after metallization and pyrolysis of the original S-IPN.

Chapter 3 features a necessary interlude to molecular chemistry, where XANES spectroscopy is used to characterize the electronic structure in donor-acceptor compounds. The reductive dehalogenation of a zwitterionic phosphine-supported Ge (II) complex yielded a rare, Ge(I) 1,2-dication. With 1,2-dications being rare because of the repulsion of the adjacent charges, the root of the stability of this compound was investigated by probing the molecular and electronic structures through crystallographic, spectroscopic and computational methods. These findings, in particular the spectroscopic characterization method, was pivotal for characterizing the donor-acceptor macromolecules described in Chapter 4 (Figure 1.8).

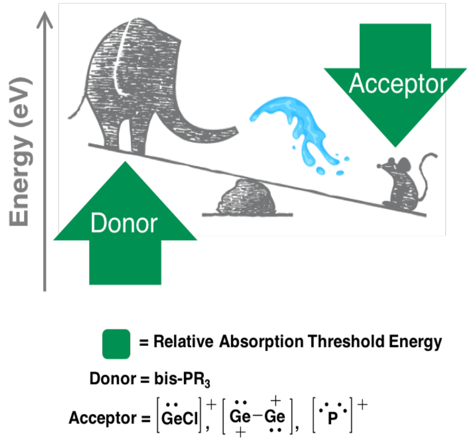

Figure 1.8: Artistic depiction of the donor-acceptor interactions observed for the adducts featured in Chapter 3.

In Chapter 4, crosslinked macromolecular phosphines were functionalized by coordination to different metal-containing Lewis acids (Figure 1.9). Not only were the materials found to be useful as precursors to shaped metal-containing ceramics, but the polymers were found to have interesting physical and electronic properties.

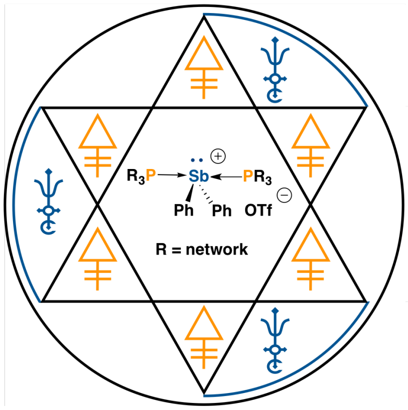

Figure 1.9: Artistic representation of how Sb cations can be used to crosslink phosphane-ene polymer networks with the result of altering the physical properties and electronic structure of the material.

In Chapter 5, the abovementioned crosslinked macromolecular phosphine was quaternized with allyl bromide. The bi-functional phosphonium cations could be bi-metallized orthogonally by reacting the allyl group with a germanium hydride species, and unaffected by this reactivity, the bromide anion could be used in an ion complexation reaction with copper bromide (Scheme 1.13). The doubly metallized photopolymer network can be pyrolyzed to yield carbon doped with copper and germanium.

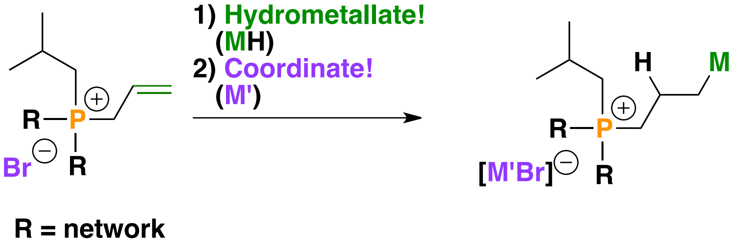

Scheme 1.13: Hydrometallation, followed by ion complexation of allyl functionalized phosphonium cationic networks.

1.6 References

(1) Nicholson, J. W. *The Chemistry of Polymers*, 4th Ed.; Chatham,Kent, UK, 2012.

(2) Buffington, J. *Peak Plastic The Rise or Fall of Our Synthetic World*; ABC-CLIO, LLC: Santa Barbara, California, USA, 2017.

(3) Haider, T. P.; Völker, C.; Kramm, J.; Landfester, K.; Wurm, F. R. *Angew. Chem. Int. Ed.* **2019**, *58* (1), 50.

(4) Lucas, N.; Bienaime, C.; Belloy, C.; Queneudec, M.; Silvestre, F.; Nava-Saucedo, J. E.

Chemosphere **2008**, *73* (4), 429.

(5) Lloyd, E. M.; Lopez Hernandez, H.; Feinberg, A. M.; Yourdkhani, M.; Zen, E. K.; Mejia, E. B.; Sottos, N. R.; Moore, J. S.; White, S. R. *Chem. Mater.* **2019**, *31* (2), 398.

(6) Ebnesajjad, S. *Expanded PTFE Applications Handbook Technology, Manufacturing and Applications*; Elsevier: Oxford, UK, 2017.

(7) *Fundamentals of Controlled/Living Radical Polymerization*; Tsarevsky, N. V, Sumerlin, B. S., Eds.; RSC Publishing: Dorchester, UK, 2013.

(8) Grubbs, R. B.; Grubbs, R. H. *Macromolecules* **2017**, *50* (18), 6979.

(9) *Handbook of RAFT Polymerization*; Barner-Kowollik, C., Ed.; Wiley-VCH: Sydney, Australia, 2008.

(10) Corrigan, N.; Yeow, J.; Judzewitsch, P.; Xu, J.; Boyer, C. *Angew. Chem. Int. Ed.* **2019**, *58* (16), 5170.

(11) Fouassier, J. P.; Lalevée, J. *Photoinitiators for Polymer Synthesis*; Wiley-VCH: Weinheim, Germany, 2012.

(12) Chen, M.; Zhong, M.; Johnson, J. A. *Chem. Rev.* **2016**, *116* (17), 10167.

(13) Bagheri, A.; Jin, J. *ACS Appl. Polym. Mater.* **2019**, *1* (4), 593.

(14) Poelma, J. E.; Fors, B. P.; Meyers, G. F.; Kramer, J. W.; Hawker, C. J. *Angew. Chem. Int. Ed.* **2013**, *52* (27), 6844.

(15) Delaittre, G.; Goldmann, A. S.; Mueller, J. O.; Barner-Kowollik, C. *Angew. Chem. Int. Ed.* **2015**, *54* (39), 11388.

(16) Barner-Kowollik, C.; Goldmann, A. S.; Schacher, F. H. *Macromolecules* **2016**, *49* (14), 5001.

(17) Wardle, B. *Principles and Applications of Photochemistry*; TJ International Limited: Padstow, Cornwall, Great Britain, 2009.

(18) Ahn, S. K.; Kasi, R. M.; Kim, S. C.; Sharma, N.; Zhou, Y. *Soft Matter* **2008**, *4* (6), 1151.

(19) Ford, W. T.; Balakrishnan, T. *Macromolecules* **1981**, *14* (2), 284.

(20) Yokota, K.; Abe, A.; Hosaka, S.; Sakai, I.; Saitô, H. *Macromolecules* **1978**, *11* (1), 95.

(21) Manatt, S. L.; Horowitz, D.; Horowitz, R.; Pinnell, R. P. *Anal. Chem.* **1980**, *52* (9), 1529.

(22) Doskočilová, D.; Schneider, B.; Jakeš, J. *J. Magn. Reson.* **1978**, *29* (1), 79.

(23) Neppel, A.; Eaton, D. R.; Hunkeler, D.; Hamielec, A. E. *Polymer* **1988**, *29* (7), 1338.

(24) Mathur, A. M.; Scranton, A. B. *Biomaterials* **1996**, *17* (6), 547.

(25) Khudyakov, I. V. *Prog. Org. Coatings* **2018**, *121*, 151.

(26) Leprince, J. G.; Palin, W. M.; Hadis, M. A.; Devaux, J.; Leloup, G. *Dent. Mater.* **2013**, *29* (2), 139.

(27) Strehmel, B. *Nachr. Chem.* **2014**, *62* (2), 128.

(28) Guterman, R.; Gillies, E. R.; Ragogna, P. J. *Can. J. Chem.* **2016**, *94* (5), 476.

(29) Kabb, C. P.; O'Bryan, C. S.; Deng, C. C.; Angelini, T. E.; Sumerlin, B. S. *ACS Appl. Mater. Interfaces* **2018**, *10* (19), 16793.

(30) Inoue, S.; Amano, T.; Itani, T.; Watanabe, H.; Mori, I.; Watanabe, T.; Kinoshita, H.; Miyai, H.; Hatakeyama, M. *Adv. Opt. Technol.* **2012**, *1* (4), 269.

(31) Stuerzebecher, L.; Fuchs, F.; Zeitner, U. D.; Tuennermann, A. *Microelectron. Eng.* **2015**, *132*, 120.

(32) Rühe, J. *ACS Nano* **2017**, *11* (9), 8537.

(33) Fedynyshyn, T. H.; Goodman, R. B.; Cabral, A.; Tarrio, C.; Lucatorto, T. B. *Proc. SPIE* **2010**, *7639*, 76390A.

(34) Ross, C. A. *Annu. Rev. Mater. Res.* **2001**, *31*, 203.

(35) Béland, V. A.; Ross, M. A. S.; Coady, M. J.; Guterman, R.; Ragogna, P. J. *Chem. Mater.* **2017**, *29* (20), 8884.

(36) Kolb, H. C.; Finn, M. G.; Sharpless, K. B. *Angew. Chem. Int. Ed.* **2001**, *40* (11), 2004.

(37) Kaur, G.; Singh, G.; Singh, J. *Mater. Today Chem.* **2018**, *8*, 56.

(38) Guterman, R.; Rabiee Kenaree, A.; Gilroy, J. B.; Gillies, E. R.; Ragogna, P. J. *Chem. Mater.* **2015**, *27* (4), 1412.

(39) Kim, D. W. *J. Fluor. Chem.* **2015**, *174*, 142.

(40) Takayama, Y.; Kusamori, K.; Nishikawa, M. *Molecules* **2019**, *24* (1), 172.

(41) Hoyle, C. E.; Bowman, C. N. *Angew. Chem. Int. Ed.* **2010**, *49* (9), 1540.

(42) Guterman, R.; Gillies, E. R.; Ragogna, P. J. *Dalton Trans.* **2015**, *44* (35), 15664.

(43) Stiles, A. R.; Rust, F. F.; Vaughan, W. E. *J. Am. Chem. Soc.* **1952**, *74* (13), 3282.

(44) *Conjugated Polymers Perspective, Theory, and New Materials*, Fourth Ed.; Reynolds, J. R., Thompson, B. C., Skotheim, T. A., Eds.; CRC Press: Boca Raton, Florida, 2019.

(45) Wang, M.; Baek, P.; Akbarinejad, A.; Barker, D.; Travas-Sejdic, J. *J. Mater. Chem. C* **2019**, *7* (19), 5534.

(46) Understanding Fluoropolymers https://www.azom.com/article.aspx?ArticleID=17673 (accessed Jul 10, 2019).

(47) Dobrynin, A. V; Rubinstein, M. *Prog. Polym. Sci.* **2005**, *30*, 1049.

(48) Cheng, S.; Beyer, F. L.; Mather, B. D.; Moore, R. B.; Long, T. E. *Macromolecules* **2011**, *44* (16), 6509.

(49) Hemp, S. T.; Smith, a E.; Allen, M. H.; Bryson, J. M.; Long, T. E. *Biomacromolecules* **2012**, *20*, 231.

(50) Pretula, J.; Kaluzynski, K.; Wisniewski, B.; Szymanski, R.; Loontjens, T.; Penczek, S. *J. Polym. Sci. A* **2007**, *45* (3), 2468.

(51) Arsenault, A. C.; Míguez, H.; Kitaev, V.; Ozin, G. A.; Manners, I. *Adv. Mater.* **2003**, *15* (6), 503.

(52) Chikh, L.; Delhorbe, V.; Fichet, O. *J. Memb. Sci.* **2011**, *368*, 1.

(53) Alagiriswamy, a a; Jäger, C.; Haarer, D.; Thelakkat, M.; Knoll, a; Krausch, G. *J. Phys. D. Appl. Phys.* **2007**, *40* (16), 4855.

(54) Guterman, R.; Berven, B. M.; Corkery, T. C.; Nie, H.; Idacavage, M.; Gillies, E. R.; Ragogna, P. J. *J. Polym. Sci. A* **2013**, 2782.

(55) Cuthbert, T. J.; Guterman, R.; Ragogna, P. J.; Gillies, E. R. *J. Mater. Chem. B* **2015**, *3* (8), 1474.

(56) Means, A. K.; Grunlan, M. A. *ACS Macro Lett.* **2019**, *8*, 705.

(57) Guterman, R.; Hesari, M.; Ragogna, P. J.; Workentin, M. S. *Langmuir.* **2013**, *29* (21), 6460.

(58) Guterman, R.; Gillies, E. R.; Ragogna, P. J. *Langmuir.* **2015**, *31* (18), 5181.

(59) Cuthbert, T. J.; Evoy, E.; Bow, J. P. J.; Guterman, R.; Stubbs, J. M.; Gillies, E. R.; Ragogna, P. J.; Blacquiere, J. M. *Catal. Sci. Technol.* **2017**, *7* (13), 2685.

(60) Whittell, G. R.; Hager, M. D.; Schubert, U. S.; Manners, I. *Nat. Mater.* **2011**, *10* (3), 176.

(61) Vidal, F.; Jäkle, F. *Angew. Chem. Int. Ed.* **2019**, *58*, 5846.

(62) Kenaree, A. R.; Gilroy, J. B. *Dalton Trans.* **2016**, *45* (45), 18229.

(63) Liu, K.; Clendenning, S. B.; Friebe, L.; Chan, W. Y.; Zhu, X.; Freeman, M. R.; Yang, G. C.; Yip, C. M.; Grozea, D.; Lu, Z.; Manners, I. *Chem. Mater.* **2006**, *18* (10), 2591.

(64) Zhang, J.; Yan, Y.; Chen, J.; Chance, W. M.; Gai, Z.; Tang, C. *Chem. Mater.* **2014**, *26* (10), 3185.

(65) Paquette, J. A.; Gilroy, J. B. *J. Polym. Sci. A* **2016**, *54*, 3257.

(66) Zou, X.; Zhang, Y. *Chem. Soc. Rev.* **2015**, *44* (15), 5148.

(67) Chang, Z. R.; Lv, H. J.; Tang, H.; Yuan, X. Z.; Wang, H. *J. Alloys Compd.* **2010**, *501* (1), 14.

(68) Fan, C. L.; Lin, C. R.; Han, S. C.; Chen, J.; Li, L. F.; Bai, Y. M.; Zhang, K. H.; Zhang, X. *New J. Chem.* **2014**, *38* (2), 795.

(69) Waldrop, M. M. *Nature* **2016**, *530*, 144.

(70) Awschalom, D. D.; Flatté, M. E.; Samarth, N. *Sci. Am.* **2002**, *286* (6), 66.

(71) Bader, S. D.; Parkin, S. S. P. *Annu. Rev. Condens. Matter Phys.* **2010**, *1*, 71.

(72) Bader, S. D. *Rev. Mod. Phys.* **2006**, *78*, 1.

(73) Ando, K. *Science.* **2006**, *312*, 1883.

(74) *Coal Gasification Processes*; Nowacki, P., Ed.; Noyes Data Corporation: New Jersey, USA, 1981.

(75) *The Efficient Use of Steam*; Goodall, P. M., Ed.; IPC Science and Technology Press: Surrey, England, 1980.

(76) Li, Y.; Dai, H. *Chem. Soc. Rev.* **2014**, *43* (15), 5257.

(77) Li, X.; Zheng, S.; Jin, L.; Li, Y.; Geng, P.; Xue, H.; Pang, H.; Xu, Q. *Adv. Energy Mater.* **2018**, *8* (23), 1800716.

(78) Li, Y.; Lu, J. *ACS Energy Lett.* **2017**, *2*, 1370.

(79) Masa, J.; Xia, W.; Sinev, I.; Zhao, A.; Sun, Z.; Grützke, S.; Weide, P.; Muhler, M.; Schuhmann, W. *Angew. Chem. Int. Ed.* **2014**, *53* (32), 8508.

(80) Serov, A.; Andersen, N. I.; Roy, A. J.; Matanovic, I.; Artyushkova, K.; Atanassov, P. *J. Electrochem. Soc.* **2015**, *162* (4), F449.

(81) Li, X.; Fang, Y.; Lin, X.; Tian, M.; An, X.; Fu, Y.; Li, R.; Jin, J.; Ma, J. *J. Mater. Chem. A* **2015**, *3* (33), 17392.

(82) Xu, Y.; Wu, R.; Zhang, J.; Shi, Y.; Zhang, B. *Chem. Commun.* **2013**, *49* (59), 6656.

(83) Callejas, J. F.; Read, C. G.; Roske, C. W.; Lewis, N. S.; Schaak, R. E. *Chem. Mater.* **2016**, *28*, 6017.

(84) Shi, Y.; Zhang, B. *Chem. Soc. Rev.* **2016**, *45* (6), 1529.

(85) Yu, J.; Li, Q.; Li, Y.; Xu, C.; Zhen, L.; Dravid, V. P.; Wu, J. *Adv. Funct. Mater.* **2016**, *26*, 7644.

(86) Tan, Y.; Wang, H.; Liu, P.; Shen, Y.; Cheng, C.; Hirata, A.; Fujita, T.; Tang, Z.; Chen, M. *Energy Environ. Sci.* **2016**, *9* (7), 2257.

(87) Pan, Y.; Lin, Y.; Chen, Y.; Liu, Y.; Liu, C. *J. Mater. Chem. A* **2016**, *4* (13), 4745.

(88) Mi, Y.; Yang, C.; Zuo, Z.; Qi, L.; Tang, C.; Zhang, W.; Zhou, H. *Electrochim. Acta* **2015**, *176*, 642.

(89) Salunkhe, R. R.; Kaneti, Y. V.; Kim, J.; Kim, J. H.; Yamauchi, Y. *Acc. Chem. Res.* **2016**, *49* (12), 2796.

(90) Tang, H.; Cai, S.; Xie, S.; Wang, Z.; Tong, Y.; Pan, M.; Lu, X. *Adv. Sci.* **2015**, *3*, 1500265.

(91) Julien, P. A.; Mottillo, C.; Friščić, T. *Green Chem.* **2017**, *19* (12), 2729.

(92) Galanakis, I.; Dederichs, P. H. *Half-metallic alloys: fundamentals and applications*; Springer Berlin Heidelberg: Berlin, Germany, 2005.

(93) Weihrich, R.; Pöttgen, R.; Pielnhofer, F. *Angew. Chem. Int. Ed.* **2018**, *57* (48), 15642.

(94) Bujak, P.; Kulszewicz-Bajer, I.; Zagorska, M.; Maurel, V.; Wielgus, I.; Pron, A. *Chem. Soc. Rev.* **2013**, *42* (23), 8895.

(95) Karla, I.; Pierre, J.; Skolozdra, R. V. *J. Alloys Compd.* **1998**, *265* (1–2), 42.

(96) Casper, F.; Felser, C. *Solid State Commun.* **2008**, *148* (5–6), 175.

(97) Bende, D.; Wagner, F. R.; Grin, Y. *Inorg. Chem.* **2015**, *54* (8), 3970.

(98) Bhattacharyya, G.; Choudhuri, I.; Pathak, B. *Phys. Chem. Chem. Phys.* **2018**, *20* (35), 22877.

(99) Bhattacharyya, G.; Choudhuri, I.; Bhauriyal, P.; Garg, P.; Pathak, B. *Nanoscale* **2018**, *10* (47), 22280.

(100) Du, J.; Dong, S.; Zhou, B.; Zhao, H.; Feng, L. *Appl. Phys. A* **2017**, *123* (4), 1.

(101) Bahramy, M. S.; Ogawa, N. *Adv. Mater.* **2017**, *29* (25).

(102) Babu, S. H.; Kaleemulla, S.; Rao, N. M.; Krishnamoorthi, C. *J. Magn. Magn. Mater.* **2016**, *416*, 66.

(103) Zhou, C.; Ghods, A.; Saravade, V. G.; Patel, P. V.; Yunghans, K. L.; Ferguson, C.; Feng, Y.; Jiang, X.; Kucukgok, B.; Lu, N. (Luna); Ferguson, I. *ECS Trans.* **2017**, *77* (6), 3.

(104) Canfield, P. C.; Thompson, J. D.; Beyermann, W. P.; Lacerda, A.; Hundley, M. F.; Peterson, E.; Fisk, Z.; Ott, H. R. *J. Appl. Phys.* **1991**, *70* (10), 5800.

(105) Fisk, Z.; Canfield, P. C.; Beyermann, W. P.; Thompson, J. D.; Hundley, M. F.; Ott, H. R.; Felder, E.; Maple, M. B.; Lopez De La Torre, M. A.; Visani, P.; Seaman, C. L. *Phys. Rev. Lett.* **1991**, *67* (23), 3310.

(106) Tang, J.; Wang, K. L. *Nanoscale* **2015**, *7* (10), 4325.

(107) Hadadpour, M.; Ragogna, P. J. *J. Polym. Sci. A* **2015**, *53* (23), 2747.

(108) Clendenning, S. B.; Han, S.; Coombs, N.; Paquet, C.; Rayat, M. S.; Grozea, D.; Brodersen, P. M.; Sodhi, R. N. S.; Yip, C. M.; Lu, Z.-H.; Manners, I. *Adv. Mater.* **2004**, *16* (4), 291.

(109) Chan, W. Y.; Clendenning, S. B.; Berenbaum, A.; Lough, A. J.; Aouba, S.; Ruda, H. E.; Manners, I. *J. Am. Chem. Soc.* **2005**, *127* (6), 1765.

(110) Dong, Q.; Li, G.; Ho, C. L.; Faisal, M.; Leung, C. W.; Pong, P. W. T.; Liu, K.; Tang, B. Z.; Manners, I.; Wong, W. Y. *Adv. Mater.* **2012**, *24* (8), 1034.

(111) She, L.; Li, J.; Wan, Y.; Yao, X.; Tu, B.; Zhao, D. *J. Mater. Chem.* **2011**, *21* (3), 795.

(112) Rider, D. A.; Liu, K.; Eloi, J.; Vanderark, L.; Yang, L.; Wang, J.; Grozea, D.; Lu, Z.; Russell, T. P.; Manners, I. *ACS Nano* **2008**, *2* (2), 263.

(113) Cheng, J. Y.; Ross, C. A.; Chan, V. Z. H.; Thomas, E. L.; Lammertink, R. G. H.; Vancso, G. J. *Adv. Mater.* **2001**, *13* (15), 1174.

(114) Zhang, J.; Yan, Y.; Chance, M. W.; Chen, J.; Hayat, J.; Ma, S.; Tang, C. *Angew. Chem. Int. Ed.* **2013**, *52* (50), 13387.

(115) Darling, S. B. *Prog. Polym. Sci.* **2007**, *32* (10), 1152.

(116) Kenaree, A. R.; Gilroy, J. B. *Organometallics.* **2017**, *36*, 2483.

(117) Zamora, M.; Bru, S.; Alonso, B.; Cuadrado, I. *Macromolecules* **2011**, *44*, 7994.

(118) Hadadpour, M.; Gwyther, J.; Manners, I.; Ragogna, P. J. *Chem. Mater.* **2015**, *27*, 3430.

Chapter 2

2 Patterned Phosphonium-Functionalized Photopolymer Networks as Ceramic Precursors

2.1 Introduction

Metallopolymers are structurally diverse and have found a role in numerous applications,[1] one in particular is their role as precursors to prepare polymer-derived ceramics.[2–5] Ceramics can have magnetic, conductive, or semiconductive properties that are dictated by their chemical architecture, and act as components in a vast array of digital electronics. These high technology ceramics (HTC) must meet performance minima, but with growing demand for smaller, more compact devices, the ability to pattern these materials on smaller and smaller length scales is a key technical challenge. For example, bit patterned media and orientation-patterned semiconductors are emerging technologies that rely on the long range uniform, nano- and micro-patterning of magnetic and semiconductive materials, respectively.[6–9] Despite the desire to push these and similar technologies forward, it is challenging to simultaneously achieve the desired composition, function and spacial control tolerances required for the devices to function.

In this context, metallopolymers have been a field of interest for their ability to act as ceramic precursors where the inorganic elements of the metalloploymer dictate the resulting ceramic composition. Introducing the desired elemental composition into these ceramic precursors can be achieved by one of two general methods; either by polymerization of a metal-containing monomer, or by post-polymerization functionalization of a pre-existing polymer scaffold. To address the second requirement of HTC, the precursor must be patterned and retain its shape upon pyrolysis. This challenge can be addressed by self-assembly or lithography of the metallopolymer with the desired pre-ceramic composition. [10–15]

Combining polymer derived ceramics with metallopolymer lithography[10–13] and block copolymer self assembly[14–16] has been an innovative approach to achieve spatial control on the nano scale. By pyrolyzing these assemblies, organic matter is volatilized, with the metal-containing ceramics occupying the same well-defined regions that were predetermined by the block copolymer assembly. This approach to patterned metal containing ceramics is underscored by the pyrolysis of a range of different elements including main group polymers,[14] polyferrocenylsilane (PFS)[15] and cobalt-containing[17] block copolymers.

While it is possible to synthesize new monomers for polymerization, incorporating elemental diversity and density into the polymer remains a challenge by this method. Further, post-polymerization modification can degrade polymeric material before self-assembly/patterning. There are countless molecular precursors with well-defined stoichiometric ratios of a wide range of element types, which in principle could be leveraged for obtaining precise control over ceramic composition. All that is required for post-polymerization functionalization is a mechanism of binding these molecular precursors to the polymer scaffold. Coordination chemistry[3,5,11,12,18–20] and ion exchange[17,21] are the mechanisms that have been explored.

An underexplored area of metallopolymer chemistry has been metal functionalization of photopolymer networks. Photopolymer networks can be synthesized by irradiating a crosslinker/photoinitiator mixture to make a crosslinked insoluble polymer network. These networks can be physically shaped at any step along the preparative pathway by spin coating the neat formulation, masking during irradiation or lithography of the final solid material (Scheme 2.1). If polymer networks could be functionalized with inorganic elements, then they would be promising candidates to act as HTC precursors because of their ability to be shaped.

Our research group has recently worked on incorporating phosphonium functionalities into photopolymer networks.[22–26] We have shown that not only can these networks be physically shaped, but they can also be patterned by ion exchange,[22] lithography or stamping[24] methodologies. While there are a handful of photopolymer networks that have been functionalized with metals, they have never been used in the context of shaped HTC precursors.

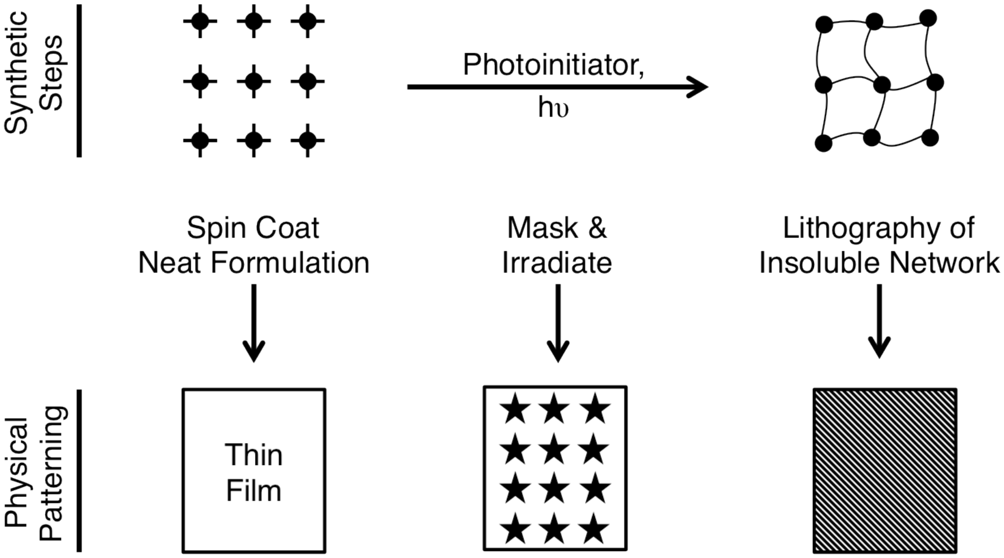

Scheme 2.1: Routes for the preparation and patterning of photopolymer networks.

In this context, we employ a phosphonium-containing semi-interpenetrating polymer network (S-IPN)[27] to act as a scaffold for the assembly of anionic metal complexes. The S-IPN are insoluble, but solvent swellable, and given that the linear phosphonium polymer (**2.1**) from which the substrates are constructed is a polyelectrolyte with labile chloride counterions, anion exchange is facile.[28] We demonstrate that phosphonium-containing S-IPN can be prepared by UV-curing methodologies, which allows for spatial control of the bulk material. The bulk material can be patterned using electron beam lithography (EBL) where the inscribed pattern is retained by the polymer network after ion exchange with **2.2Mo** and then even *after* pyrolysis. This is underscored by the preparation of uniformly amorphous ceramic material patterned as Sierpinski triangles and "microchips" with features on the micron scale (10^{-6}m). These results represent a brand-new application of metallized photopolymer networks and a method that has the potential to be applied towards making patterned HTC ceramics using photopolymer networks and small molecules/ organometallics or main group compounds. This has the potential general method to patterned ceramics that employs simple to prepare, easy to shape, UV curable polymer precursors amenable to onwards functionalization after patterning. Results and Discussion

2.2 Results and Discussion

Polymer networks **2.4P$^+$** and **2.5P$^+$** (Scheme 2.2) consist of a linear homopolymer of phosphonum salt repeat units interlaced within a UV-cured network constructed from tetra(ethylene glycol) diacrylate (TEGDA) and 2-hydroxyethyl acrylate (HEA), to give a semi-interpenetrating polymer network.[29] Analysis by DSC revealed identical thermal behaviour between phosphonium-containing and phosphonium-free networks, indicative of a true semi-interpenetrating polymer network.[23,25]

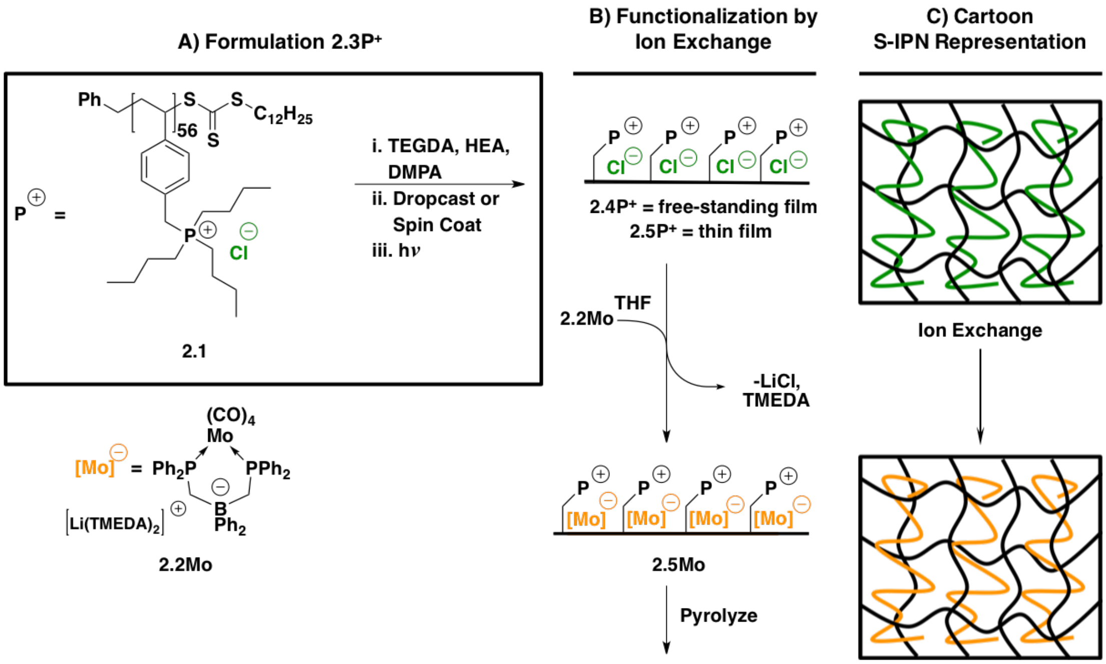

Scheme 2.2: A) Showing the composition of formulation **2.3P$^+$** followed by UV curing to form S-IPN networks **2.4P$^+$** and **2.5P$^+$**. B) Functionalization with the metallic anion **2.2Mo** by ion exchange. C) Cartoon S-IPN representation showing the polymer **2.1** is intercalated in the photopolymer network.

This approach for phosphonium immobilization is simple and can be applied to virtually any UV-curable system while still having access to the anion-exchange capabilities.[22] A class of bis(phosphino)borate ligands that are anionic at the borate site and remain so once coordinated to a metal have been synthesized by Peters and coworkers.[30] Benefits of this particular system include tight binding of a metal centre because of the bidentate nature of the ligand as well as the increased electron-donation ability that arises from the anionic borate in the ligand backbone.[30] Using the phosphonium S-IPN as a platform for ion exchange, the bis(phosphino)borate ligand can be used as an anionic shuttle to bring different inorganic elements onto the polymeric support (e.g. **2.2Mo**; Scheme 2.2).

2.2.1 S-IPN Optimization and Characterization

Polymer **2.1** was dissolved in a UV-curable formulation to make a freestanding semi-interpenetrating polymer network (**2.4P$^+$**). The amount of **2.1** dissolved in the formulation was optimized so that delamination from the substrate did not occur during UV curing, anion exchange with **2.2Mo** or pyrolysis. Formulations with 9.1 weight % of **2.1** was the optimal phosphonium content in this regard, however these formulations did not yield Mo-containing ceramics upon pyrolysis. The optimized formulation of 38.4:38.4-weight % mixture of TEGDA, and HEA, an additive with 0.1 weight % photoinitiator, DMPA with the remainder being compound **2.1** (23.1 wt. %), yielded Mo-containing ceramics after pyrolysis. Formulations with the content of **2.1** greater than this easily delaminated and subsequent pyrolysis experiments were not successful in generating Mo-containing materials.

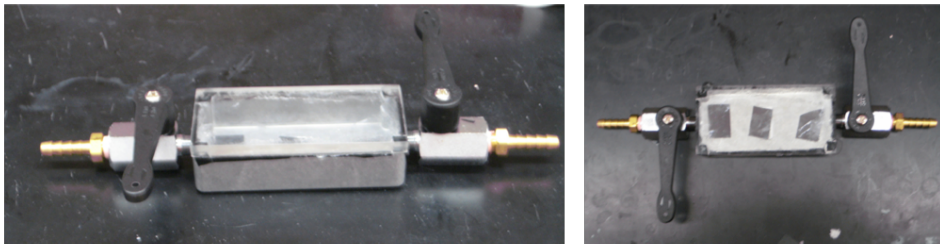

Figure 2.1: Side and top view of the inert atmosphere curing cell.

Networks **2.4C** and **2.4P$^+$** were prepared by sandwiching the UV-curable formulation (**2.3C** and **2.3P$^+$,** respectively) between two glass slides followed by UV curing (Figure 2.8). Films **2.5P$^+$** were prepared by spin coating **2.3P$^+$** onto Si wafers, loaded into a UV curing cell, purged with N_2 for 20 seconds and cured (Figure 2.1). **2.4P$^+$** was used for the bulk characterization of the S-IPN network, while **2.4C** was used as a control (Scheme 2.3). Network **2.5P$^+$** was used as a thin film platform to make patterned ceramic precursors.

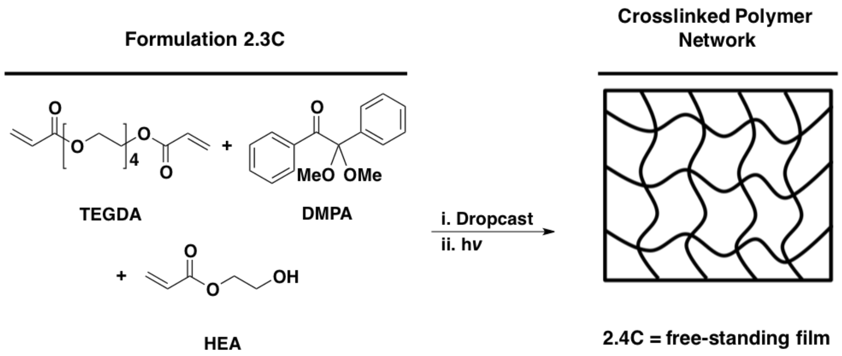

Scheme 2.3: Photopolymerization of TEGDA and HEA using DMPA as a photoinitiator to make a crosslinked polymer network for use as a control against the S-IPN while testing for physical properties.

While polymer networks can be swelled in a solvent thus promoting anion exchange within the bulk material, a drawback is that while this promotes anion exchange, small amounts of **2.1** can simultaneously leach out. Therefore, the swellability and degree of polymer leaching were assessed first.

A THF solution of **2.2Mo** was used for ion exchange, followed by workup of the functionalized film with water, then ethanol. All three solvents promoted swelling of the network, which is necessary for uniform ion exchange and workup throughout the bulk film (Table 2.1). After swelling **2.4P$^+$** in THF the Cl^- test of the supernatant using $AgNO_{3(aq)}$ was negative, congruous with the fact that **2.1** is insoluble in THF. However, both the water and ethanol supernatants from **2.4P$^+$** swelling experiments yielded a small amount of white precipitate, indicative of small amounts of **2.1** leaching from the bulk. Identical experiments performed on the control sample, **2.4C** resulted in clear, colourless solutions.

After swelling in each solvent, the films were vacuum dried, weighed and gel content was determined. Similar gel content values were obtained for **2.4C** and **2.4P$^+$** underscoring that **2.1** does not leach from the network in THF. **2.4P$^+$** networks swelled in water or ethanol showed gel contents 6.8% and 8.5% lower than those for **2.4C**, respectively. Nevertheless, this did not impose a negative impact on the formation of Mo-containing ceramics.

Table 2.1: Mean Swell % and Gel Content % data for **2.4C** and **2.4P$^+$** in THF, H_2O and ethanol.

Solvent	Sample	Swell %	Gel Content %
THF	**2.4C**	19.86 ± 0.74	80.07 ± 0.09
	2.4P$^+$	19.37 ± 0.23	81.26 ± 0.17
H_2O	**2.4C**	24.76 ± 0.53	76.69 ± 0.20
	2.4P$^+$	36.53 ± 1.11	69.84 ± 0.42
Ethanol	**2.4C**	19.69 ± 0.40	79.59 ± 0.15
	2.4P$^+$	32.22 ± 1.13	71.07 ± 0.62

2.2.2 Calibration

While the ratio of Mo:P in the ion exchanged polymer networks (**2.5Mo**) were ultimately quantified by EDX, it was necessary to devise an efficient method to approximate the conversion of the anion exchange process with **2.2Mo**. Given that **2.2Mo** contains a carbonyl ligand, this functional group offers a convenient spectroscopic handle (IR), one that is already utilized to characterize cure percentage for the polymer networks. By dissolving different known amounts of **2.2Mo** into **2.3P**$^+$ to form solutions of **2.6Mo** and recording the IR spectrum, a calibration curve of the ratio of **2.3P**$^+$ vs. concentration could be plotted (Figure 2.2). For simplicity, the concentration of **2.2Mo** dissolved in **2.6Mo** was converted to % conversion for the ion exchange reaction of **2.2Mo** into **2.3P**$^+$.

A ratio of peak heights from the *trans*-carbonyl signal of **2.2Mo** (2003 cm^{-1}) versus the acrylate carbonyl signal (1724 cm^{-1}) can be determined (Ratio 1). These signals were well-resolved and a calibration curve was generated by varying the concentration of **2.2Mo** and the acrylate signal as an internal standard.

2.2.3 Ion Exchange

The initial IR spectrum collected immediately after ion exchange reveals a large excess of **2.2Mo**. The films were rinsed with water to selectively remove LiCl and excess **2.2Mo** was washed away with ethanol, restoring film transparency. It is important to remove LiCl first in order to avoid reversing the salt metathesis.

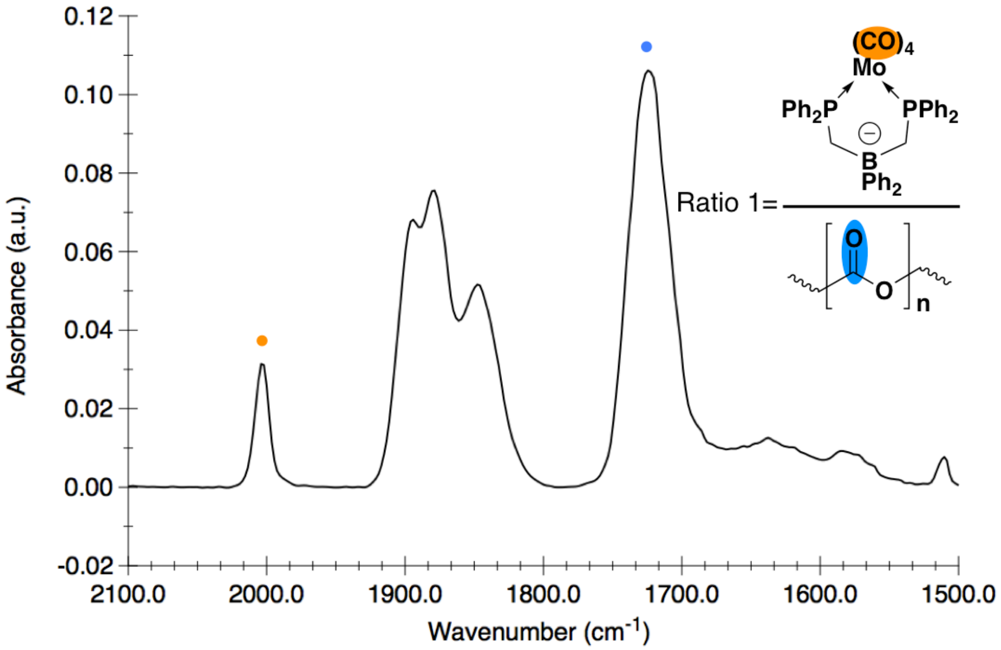

Figure 2.2: ATR-IR spectrum of **2.5Mo**. % conversion was calculated to be 71% by using the peak intensities at $\nu_{Mo(CO)}$ (orange) and $\nu_{(acrylate)C=O}$ (blue) in Ratio 1 and the calibration curve equation from the SI.

The results show a large drop in **2.2Mo** concentration after the first ethanol wash, followed by a steady decline and ultimate leveling of **2.2Mo** content after six washes (Figure 2.3). This work up procedure was applied to **2.5P$^+$** exchanged with **2.2Mo**, and revealed an ion exchange conversion of 71% (Figure 2.2). For this exchange amount, the ratio of Mo:P in **2.5Mo** should be 1:3.4. Network **2.5Mo** was analyzed by EDX spectroscopy, revealing a ratio of 1:5 for Mo:P and although this is not an exact match from the IR calibration curve, the method gives a close approximation for the degree of exchange.

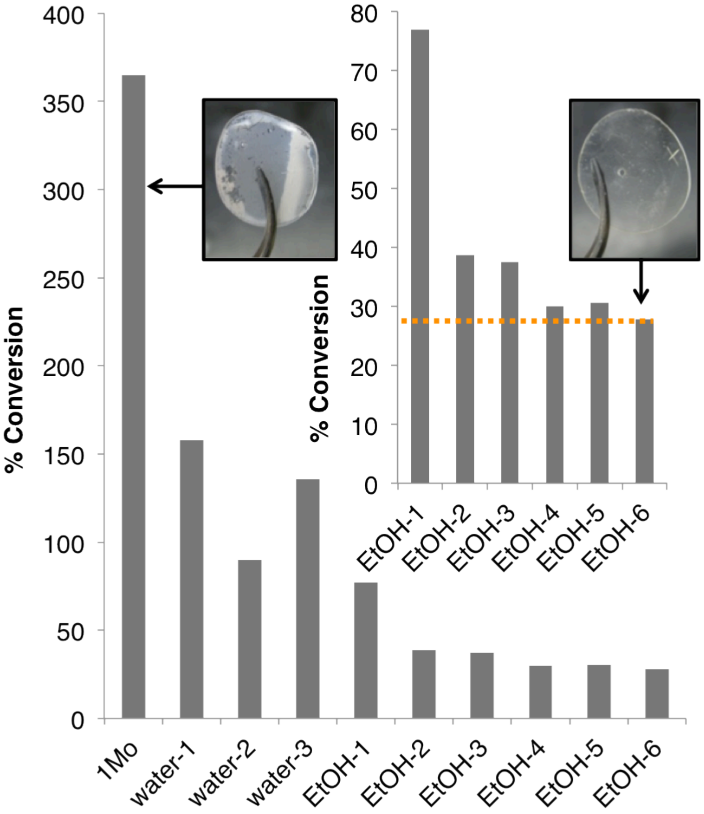

Figure 2.3: Conversion % data from the workup of **2.4Mo**, "leveling out" is denoted by the orange dotted line. Network **2.4Mo** before and after rinsing are pictured on the left and right, respectively.

2.2.4 Ceramic Composition

Network **2.5Mo** was pyrolyzed at different temperatures and for different time durations and the atomic % data is outlined in Table 2.2. The composition did not yield the ratio of Mo:P that was present in parent films, it is clear from the data that at higher temperatures, the P content was much lower. In order to rule out air oxidation, after pyrolysis the samples were sealed in the pyrolysis tube under N_2, then subjected to analysis. There was no significant difference between the samples stored in the atmosphere or under N_2, thus O arising from the network itself is the likely source.

The EDX data shows that all of the ceramics contain more Mo than P and point to the presence of P-doped molybdenum oxide (Table 2.2). The missing P can be attributed to the fact that phosphorus is oxophilic and acrylates are O-rich molecules and we hypothesize that at these elevated temperatures P_4O_{10} is being generated (b.p. = 360 °C) and expelled during heating. Similarly, it is likely that the acrylates are also the source of O in the resulting molybdenum oxide.

Table 2.2: Atomic ratios of C, O, P and Mo acquired by EDX spectroscopy for ceramics formed at different temperatures and times. * = not detected.

Time (h)	Temp. (°C)	Atomic Ratio (C:O:P:Mo)			
		Elements			
		C	O	P	Mo
3	800	61.0	33.7	3.5	1.8
	900	61.7	35.6	1.9	0.8
	1000	6.4	90.1	0.9	2.6
4	800	19.8	71.1	7.4	1.7
	900	14.5	82.9	1.0	1.6
	1000	*	89.2	3.2	7.6

The formation of P_4O_{10} is corroborated by the XPS data, which revealed the oxidation states of P in the ceramics formed at different temperatures. The XPS data showed the presence of phosphate in the samples, which supports our above hypothesis as P_4O_{10} reacts with water in air to form phosphoric acid, thus explaining the presence of the phosphate edge in the XPS data. It seems that at the elevated temperature of 1000 °C and in the presence of H_2, the phosphate (P(V)) was reduced to phosphide (P^{3-}) and therefore, these ceramics are best described as phosphide doped molybdenum oxide.

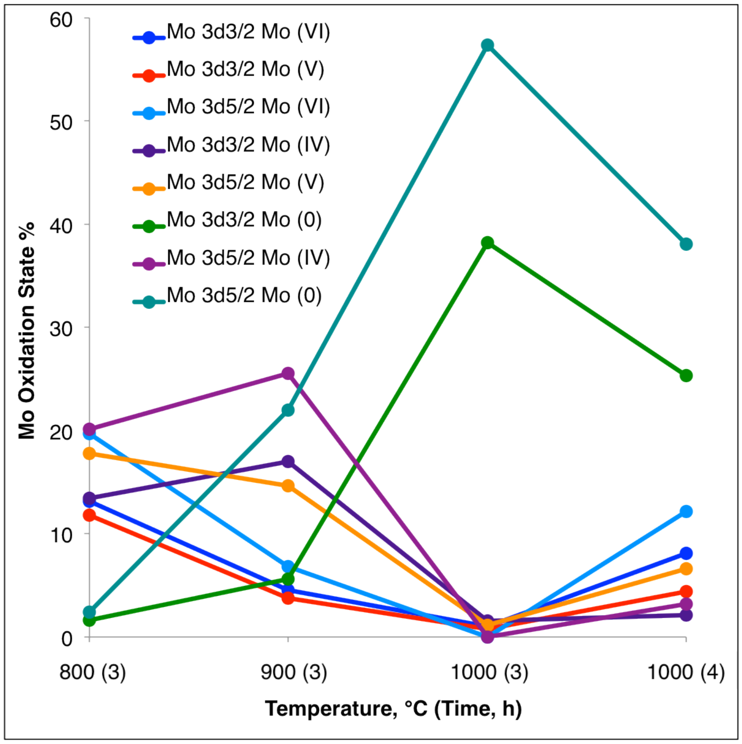

Figure 2.4: Distribution of oxidation states of Mo for different pyrolysis temperatures and times determined by XPS.

The ceramics formed at 800 and 900 °C for 3 hours are relatively carbon rich, but there is a stark decrease in the carbon content when either the temperature is elevated to 1000 °C, or the pyrolysis time is increased to 4 hours. No carbon was detected in the sample that was pyrolyzed at 1000 °C for 4 hours (Table 2.2).

The XPS results revealed that the ceramics are composed of a mixture of Mo(0), IV, V and VI, which is an established phenomenon for molybdenum oxide (Figure 2.4).[31,32] It appears that while the reducing conditions at elevated temperatures are beneficial in removing unwanted carbon and reducing phosphate in favour of phosphide, it can also have the detrimental effect of decomposing the metal-containing ceramic through the loss of H_2O and CH_4.

The PXRD data is consistent with the composition and oxidation state data extracted from EDX and XPS and points to a mixture of amorphous materials in all ceramics. Those formed at 800 and 900 °C for 4 hours and 1000 °C for 3 hours all show evidence for MoO_3 and $Mo(PO_3)_3$, which accounts for the phosphate edge in the XPS.[33,34] Ceramics formed at 1000°C for 3 hours also show that there is a mixture of phosphate and phosphide with the presence of the Mo-rich phosphide, Mo_3P,[35] while those held at 1000 °C for 4 hours show no phosphate, yet a mixture of Mo_3P with MoO_3. Only ceramics formed at 800 °C for 4 hours showed the presence of any Mo_2C,[36] likely due to the relatively high concentration of carbon in those samples, which was observed using EDX. All ceramics formed at 900 °C or higher showed evidence for Mo metal (Figure 2.4).[37]

2.2.5 Ceramic Morphology:

In order to determine the necessity of the **2.5P$^+$** as a platform to controllably deposit ceramics, **2.2Mo** was dropcast onto a Si wafer and pyrolyzed. The morphology of the resulting ceramic was inconsistent across the surface. Meanwhile, the images of pyrolyzed **2.5Mo** demonstrate a uniform amorphous ceramic (Figure 2.5).

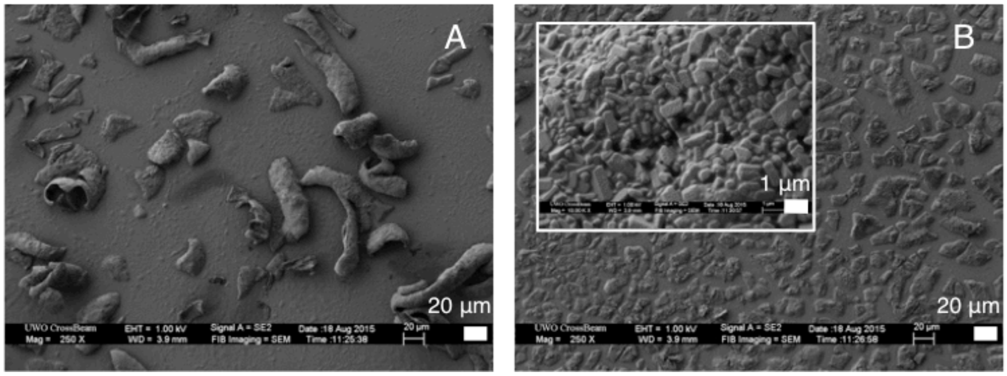

Figure 2.5: SEM images of different regions of dropcast and pyrolyzed **2.2Mo** on Si: A) Amorphous ceramic B) A flat, non-uniform region imaged at different magnifications.

The substrate containing **2.5Mo** was pyrolyzed at 800, 900 or 1000 °C for either 3 or 4 hours. With increased temperature, the ceramic particles appear to remain amorphous and their presence is uniform over the bulk of the film, but they are spaced farther apart (Figure 2.6). This observation is consistent with the XPS data that reveals that the ceramic degrades at high temperature. Therefore, subsequent pyrolysis experiments on patterned ceramic precursors were conducted at 800 °C for 4 hours.

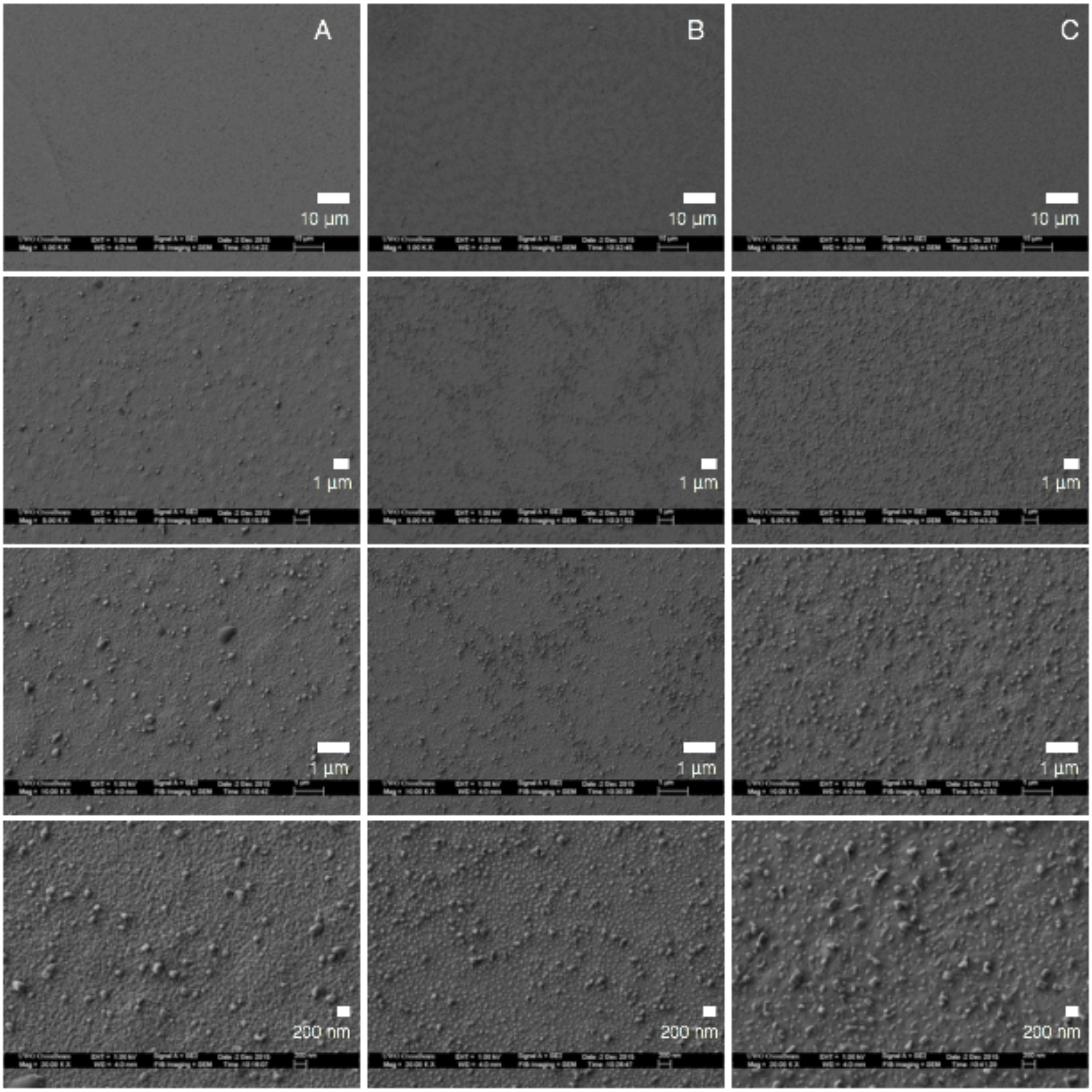

Figure 2.6: SEM images of **2.5Mo** pyrolyzed at A) 800 °C, B) 900 °C and C) 1000 °C for 4 hours.

2.2.6 Patterning

$2.5P^+$ was patterned by EBL with an array of “W[ester]N CHEMISTRY microchip” and Sierpinski triangle images of different sizes (either 45x45, 70x70 or 95x95 µm) and with cross-sectional features as small as 1µm. The patterned polymer network (Figure 2.7A) was then functionalized with **2.2Mo** using the same method for the preparation of **2.5Mo**. This patterned metal-functionalized polymer network was then pyrolyzed to give patterned ceramics (Scheme 2.4).

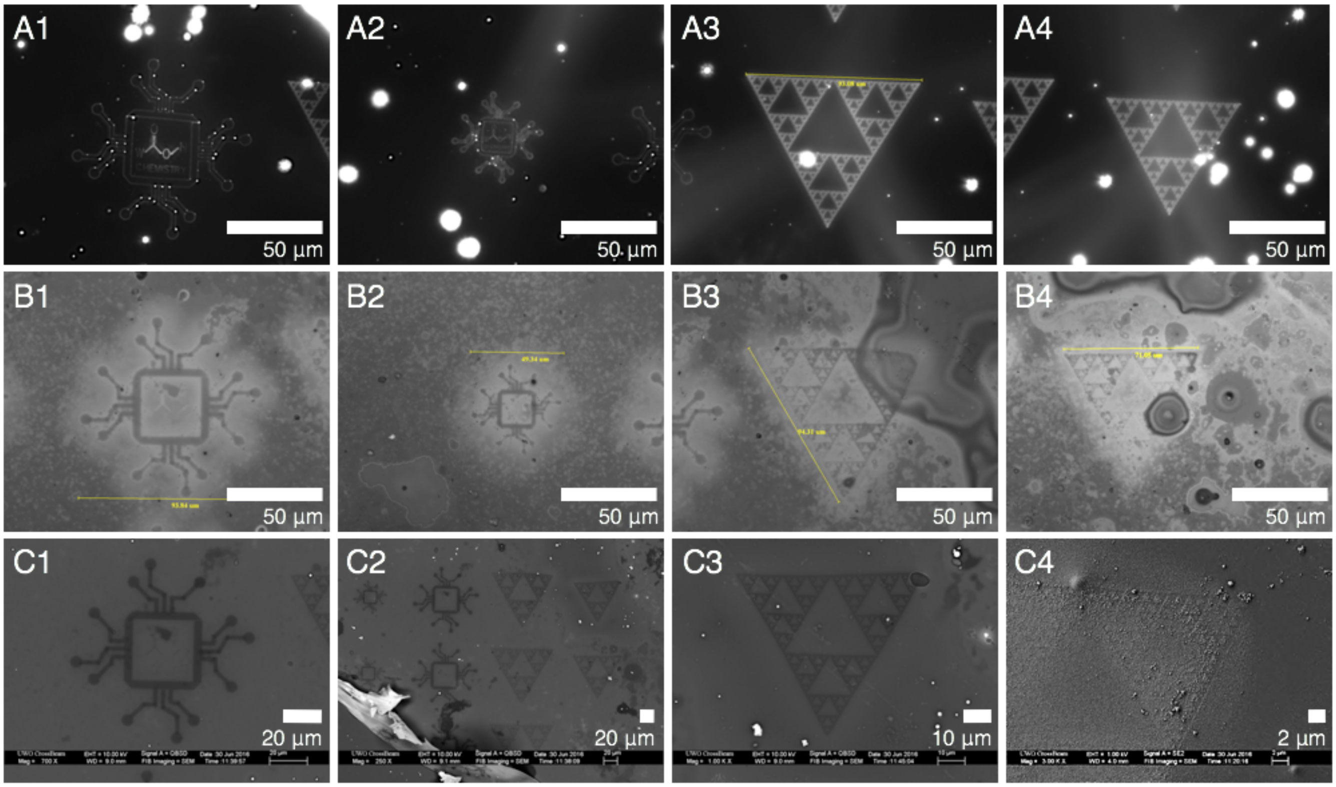

Figure 2.7: A) Dark field optical microscope pictures of patterned **$2.5P^+$**. B) Bright field optical microscope pictures of the patterned **$2.5P^+$** that were functionalized with **2.2Mo** and pyrolyzed. C) SEM images of pyrolyzed patterns.

Figure 2.7C2 shows how this method can result in deformities, which are thought to be the result of some degree of delamination in the polymer precursor during the processing steps. Nonetheless, this same image demonstrates the uniformity of the ceramic over the course of the bulk pattern. Figure 2.7B1, B2 and C1 show how the outline of the microchip image is retained from the polymer precursor to the ceramic, and that the 95x95 µm ceramic microchip has retained the writing. Figure 2.7B3, C3 and C4 show that the Sierpinski triangle pattern has excellent shape retention in that the 1µm features from the polymer precursor are discernible in the ceramic.

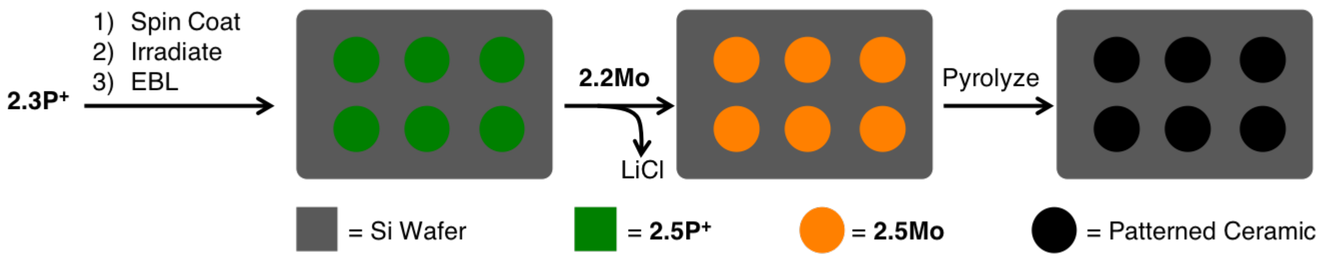

Scheme 2.4: Processing method to make patterned ceramics using **2.5Mo** as a precursor.

2.3 Conclusion

This work is the first example where the ease of shaping photopolymer networks has been exploited to make patterned ceramics. We have shown that the photopolymer network thin film **2.5P$^+$** can be functionalized by salt metathesis with **2.2Mo** to make a metallophotopolymer network. We have also shown that **2.5P$^+$** can be first patterned, subsequently functionalized and ultimately pyrolyzed to make patterned Mo-containing ceramics with shape retention of the initial inscription. The true value of this work lies in the fact that the method has the potential to be generally applied to not only other ionic systems, but also different types of functional photopolymer networks. Some examples being thiol-ene and phosphane-ene networks[38,39] where coordination chemistry[20] can be used over ion exchange to introduce the inorganic elements. There are many different metallic anions that can be applied to our current system and the coordination chemistry of thioethers and alkylphosphines is rich. Expanding this work to other systems offers the possibility to prepare a wide breadth of metal containing ceramics.

2.4 Instrumentation

Nuclear magnetic resonance (NMR) spectroscopy was conducted on a Varian INOVA 400 MHz spectrometer (^{1}H 400.09 MHz, ^{11}B{^{1}H} 128.2 MHz, ^{13}C{^{1}H} 100.5 MHz, ^{31}P{^{1}H} 161.82 MHz). All ^{1}H and ^{13}C{^{1}H} spectra were referenced relative to residual solvent signal ($CHCl_3$; ^{1}H $\delta = 7.26$ and ^{13}C $\delta = 77.2$). The chemical shifts for ^{31}P{^{1}H} spectroscopy were referenced using an external standard (85% H_3PO_4; $\delta_P = 0$). FT-IR spectra were recorded using a Bruker Tensor 27 spectrometer using attenuated total reflectance (ATR) with a ZnSe crystal. Photopolymerization was performed using a modified UV-curing system purchased from UV Process and Supply Inc. equipped with a medium pressure mercury vapour lamp (λ = 200-600 nm). The thicknesses of **2.4C** and **2.4P$^+$** were determined using an IP65 digital calliper. A PP2-H-U Power Puck II purchased from EIT Instrument Markets was used to determine light energy and power. The Power Puck was altered for the preparation of **2.4P$^+$** and **2.4C**. A glass slide was placed over the receiver of the power puck before it was passed under the UV-conveyer belt to determine the energy and power that passes through glass (402.352 mJ/cm^2, 185.550 mW/cm^2 UVA). A SDT Q600 thermogravimetric analyzer (TGA) was used to determine char yields. A TA Q20 differential scanning calorimeter (DSC) was used to determine glass transition temperatures (T_g). All T_g values are reported using the onset temperature from the last heating cycle. Si wafers were cut into squares (ca. 1x1 cm), treated with Piranha solution, rinsed with deionized water and dried before use. Pyrolysis was performed under 5 % H_2 (balance N_2) in a Lindberg furnace equipped with a quartz tube. A Hitachi S4500 FESEM instrument with a 10 kV electron beam was used to collect scanning electron microscopy (SEM) images and energy dispersive X-ray (EDX) spectra. Samples were osmium coated before SEM and EDX analysis. X-ray photoelectron spectroscopy (XPS) was performed using a Kratos AXIS Nova Spectrometer. An Intel CPS Powder Diffractometer was used with Cu K-α radiation to collect powder X-ray diffraction (PXRD) data. The diffraction patterns were assigned using the ICSD database and Match! software. Electron beam lithography (EBL) was performed using a LEO 1530 field emission scanning electron microscope (FE-SEM) fitted with a laser interferometer-controlled stage. EBL conditions consisted of 25 pA beam current, 30 keV electron acceleration and a 10 μm aperture. EBL-treated polymer films were rinsed in ethanol and imaged using a Zeiss Axioscop 2 MAT in dark field with a 50x objective lens. The same microscope was used in bright field mode to image the pyrolyzed patterns.

2.5 Synthesis and Reagents

The synthesis of all compounds and materials were performed on the bench top unless otherwise noted. When necessary, compounds were prepared in a nitrogen filled MBraun Labmaster dp glovebox or by using standard Schlenk techniques. All solvents were purchased from Caledon and dried using an MBraun controlled atmosphere solvent purification system and stored in Straus flasks under an N_2 atmosphere or over 4 Å molecular sieves. The synthesis of $[PBu_3(C_9H_9)][Cl]$, the corresponding polymer (**2.1**),[40] and $[Li(tmeda)_2][(PPh_2CH_2)_2BPh_2]$ (**2.2Mo**) were prepared using modified literature procedures.[30] Molybdenum hexacarbonyl (Strem Chemicals) was freshly sublimed under vacuum (-20 °C cold finger; 40 °C oil bath) before use, while all other reagents were used without further purification.

2.1. $[PBu_3(C_7H_9)][Cl]$ (3.233 g, 9.121 mol) was loaded into a 100 mL roundbottom flask equipped with a stir bar. A solution of the RAFT agent, benzyl dodecyl trithiocarbonate (42 mg, 0.11 mmol, 16 mL MeCN) and a solution (0.1 mL) of AIBN (31 mg, 0.19 mmol in 1 mL MeCN) were added to the round bottom, which was sealed and degassed for twenty minutes in an ice bath (0 °C). The vessel was placed in an oil bath at 80 °C for 6 hours. The flask was removed from the oil bath and cooled under running cold water to quench the reaction. The reaction mixture was concentrated on a rotovap and then added to a flask of stirring THF (500 mL) to give a large amount of fine white precipitate. The precipitate was separated by centrifugation and rinsed a second time before it was dried *in vacuo* to give a pale yellow powder. Yield: 70%. An integration ratio of polymerizable groups to non-polymerizable groups in a ^{1}H NMR spectrum of the reaction mixture were used to determine the conversion from monomer to polymer and the molecular weight of the polymer, MW: 22 000 g/mol. ^{1}H NMR: δ 7.35-7.45 (m, 1.10 H), 6.50 (dd, $^1J_{1H-1H}$, cis = 12 Hz, $^1J_{1H-1H}$, trans = 20 Hz, 0.22 H), 5.58 (d, $^1J_{1H-1H}$ trans = 20 Hz, 0.22 H), 5.11 (d, $^1J_{1H-1H}$ cis = 12 Hz, 0.23 H), 4.10 (d, $^2J_{1H-31P}$ = 16 Hz, 0.44 H), 2.35-2.45 (m, 4.82 H), 1.28 (br, 12.01 H), 0.74 (br, 9 H). Conversion: 78%, MW: 22000 g/mol. ^{1}H NMR: δ 7.13 (br), 6.75 (br), 3.81 (br), 2.26 (br), 1.87 (br), 1.25 (br), 1.01 (br), 0.98 (br), 0.70 (br). ^{13}C{^{1}H} NMR: δ 130.4 (br), 128.0 (br), 23.8 (d, $^3J_{31P-13C}$=27 Hz), 18.6 (d, $^2J_{31P-13C}$=40 Hz). FT-IR (cm^{-1} (ranked intensity)), 718 (10), 847 (7), 912 (3), 968 (11), 1010, (15), 1098 (5), 1235 (8), 1415 (12), 1457 (2), 1511 (4), 1627 (6), 2335 (13), 2863 (9), 2910 (14), 2932 (15). T_g = 161.2 °C.

2.2Mo. [Li(tmeda)(thf)]$^+$ was used as the cation for the bis(phosphino) borate starting material instead of [$C_8H_{16}N$]$^+$ (5-azaspiro[4,4]nona-2,7-dienium, ASN) due to the lack of availability of ASN. There is a solid state structure reported for the ASN counterion in the literature.[4] A solution of [Li(tmeda)$_2$][(PPh$_2$CH$_2$)BPh$_2$] (1300 mg, 1.62 mmol; 10 mL THF) was added to a solution of molybdenum hexacarbonyl (450 mg, 1.70 mmol; 20 mL THF). The reaction mixture was set to reflux (78 °C) for 18 hours under N_2 on the Schlenk line to give a bright yellow solution. Volatiles were removed *in vacuo* to give a yellow residue, which was triturated in diethyl ether (3 x 6 mL). The supernatant was decanted and the volatiles were removed from the precipitate *in vacuo* to give a white powder. Yield: 87%. Melting point: 158.9 – 165.0 °C, decomposition point: 198 °C. Single crystals suitable for X-ray diffraction were grown from the triturated ether supernatant and hexane in the freezer (18 hours, -30 °C). ^{1}H NMR: δ 7.29-7.33 (m, 8H), 6.99-7.05 (m, 12H), 6.89-6.91 (m, 4H), 6.61-6.62 (m, 4H), 6.56-6.57 (m, 2H), 3.70-3.72 (m, 4H), 2.33 (s, 4H), 2.17 (s, 12H), 2.03 (br, 4H), 1.84-1.87 (m, 4H). ^{13}C{^{1}H} NMR: δ 218.5 (d, $^2J_{31P-13C}$ = 13 Hz), 212.4 (t, $^2J_{31P-13C}$ = 9 Hz), 142.6-142.9 (m), 132.7, 131.8-131.9 (m), 126.7, 126.3-126.7 (m), 125.1, 121.0, 67.4, 56.4, 44.3, 37.8, 25.0. ^{31}P{^{1}H} NMR: δ 27.4. ^{11}B{^{1}H} NMR: δ 13.8 (s). FT-IR (cm^{-1} (ranked intensity)), (ν_{CO} denoted with *) 619 (6), 692 (3), 736 (4), 772 (15), 872 (7), 946 (13), 1033 (11), 1092 (9), 1432 (8), 1467 (10), 1480 (12), 1622 (14), 1847 (2)*, 1876 (1)*, 2003 (5)*. Raman (cm^{-1} (ranked intensity)) 169 (14), 229 (9), 417 (12), 458 (7), 620 (10), 1000 (1), 1030 (4), 1097 (11), 1186 (13), 1586 (3), 1892 (6), 2006 (5), 2802 (15), 2963 (8), 3055 (2). ESI^{-}MS: 771.1 *m/z* ($C_{42}H_{34}BMoO_4P_2$; [M$^-$]), 743.1 *m/z* ($C_{41}H_{34}BMoO_3P_2$; [M$^-$-CO]) ESI$^+$-MS: 295.1 *m/z* ($C_{16}H_{32}LiO_4$), 787.6 *m/z* ($C_{42}H_{34}BLi_2MoO_4P_2$; [M$^-$+2Li$^+$], 759.1 *m/z* ($C_{41}H_{34}BLi_2MoO_3P_2$; [M$^-$+2Li$^+$-CO]).

Control Formulation (2.3C). 2-hydroxyethyl acrylate (HEA) (1.504 g, 12.95 mmol, 49.95 wt%) was mixed with tetra(ethylene glycol) diacrylate (TEGDA) (1.513 g, 5.005 mmol, 49.95 wt%) neat. Solid

2,2-dimethoxy-2-phenylacetophenone (DMPA) (67 mg, 0.26 mmol) was dissolved in HEA (10 mL) to make a 0.067 g/mL stock solution. The DMPA solution (45 µL, additional 0.1 wt%) was thoroughly mixed into the HEA-TEGDA mixture. The control films were made solely from the above formulation. The formulation was passed through a 0.22 µm syringe filter into a clean vial and cured as described below. Cure % = 84.48 ± 1.47 %. Thickness = 0.459 ± 0.015 mm. ATR-IR (cm^{-1}) $\nu_{C=O(acrylate)}$ = 1724, $\nu_{C=C(acrylate)}$ = 1636, $\nu_{C-O(acrylate)}$ = 812. T_g = 21.7 °C.

S-IPN Formulation (2.3P$^+$): 2-hydroxyethyl acrylate (HEA) (1.504 g, 12.95 mmol, 38.4 wt%) was mixed with tetra(ethylene glycol) diacrylate (TEGDA) (1.513 g, 5.005 mmol, 38.4 wt%) neat. Solid 2,2-dimethoxy-2-phenylacetophenone (DMPA) (67 mg, 0.26 mmol) was dissolved in HEA (10 mL) to make a 0.067 g/mL stock solution. The DMPA solution (45 µL, additional 0.1 wt%) was thoroughly mixed into the HEA-TEGDA mixture. **2.1** (473 mg, 23.1 wt%) was added to a measured amount of the above formulation (1.600 g) and sonicated for 40 minutes. Once dissolved, the formulation was passed through a 0.22 µm syringe filter into a clean vial. The formulation was cured as described below. 85.12 ± 0.91 %. Thickness = 0.347 ± 0.011 mm. ATR-IR (cm^{-1}) $\nu_{C=O(acrylate)}$ = 1724, $\nu_{C=C(acrylate)}$ = 1636, $\nu_{C-O(acrylate)}$ = 812. T_g = 24.0 °C. Char yield = 0.059 %.

Freestanding S-IPN (2.4C and 2.4P$^+$). The curable formulation (50 µL) was sandwiched between two glass slides with a spacer and subjected to UV irradiation. The assembly was flipped and passed under the lamp a second time to ensure a complete cure. The slides were pried apart with a razor blade and the Free Standing Film (FSF) was peeled away using clean tweezers (Figure 2.8).

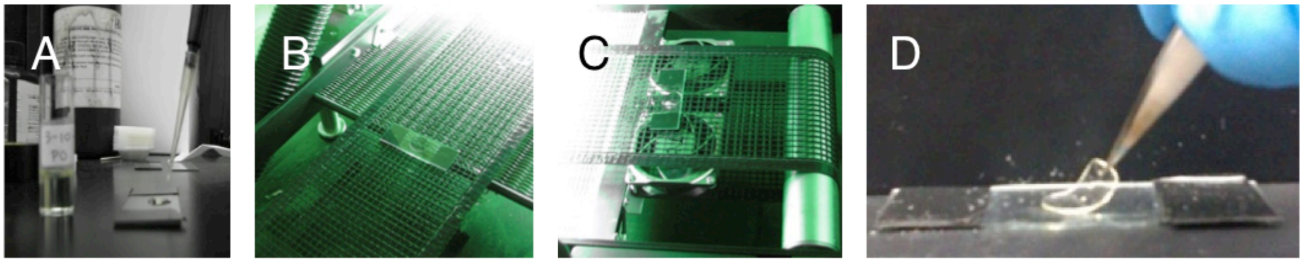

Figure 2.8: Curing process for **2.4C** and **2.4P$^+$**: A) the curable formulation (50 µL) was dropped onto a glass slide and a second slide was placed on top to make a sandwich. B) The resulting sandwich was passed under the UV-conveyer belt; C) the sandwich was flipped over and passed under the lamp again, in order to cure the reverse side. D) The slides were pried apart with a razor blade and either **2.4C** or **2.4P$^+$** was peeled off with clean tweezers.

S-IPN Thin Film (2.5P$^+$): Freshly prepared Si wafers were coated with the phosphonium UV-curable formulation and spun at 2000 rpm for 90 seconds, then ramped to 3000 rpm for 30 seconds. The samples were quickly transferred into a quartz-covered vessel that was purged with N_2 for 15 seconds before being subjected to UV irradiation (399.028 mJ/cm^2, 172.387 mW/cm^2 x5). The resulting films were iridescent. Thickness as measured by SEM = 1.02 ± 0.15 µm.

Gel Content and Swelling: Three of each **2.4C** and **$2.4P^+$** were prepared, then dried in a vacuum oven for 18 hours. Each film was weighed to four decimal places and then placed in separate vials that were filled with 3 mL of solvent (either THF, H_2O or ethanol), capped, sealed with electrical tape and left to swell for 12 hours. The films were removed from their vials and gently patted dry with a Kimwipe before being weighed to four decimal places in a clean weighing boat and placed in a clean tared vial. Swell % was calculated based on these data. The supernatant from each film was kept for a qualitative test for Cl^- ions using an aqueous solution of $AgNO_3$. Upon addition, the THF solutions remained transparent, while the water and ethanol samples became translucent for **$2.4P^+$**. The films were kept in the vacuum oven for 12 hours after which they were weighed in their respective vials; gel % was calculated based on these data.

Freestanding S-IPN Metathesis (2.4Mo): **$2.4P^+$** was soaked in a THF solution of **2.2Mo** (124.7 mg in 1.5 mL) for five minutes. The films were soaked in a fresh vial of water (x3), then ethanol (x6) for five minutes each. ATR-IR (cm^{-1}) $\nu_{(Mo)CO}$ = 2004, 1895, 1882, 1852, $\nu_{(acrylate)=O}$ = 1724, $\nu_{(acrylate)C=C}$ = 1636, $\nu_{(acrylate)C-C}$ = 812. 28% conversion by ATR-IR. T_g = 26.0 °C. Char yield = 9.2%.

S-IPN Thin Film Metathesis (2.5Mo): A THF solution of **2.2Mo** (78.3 mg in 1mL) was used to cover the surface of a **$2.5P^+$** and allowed to stand for 30 seconds. The excess solvent was removed from the side of the Si wafer to reveal a cloudy surface. The films were washed using D.I. water and removing the water from the sides with a pipette (x6). At this point the films appeared cloudy. The films were then rinsed in the same way with ethanol (x3), restoring the original iridescence of the film. The films were allowed to air dry before analysis and pyrolysis. ATR-IR (cm^{-1}) $\nu_{(Mo)CO}$ = 2004, 1895, 1882, 1852, $\nu_{(acrylate)=O}$ = 1724, $\nu_{(acrylate)C=C}$ = 1636, $\nu_{(acrylate)C-C}$ = 812. 71% conversion by ATR-IR. Composition by EDX (atomic %): C, 80.54%; O, 17.98%; Si, 0.13%; P, 0.93%; Cl, 0.26%; Mo, 0.17%.

Calibration Curve (2.6Mo): HEA (3.505 g, 0.03184 mol, 38.5 wt%) was mixed with TEGDA (3.501 g, 0.01158 mol, 38.5 wt%) neat. The DMPA stock solution (105 µL, additional 0.1 wt%) was thoroughly mixed into the HEA-TEGDA mixture. Polymer **2.1** (187 mg, 23 wt%) was sonicated into the above formulation, which was passed through a 0.22 µm syringe filter. Compound **2.2Mo** (200 mg, $1.93x10^{-1}$ mmol) was sonicated into the above formulation (313 mg, contains $2.03x10^{-1}$ mmol phosphonium sites) to make a solution representative of 95.0 % conversion of **2.2Mo** into the formulation. The 95.0 % stock solution was diluted with the leftover curable formulation, in order to create samples that represent different degrees of ion exchange (8.9, 20.4, 29.6, 42.9, 47.7, 55.0, 63.0, 73.6, 86.7 %). Ratio 1 was used in conjunction with the resulting ATR-IR data to generate a calibration curve (Figure 1). ATR-IR (cm^{-1}) (varying intensities for each sample) $\nu_{(Mo)CO}$ = 2004, $\nu_{(acrylate)C=O}$ = 1724, $\nu_{(acrylate)C=C}$ = 1636, $\nu_{(acrylate)C-C}$ = 812.

Ratio 1: $\frac{\text{Peak Height } \upsilon_{(\text{Mo})\text{CO}}}{\text{Peak Height } \upsilon_{(\text{acrylate})\text{CO}}}$

Dropcasting: A THF solution of **2.2Mo** (78.3 mg in 1mL) was used to cover a freshly prepared Si wafer. The solvent was allowed to air-dry before the sample was loaded into the tube furnace.

Pyrolysis: Samples were loaded into a quartz tube, purged with 5% H_2 (balanced with N_2) for 20 minutes and then ramped at 10 °C per minute to either 800, 900 or 1000 °C. The furnace was held at the prescribed temperature for either 3 or 4 hours before the tube furnace was turned off and allowed to cool to room temperature. Samples were unloaded from the tube either on the bench top and stored under air, or were unloaded in the glovebox and stored under N_2 until analysis.

2.6 References

(1) Whittell, G. R.; Hager, M. D.; Schubert, U. S.; Manners, I. *Nat. Mater.* **2011**, *10* (3), 176.

(2) Kenaree, A. R.; Gilroy, J. B. *Dalton Trans.* **2016**, *45* (45), 18229.

(3) Liu, K.; Clendenning, S. B.; Friebe, L.; Chan, W. Y.; Zhu, X.; Freeman, M. R.; Yang, G. C.; Yip, C. M.; Grozea, D.; Lu, Z.; Manners, I. *Chem. Mater.* **2006**, *18* (10), 2591.

(4) Zhang, J.; Yan, Y.; Chen, J.; Chance, W. M.; Gai, Z.; Tang, C. *Chem. Mater.* **2014**, *26* (10), 3185.

(5) Paquette, J. A.; Gilroy, J. B. *J. Polym. Sci. Part A Polym. Chem.* **2016**, *54*, 3257.

(6) Kikitsu, A. *J. Magn. Magn. Mater.* **2009**, *321*, 526.

(7) Lynch, C.; Bliss, D. F.; Zens, T.; Lin, A.; Harris, J. S.; Kuo, P. S.; Fejer, M. M. *J. Cryst. Growth* **2008**, *310*, 5241.

(8) Koh, S.; Kondo, T.; Shiraki, Y.; Ito, R. *J. Cryst. Growth* **2001**, *228*, 183.

(9) Schunemann, P. G.; Zawilski, K. T.; Pomeranz, L. A.; Creeden, D. J.; Budni, P. A. *J. Opt. Soc. Am. B* **2016**, *33* (11), D36.

(10) Hadadpour, M.; Ragogna, P. J. *J. Polym. Sci. Part A Polym. Chem.* **2015**, *53* (23), 2747.

(11) Clendenning, S. B.; Han, S.; Coombs, N.; Paquet, C.; Rayat, M. S.; Grozea, D.; Brodersen, P. M.; Sodhi, R. N. S.; Yip, C. M.; Lu, Z.-H.; Manners, I. *Adv. Mater.* **2004**, *16* (4), 291.

(12) Chan, W. Y.; Clendenning, S. B.; Berenbaum, A.; Lough, A. J.; Aouba, S.; Ruda, H. E.; Manners, I. *J. Am. Chem. Soc.* **2005**, *127* (6), 1765.

(13) Dong, Q.; Li, G.; Ho, C. L.; Faisal, M.; Leung, C. W.; Pong, P. W. T.; Liu, K.; Tang, B. Z.; Manners, I.; Wong, W. Y. *Adv. Mater.* **2012**, *24* (8), 1034.

(14) She, L.; Li, J.; Wan, Y.; Yao, X.; Tu, B.; Zhao, D. *J. Mater. Chem.* **2011**, *21* (3), 795.

(15) Rider, D. A.; Liu, K.; Eloi, J.; Vanderark, L.; Yang, L.; Wang, J.; Grozea, D.; Lu, Z.; Russell, T. P.; Manners, I. *ACS Nano* **2008**, *2* (2), 263.

(16) Cheng, J. Y.; Ross, C. A.; Chan, V. Z. H.; Thomas, E. L.; Lammertink, R. G. H.; Vancso, G. J. *Adv. Mater.* **2001**, *13* (15), 1174.

(17) Zhang, J.; Yan, Y.; Chance, M. W.; Chen, J.; Hayat, J.; Ma, S.; Tang, C. *Angew. Chem. Int. Ed.* **2013**, *52* (50), 13387.

(18) Kenaree, A. R.; Gilroy, J. B. *Organometallics.* **2017**, *36*, 2483.

(19) Zamora, M.; Bru, S.; Alonso, B.; Cuadrado, I. *Macromolecules* **2011**, *44*, 7994.

(20) Cuthbert, T. J.; Evoy, E.; Bow, J. P. J.; Guterman, R.; Stubbs, J. M.; Gillies, E. R.; Ragogna, P. J.; Blacquiere, J. M. *Catal. Sci. Technol.* **2017**, *7* (13), 2685.

(21) Hadadpour, M.; Gwyther, J.; Manners, I.; Ragogna, P. J. *Chem. Mater.* **2015**, *27*, 3430.

(22) Guterman, R.; Gillies, E. R.; Ragogna, P. J. *Can. J. Chem.* **2016**, *94* (5), 476.

(23) Cuthbert, T. J.; Guterman, R.; Ragogna, J.; Gillies, E. R. *J. Mater. Chem. B Mater. Biol. Med.* **2015**, *3*, 1474.

(24) Guterman, R.; Gillies, E. R.; Ragogna, P. J. *Langmuir.* **2015**, *31* (18), 5181.

(25) Cuthbert, T. J.; Harrison, T. D.; Ragogna, J.; Gillies, E. R. *J. Mater. Chem. B* **2016**, *4*, 4872.

(26) Guterman, R.; Hesari, M.; Ragogna, P. J.; Workentin, M. S. *Langmuir.* **2013**, *29* (21), 6460.

(27) Chikh, L.; Delhorbe, V.; Fichet, O. *J. Memb. Sci.* **2011**, *368* (1–2), 1.

(28) Dobrynin, A. V; Rubinstein, M. *Prog. Polym. Sci.* **2005**, *30*, 1049.

(29) Chikh, L.; Delhorbe, V.; Fichet, O. *J. Memb. Sci.* **2011**, *368*, 1.

(30) Thomas, J. C.; Peters, J. C. *Inorg. Chem.* **2003**, *42* (17), 5055.

(31) Donegani, M. G.; Fauser, V. G. *Inorganica Chim. Acta* **1981**, *48*, 97.

(32) Guyot, H.; Motta, N.; Marcus, J.; Drouard, S.; Balaska, B. *Surf. Sci.* **2001**, *485*, 759.

(33) Leisegang, T.; Levin, A. A.; Walter, J.; Meyer, D. C. *Cryst. Res. Technol.* **2005**, *40* (1–2), 95.

(34) Rojo, J. M.; Pizarro, J. L.; Fernández, J. R.; Greneche, J. M.; Arriortua, M. I.; Fernández-Díaz, M. T.; Rojo, T. *J. Mater. Chem.* **2003**, *13*, 1723.

(35) Oliynyk, A. O.; Lomnytska, Y. F.; Dzevenko, M. V.; Stoyko, S. S.; Mar, A. *Inorg. Chem.* **2013**, *52* (2), 983.

(36) Christensen, A. N. *Acta Chem. Scand.* **1977**, *A 31*, 509.

(37) Pawar, R. R. *Curr. Sci.* **1967**, *36*, 428.

(38) Hoyle, C. E.; Bowman, C. N. *Angew. Chem. Int. Ed.* **2010**, *49* (9), 1540.

(39) Guterman, R.; Rabiee Kenaree, A.; Gilroy, J. B.; Gillies, E. R.; Ragogna, P. J. *Chem. Mater.* **2015**, *27* (4), 1412.

(40) Hemp, S. T.; Allen, M. H.; Green, M. D.; Long, T. E. *Biomacromolecules* **2012**, *13* (1), 231.

Chapter 3

3 A Comprehensive Investigation of a Zwitterionic Ge(I) Dimer with a 1,2-Dicationic Core

3.1 Introduction

From gas phase diatomics to Group 13 through 16 compounds, 1,2-dications have garnered theoretical, spectroscopic and synthetic attention for decades.[1] Chemists have been intrigued by balancing the threshold between Coulombic explosion from the proximal positive charges and the electronic nature of the bonds that overcome those repulsive forces. The stability of these compounds depends on the polarizability, electronegativity, bond order and the role of non-bonding electrons on the atoms involved, as well as substituent effects.[2–6]

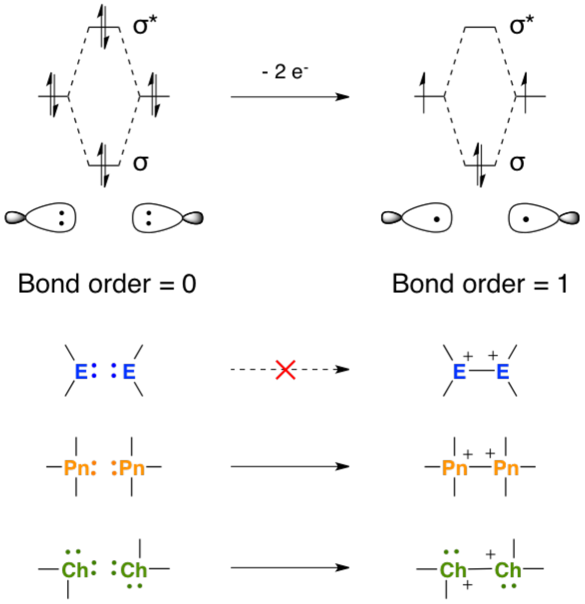

Scheme 3.1: Simplified molecular orbital diagram[4] for the oxidation of lone pair bearing species to their respective 1,2-dications (E^{14} = heavy tetrel; Pn = pnictogen; Ch = chalcogen).

1,2-dications are typically formed by the one-electron oxidation of a lone pair bearing species, where a common stabilizing factor is the increase in bond order from zero to one after the two-electron oxidation (Scheme 3.1). For this reason, 1,2-dications are well-established for the chalcogens and pnictogens.[1,7–9] Despite the work that has been done with carbon[1] and the long list of low valent, heavy tetrel(II) compounds that bear a lone pair of electrons,[10–16] there are no reported heavy tetrel (III) 1,2-dications. This is surprising considering the high polarizability and low electronegativity of the heavy tetrel elements that makes them good candidates to diffuse the repulsive electrostatic forces in a 1,2-

dication.[2] This dearth in examples could be attributed to the fact that more electron density is necessary to help soften the repulsive Coulombic force. Instead of oxidation to tetrel (III), a tetrel (I) species could be targeted using L-type ligands, which has been a useful approach in accessing Ga(II) 1,2-dications.[17,18]

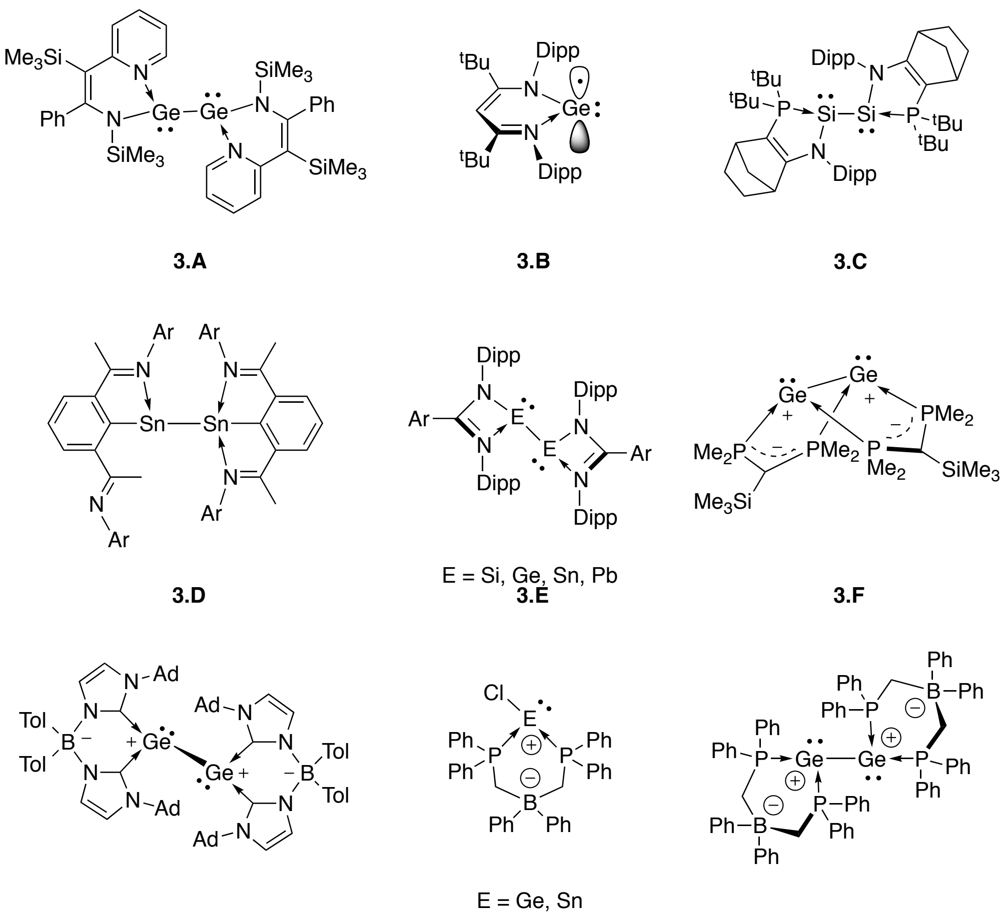

3.A 3.B 3.C

3.D

E = Si, Ge, Sn, Pb
3.E

3.F

3.G

E = Ge, Sn
3.1ECl

3.1Ge

Figure 3.1: Structures of tetrel (I) compounds supported by monoanionic chelating ligands, **3.1GeCl** and **3.1Ge** from this work.

There are a handful of compounds containing heavy tetrel elements with an oxidation state of (I). Aside from some exceptions,[19–21] the field has been dominated by two main classes, the heavy alkyne analogues[22–25] and those supported by monoanionic chelating ligands (**3.A-3.E** in Figure 3.1). [26–29] Two outliers from this group are the Ge centered 1,2-dications **3.F** and **3.G**, supported by neutral donors with the anionic charge insulated in the ligand backbone. In the case of **3.F** and **3.G**, the remote anionic charge and use of a dative model are assets in making the Ge centers formally dicationic. They are both formed by the reduction of a Ge(II) precursor; **3.F** by disproportionation, and **3.G** by photodegradation.[30,31] We now report the synthesis of a third member of this family of Ge(I) 1,2-dications, **3.1Ge** by the reductive dehalogenation of **3.1GeCl**.

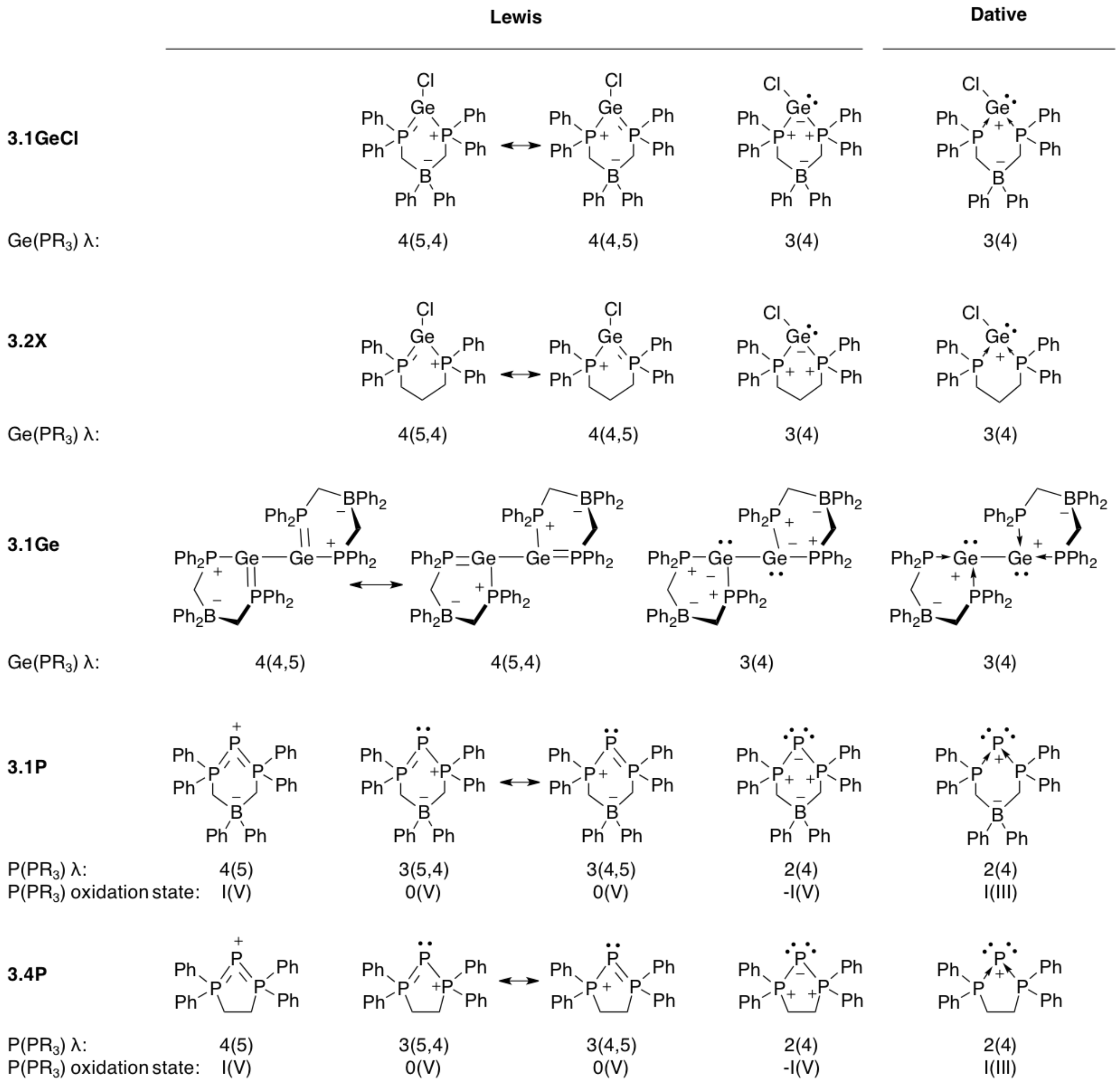

Figure 3.2: Lewis and dative bonding models for the bis-phosphine supported main group compounds used in Ge and P K-edge studies. Only the cations of compounds **3.2X** and **3.4P** are shown.

It is instructive to examine the various canonical forms, where the validity of certain representations can be debated. Nevertheless, Lewis structures have stood the test of time for nearly 100 years and they remain the benchmark for understanding atom connectivity, especially for the p-block elements. Dative models are also instructive in some instances; the merits of each will not be discussed here as this has been done recently.[32–34] Figure 3.2 underscores how the representation can impact the perceived charge on the central element for compounds **3.1GeCl**, **3.2X** and **3.1Ge**, and can even impact oxidation state assignments in, for example, compounds **3.1P** and **3.4P**. Experimentally probing the electronic nature of functional materials and transition metal centers is common, but less so for main group compounds.[35,36] With a strong computational argument in hand that a dative model is indeed appropriate to represent the interaction between phosphorus and germanium, we sought to characterize and describe the electronic structure in **3.1Ge** using X-ray absorption near edge structure (XANES) spectroscopy. Our experimental data demonstrate that the charge transfer between the donor atom on the ligand and the acceptor site manifests differently for closed shell Ge compounds versus the triphosphenium compounds that have better orbital overlap. By shedding light on these different systems, we were able to glean a snapshot of insight on the fundamentals behind the spectrum of covalency in chemical bonds.

3.2 Results & Discussion

3.2.1 Synthesis

The one-electron reduction of **3.1GeCl** was first attempted using traditional reducing agents. Sodium amalgam resulted in free bis(phosphino)borate ligand (**3.1**) after stirring for twelve hours. Cobaltocene, sodium napthlenide and potassium graphite resulted in slow conversion to previously observed insertion products (Scheme 3.2).[15] As an alternative to the more standard reducing agents, the Mg(I) β-diketiminate dimer, **3.3Mg** was employed. The reaction of **3.1GeCl** with a 0.5 stoichiometric equivalent of **3.3Mg** in toluene at room temperature gave a yellow solution with a white precipitate, where the reaction mixture contained a single phosphorus-containing product as indicated by the singlet in the $^{31}P\{^{1}H\}$ NMR spectrum ($\delta_P = 19.4$). Upon isolation of the product, single crystals were grown, and X-ray diffraction studies revealed the reductive dehalogenation product (**3.1Ge**, 65 %; Scheme 3.2). Compound **3.1Ge** maintains a twist boat conformation in the solid state with a trigonal pyramidal geometry about the *trans*-bent germanium centers (Figure 3.3). Compound **3.3Mg** was also used in an analogous reaction for the Sn analogue of **3.1GeCl**, resulting in the deposition of Sn metal and free ligand ($\delta_P = -8.8$).[15]

In an attempt at a two electron reduction of **3.1GeCl** to synthesize a phosphine-supported allotrope of germanium, germadiphosphorane,[37,38] one stoichiometric equivalent of **3.3Mg** was used and immediately the formation of **3.1Ge** was observed. After stirring the reaction mixture for an extended period (10 h), it became dark orange and the free bis(phosphino)borate ligand (**[3.1]**) was observed in solution ($\delta_P = -8.8$).

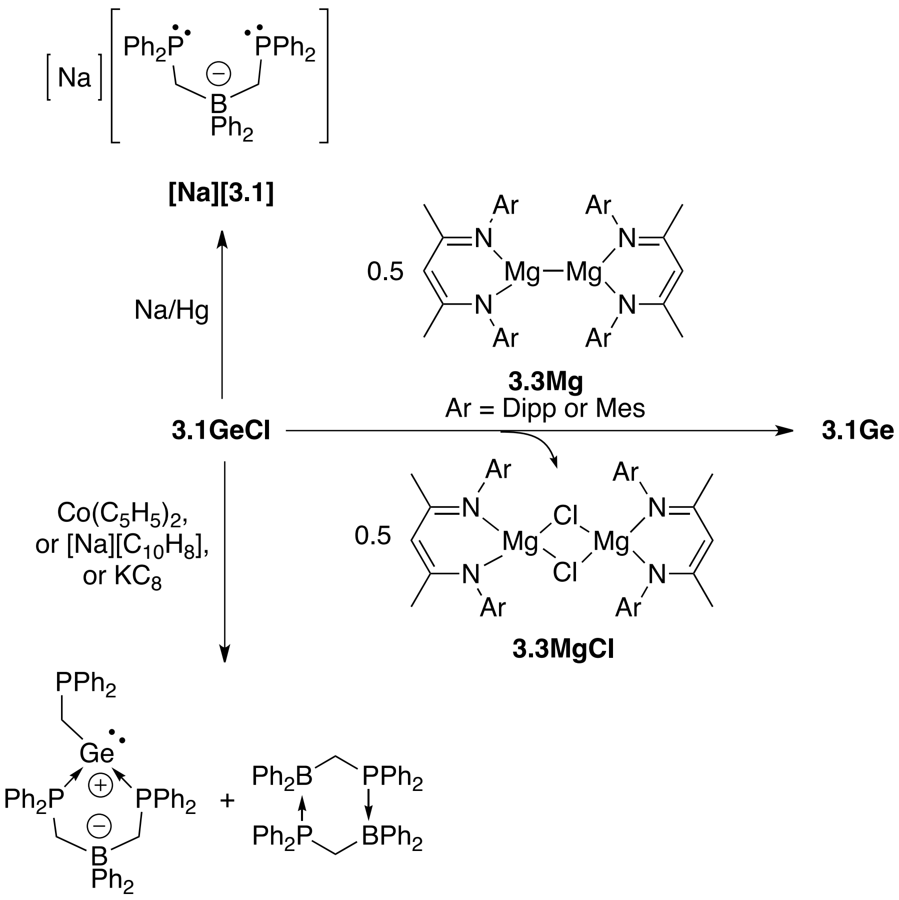

Scheme 3.2: One-electron reduction of **3.1GeCl** to form **3.1Ge**.

In order to characterize the electronic structure of **3.1Ge** using XANES, suitable standards were necessary. Compound **3.1Ge** is pyramidal about Ge and chelated by a bis(phosphine) ligand, so a suitable standard should reflect these molecular parameters. Compound **3.1GeCl** is ideal in this regard as it is structurally similar yet contains Ge in a different oxidation state. A stand out feature with compound **3.1Ge** is the anionic borate in the backbone and whether this plays a significant role in the stabilization of the 1,2-dication is an important question.[39] An analogue of **3.1GeCl** was prepared using a neutral bis(phosphine) ligand (**3.2X**) via the reaction of $GeCl_2$(dioxane) and 1,3-bis(diphenylphosphino)propane (**3.2**). Single crystals for X-ray diffraction experiments of the only phosphorus-containing product (δ_P = -5.2) were grown from a toluene-cyclohexane vapor diffusion. Instead of displacement of the dioxane to form a neutral phosphine adduct of the $GeCl_2$ fragment,[13] the reaction resulted in the redistribution of the chlorine atoms to yield a trigonal pyramidal Ge cation supported by **3.2**, partnered with a $[GeCl_3]^-$ anion (**3.2GeCl$_3$**) and again provided a pyramidal Ge center but with a neutral rather than charged bis-phosphine ligand.

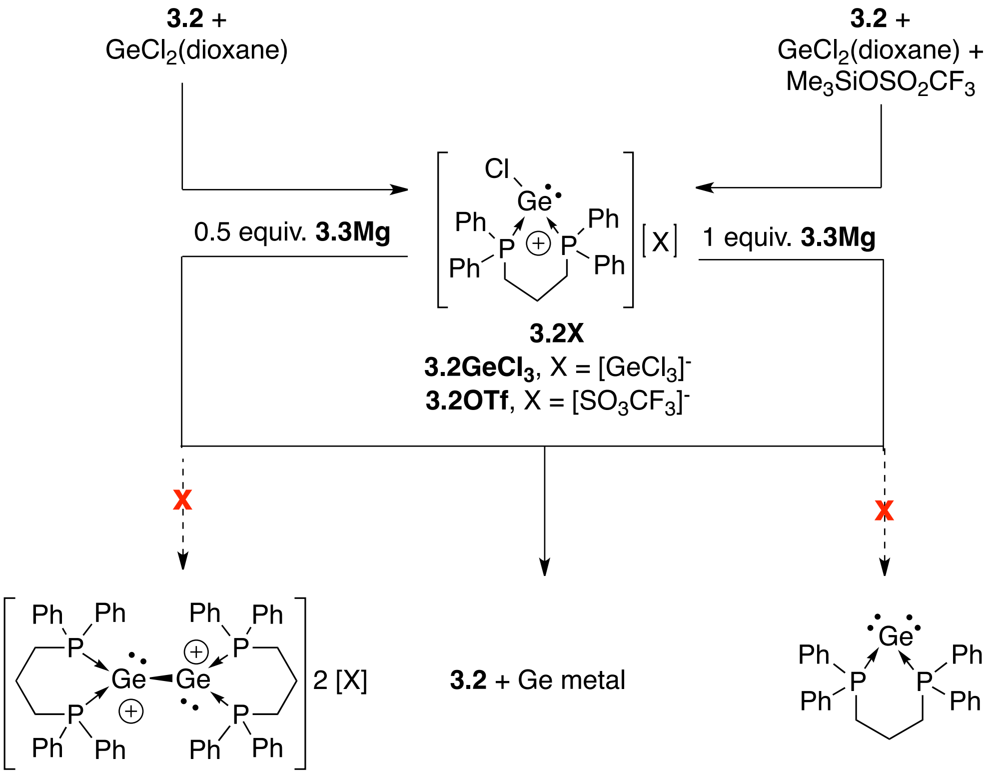

Scheme 3.3: Synthesis and reductions of **3.2X** (X = $[GeCl_3]^-$ or $[SO_3CF_3]^-$).

The problem with **3.2GeCl₃** as a XANES standard is that it contains two different Ge environments, creating the possibility for overlapping Ge K-edge signals and therefore, the redistribution reaction was attempted in the presence of $Me_3SiOSO_2CF_3$ (**3.2OTf**; Scheme 3.3). Compound **3.2OTf** has the same chemical shift as **3.2GeCl₃** (δ_P = -5.2) and crystallizes in the monoclinic space group ($P2_1/c$). Comparison of the solid-state structures revealed that the cations in both salts adopt the same pyramidal geometry at Ge and with the 6-membered ring in the chair conformation (Figure 3.3). An attempt was made to synthesize a neutral ligand analogue of **3.1Ge** from the one electron reduction of either **3.2GeCl₃** or **3.2OTf** using **3.3Mg**, resulting in the deposition of germanium metal and unbound **3.2** (δ_P = -17.1; Scheme 3.3).

3.2.2 X-Ray Crystallography

The Ge–Ge bond distance in **3.1Ge** (2.5687(9) Å) is short relative to reported dimeric Ge (I) compounds featuring monoanionic ligands (2.569(5) – 2.6380(8) Å),[29,40–42] and is comparable to the only other reported example of a phosphine-supported Ge 1,2-dicationic core (**3.F**) (2.540(1) Å).[30] 1,2-dications are known to have short E-E bonds despite the Coulombic repulsion, a phenomenon linked to the electronic structure of the compound.[1,3,6,43] For 1,2-dications formed by oxidation, the short bond lengths have been attributed to the nuclear attraction that occurs on removal of non-bonding electrons

(Scheme 3.1),[5] as well as the increase in effective nuclear charge that results in ion contraction. Substituents can also play a role in the E-E bond length of a 1,2-dication,[6] and in this context, it is noteworthy that the Ge–Ge distance in the N-heterocyclic carbene (NHC) stabilized Ge 1,2-dicationic core (**3.G**) reported by Xiong *et al.* is the longest of the reported Ge (I) dimers (2.673(1) Å).[31] This discrepancy is likely a hallmark of the inherent difference in electronic structure between phosphines and NHC ligands[44] and further piqued our curiosity on the bonding in **3.1Ge**.

Table 3.1: Selected bond lengths and angles.

	3.1Ge	**3.1GeCl**[15]	**3.2GeCl$_3$**	**3.2OTf**
Ge–P (Å)	2.4166(11) 2.4431(10) 2.3965(10) 2.4233(10)	2.4568(9) 2.4566(10)	2.4231(9) 2.4309(6)	2.4306(6) 2.4308(6)
Ge–Cl (Å)	-	2.2895(9)	2.2490(6)	2.2654(7)
Ge–Ge (Å)	2.5687(9)	-	-	-
B···Ge (Å)	4.056 4.079	3.713	-	-
P–Ge–P (°)	88.58(3)	85.50(3)	87.923(10)	87.13(3)

There is variation in the Ge–P bond distances in **3.1Ge** (Table 3.1), where they are overall shorter than those in **3.1GeCl**.[45] The anionic phosphinoborate ligand is electronically insulated within the backbone, however a contraction of the boron-metal distance has been observed to occur for increasingly electron-poor metal centers and indicates a through space B···M interaction.[46] The B···Ge distance elongates by 0.3 Å (from **3.1GeCl** to **3.1Ge**) and taken together, the contraction of the P–Ge bond lengths in **3.1Ge** and the thru-space B···Ge interaction in **3.1GeCl** indicates that the Ge atoms are electron poor. In the case of **3.1Ge**, the metal binds tightly to the ligand donor atoms whereas in **3.1GeCl**, the electron poor Ge center garners additional electrostatic stability from a thru-space interaction with the borate backbone.

It is established that bond angles have minimal impact on the P K-edge XANES of phosphines in transition metal complexes, while molecular geometry (i.e. square planar versus tetrahedral) has a much larger impact.[47] While there is a variation in the P–Ge–P bond angle of more than 3° between **3.1Ge** (88.58(3)°), **3.1GeCl** (85.50(3)°) and **3.2OTf** (87.13(3)°) they were deemed suitable standards, with **3.1GeCl** being a structural standard for a Ge(II) center bound to ligand **[3.1]**, and compound **3.2OTf** offering a probe for whether the anionic backbone in **3.1GeCl** has an effect on the edge energy. Ge metal, $GeCl_2$(dioxane) and GeO_2 were used as general standards to benchmark Ge(0), Ge(II), and Ge (IV), respectively.

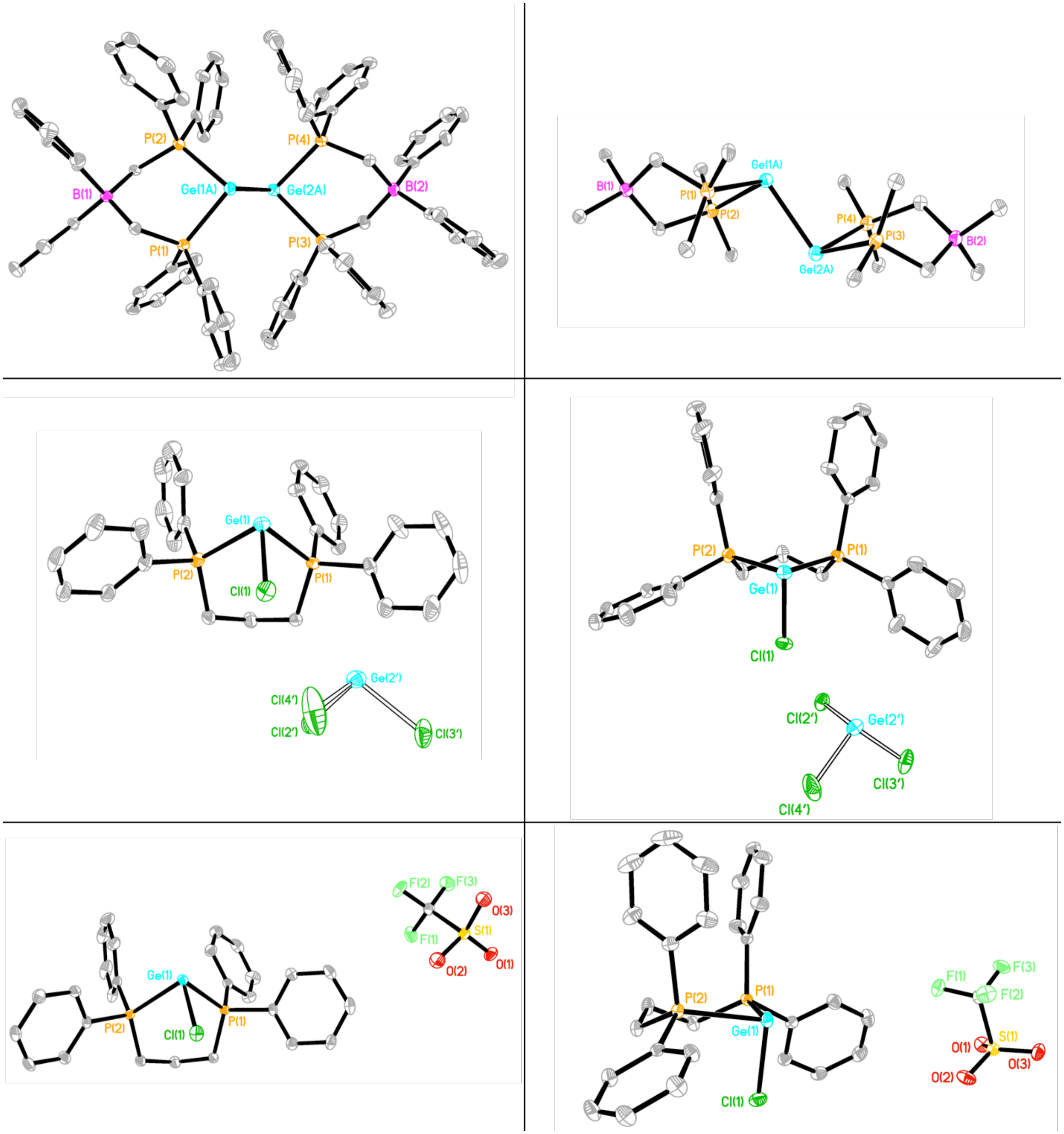

Figure 3.3: Solid-state structures (from top to bottom) of **3.1Ge** (right: phenyl groups omitted), **3.2GeCl₃** and **3.2OTf**. Thermal ellipsoids are drawn at 50% probability. Hydrogen atoms are omitted and only one PART of the disordered $[GeCl_3]^-$ counterion is shown for clarity. See Table 3.1 for selected bond lengths (Å) and angles (degrees).

3.2.3 XANES Spectroscopy

In order to shed some light on the stability of **3.1Ge**, the electronic structure of Ge and P were probed using XANES spectroscopy. XANES data can provide valuable information on the element contribution to the lowest unoccupied molecular orbital (LUMO) by inspection of the absorption threshold energy (E_0) and the whiteline (WL) intensity due to dipole transition selection rules (e.g. Ge and P K-edge tracks 1s to 4p and 3p transitions, respectively).[35,48] The E_0 of an element, increases with its oxidation state as the core electrons become more tightly bound to the nucleus. It should be noted that a given oxidation state cannot be fixed to a specific E_0 since E_0 is also influenced by the ionic component of the E-E' bond, the coordination number, substituent type(s) and geometry.[36,47,48]

Phosphinoborate ligands are well documented as being superior σ-donors to their neutral analogues. This has typically been demonstrated by monitoring the behavior of charged versus neutral ligands in coordination compounds.[39,46,49,50] Table 3.2 lists the P K-edge E_0 of free ligand **[Li(tmeda)$_2$][3.1]** (2146.65 eV) as being lower than **3.2** (2146.80 eV), an indication that **[Li(tmeda)$_2$][3.1]** is more electron rich than **3.2** and is corroborated by **[Li(tmeda)$_2$][3.1]** having a lower WL intensity (Figure 3.6). This ultimately translated to greater electron density for the phosphorus atoms to donate to Ge, and is direct spectroscopic evidence for the superior electron richness of uncoordinated **[Li(tmeda)$_2$][3.1]** compared to its neutral analogue, **3.2**.[39]

The Ge K-edge XANES E_0 of **3.1GeCl** and **3.2OTf** (both 11103.6 eV) is 0.6 eV higher than **3.1Ge** and 0.6 eV lower than that of $GeCl_2$(dioxane) (11104.2 eV). The Ge(II) atoms in **3.1GeCl** and **3.2OTf** are therefore electron poor relative to Ge metal (11103.0 eV) and **3.1Ge**, and electron rich relative to the Ge(II) in $GeCl_2$(dioxane). These distinctions arise from differences in oxidation state, substituent types and geometry.

In principle, the E_0 for **3.1Ge** (Ge(I)) is expected to fall between that of Ge(0) and Ge(II). However, given the electron rich anionic phosphinoborate ligand, the measured E_0 of **3.1Ge** aligns with that of Ge metal (11103.0 eV). Compound **3.1Ge** was observed to be electron poor relative to the Ge(0) standard by its relatively high WL intensity (Figure 3.4). Put together with the relatively low E_0, these data indicated that **3.1Ge** was an electron-rich Ge(I) species. This observation is echoed by how the ligating P atoms displayed the opposite trend in the P K-edge E_0 and were electron poor relative to the free ligand (2147.40 *cf.* 2146.65 eV, see below). This shift in energetically opposite directions for P and Ge is spectroscopic evidence of the charge transfer from P to Ge.

Table 3.2: P and Ge K-edge *E*$_0$ values including the oxidation states of P and Ge in reference compounds using the dative bonding models.

Compound	Oxidation State		P K-edge *E*$_0$ (eV)	Ge K-edge *E*$_0$ (eV)
	P	Ge		
Ge Powder	-	0	-	11103.0
Red P	0	-	2145.45	-
Black P	0	-	2145.60	-
3.1P	I and III	-	2145.45 and 2148.30	-
3.4P	I and III	-	2145.45 and 2148.00	-
PPh_3	III	-	2146.65	-
[Li(tmeda)$_2$][3.1]	III	-	2146.65	-
3.2	III	-	2146.80	-
$(PPh_3)_3RuCl$	III	-	2147.10	-
3.1GeCl	III	II	2147.25	11103.6
3.1Ge	III	I	2147.40	11103.0
3.2OTf	III	II	2147.40	11103.6
$OPPh_3$	V	-	2148.60	-
$[P(C_9H_9)(C_4H_9)_3][Cl]$	V	-	2148.90	-
P_4O_{10}	V	-	2152.35	-
$GeCl_2$(dioxane)	-	II	-	11104.2
GeO_2	-	IV	-	11108.6

When **3.1GeCl** was compared to **3.2OTf**, it could be observed that the two compounds experience the same P K-edge *E*$_0$ blue shift of 0.6 eV from their respective free ligands. This observation was on par with the comparable Ge–P distances between the two compounds (ca. 2.44 Å; Table 3.1). However, the absolute P K-edge *E*$_0$ values reveal that the coordinated phosphine in **3.1GeCl** (2147.25 eV) is more electron rich than that in **3.2OTf** (2147.40 eV) and furthermore, while the compounds had the same Ge K-edge *E*$_0$ (11103.6 eV), the Ge K-edge WL intensity for **3.1GeCl** was lower than that for **3.2OTf** (Figure 3.4). This ultimately translated to a more electron-rich Ge center in **3.1GeCl** and taken together, with the observed B···Ge interaction demonstrates the effectiveness of the remote anionic charge in the ligand backbone at increasing the electron-richness of the Ge center.

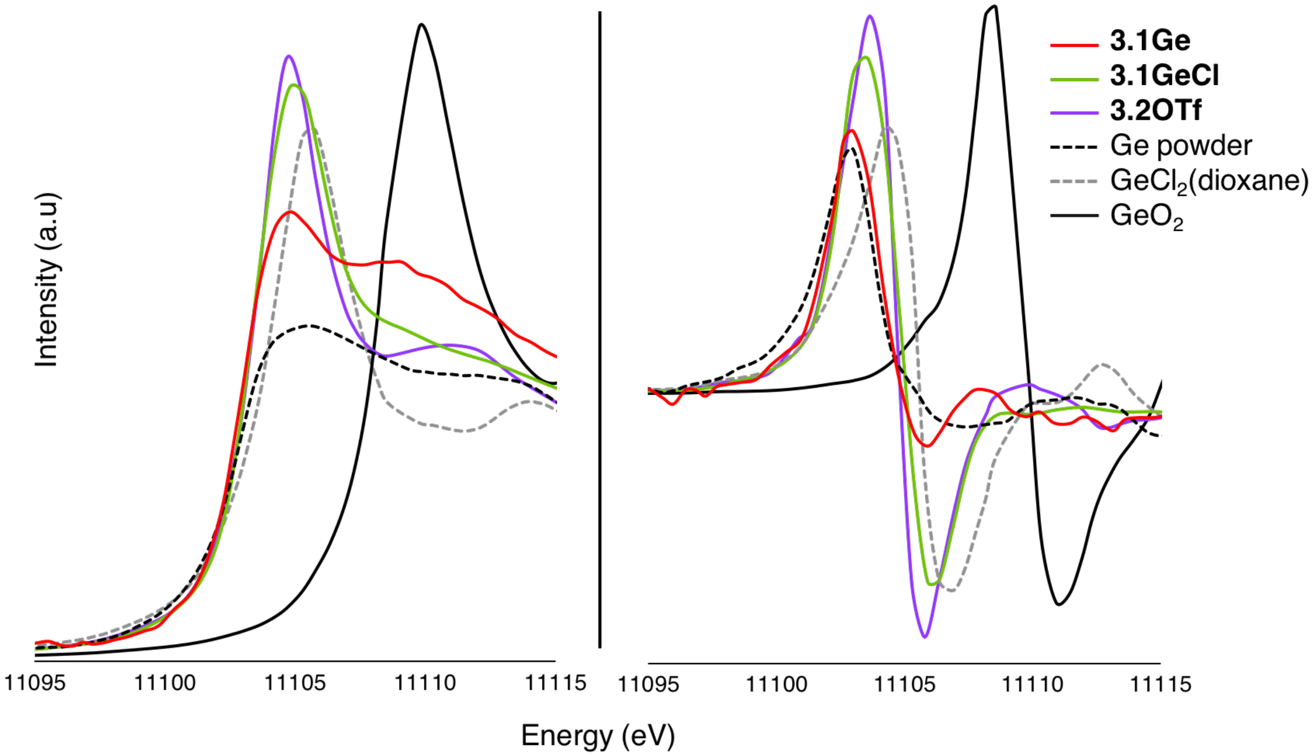

Figure 3.4: Ge K-edge XANES (left) and first derivative (right) spectra. The first derivative is taken to visualize the E_0, which is recorded at the point of inflection of the rising edge.

The Ge K-edge WL intensity of **3.1Ge** is even lower than that of **3.1GeCl** (Figure 3.4). Combined with the relatively low E_0 of **3.1Ge**, these data point to relatively electron-rich Ge-centers in the 1,2-dication. This can be attributed to the difference in oxidation states and substituent types. The 1,2-dication contains Ge in a lower oxidation state and therefore has more electron density than **3.1GeCl**. Further, the Ge in **3.1GeCl** bears an electron-withdrawing Cl^- ligand, which undoubtedly increases the E_0.

The coordinated phosphines in **3.1Ge** and **3.1GeCl** show a blue shift of 0.75 and 0.6 eV, respectively relative to the free ligand (**[Li(tmeda)$_2$][3.1]**) (Figure 3.5). These results clearly indicate charge transfer from P to Ge, and are consistent for what has been reported for phosphine ligands bound to increasingly electron poor metals.[51,52] In this context, the greater increase in E_0 energy for **3.1Ge** relative to **3.1GeCl** points to a stronger σ-donation from ligand **[3.1]**. These data suggest that inductive through-bond effects allow the borate to increase the donor ability of the remote phosphine fragments. This corroborates the P-Ge bond length contraction observed in the solid-state structure of **3.1Ge** and supports the hypothesis that a sufficiently electron rich phosphine is necessary to stabilize the 1,2-dicationic core.

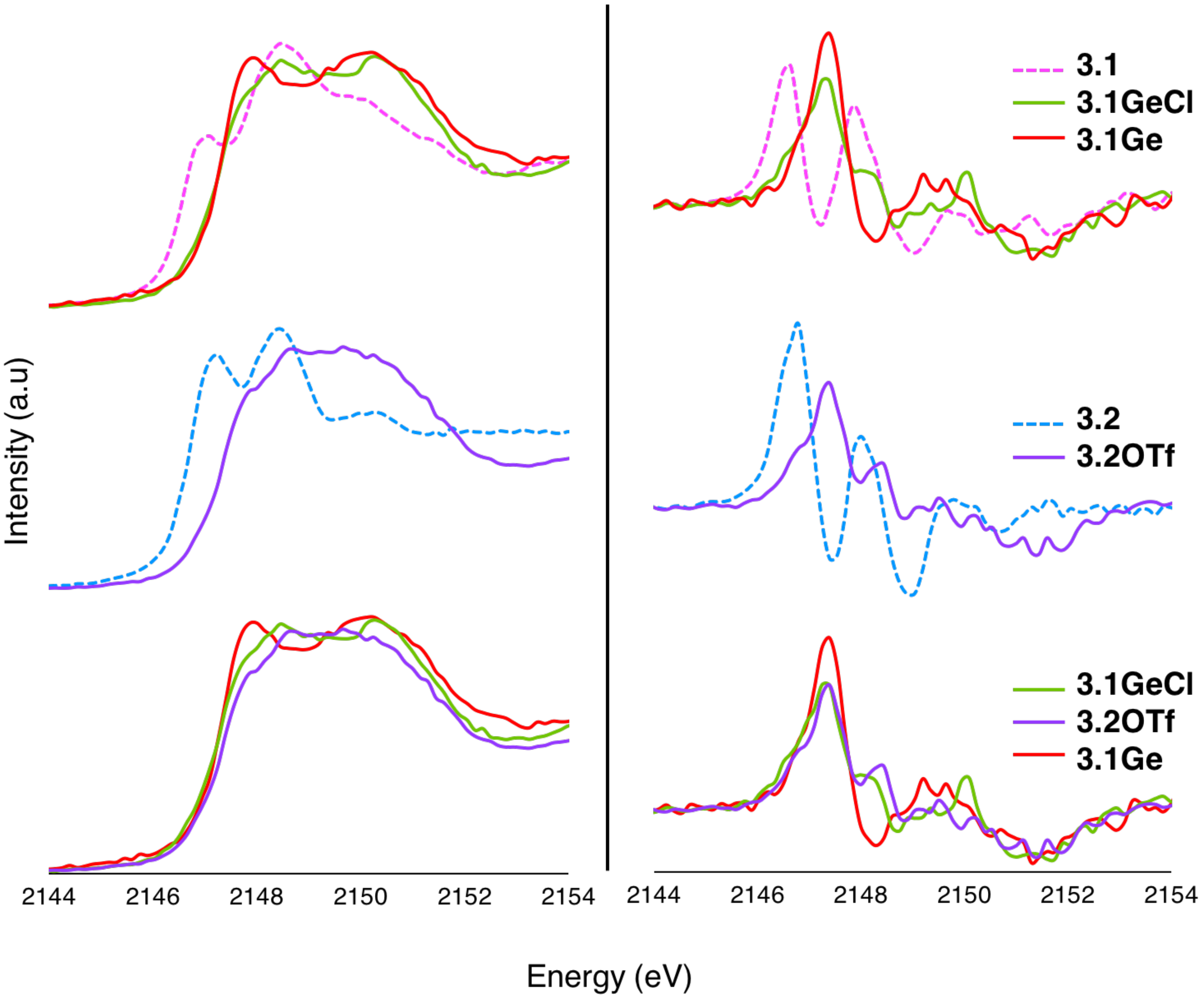

Figure 3.5: P K-edge XANES (left) and first derivative (right) spectra of **3.1Ge**, **3.1GeCl**, **3.2OTf** and their respective free phosphine ligands.

The superior electron-richness of **[Li(tmeda)$_2$][3.1]** over **3.2**, the subtle difference in electron density of the coordinated phosphines in **3.1GeCl** and **3.2OTf** combined with the extra charge transfer that the Ge atoms in **3.1Ge** are able to draw from ligand **[3.1]** explain our inability to synthesize a neutral ligand analogue of **3.1Ge** using **3.2**. Ligand **3.2** simply does not have enough electron density to stabilize the 1,2-dication.

The above results involving **3.1Ge** prompted a study of the electronic structure in triphosphenium cations; a class of phosphine-supported P(I) compounds that also suffer from ambiguity based on a Lewis or dative representation. In the triphosphenium cations the ambiguity is more extreme than for **3.1Ge** given the representation not only dictates the charge, but also the oxidation state of the phosphanide-type center (Figure 3.2). The dative bonding model for compounds **3.1P** and **3.4P** has been corroborated through computational and reactivity studies, demonstrating **3.4P** as a P(I) transfer reagent.[53–59] Can the same charge transfer that was observed in **3.1Ge**, **3.1GeCl** and **3.2OTf** be spectroscopically verified in **3.1P** and **3.4P**?

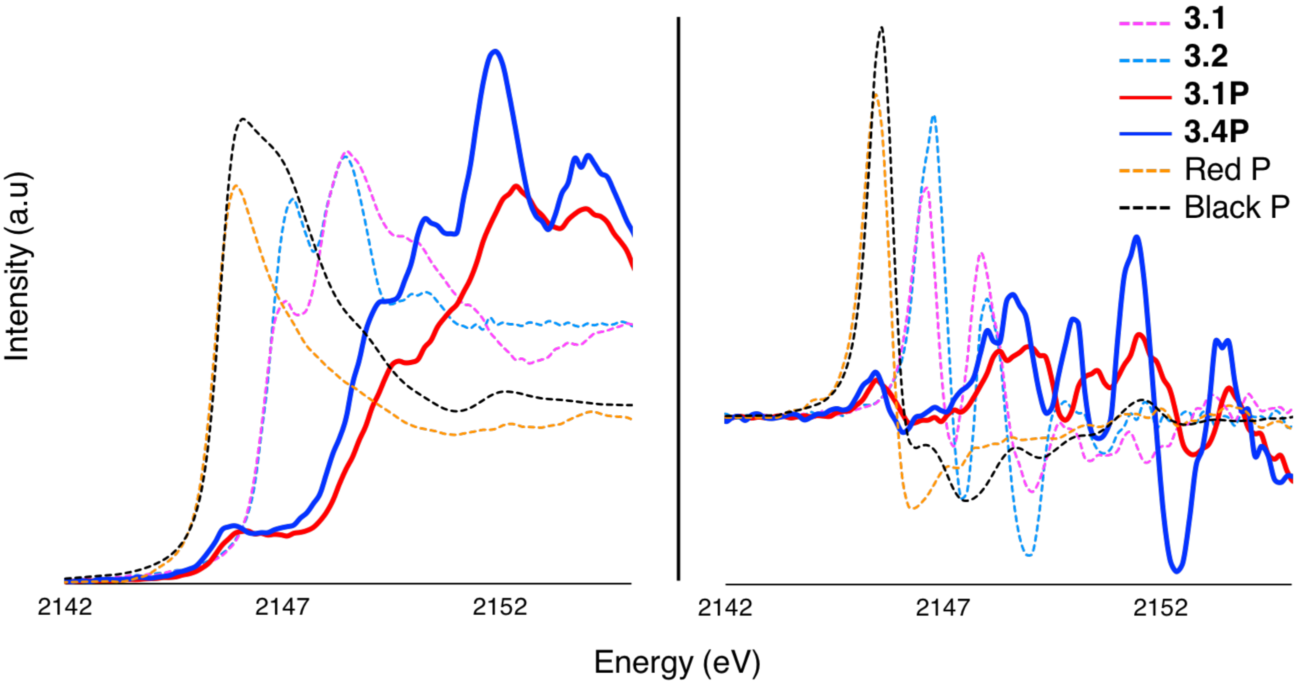

Figure 3.6: P K-edge XANES (left) and first derivative (right) spectra of triphosphenium cations **3.1P** and **3.4P** and the respective free phosphine ligands.

Since triphosphenium cations exhibit two P environments, the phosphanide-type center and the phosphines coordinated to it, the P K-edge XANES spectra correspondingly exhibit two absorption edges (Figure 3.6). The E_0 for the phosphanide-type center in both **3.1P** and **3.4P** appears at 2145.45 eV and aligns exactly with the main feature of red phosphorus. Although this result gives veracity to the Lewis model where the oxidation state of the phosphanide-type center is zero, E_0 values can vary within an oxidation state and given the electron rich phosphine supporting ligands, this edge value is congruous with an electron-rich P(I) center (Figure 3.2). This was echoed by the significant blue shift from free to coordinated phosphine ligands. Relative to free ligands **[Li(tmeda)$_2$][3.1]** and **3.2**, the E_0 of **3.1P** and **3.4P** experienced blue shifts of 1.65 and 1.35 eV, respectively. This noteworthy difference in charge transfer between charged and neutral ligands, is consistent with the electron richness of free ligands **[Li(tmeda)$_2$][3.1]** and **3.2**. This blue shift from free ligand resulted in the phosphines in **3.1P** having a higher E_0 than in **3.4P** (2148.30 and 2148.00 eV, respectively). These data demonstrate superior charge transfer from phosphine to phosphanide in **3.1P**, and once again demonstrate the superior electronic stabilization ability of ligand **[3.1]** over its neutral analogue.

The above triphosphenium data mark a distinction in the way that charge transfer is manifested spectroscopically compared to the Ge compounds. It is apparent that the triphosphenium compounds experience a greater charge transfer by the magnitude of the blue shift compared to the Ge compounds. Further, the distinction between charged and neutral ligands is manifested as a difference in WL intensity for the Ge compounds, where the same distinction is observed as a difference in magnitude of the blue shift for the triphosphenium compounds. These findings demonstrate that the bonding in these compounds is not as simple as a single drawn model can suggest and there is a continuum of covalency at play.

3.2.4 Computational Calculations

As illustrated in Figure 3.7, the LUMO and LUMO+1 of the model of [LGeCl] is localized almost exclusively on Ge and featuring π-type symmetry at the Ge atom. The LUMO and LUMO+1 of the [LGeGeL] model are similarly almost entirely localized on the $[Ge\text{-}Ge]^{2+}$ fragment, with the LUMO having in-phase π-type symmetry along the Ge-Ge bond and LUMO+1 being the out-of-phase π-type component. Correspondingly, the ADF SFO (symmetrized fragment orbital) analyses of the LUMO for [LGeCl] suggests that at least 78% of the orbital contribution to the LUMO can be attributable to the $3p_y$ (70%) and $4p_y$ (8%) orbitals on Ge. For LUMO+1, the $3p_x$ and $3p_y$ orbitals on Ge contribute more than 65% of the molecular orbital. Similarly, the ADF SFO analyses of the LUMO for [LGeGeL] suggests that at least 72% of the orbital contribution to the LUMO can be attributable to the $3p_y$ (60%) and $4p_y$ (12%) orbitals on the two Ge atoms. For LUMO+1, the $3p_x$ and $3p_y$ orbitals on the pair of Ge atoms contribute more than 64% of the molecular orbital. With the majority of the LUMO being composed of Ge character, XANES experiments are an appropriate method to probe the electronic structure about Ge.

The NBO analysis does not indicate any particularly large delocalizations for any of the lone pairs in the Ge systems. This is consistent with the trigonal pyramidal geometry about Ge that is observed in the solid-state structures. This also means that the Lewis structures, where $\lambda = 4$ for Ge, can be counted as minor contributions to describe the bonding in **3.1Ge**, **3.1GeCl** and **3.2OTf** (Figure 3.2).

NRT analyses on the compounds revealed all of the multiple-bonded structures ($\lambda_P = 5$; Figure 3.2) contribute less than 5% to the actual electronic distribution. The dominant Lewis structure in every case (for **3.1GeCl**, **3.1Ge**, **3.1P**) is always the single-bond only structure ($\lambda_P = 4$; Figure 3.2). The highest percentage of contribution following that, which was always under 5%, were ionic structures in which the P-H (modeling P-Ph) bond is cleaved to give a contact ion pair and a double bond between P and E.

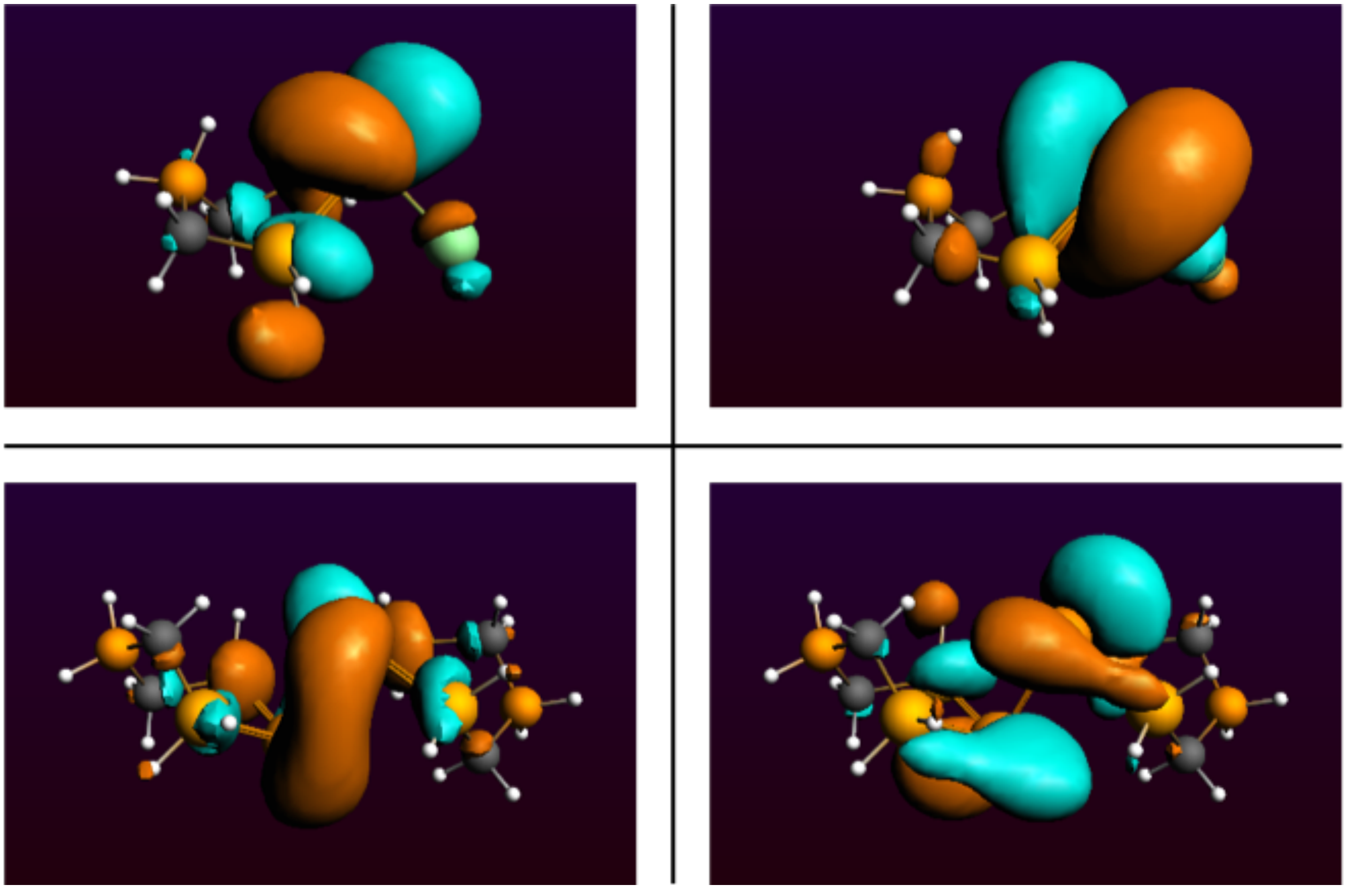

Figure 3.7: LUMO (left) and LUMO+1 (right) illustrations of [LGeCl] (top) and [LGeGeL] (bottom).

The NBO charges were used as a simple proxy to assess the magnitude of charge transfer from the ligand (either charged **3.1** or neutral **3.2**) to the germanium; the results suggest that approximately 0.98 e are transferred from the putative L^{1-} ligand to the $[GeCl]^{1+}$ fragment in [LGeCl], whereas the magnitude of the analogous charge transfer (0.78 e) is notably smaller for the system derived from the neutral ligand, as one would perhaps anticipate. An alternative estimate of charge transfer gleaned from the Voronoi deformation densities is consistent with the anticipated trend: an additional ca. 0.2 e appear to be transferred to the $[GeCl]^+$ fragment by the anionic ligand in comparison to the neutral ligand. This is consistent with the additional stabilization achieved from the thru-space B···Ge interaction in **3.1GeCl**.

The Bader charge ascribes a positive charge of +0.32 to the Ge atoms in **3.1Ge** and +0.86 for the Ge atom in **3.1GeCl**. This confirms that the adjacent Ge atoms in **3.1Ge** bear a positive charge, albeit a small one. Put together with the electron rich Ge centers observed by XANES spectroscopy and the short Ge–Ge distances observed in the solid-state for **3.1Ge**, it appears that the 1,2-dication is stabilized by the attraction of the simultaneously electron rich, yet putatively positively charged Ge atoms.

Table 3.3: Computed partial charges (au).

EL_n	Partial Charge on Ge		
	NBO	Voronoi	Bader
E=$[GeCl]^+$, n=1 L=$(PH_2CH_2)_2BH_2$	+0.55	+0.11	+0.86
E=$[GeCl]^+$, n=1 L=**3.2**	+0.72	+0.26	+1.00
E=$[Ge\text{-}Ge]^{2+}$, n=2, L=**3.1**	-0.02	-0.13	+0.32

In the context of the series of compounds, it is perhaps noteworthy that the trends observed in all of the partial charge analyses (NBO, Voronoi, Bader; Table 3.3) are all consistent with each other and are all consistent with the experimental XANES results: the least positively charged Ge atoms are those in [LGeGeL] (least oxidized, shortest Ge-P bonds and strongest charge transfer by XANES spectroscopy), those in [LGeCl] are intermediate (stabilized by thru-space interaction, yet bound to electron-withdrawing Cl), and those in $[(dHpe)GeCl]^{1+}$ are the most positively charged (no extra stabilization and bound to electron-withdrawing Cl).

For the Ge systems, one can see that the HOMO-LUMO gap is considerably smaller for the $[Ge\text{-}Ge]^{2+}$ (0.224938 au) system than for either of the $[GeCl]^+$ models (**3.1GeCl**: 0.278054; **3.2OTf**: 0.28377 au). The relatively high HOMO energies for the **3.1Ge** and **3.1GeCl** (-0.25215 and -0.29309 au, respectively) models, which can be ascribed to the stabilization achieved from coordination to the anionic ligand. In contrast, the LUMO energies for models of **3.1Ge** and **3.1GeCl** (-0.02721 and -0.01504 au, respectively) are comparable whereas the LUMO for model **3.2OTf** (-0.16668 au) is much lower in energy (Table 3.4).

Computational results confirm that the amount of P–P charge transfer in the triphosphenium compounds is significantly greater than the P–Ge charge transfer in the above compounds and suggests different degrees of covalency. With this in mind, it is interesting that the QT-AIM analysis[60] of the model compounds reveals dramatic differences in the nature of the bonding between the bis(phosphine) ligands and the Ge or P atoms. In particular, analysis of the bond critical points (BCPs) suggests that the electron distribution in the case of all of the germanium complexes is consistent with closed shell binding between germanium and the phosphorus atoms whereas the topology of the electron density in the phosphorus complexes is more consistent with covalent binding. In particular, the small positive value of the Laplacian and the ellipticity of the BCP ca. 0 in the cases of the germanium complexes is in stark contrast to the negative Laplacian and large ellipticity (ca. 0.4) observed for both of the triphosphenium models.

Table 3.4: HOMO and LUMO energies for the Kohn-Sham orbitals.

EL_n	Model	K-S Orbital		HOMO-LUMO Gap
		HOMO	LUMO	
E=$[GeCl]^+$, n=1 L=$(PH_2CH_2)_2BH_2$	(au)	-0.29309	-0.01504	0.278054
	(eV)	-7.97549	-0.40926	7.566235
E=$[GeCl]^+$, n=1 L=dppp	(au)	-0.45045	-0.16668	0.28377
	(eV)	-12.2573	-4.53554	7.721775
E=$[Ge\text{-}Ge]^{2+}$, n=2, L=**3.1**	(au)	-0.25215	-0.02721	0.224938
	(eV)	-6.86122	-0.74034	6.120875

This revelation about the difference in bonding between the two groups of compounds helps to explain why the difference between charged and neutral ligands manifests differently in the XANES data. The closed shell Ge compounds indicate the difference between ligands by the WL intensity, while the triphosphenium compounds – with better orbital overlap – indicate this difference by the magnitude of the E_0 blue shift. Further, the better orbital overlap in the triphosphenium compounds accounts for the greater charger transfer compared to the Ge compounds.

3.3 Conclusion

In this study a zwitterionic Ge(I) dimer with a 1,2-dicationic core was prepared and the factors that stabilize it were established. The short Ge–Ge distance, the relatively low E_0 and WL intensity from the Ge K-edge data, and small Bader positive charge on Ge point to attractive ambiphilic Ge centers. The relatively short Ge–P distances and edge shifts in energetically opposite directions for P and Ge relative to standards suggests that the stability at the $[Ge–Ge]^{2+}$ core arises from the (semi-insulated) borate backbone of ligand **3.1**.

Phosphinoborate ligand **[3.1]** was observed to have two means of donating electron density – by through-bond inductive effect or by electrostatic interaction – due to the borate backbone. Although this has been previously observed in solid-state structures, in this work we were able to corroborate that these interactions have an impact on electronic structure.[46]

In comparing the electronic structures of the Ge phosphine coordination compounds and triphosphenium compounds we deduced that although a dative representation is appropriate in either case, the electronic structures are markedly different. In this regard, the difference in bond critical point ellipticity suggests a continuum of covalency in which Lewis and dative models reside at the extremities. These differences in electronic structure can be spectroscopically probed by examining how the charge transfer is manifested in the XANES data. Having a fundamental understanding of the electronic structure can be valuable in understanding stability, or lack thereof in a compound.

3.4 Experimental Section

3.1Ge. A toluene solution of **3.3Mg** (78.7 mg, 0.089 mmol, 1 mL) was added to a toluene solution of **3.1GeCl** (100.1 mg, 0.149 mmol, 1 mL) at room temperature. Upon addition, the mixture remained yellow and a white precipitate formed. The mixture was filtered over Celite and the volume was reduced to half *in vacuo*. Pentane (15 mL) was added to the solution to afford a yellow precipitate. The supernatant was removed and the solids were recrystallized from a 1:5 THF:Et_2O mixture at -30 °C overnight. Yield: 65 %. Single crystals suitable for X-ray diffraction studies were grown from a concentrated solution of toluene over the course of three days at -30 °C. Mp = 203.4 °C. ^1H NMR (400 MHz, C_6D_6): δ = 6.92-7.16 (m, 36H), 6.80-6.84 (m, 16H), 6.64-6.66 (m, 8H), 2.27 (br s, 8H) ppm; $^{13}C\{^1H\}$ NMR (100.6 MHz, C_6D_6): δ = 133.6, 133.3, 132.9, 132.6, 132.2, 131.0, 130.4, 130.2, 122.9, 122.8, 23.8 ppm; $^{31}P\{^1H\}$ NMR (161.8 MHz, C_6D_6): δ = 19.4 ppm; $^{11}B\{^1H\}$ NMR (128.3 MHz, C_6D_6): δ = -14.4 ppm; FT-IR (ranked intensity): ν = 86(4), 102(3), 174(7), 197(9), 237(8), 267(12), 509(20), 617(14), 651(19), 688(17), 999(1), 1029(6), 1095(10), 1159(15), 1188(16), 1379(18), 2908(13), 3054(2); FT-Raman (ranked intensity): ν = 693(1), 738(5), 768(11), 867(4), 932(17), 999(6), 1028(9), 1055(19), 1097(3), 1140(15), 1186(20), 1262(10), 1308(14), 1381(14), 1434(15), 1483(16), 1586(17), 2908(18), 3004(18), 3057(6); MALDI-MS (pyrene): m/z 637.2 $[C_{38}H_{34}BP_2Ge]^+$ ($[M/2]^+$). Elemental analysis found (calculated) for $C_{76}H_{68}B_2P_4Ge_2$: C 71.17 (71.75), H 5.80 (5.39) %.

3.2GeCl$_3$. A THF solution of 1,3-bis(diphenylphosphino)propane (dppp) (80.4 mg, 0.195 mmol, 3mL) was added to a THF solution of $GeCl_2$(dioxane) (90.3, 0.390 mmol, 3 mL). Volatiles were removed from the reaction mixture *in vacuo* and the product was recrystallized by vapor diffusion of cyclohexane into toluene at room temperature overnight, these crystals were suitable for single crystal X-ray diffraction studies. Yield: 38%. Mp = 148.3 °C. ^1H NMR (400 MHz, methanol-d4): δ = 7.53-7.81 (m, 8H), 7.46-7.53 (m, 4H), 7.44-7.46 (m, 8H), 3.07-3.11 (br m, 4H), 2.23 (br, 2H) ppm; $^{13}C\{^1H\}$ NMR (100.6 MHz, CD_3CN): δ = 134.0, 133.2, 130.9, 18.8, 18.3 (br) ppm; $^{31}P\{^1H\}$ NMR (161.8 MHz, C_6D_6): δ = -5.2 ppm; FT-IR (ranked intensity): ν = 620.9 (2), 764.5 (1), 801.0 (3), 833.9 (4), 856.0 (6), 723.8 (6), 912.7 (8), 931.0 (7), 981.7 (10), 1007.2 (11), 1054.8 (15), 1137.7 (16), 1174.4 (17), 1220.4 (14), 1458.9 (18), 1496.0 (13), 2737.8 (20), 3149.9 (19), 3326.1 (10), 3406.9 (21). ESI-MS: m/z 521.0 $[C_{27}H_{26}P_2ClGe]^+$ ($[M]^+$), m/z 178.8 $[GeCl_3]^-$ ($[M]^-$). Elemental analysis found (calculated) for $C_{27}H_{26}P_2Cl_4Ge_2$: C 45.92 (46.36), H 3.61 (3.75) %.

3.2OTf. A diethyl ether solution of $GeCl_2$(dioxane) (44.8 mg, 0.194 mmol) was added to a mixture of dppp (75.2 mg, 0.182 mmol, 3 mL) and $Me_3SiOSO_2CF_3$ (66 μL, 0.36 mmol) in diethyl ether (7 mL) resulting in a white precipitate. The supernatant was decanted, the solids were washed with diethyl ether (2 x 2 mL) and dried *in vacuo* to afford analytically pure **3.2OTf**. Single crystals suitable for X-ray diffraction studies were grown by vapor diffusion of diethyl ether into an acetonitrile solution of **3.2OTf** over the course of three days at -30°C. Yield: 82%. Mp = 204.9 – 210.9 °C. ^1H NMR (400 MHz, methanol-d4): δ = 7.57-7.62 (m, 8H), 7.47-7.54 (m, 4H), 7.44-7.46 (m, 8H), 3.03-3.09 (br m, 4H), 2.14-2.24 (br m, 2H) ppm; $^{13}C\{^1H\}$ NMR (100.6 MHz, CD_3CN): δ = 144.3, 143.6, 141.4, 29.2, 28.9 ppm; $^{31}P\{^1H\}$ NMR (161.8 MHz, C_6D_6): δ = -5.2 ppm; $^{19}F\{^1H\}$ NMR (376.3 MHz, CD_3CN): δ = -78.0 ppm; FT-IR (ranked intensity): ν = 651 (3), 722.8 (8), 773.3 (1), 801.7 (10), 834.0 (16), 870.9 (7), 980.6 (13), 1004.9 (15), 1043.7 (4), 1200.4 (11), 1368.5 (2), 1410.2 (18), 1423.6 (19), 1464.8 (6), 1512.7 (9), 1628.7 (14), 1862.9 (20), 2151.3 (5), 2775.5 (12), 3000.2 (17). ESI-MS: m/z 521.0 $[C_{27}H_{26}P_2ClGe]^+$ ($[M]^+$), m/z 149.0 $[CO_3F_3S]^-$ ($[M]^-$). Elemental analysis found (calculated) for $C_{28}H_{26}O_3F_3P_2SClGe$: C 49.95 (50.22), H 3.59 (3.91), S 4.22 (4.79) %.

3.5 References

(1) Nenagdenko, V. G.; Shevchenko, N. E.; Balenkova, E. S.; Alabugin, I. V. *Chem. Rev.* **2003**, 229.

(2) Koch, W.; Frenking, G.; Schwarz, H. *J. Chem. Soc. Perkin Trans. II* **1986**, No. 1, 757.

(3) Wong, M. W.; Nobes, R. H.; Bouma, W. J.; Radom, L. *J. Chem. Phys.* **1989**, *91* (5), 2971.

(4) Furukawa, N.; Kobayashi, K. *J. Synth. Org. Chem., Jpn.* **1997**, *55* (11), 1006.

(5) Furukawa, N.; Kobayashi, K.; Sato, S. *J. Organomet. Chem.* **2000**, *611*, 116.

(6) Dunitz, J. D.; Ha, T. K. *J.C.S. Chem. Comm.* **1972**, 568.

(7) Weigand, J. J.; Riegel, S. D.; Burford, N.; Decken, A. *J. Am. Chem. Soc.* **2007**, *129* (25), 7969.

(8) Wolstenholme, D. J.; Weigand, J. J.; Davidson, R. J.; Pearson, J. K.; Cameron, T. S. *J. Phys. Chem. A* **2008**, *112* (15), 3424.

(9) Somisara, D. M.; Bühl, M.; Lebl, T.; Richardson, N. V.; Slawin, A. M.; Woollins, J. D.; Kilian, P. *Chem. Eur. J.* **2011**, *17* (9), 2666.

(10) Simons, R. S.; Pu, L.; Olmstead, M. M.; Power, P. P. *Organometallics.* **1997**, *16* (9), 1920.

(11) Barney, A. A.; Heyduk, A. F.; Nocera, D. G. *Chem. Commun.* **1999**, (23), 2379.

(12) Nagendran, S.; Roesky, H. W. *Organometallics.* **2008**, *27*, 457.

(13) Cheng, F.; Hector, A. L.; Levason, W.; Reid, G.; Webster, M.; Zhang, W. *Inorg. Chem.* **2010**, *49*, 752.

(14) Champness, N. R. *Dalton Trans.* **2011**, *40* (40), 10311.

(15) Weicker, S. A.; Dube, J. W.; Ragogna, P. J. *Organometallics.* **2013**, *32* (22), 6681.

(16) Budimac, Z.; Grbac, T. G. *Topics in Organometallic Chemistry 13*; 2013.

(17) Malbrecht, B. J.; Dube, J. W.; Willans, M. J.; Ragogna, P. J. *Inorg. Chem.* **2014**, *53* (18), 9644.

(18) Bourque, J. L.; Boyle, P. D.; Baines, K. M. *Chem. Eur. J.* **2015**, *21* (27), 9790.

(19) Wang, Y.; Xie, Y.; Wei, P.; King, R. B.; Schaefer, H. F.; Schleyer, P. R.; Robinson, G. H. *Science.* **2008**, *321* (5892), 1069.

(20) Li, J.; Schenk, C.; Goedecke, C.; Frenking, G.; Jones, C. *J. Am. Chem. Soc.* **2011**, *133* (46), 18622.

(21) Siddiqui, M. M.; Sarkar, S. K.; Sinhababu, S.; Ruth, P. N.; Herbst-Irmer, R.; Stalke, D.; Ghosh, M.; Fu, M.; Zhao, L.; Casanova, D.; Frenking, G.; Schwederski, B.; Kaim, W.; Roesky, H. W. *J. Am. Chem. Soc.* **2019**, *141*, 1908.

(22) Sekiguchi, A.; Kinjo, R.; Ichinohe, M. *Science.* **2004**, *305*, 1755.

(23) Pu, L.; Twamley, B.; Power, P. P. *J. Am. Chem. Soc.* **2000**, *122*, 3524.

(24) Stender, M.; Phillips, A. D.; Wright, R. J.; Power, P. P. *Angew. Chem. Int. Ed.* **2002**, *41*, 1785.

(25) Phillips, A. D.; Wright, R. J.; Olmstead, M. M.; Power, P. P. *J. Am. Chem. Soc.* **2002**, *124* (21), 5930.

(26) Gau, D.; Rodriguez, R.; Kato, T.; Saffon-Merceron, N.; De Cózar, A.; Cossío, F. P.; Baceiredo, A. *Angew. Chem. Int. Ed.* **2011**, *50*, 1092.

(27) Leung, W. P.; Chiu, W. K.; Mak, T. C. W. *Organometallics.* **2014**, *33* (1), 225.

(28) Khan, S.; Michel, R.; Dieterich, J. M.; Mata, R. A.; Roesky, H. W.; Demers, J. P.; Lange, A.;

Stalke, D. *J. Am. Chem. Soc.* **2011**, *133*, 17889.

(29) Jones, C.; Bonyhady, S. J.; Holzmann, N.; Frenking, G.; Stasch, A. *Inorg. Chem.* **2011**, *50* (I), 12315.

(30) Karsch, H. H.; Deubelly, B.; Riede, J.; Muller, G. *Angew. Int. Ed. Engl.* **1987**, *26* (7), 673.

(31) Xiong, Y.; Yao, S.; Szilvási, T.; Ballestero-Martínez, E.; Grützmacher, H.; Driess, M. *Angew. Chem. Int. Ed.* **2017**, *56* (15), 4333.

(32) Himmel, D.; Krossing, I.; Schnepf, A. *Angew. Chem. Int. Ed.* **2014**, *53* (24), 6047.

(33) Himmel, D.; Krossing, I.; Schnepf, A. *Angew. Chem. Int. Ed.* **2014**, *53* (2), 370.

(34) Frenking, G. *Angew. Chem. Int. Ed.* **2014**, *53* (24), 6040.

(35) Ward, M. J.; Rupar, P. A.; Murphy, M. W.; Yiu, Y.-M.; Baines, K. M.; Sham, T. K. *Chem. Commun.* **2010**, *46* (37), 7016.

(36) Bourque, J. L.; Biesinger, C.; Baines, K. M. *Dalton Trans.* **2016**, *45*, 7678.

(37) Jones, C.; Sidiropoulos, A.; Holzmann, N.; Frenking, G.; Stasch, A. *Chem. Commun.* **2012**, *48* (79), 9855.

(38) Takagi, N.; Tonner, R.; Frenking, G. *Chem. Eur. J.* **2012**, *18* (6), 1772.

(39) Thomas, J. C.; Peters, J. C. *Inorg. Chem.* **2003**, *42* (17), 5055.

(40) Leung, W.; Chiu, W.; Chong, K.; Mak, T. C. W. *Chem. Commun.* **2009**, 6822.

(41) Green, S. P.; Jones, C.; Junk, P. C.; Lippert, K.; Stasch, A. *Chem. Commun.* **2006**, *174* (1), 3978.

(42) Nagendran, S.; Sen, S. S.; Roesky, H. W.; Koley, D. *Organometallics.* **2008**, *27* (21), 5459.

(43) Lammertsma, K.; von Ragué Schleyer, P.; Schwarz, H. *Angew. Chem. Int. Ed. Engl.* **1989**, *28* (10), 1321.

(44) Wilson, D. J. D.; Couchman, S. A.; Dutton, J. L. *Inorg. Chem.* **2012**, *51* (14), 7657.

(45) Haaland, A. *Angew. Chem. Int. Ed. Engl.* **1989**, *28* (8), 992.

(46) Betley, T. A.; Peters, J. C. *Angew. Chem. Int. Ed.* **2003**, *42*, 2385.

(47) Donahue, C. M.; McCollom, S. P.; Forrest, C. M.; Blake, A. V.; Bellott, B. J.; Keith, J. M.; Daly, S. R. *Inorg. Chem.* **2015**, *54* (12), 5646.

(48) Engemann, C.; Franke, R.; Hormes, J.; Lauterbach, C.; Hartmann, E.; Clade, J.; Jansen, M. *Chem. Phys.* **1999**, *243* (1–2), 61.

(49) Lu, C. C.; Peters, J. C. *J. Am. Chem. Soc.* **2002**, *124*, 5272.

(50) Thomas, J. C.; Peters, J. C. *J. Am. Chem. Soc.* **2003**, *125*, 8870.

(51) Mossin, S.; Tran, B. L.; Adhikari, D.; Pink, M.; Heinemann, F. W.; Sutter, J.; Szilagyi, R. K.; Meyer, K.; Mindiola, D. J. *J. Am. Chem. Soc.* **2012**, *134* (33), 13651.

(52) Shearer, J.; Callan, P. E.; Masitas, C.; Grapperhaus, C. *Inorg. Chem.* **2012**, *51* (11), 6032.

(53) Dube, J. W.; MacDonald, C. L. B.; Ragogna, P. J. *Angew. Chem. Int. Ed.* **2012**, *51* (52), 13026.

(54) Ellis, B. D.; Carlesimo, M.; Macdonald, C. L. B. *Chem. Commun.* **2003**, *64* (15), 1946.

(55) Norton, E. L.; Szekely, K. L. S.; Dube, J. W.; Bomben, P. G.; Macdonald, C. L. B. *Inorg. Chem.* **2008**, *47* (3), 1196.

(56) Kosnik, S. C.; Farrar, G. J.; Norton, E. L.; Cooper, B. F. T.; Ellis, B. D.; Macdonald, C. L. B. *Inorg. Chem.* **2014**, *53* (24), 13061.

(57) Binder, J. F.; Swidan, A.; Tang, M.; Nguyen, J. H.; Macdonald, C. L. B. *Chem. Commun.* **2015**, *51* (36), 7741.

(58) Kosnik, S. C.; Macdonald, C. L. B. *Dalton Trans.* **2016**, No. 14, 6251.

(59) Binder, J. F.; Corrente, A. M.; Macdonald, C. L. B. *Dalton Trans.* **2016**, *45* (5), 2138.

(60) Bader, R. F. W. *Chem. Rev.* **1991**, *91*, 893.

Chapter 4

4 Coordination Chemistry of Phosphane-ene Polymer Networks

4.1 Introduction

Metal containing ceramics have been investigated for an array of applications including the fields of electrochemistry, electrocatalysis and information technology (IT).[1–5] It can be challenging to prepare ceramic materials so that the composition and morphology simultaneously fit the application.

In a quest to lower the carbon footprint of vehicles, scientists have been striving to improve battery performance and develop efficient hydrogen evolution reaction (HER) catalysts for the clean generation of H_2 as an alternative to fossil fuels.[6–8] The ceramics that currently show promise in battery development are transition metal doped $LiFePO_4$ cathode materials and metal oxide electrocatalysts.[7–12] Other types of materials have emerged as promising, low-cost electrocatalysts for HER, namely phosphides of Fe, Co, Ni, Cu, Mo and W, whose activity can be tuned by varying the metal to phosphorus ratio.[6,13]

Despite their desired electrochemical properties, a major drawback of the above-mentioned ceramics in the context of batteries or fuel cells is their lack of conductivity. To improve the electrochemical activity of these ceramics they have been incorporated into carbon supports, which have the advantage of being conductive and are amenable to doping with heteroatoms that further enhance conductivity.[6,14,15] Recent work to address this issue has centered on the pyrolysis of metal organic frameworks (MOFs) to form carbon that is homogeneously doped with metals, however the scalability of MOFs remains a challenge.[14,16,17,18]

The field of polymer derived ceramics has been dominated by metallopolymer self-assembly and lithography followed by pyrolysis.[19–25] These systems provide spacial and compositional control via the polymer precursor through the presence of metals in the segregated domains. Upon pyrolysis, the composition and shape of the resulting ceramics are dictated by that of the polymer precursor. Recently we have shown that a similar effect can be achieved by metal functionalization of a patterned, phosphorus-based photopolymer network (Scheme 4.1).[26] On top of being scalable, the main advantage to photopolymer networks in this context is that they can be shaped before, during and after irradiation, by molding, masking and lithographic techniques, respectively.[26–28] This ability to be shaped at multiple points in a process opens several potential avenues to gain spacial control over the ceramic precursor.

Depending on the chemical functional groups present within the photopolymer network, it has been shown that the material can be metallized by salt metathesis or metal coordination reactions, giving them the potential to impart varied elemental composition of the resulting ceramic after pyrolysis.[26,28–31] These assets could be leveraged in IT applications as the industry currently faces a challenge in identifying room temperature ferromagnetic semiconductors that can be patterned on micro to nano length scales.[32] The broad search for an appropriate composition is ongoing with candidates composed of elements spanning the periodic table.[33,34,43–45,35–42]

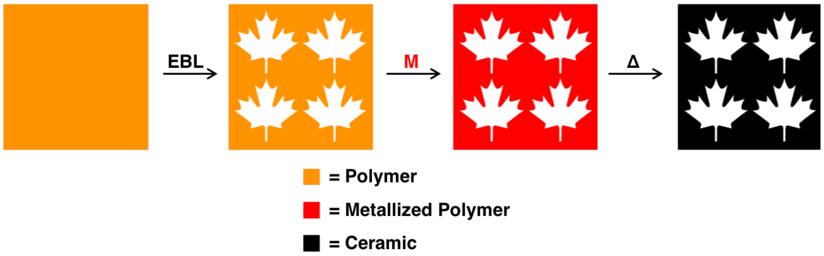

Scheme 4.1: Shape retention on pyrolysis of patterned metal functionalized photopolymer networks. EBL = Electron Beam Lithography, M = Metallic species, Δ = heat.

The coordination chemistry of phosphines is rich and the phosphine sites within phosphane-ene networks can be accessed using simple solution chemistry common to molecular phosphines.[31,46] Coordination chemistry is not restricted to the transition metals as there are now wide-ranging examples of electron rich, Lewis acidic, main group metals that can be coordinated by phosphorus donors.[47] This rich coordination chemistry can be used to incorporate elemental diversity into a polymer network in a controlled fashion. For example, a *mono*-cationic Sb center can be bound by either one or two phosphines depending on the reaction conditions.[48,49] These molecular complexes provide precise ratios of inorganic elements within a material and therefore, by merging this methodology of E-E bond formation with polymer network chemistry, it provides control over the stoichiometry of the inorganic elements in a precursor and in turn, control over the resulting ceramic composition.

We now have merged stibino-phosphonium and stibino-*bis*(phosphonium) chemistry with phosphane-ene photopolymer networks with the result of controlling the stoichiometric ratios of P:Sb within the material. This was achieved by simply varying the coordination environment about Sb. In addition, we have observed that the variation in coordination environment about Sb gave us the ability to tune both the physical and electronic properties of the functionalized networks. These results have prompted us to take a deeper look into this as well as the electronic environment(s) around the main group elements. We have employed XANES (X-ray Absorption Near Edge Structure) spectroscopy to compare the macromolecular system to the comprehensively characterized small molecules, which gave us a unique and definitive window into the nature of the main group atoms in the material.

We have extended this fundamental chemistry to phosphorus-based Lewis acids and explored the susceptibility of the material to be metallized through coordination with metallic Lewis acids containing germanium, aluminum and cobalt. The metallized networks were assessed as ceramic precursors and showed excellent shape retention on pyrolysis of patterns prescribed by electron beam lithography (EBL) prior to metallization.

4.2 Polymer Network Synthesis

Phosphane-ene polymer networks have been previously prepared by the photoinitiated hydrophosphination of primary phosphines and multi-functional olefins.[50] In this work, the synthetic route was modified so that the resulting network contained *only* tertiary phosphines, with no further processing or reaction step. Monoisobutyl phosphine (^{i}BuPH$_2$) was combined in a 3:4 molar ratio with 1,3,5-triallyl-1,3,5-triazine-2,4,6(1*H*,3*H*,5*H*)-trione (TTT) and irradiated in the presence of the photoinitiator Irgacure 819 to yield polymer network (**4.1**; Scheme 4.2). This stoichiometry provides a twofold excess of olefin relative to P-H bonds and all P-H functional groups were consumed as confirmed by the absence of P-H coupling in the ^{31}P NMR spectrum and no evidence for P-H vibrations in the IR spectrum, indicative of 100 % cure (*cf.* ^{i}BuPH$_2$ has $\nu_{(P\text{-}H)}$ = 2298 cm^{-1}). Cure percentages were calculated using IR spectroscopic data based on the relative ratios of the peak intensities from the olefin ($\nu_{(C=C)}$ = 991 cm^{-1}) and carbonyl (($\nu_{(C=O)}$ =1675 cm^{-1}) signals of TTT. On average, cure percentages reached 47% and indicated that half of the olefins remained unreacted, while bound to the network (Figure 4.1).

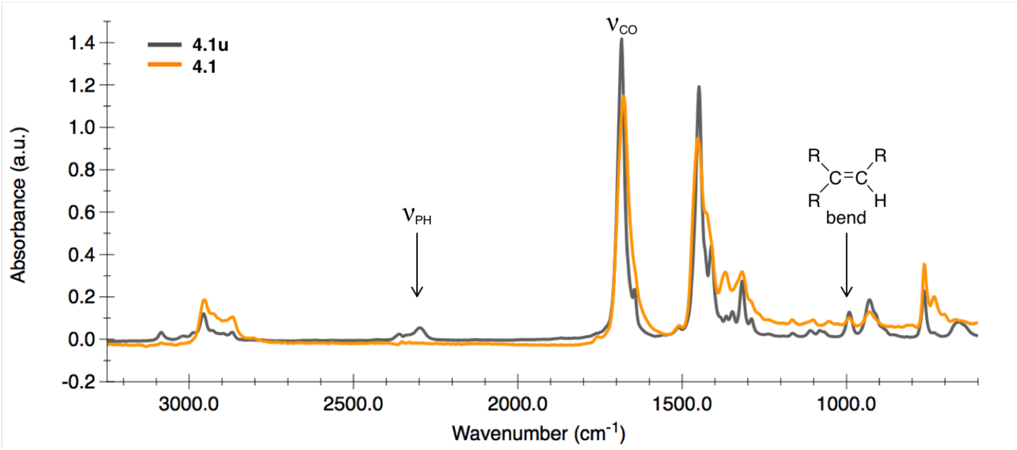

Figure 4.1: ATR-IR spectra of **4.1u** (grey; u = uncured) and cured polymer network **4.1** (orange; cured).

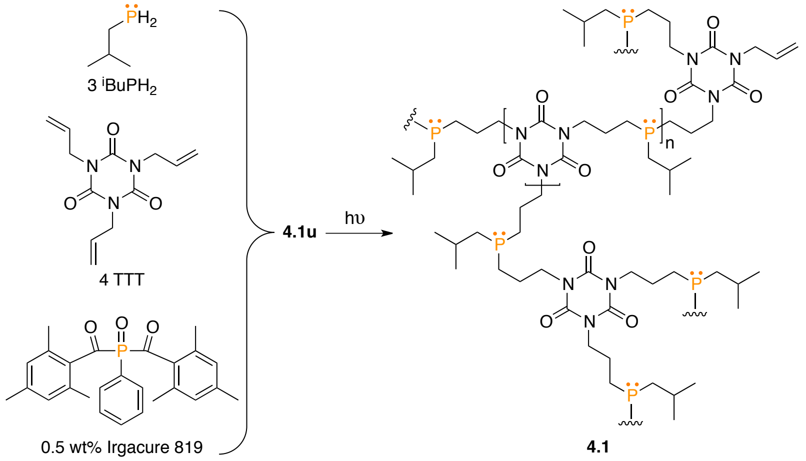

Scheme 4.2: Photopolymerization of neat liquid formulation **4.1u** to make phosphane-ene network **4.1**.

Network **4.1** was insoluble, yet solvent swellable, which was advantageous as it allowed for the acquisition of solution-like ^{31}P NMR spectra, enabling easy assessment of the material as well as solution-like chemistry.[50,51] The swellability of **4.1** was measured for a variety of common laboratory solvents and were ranked in terms of molar swellability in the order H_2O > MeCN > CH_2Cl_2 > THF > Toluene > Et_2O > Pentane (Figure 4.3). There was a clear qualitative relationship between line-width and the molar swellability of the network in a given solvent. With more solvation, the polymer chains were more mobile and thus gave a sharper signal. Water was an anomaly because while it gave the highest molar swellability for **4.1**, the line-width remained broad and we hypothesize that given the organic nature of the phosphorus environment, the poor interaction of the solvent with the polymer chains limited mobility at the molecular level. Ultimately this implied that both swellability *and* solvation contribute to the solution NMR line-width and therefore, a suitable solvent for obtaining a strong signal is one that can both swell the network and interact with the polymer chains.[52]

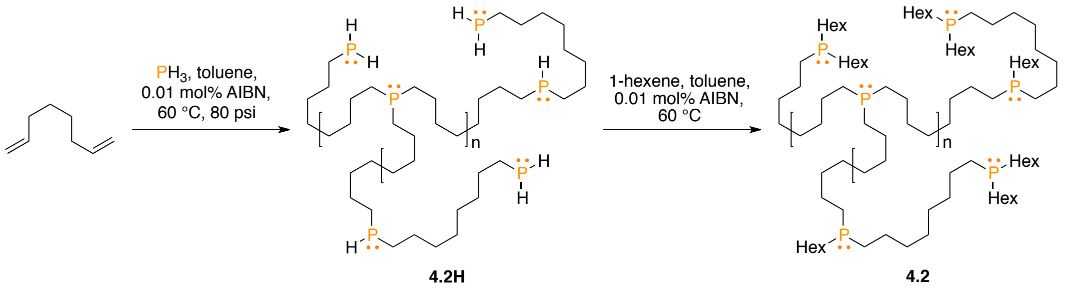

Scheme 4.3: Synthesis of **4.2H** and **4.2** from hydrophosphination of 1,7-octadiene with PH_3.

An excess of phosphine gas was reacted with 1,7-octadiene in the presence of azobisisobutyronitrile (AIBN) as a thermal initiator (Scheme 4.3). Multinuclear NMR spectroscopic analysis of the reaction mixture revealed the disappearance of the olefin signals in the $^{13}C\{^{1}H\}$ NMR spectrum, while the ^{31}P NMR spectrum displayed the characteristic singlet, doublet, triplet and quartet, corresponding to a mixture of tertiary (-31.5 ppm), secondary (-68.7 ppm, $^{1}J_{PH}$ = 194.2 Hz), primary (-137.7 ppm, $^{1}J_{PH}$ = 186.1 Hz) and unreacted (dissolved) PH_3 (-241.7 ppm, $^{1}J_{PH}$ = 178 Hz), respectively. The volatiles were removed *in vacuo* to give a colourless oil (**4.2H**), which displayed a P-H vibration in the IR spectrum ($\nu_{P\text{-}H}$ = 2280 cm^{-1}; Figure 4.2).

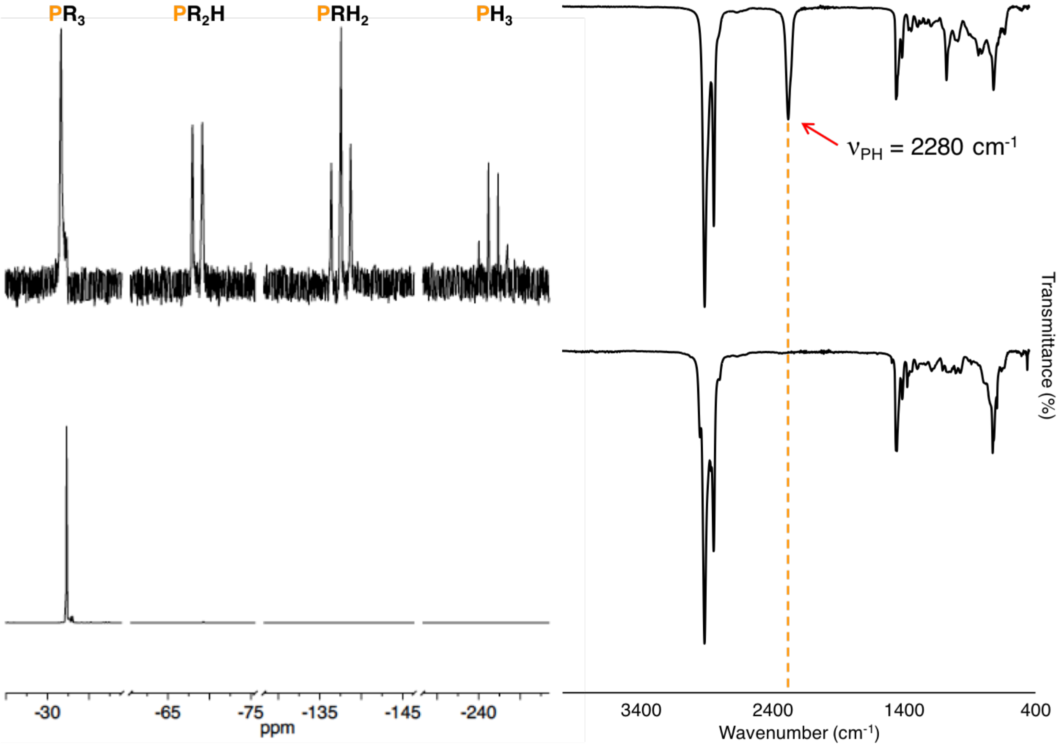

Figure 4.2. Left: ^{31}P NMR of **4.2H** reaction mixture (top) and purified **4.2** (bottom). Right: IR spectrum of purified **4.2H** (top) and **4.2** (bottom).

Network **4.2H** was subjected to a second hydrophosphination reaction with 1-hexene and AIBN as a thermal initiator in order to convert the primary and secondary phosphines to tertiary (Scheme 4.3). After workup, the resulting colourless oil showed no P-H stretches in the IR spectrum and only one singlet indicative of tertiary phosphine was observed in the ^{31}P NMR spectrum (Figure 4.2). The broad, amorphous melting temperature centered at -90 °C, observed for **4.2H** using DSC, could be justified by the mixture of chemical environments in the material. This broad feature transforms into a sharp glass transition onset temperature in **4.2**. Leaching of low molecular weight oligomers and swelling experiments on **4.2** were impossible due to its solubility.

4.3 Preliminary Functionalization with Antimony Lewis Acids

The swellability of **4.1** was not only important for the ease of material characterization, it also opened an avenue for monitoring changes at the tertiary phosphine sites *in situ*. As proof of principle, network **4.1** was swelled in CH_2Cl_2 solutions of $SbClPh_2$ and trimethylsilyl trifluoromethanesulfonate in different stoichiometric ratios to give new, polynuclear networks of **4.1(Sb)$_{0.5}$**, **4.1(Sb)$_{0.75}$** and **4.1Sb** (Scheme 4.4). The reaction stoichiometries were chosen to align with established molecular, model compounds $[Ph_2Sb(PMe_3)_2][OTf]$ and $[Ph_2Sb(PMe_3)][OTf]$, for which **4.1(Sb)$_{0.5}$** and **4.1Sb** were the respective analogues. The small molecule to network comparison was verified by the chemical shift difference (Δδ) observed in the $^{31}P\{^1H\}$ NMR spectra and using XANES spectroscopy, measured relative to the uncoordinated phosphines, network **4.1** and PMe_3, respectively (Table 4.1).

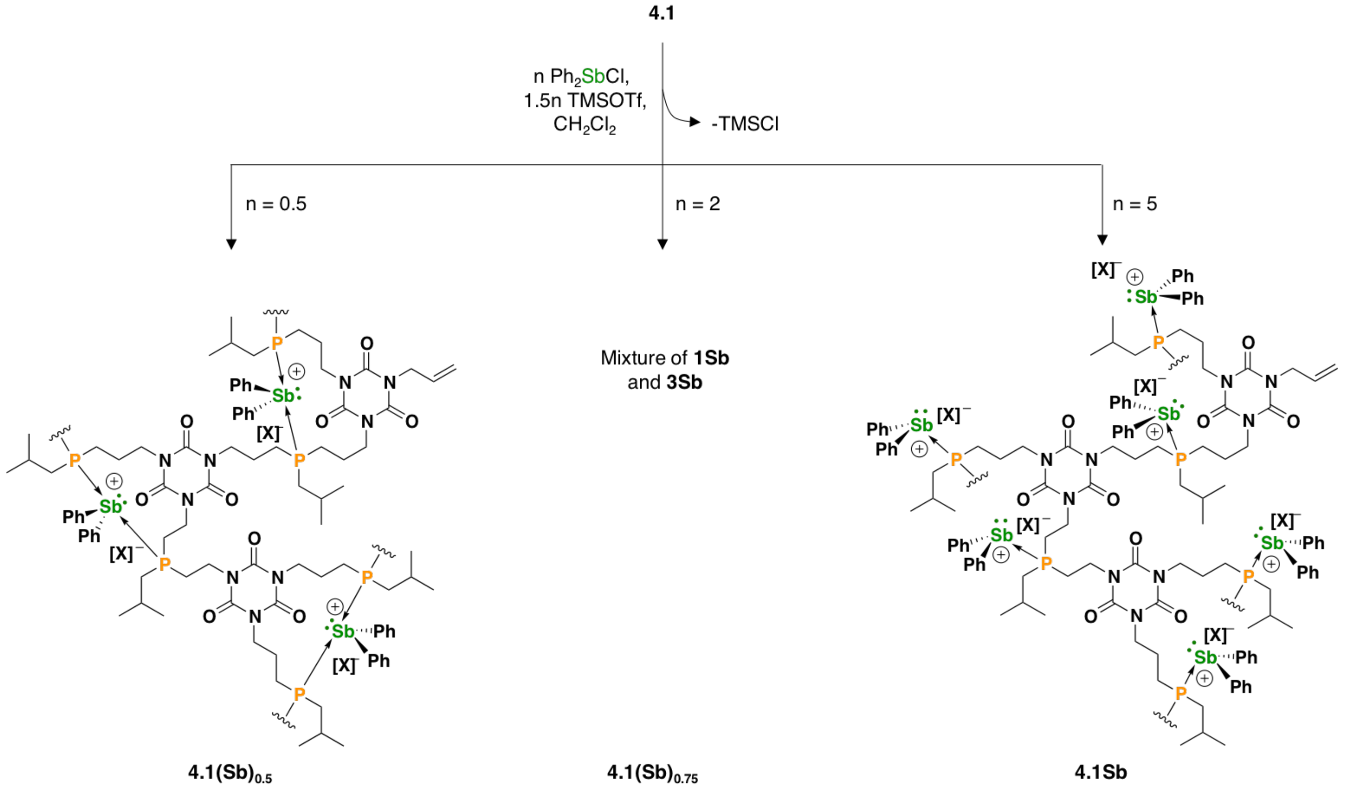

Scheme 4.4: Synthetic route to stibino-phosphonium photopolymer networks, **4.1(Sb)$_{0.5}$**, **4.1(Sb)$_{0.75}$** and **4.1Sb**, $[X]^- = [OTf]^-$.

Both the small molecule model ($[Ph_2Sb(PMe_3)][OTf]$) (δ_P = -21.2 ppm)[48] and polymer network **4.1Sb** (δ_P = 10.1 ppm) shifted by 40 ppm downfield relative to the uncoordinated phosphines (PMe_3 and **4.1**; δ_P = -62 and -34.4 ppm, respectively). These data combined with the reaction stoichiometry indicated that **4.1Sb** had a stibino-phosphonium structure. The more inductively donating 3° phosphine sites in **4.1** relative to PMe_3 explained why the difference in chemical shift between **4.1(Sb)$_{0.5}$** (δ_P = -3.5

ppm) and **4.1** was 10 ppm greater than the difference between $[Ph_2Sb(PMe_3)_2][OTf]$ (δ_P = -41.3 ppm)[48] and free PMe_3. This discrepancy was however small and likely unimportant given the broad signal for **4.1(Sb)$_{0.5}$**. It was clear that the spectrum for **4.(Sb)$_{0.75}$** was simply a mixed polymer containing the presence of both **4.1(Sb)$_{0.5}$** and **4.1Sb** (Figure 4.4).

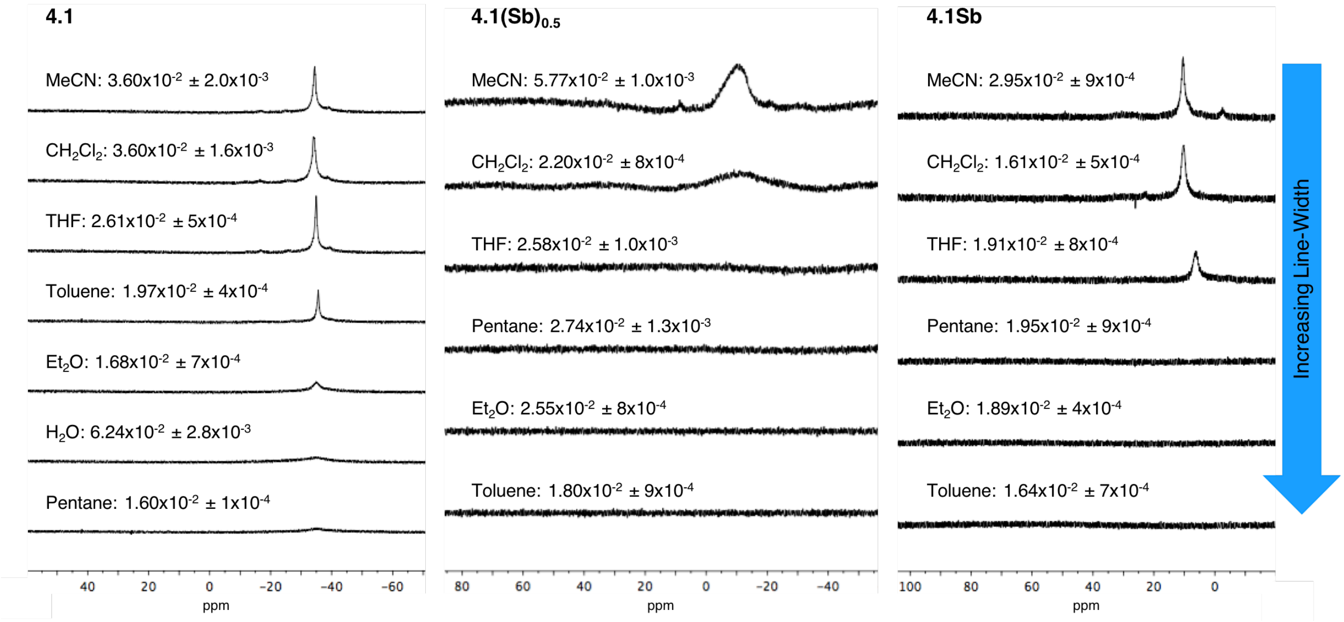

Figure 4.3: Stacked $^{31}P\{^1H\}$ NMR solution NMR spectra of **4.1**, **4.1(Sb)$_{0.5}$** and **4.1Sb** in different solvents showing a qualitative relationship between molar swellability (mol/g) and line width. Exceptions are a result of limited solvation.

The T_g of **4.1Sb** decreased from that of **4.1** by 14 °C with the introduction of the stibino-fragment, which was expected as the presence of a $[Ph_2Sb^+]$ fragment perturbed the network. However, the measured T_g of **4.1(Sb)$_{0.5}$** increased by 25 °C relative to **4.1**, and was consistent with increased crosslinking and a decreased mobility of polymer chains. This further corroborated that **4.1(Sb)$_{0.5}$** contains cationic stibino-*bis*(phosphonium) sites and also rationalized the broadened signals in the NMR spectra. The intermediate transition (43 °C) for **4.1(Sb)$_{0.75}$** corroborated its hybrid composition.

The swellability of **4.1(Sb)$_{0.5}$** and **4.1Sb** was measured for different solvents. The magnitudes were found to be significantly different from **4.1** with the following hierarchies:

4.1(Sb)$_{0.5}$: MeCN > CH_2Cl_2 > THF > Pentane > Et_2O > Toluene

4.1Sb: MeCN > CH_2Cl_2 > Pentane > THF > Et_2O > Toluene

The change in line-width for **4.1(Sb)$_{0.5}$** was a hallmark of the added crosslinking within the material facilitated by the *bis*-coordination at Sb. These molar swellability hierarchies qualitatively matched with the observed line-width with one exception. The molar swellability for **4.1Sb** is higher in pentane than THF, yet THF gives a solution NMR spectroscopic signal, while the pentane spectrum is silent (Figure 4.3). This observation is congruous with the solubility of the molecular model [$Ph_2Sb(PMe_3)$][OTf], which is soluble in THF, but not pentane and once again emphasized the importance of swellability combined with chain solvation in order to obtain a signal.

Table 4.1: P K-edges for model compounds and stibino-phosphonium photopolymer networks.

Compound	*Δδ (ppm)*	*P K-edge (eV)*	*ΔE (eV)*
4.1	-	2145.50	-
4.1(Sb)$_{0.5}$	30	2145.50 (**4.1**), 2147.15	1.65
4.1(Sb)$_{0.75}$	30 (**4.1(Sb)$_{0.5}$**) 40 (**1Sb**)	2145.50 (**4.1**), 2147.45	1.95
4.1Sb	40	2147.00	1.50
[$Ph_2Sb(PMe_3)_2$][OTf]	20	2145.65 (PMe_3), 2147.00	1.35
[$Ph_2Sb(PMe_3)$][OTf]	40	2145.65 (PMe_3), 2147.30	1.65
PPh_3	-	2145.05	-
[$Ph_2Sb(PPh_3)_2$][OTf]	0	2145.50	0.45
[$Ph_2Sb(PPh_3)$][OTf]	0	2145.65	0.60

Networks **4.1(Sb)$_{0.5}$**, **4.1(Sb)$_{0.75}$** and **4.1Sb** were pyrolyzed using optimized conditions at 800°C for 4 hours under reducing conditions (5% H_2, balanced by N_2). The amount of Sb in the bulk char material formed from **4.1Sb** (2.6%) was twice that of **4.1(Sb)$_{0.5}$** (1.3%), and char from **4.1(Sb)$_{0.75}$** (2.3 %) had an intermediate amount, consistent with the order of Sb in the polymer precursors. The char yields of the stibino-phosphonium networks were higher than that of **4.1** (9.16%) with values of 13.70%, 13.39% and 17.30% for **4.1(Sb)$_{0.5}$**, **4.1(Sb)$_{0.75}$** and **4.1Sb**, respectively. This was also an indication that the inorganic elements were retained in the char after pyrolysis and underscored the utility of coordination chemistry to introduce and control elemental diversity.

XPS revealed that the char was composed from a mixture of metallic Sb and Sb_2O_3. Chars from **4.1(Sb)$_{0.5}$**, **4.1(Sb)$_{0.75}$** and **4.1Sb** are also composed of C (86.1, 83.0 and 84.9%), N (4.6, 3.6 and 4.3%), O (7.1, 10.1 and 7.7%) and P (1.0, 0.7 and 0.4%), respectively. The C content was high despite the reducing conditions and the presence of N and O is attributed to the TTT backbone of the polymer precursor. Interestingly, the presence of O also explained the low P content relative to Sb. Given the highly oxophilic nature of P, the formation of P_4O_{10} and its sublimation (360 °C) during the pyrolysis experiment was likely.[26] This was corroborated by the XPS data that showed the identity of P in the char to be phosphate. The PXRD patterns for all three materials matched that of Sb metal[53] with no superimposed sharp signals, indicating all other components of the char were amorphous. The char could be characterized as doped carbon black with low crystallinity based on the high C content, broad low angle signals (<100° 2θ) in the PXRD pattern and the presence of carboxyl, ketone, alcohol and ether C XPS signals typical of carbon black.[54]

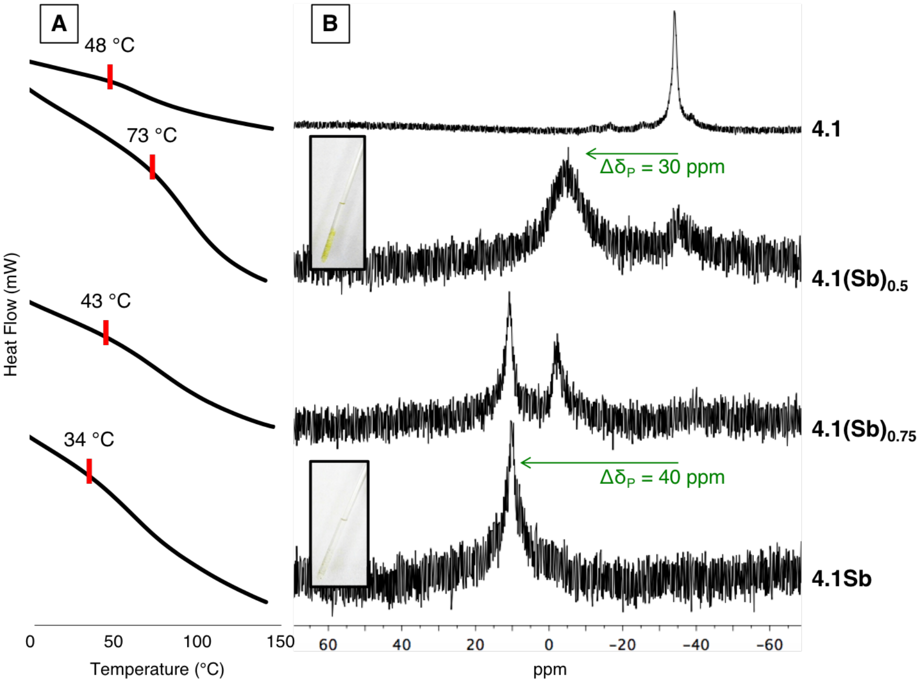

Figure 4.4: A) DSC plots, for **4.1** and stibino-phosphonium polymer networks. T_g onset temperatures are marked in red. B) $^{31}P\{^1H\}$ NMR spectra for **4.1** and stibino-phosphonium networks (pictures inset) of **4.1(Sb)$_{0.5}$** (yellow) and **4.1Sb** (colourless) swelled with CH_2Cl_2 in NMR tubes.

X-ray absorption near edge structure (XANES) spectroscopy was used to characterize the electronic structure of P in the model compounds and functionalized networks by measuring the P K-edge. Given that the P atoms in $[Ph_2Sb(PMe_3)_2][OTf]$ were more electron rich compared to those in $[Ph_2Sb(PMe_3)][OTf]$ the distinction was manifested in the XANES spectra of the materials as the edges shifted by 1.35 and 1.65 eV relative to PMe_3, respectively. The PPh_3 analogues of these two compounds showed the same trend, where $[Ph_2Sb(PPh_3)_2][OTf]$ had a lower edge energy than $[Ph_2Sb(PPh_3)][OTf]$, however the magnitude of the edge shift was drastically lower at 0.45 eV and 0.60 eV relative to uncoordinated PPh_3, respectively (Table 4.1). This followed the greater sigma donor strength of PMe_3 relative to PPh_3, and therefore PMe_3 became more electron poor than PPh_3 upon coordination and is a signpost that the donor ability of the phosphine must be considered when comparing model compounds to polymer networks.[55]

Network **4.1Sb** had an edge shift of 1.50 eV relative to **4.1**, which was comparable to the 1.65 eV edge shift of $[Ph_2Sb(PMe_3)][OTf]$ from PMe_3. Networks **4.1(Sb)$_{0.5}$** and **4.1(Sb)$_{0.75}$** had edge shifts of 1.65 and 1.95 eV relative to **4.1**, respectively. In this case, the edge shifts were higher than expected based on the observed trends in the model compounds and the macromolecular structure of the materials must be taken into account. Crosslinking inherently elongates the involved polymer chains. In the case of **4.1(Sb)$_{0.5}$**, the Sb coordination environment further crosslinked the network. As a result of these lengthened polymer chains, the phosphines in **4.1(Sb)$_{0.5}$** became more inductively donating and therefore exhibited a larger than expected edge shift relative to **4.1**. Since **4.1(Sb)$_{0.75}$** was a hybrid material of **4.1(Sb)$_{0.5}$** and **4.1Sb**, the phosphines were more electron donating due to the crosslinked environments from stibino-*bis*(phosphonium) sites and consequently there was a greater sigma-donation at the stibino-*mono*(phosphonium) sites compared to **4.1Sb**, where there was no additional crosslinking. It was likely that the edge energies for the stibino-*mono* and -*bis*(phosphonium) environments were energetically similar as indicated by the single broad edge feature in the first derivative XANES spectrum.

4.4 Functionalization with Phosphorus Lewis Acids

The ability to tune the physical properties and electronic structure of **4.1** by biasing the reaction stoichiometry with Sb was an unexpected result that piqued our curiosity. We wanted to see if similar results could be reproduced with other elements. Pnictino(phosphonium) chemistry is known from phosphorus through to bismuth.[48,49,56,57] With the bismuth derivatives being light sensitive and there being no reports of arsino-*bis*(phosphonium) cations, we focused our efforts on targeting phosphino(phosphonium) cation functionalized photopolymer networks.

The dimethyl analogue, **4.1PMe$_2$** was synthesized by swelling **4.1** in a dichloromethane solution of trimethylsilyl trifluoromethanesulfonate and chloro(dimethyl)phosphine for one week (Scheme 4.5). After workup, the solution NMR spectrum of the gel revealed two doublets (δ_P = 26.0, -58.4 ppm; $^1J_{PP}$ = 307.4 Hz) with comparable chemicals shifts to the small molecule analogue, $[(PMe_3)(PMe_2)][OTf]$ (δ_P = 18, -60 ppm; $^1J_{PP}$ = 275 Hz; Figure 4.5).[56] The larger coupling constants in **4.1PMe$_2$** could be attributed to the higher inductive effect from the longer alkyl chains that comprise the polymer network backbone.

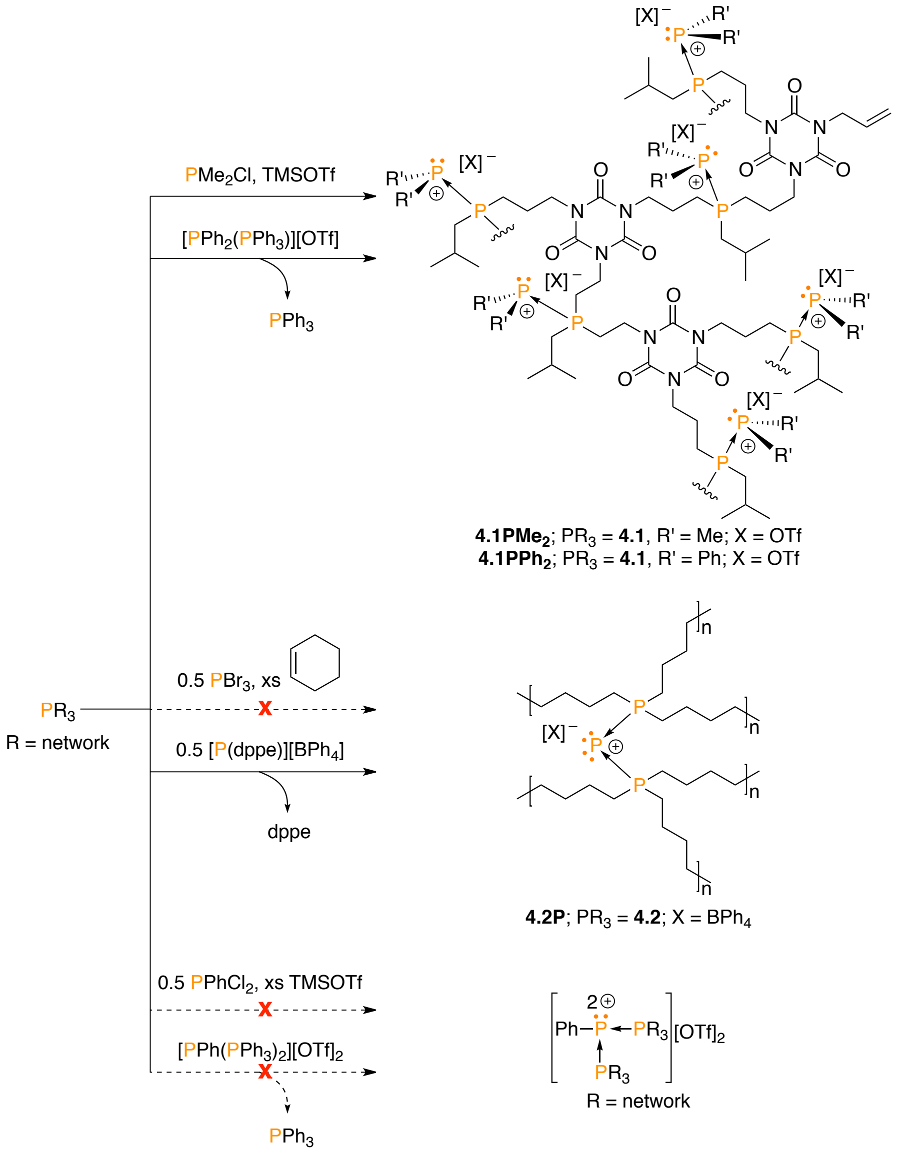

Scheme 4.5: Synthesis of **4.1PMe$_2$**, **4.1PPh$_2$** and **4.2P** as well as attempted routes to phosphino-bis(phosphonium) dicationic polymer networks.

The same reaction was attempted with **4.1** combined with chloro(diphenyl)phosphine and trimethylsilyl trifluoromethanesulfonate but did not proceed cleanly and the resulting gel could not be purified. Network **4.1PPh$_2$** was synthesized cleanly in a ligand exchange reaction of **4.1** with [(PPh$_3$)(PPh$_2$)][OTf] (Scheme 4.5). The PPh$_3$ could be leached out and the ^{31}P{^{1}H} NMR spectrum of the clean material revealed two doublets (δ_P = 24.3, -27.1; $^1J_{PP}$ = 324.6 Hz) with chemicals shifts consistent with [(PMe$_3$)(PPh$_2$)][OTf] (δ_P = 15, -23 ppm; $^1J_{PP}$ = 289 Hz; Figure 4.5).[57] Again, the larger coupling constant was an indication of the stronger P–P interaction brought on by the stronger inductive effect of the polymer network. The ^{19}F{^{1}H} NMR spectrum for both **4.1PMe$_2$** and **4.1PPh$_2$** (δ_F = -78.6 ppm for both) was consistent with the non-coordinating triflate in the molecular analogues.

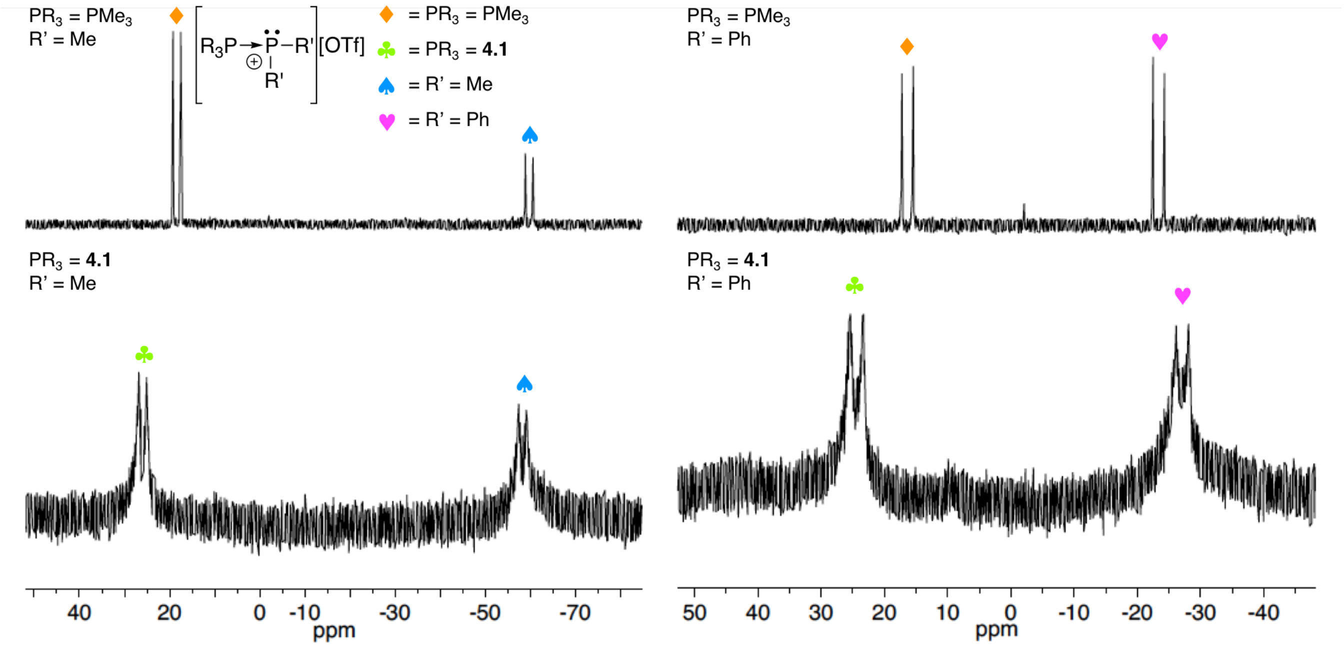

Figure 4.5: Stacked $^{31}P\{^{1}H\}$ NMR spectra of **4.1PMe₂** (bottom left) and **4.1PPh₂** (bottom right) with their respective molecular analogues.

The glass transition onset temperatures of **4.1PMe₂** and **4.1PPh₂** (T_g = 82.7 and 96.7 °C, respectively) increased relative to native **4.1**. This was contrary to the analogous network **4.1Sb**, which showed a decrease. It is likely that the phosphino group imposes an ionic component on the material, decreasing chain mobility, whereas the much higher polarizability of Sb diffuses the positive charge enough to minimize these ionic forces.

In order to crosslink the material we looked to the known phosphino-*bis*(phosphonium) dications.[58] Both halide abstraction and ligand exchange reactions were attempted with **4.1** to no avail (Scheme 4.5). Any attempts to synthesize a phosphino-bis(phosphonium) functionalized network were met with futility as the reactions did not proceed cleanly and the nature of the crosslinked material prevented straight forward purification. Triphosphenium cations are another well-established form of cationic phosphorus supported by phosphine ligands and this functionality was also investigated for crosslinking the networks.[59–61]

Triphosphenium cations can be synthesized by reduction of phosphorus (III) halides in the presence of two stoichiometric equivalents of tertiary phosphine and cyclohexene, where the latter acts as a scavenger for the elemental halogen byproduct.[59,61] When **4.1**, **4.2** and $POct_3$ were reacted with PBr_3 and cyclohexene, the result was an insoluble orange precipitate, usually attributed to red phosphorus and was a sign of over reduction. Reactivity studies of triphosphenium cations have shown that they can act as a P(I) transfer reagent.[36–39] The superior sigma donating alkyl phosphines, **4.1**, **4.2** and PMe_3 were reacted with $[P(dppe)][BPh_4]$ to replace the aryl phosphines in 1,2-bis(diphenylphosphino)ethane (dppe; Scheme 4.5). While the material changed from colourless to red overnight after addition, no significant change was observed by NMR spectroscopy for this reaction using **4.1**. The reaction with **4.2** resulted in the formation of a gel, which could be probed using solution NMR spectroscopy. The $^{31}P\{^1H\}$ spectrum revealed the release of dppe and the formation of a new doublet (d, 33.2 ppm, $^1J_{PP}$ = 469.2 Hz; Figure 4.6). The coupling constant and chemical shift was consistent with those of the molecular analogue, $[P(POct_3)_2][BPh_4]$ (d, 33.2, t, -230.2 ppm, $^1J_{PP}$ = 477.3 Hz). The newly formed network precipitated from solution during workup and became completely insoluble. The solid was analyzed by solid state NMR spectroscopy, which revealed two broad signals in the expected chemical shift range for both the supporting phosphines and phosphanide center (Figure 4.6).

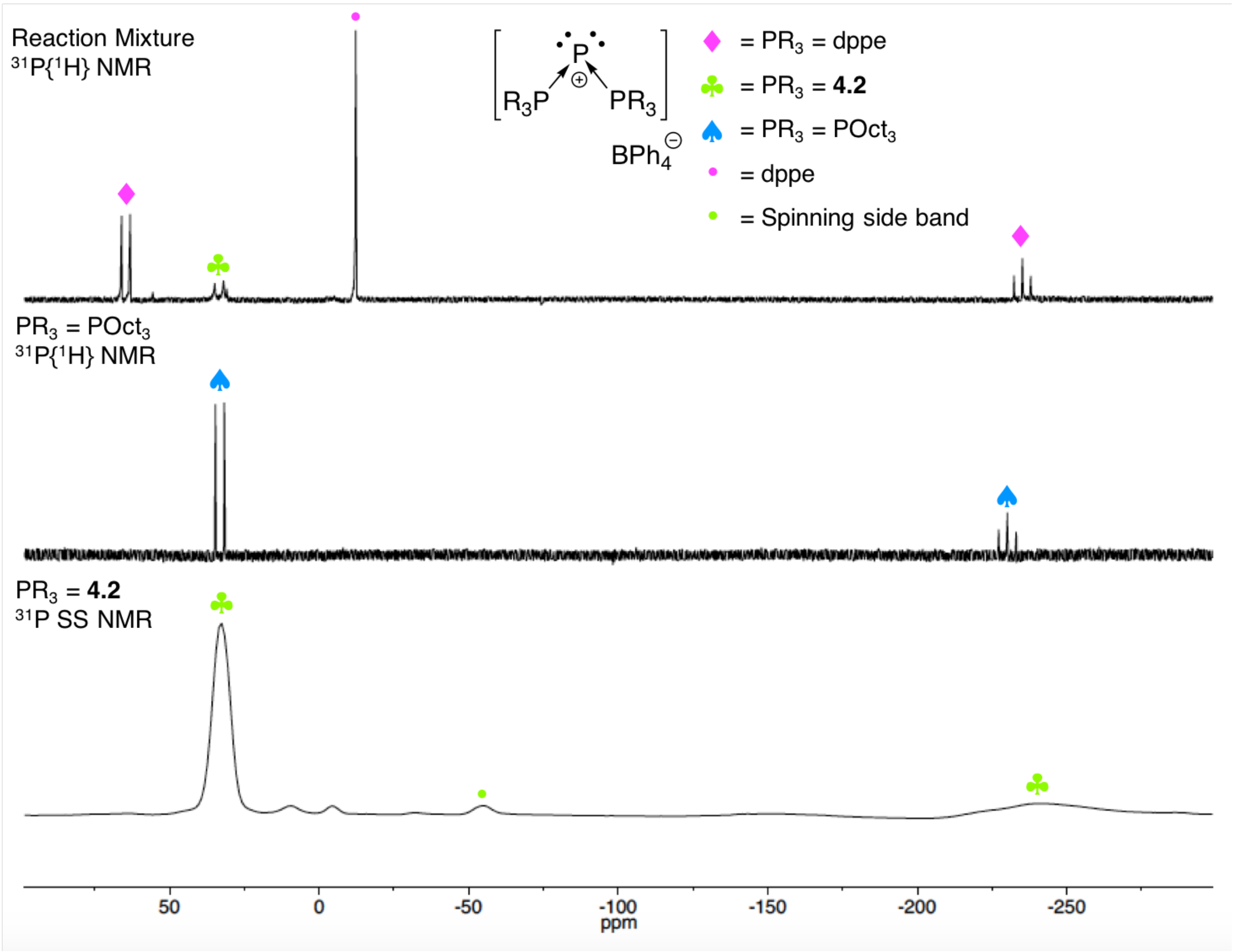

Figure 4.6: Stacked NMR spectra of the reaction mixture for **4.2P** (top), $[P(POct_3)_2][BPh_4]$ (middle) and isolated solid state **4.2P.**

Despite the additional crosslinking in **4.2P** (T_g = -114 °C) relative to **4.2** (T_g = -90 °C), the glass transition temperature decreased by 24 °C. This could be justified by the steric imposition of the tetraphenylborate anion and bent structure of the phosphanide center, which would both decrease the polymer chains' ability to pack into a glassy state. An investigation on the electronic structure in the molecular $[P(P(POct_3)_2][BPh_4]$ and macromolecular **4.2P** is currently underway.

4.5 Functionalization with Metallic Lewis Acids

In order to demonstrate the versatility of **4.1** and the potential for installing a highly versatile complement of elements, the network was reacted with different metallic Lewis acids namely, $AlMe_3$, $AlMe_2Cl$, $GeCl_2$(dioxane) and $CpCo(CO)_2$ (Scheme 4.6). Slight phosphorus chemical shift differences between free phosphine and aluminum adducts are typical,[66] for example when **4.1** was reacted with trimethylaluminum and chlorodimethylaluminum, the ^{31}P NMR spectroscopic signal shifted by 4 ppm to higher frequency and indicated successful adduct formation of networks **4.1AlMe$_3$** and **4.1AlMe$_2$Cl**, respectively. The appearance of a low frequency singlet ($\delta_C \approx -7$ ppm) in the carbon NMR spectrum of both networks is characteristic of a methyl group bound to an electropositive main group center and corroborated adduct formation.[66] The higher char yield of **4.1AlMe$_2$Cl** (52.8 %) relative to **4.1AlMe$_3$** (41.0 %) is consistent with the presence of the heavy chlorine atoms in the polymer precursor, which was confirmed by EDX spectroscopy.

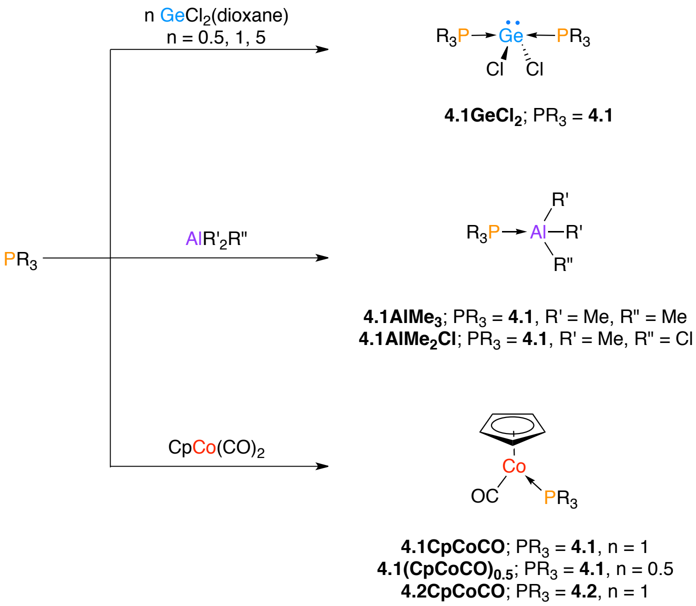

Scheme 4.6: Metal functionalization by coordination of phosphane-ene networks **4.1** and **4.2**.

Network **4.1** was reacted with $GeCl_2$(dioxane) in 1:0.5, 1:1 and 1:5 stoichiometries, always with the complete conversion of the native phosphine and appearance of a single broad signal in the ^{31}P

NMR spectrum (δ_P = -4.0 ppm; Figure 4.7) to give **4.1GeCl$_2$**. Complete conversion of the phosphine using only half an equivalent of the germanium starting material points to crosslinking at germanium as was previously observed in stibino-*bis*(phosphonium) networks.[46] This was corroborated by the 43 °C increase in glass transition temperature from native to coordinated phosphine, which was indicative of the decreased mobility of the polymer chains crosslinked by germanium (Figure 4.7). The relatively low char yield of 26.2 % could be attributed to the low stoichiometry of Ge in the material.

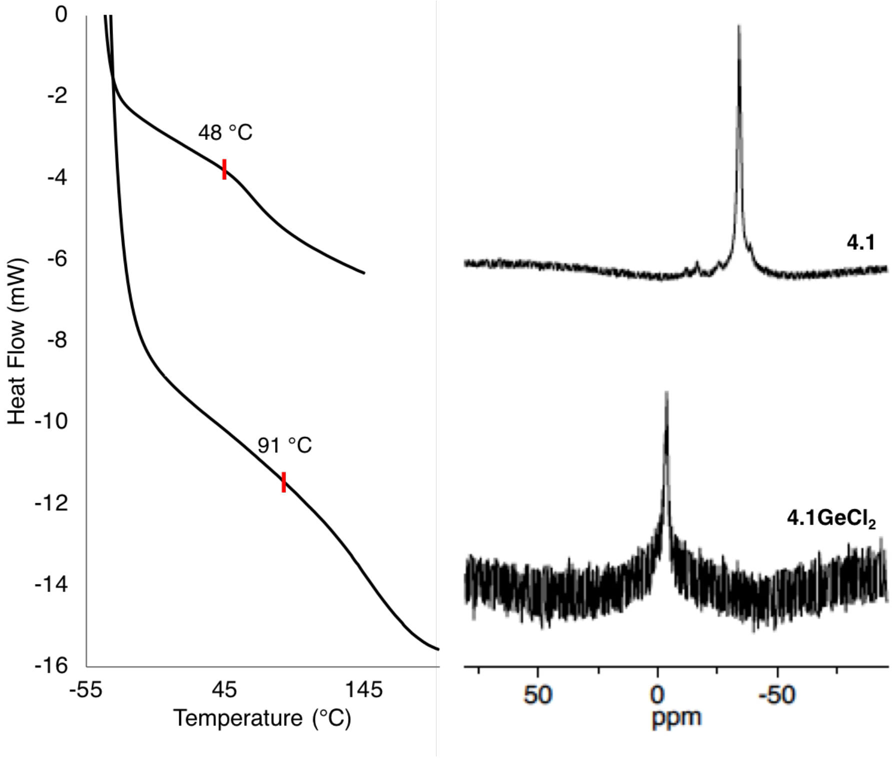

Figure 4.7: Stacked DSC plots (left) and $^{31}P\{^1H\}$ NMR spectra (right) of **4.1** (top) and **4.1GeCl$_2$** (bottom).

Network **4.1** was refluxed in a THF solution with either half or one stoichiometric equivalent of cyclopentadienylcobalt dicarbonyl for one week to give a red polymer gel post work up (**4.1(CpCoCO)$_{0.5}$** and **4.1CpCoCO**, respectively). Both materials displayed a single metal carbonyl stretch in the IR spectrum ($\nu_{CoCO} \approx$ 1907 cm^{-1}) as well as a singlet in the $^{31}P\{^1H\}$ NMR spectra (δ_P=51 ppm). While this was the sole signal for **4.1CpCoCO**, **4.1(CpCoCO)$_{0.5}$** displayed a second singlet (δ_P = -35ppm) of approximately equal intensity, which corresponded to unreacted P sites within **4.1** (Figure 4.8A). The $^{13}C\{^1H\}$ NMR spectra for both cobalt functionalized networks displayed signals that corresponded to the metal carbonyl and metal bound cyclopentadienyl groups ($\delta_C \approx$ 208, 81 ppm, respectively). The EDX data for both networks confirmed the presence of cobalt. Together these data pointed to the addition of a [CpCoCO] moiety to **4.1**, with all phosphines coordinated in **4.1CpCoCO** and approximately half coordinated in **4.1(CpCoCO)$_{0.5}$**, showing that the M:P ratio in the polymer precursor could be easily regulated by adjusting the reaction stoichiometry. These results were echoed by the thermal data, which showed a lower char yield for **4.1(CpCoCO)$_{0.5}$** relative to **4.1CpCoCO** (26.2 and 33.2 %, respectively), indicative of the lower concentration of cobalt in the polymer precursor. The glass transition temperatures of **4.1(CpCoCO)$_{0.5}$** and **4.1CpCoCO** decreased relative to **4.1** (30, 27 and 48 °C, respectively), consistent with a disruption in polymer chain packing that would arise from the addition of a [CpCoCO] fragment. The glass transition temperature of **4.1CpCoCO** was slightly more depressed than that of **4.1(CpCoCO)$_{0.5}$**, consistent with a larger amount of organometallic moiety.

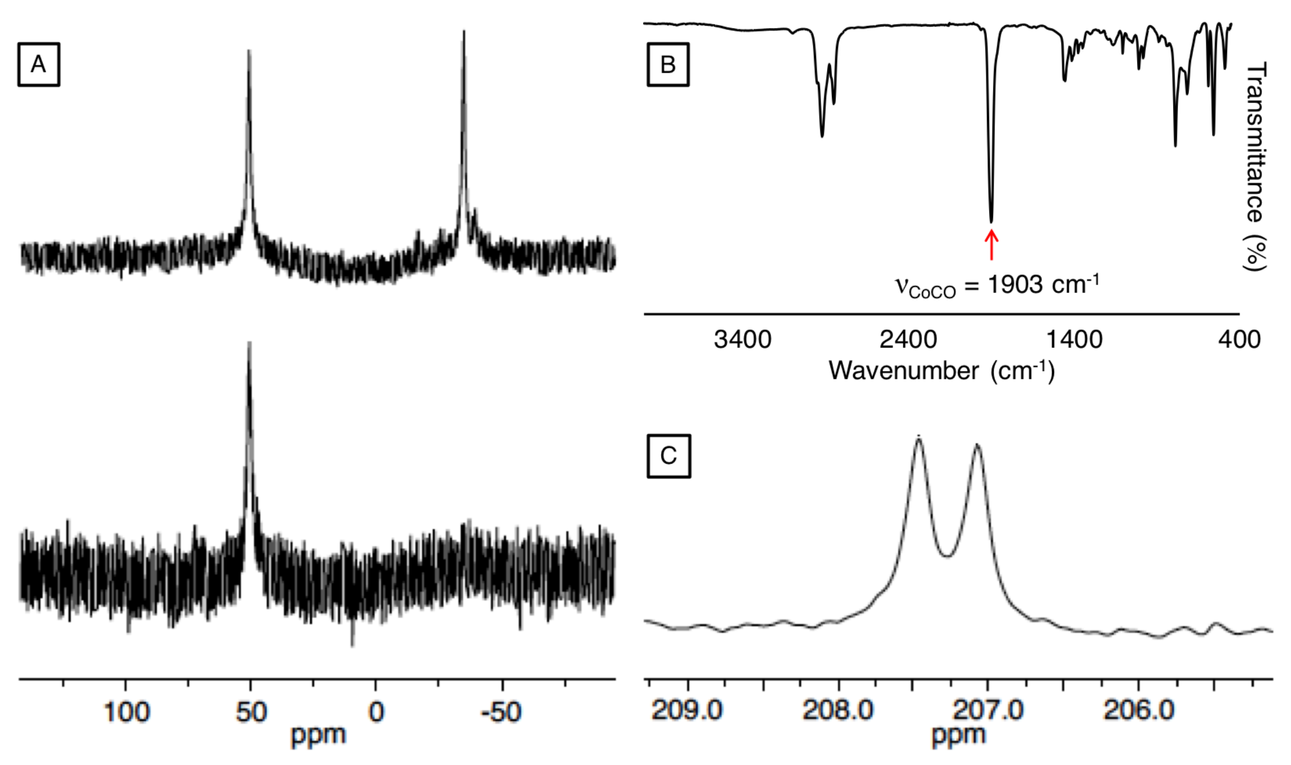

Figure 4.8: A) Stacked $^{31}P\{^1H\}$ NMR spectra of **4.1(CpCoCO)$_{0.5}$** (top) and **4.1CpCoCO** (bottom); B) IR spectrum of **4.2CpCoCO**; C) Carbonyl region from the $^{13}C\{^1H\}$ NMR spectrum of **4.2CpCoCO** showing P-C J coupling.

An effort was made to crosslink the material at cobalt by ejecting carbon monoxide from **4.1(CpCoCO)$_{0.5}$**. This was attempted thermally and photochemically, either in solution or the solid state with the result of either no reaction, or the deposition of cobalt metal.

Previous work in using phosphorus-based photopolymer networks as ceramic precursors has shown utility in producing carbon doped with a mixture of metal phosphides and oxides, where the oxides result from a high portion of O in the network backbone.[26,46] As the backbone degrades and releases oxygen, it reacts with the oxophilic elements to form phosphate and metal oxides. The obvious solution to this problem was to eliminate heteroatoms from the polymer backbone. Since most photopolymerizable groups contain heteroatoms, thermally initiated hydrophosphination was used to make network **4.2** with an "all-alkyl" backbone

In a similar fashion to the production of **4.1CpCoCO**, network **4.2** was refluxed in a THF solution of cyclopentadienylcobalt dicarbonyl for one week to give **4.2CpCoCO**. Removal of the volatiles from the reaction mixture resulted in a red oil, which after trituration with hexanes, yielded a red gel. The glass transition onset temperature of **4.2CpCoCO** was -19 °C, more than 70 °C higher than that of **4.2**.

Network **4.2CpCoCO** displayed similar spectroscopic handles to those in **4.1CpCoCO**. There was one signal (ν_{CoCO} = 1903 cm^{-1}, Figure 4.8B) in the metal carbonyl region of the IR spectrum, which confirmed the removal of excess $CpCo(CO)_2$ and the presence of a single metal carbonyl functional group. The $^{31}P\{^1H\}$ NMR chemical shift (δ_P = 49.9 ppm) was consistent with that of **4.1CpCoCO** and the carbon NMR spectrum revealed a doublet (δ_C = 207.3 ppm, $^2J_{CP}$ = 40.2 Hz; Figure 4.8C) consistent with the carbonyl carbon coupling with the phosphorus. The singlet at δ_C=80.5 ppm was consistent with the presence of a coordinated cyclopentadienyl ring and corroborates the IR data that indicated the addition of a CpCoCO fragment to the material. The char yield of **4.2CpCoCO** (27.6 %) was low relative to **4.1CpCoCO** (33.2 %), likely a result of the higher molecular weight of the alkyl backbone.

4.6 Ceramic Morphology and Composition

Networks **4.1AlMe$_3$** and **4.1CpCoCO** were selected for pyrolysis experiments because of their high char yields. The functionalized polymer networks were pyrolyzed at 800, 900 and 1000 °C for either 3 or 4 hours under reducing conditions (5% H_2, balanced by N_2). The resulting char was analyzed using EDX and XPS to assess composition as well as SEM and PXRD to probe the morphology.

Table 4.2. XPS composition data for char derived from the pyrolysis of **4.1AlMe$_3$** at 800 °C for 4 hours. Area % is derived from the P XPS.

Area %	*Atomic %*				
Phosphate	*Al*	*O*	*C*	*N*	*P*
100.0	20.0	40.0	37.0	2.5	0.5

The black char that resulted from the pyrolysis of **4.1AlMe$_3$** was amorphous given the broad PXRD signals observed as well as the porous, non-uniform structure noted in the SEM images (see SI). On average, the chars formed at different conditions were found to be composed of 20% aluminum, 40% oxygen, 37% carbon, 2.5% nitrogen and 0.5% phosphorus by XPS (Table 4.2). The low phosphorus content can be attributed to its oxophilic nature and conversion to volatile P_4O_{10} upon reaction with the oxygen contained in the polymer backbone as it decomposes. This hypothesis was corroborated by the XPS data which revealed 100% of P in the material to be phosphate. The presence of Al(III), as Al_2O_3 was also a result of the oxophilicity of aluminum. These data best characterize the char as a mixture of aluminum oxide and carbon black doped with nitrogen and phosphate.

Table 4.3. XPS composition data for char derived from the pyrolysis of **4.1CoCoCO** and **4.2CpCoCO** at 800 °C for 4 hours. Area % is derived from the Co XPS.

	Component	**4.1CpCoCO**	**4.2CpCoCO**
Area %	Co_2P	8.4	25.9
	$Co_3(PO_4)_2$	94.0	74.0
Atomic %	C	79.1	68.5
	O	12.9	14.5
	N	1.8	3.0
	Co	2.5	6.9
	P	3.0	6.7

Similarly, when **4.1CpCoCO** was pyrolyzed, a black amorphous char resulted based on broad PXRD and SEM data. The chars formed at different conditions were similar, and on average were composed of 2.5% cobalt, 83.5% carbon, 10% oxygen, 2.5% phosphorus and 1.5% nitrogen by XPS (Table 4.3). The high carbon content in these samples pointed to doped carbon black. Interestingly, the oxygen content in this char was much lower than the aluminum functionalized samples however, no cobalt oxide was formed and the state of cobalt was found to be a mixture of ~90% cobalt (II) phosphate and ~10% cobalt (I/II) phosphide (Co_2P; Table 4.3). The P 2p XPS revealed the presence of phosphate and phosphide binding energies at 132.9-133.5 and 129.0-129.6 eV, respectively. There was an additional binding energy at 131.2-132.0 eV, which was consistent with P(III) incorporated as a dopant in the carbon black.[67,68]

The char from **4.1CpCoCO** confirmed the possibility of making metal phosphides using these polymers as precursors, yet the oxygen contained in the polymer backbone was clearly detrimental as element oxidation was dominant. In contrast, pyrolysis of network **4.2CpCoCO** showed that replacing the polymer backbone with alkyl chains was effective in increasing the amount of phosphide (25.9%) relative to phosphate (74.0%; Table 4.3). Despite the relatively low char yield, the char derived from **4.2CpCoCO** contained more than double the amount of P and Co than the char derived from **4.1CpCoCO** and the ratio of P to Co of 1:1 from the polymer precursor was manifested in the char after pyrolysis, showing retention of the desired inorganic elements and a degree of control over ceramic composition.

4.7 Patterning and Shape Retention

Thin films of **4.1** were cast by spin coating the neat formulation, **4.1u** onto silicon wafers in the glovebox and curing with UV irradiation in the inert cell from Figure 2.1 to give **4.1**$^{\mathbf{thin}}$. The material was determined to have the same IR and $^{31}P\{^{1}H\}$ NMR spectroscopic signatures as the bulk material of **4.1** as well as the same susceptibility to solution chemistry with trimethylaluminum.

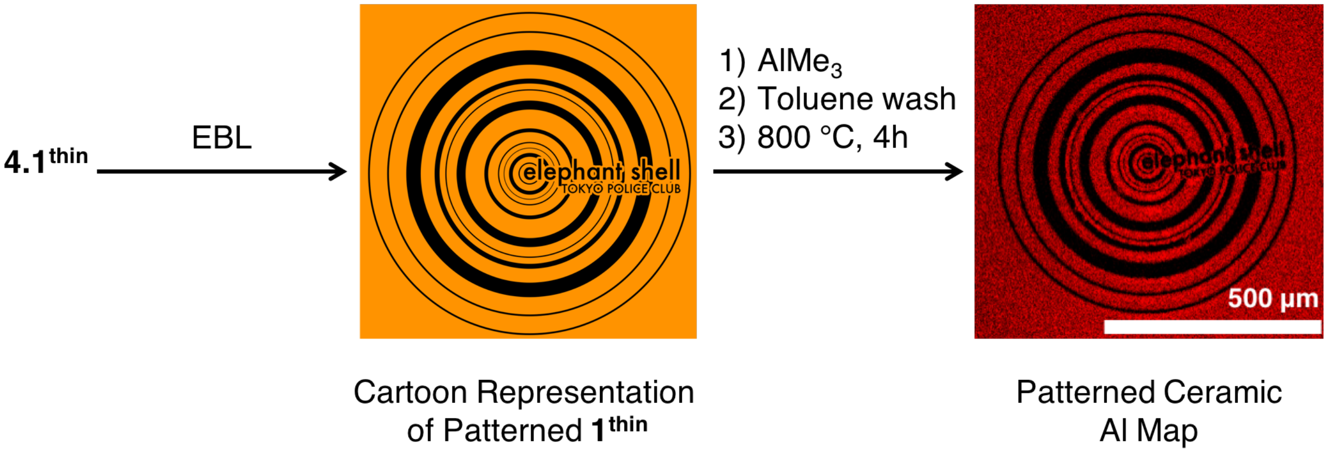

Scheme 4.7: Patterning, metal functionalization, workup and pyrolysis of phosphane-ene thin film, **4.1**$^{\mathbf{thin}}$.

Network **4.1**$^{\mathbf{thin}}$ was tested as a positive resist for electron beam lithography (EBL), which is a good technique to use in prototyping small scale patterns.[69] Arrays of squares were scribed onto **4.1**$^{\mathbf{thin}}$ using varied electron doses (1.00, 1.50, 2.25, 3.38, 5.06, 7.59, 11.39, 17.09 and 25.63 µC/cm^2). Patterned **4.1**$^{\mathbf{thin}}$ was then functionalized with trimethylaluminum solution, followed by a toluene wash, then allowed to dry before being loaded into the tube furnace for pyrolysis (Scheme 4.7). Confocal microscopy and SEM Analysis of the patterned, metallized and pyrolyzed film showed excellent shape retention of the square array and definitive elemental segregation with Al present in the areas where the film was left intact and found in trace amounts where the beam wrote (Figure 4.9). Overall, the material was found to be sensitive to the electron beam relative to standard polymethylmethacrylate and the optimal dose was found to be between 3.38 and 5.06 µC/cm^2. This dose range was effective at degrading the polymer network and resulted in well resolved square edges.

In tribute to the indie rock band Tokyo Police Club (TPC), selected, modified album covers were chosen for EBL patterns (Figure 4.10). It was also necessary to pay tribute to the paradigm of shape retention, the fossil, and so a raptor fossil and primitive T-rex image were patterned onto a sample of **4.1**$^{\mathbf{thin}}$ in order to explore the shape retention limits of the material upon pyrolysis.

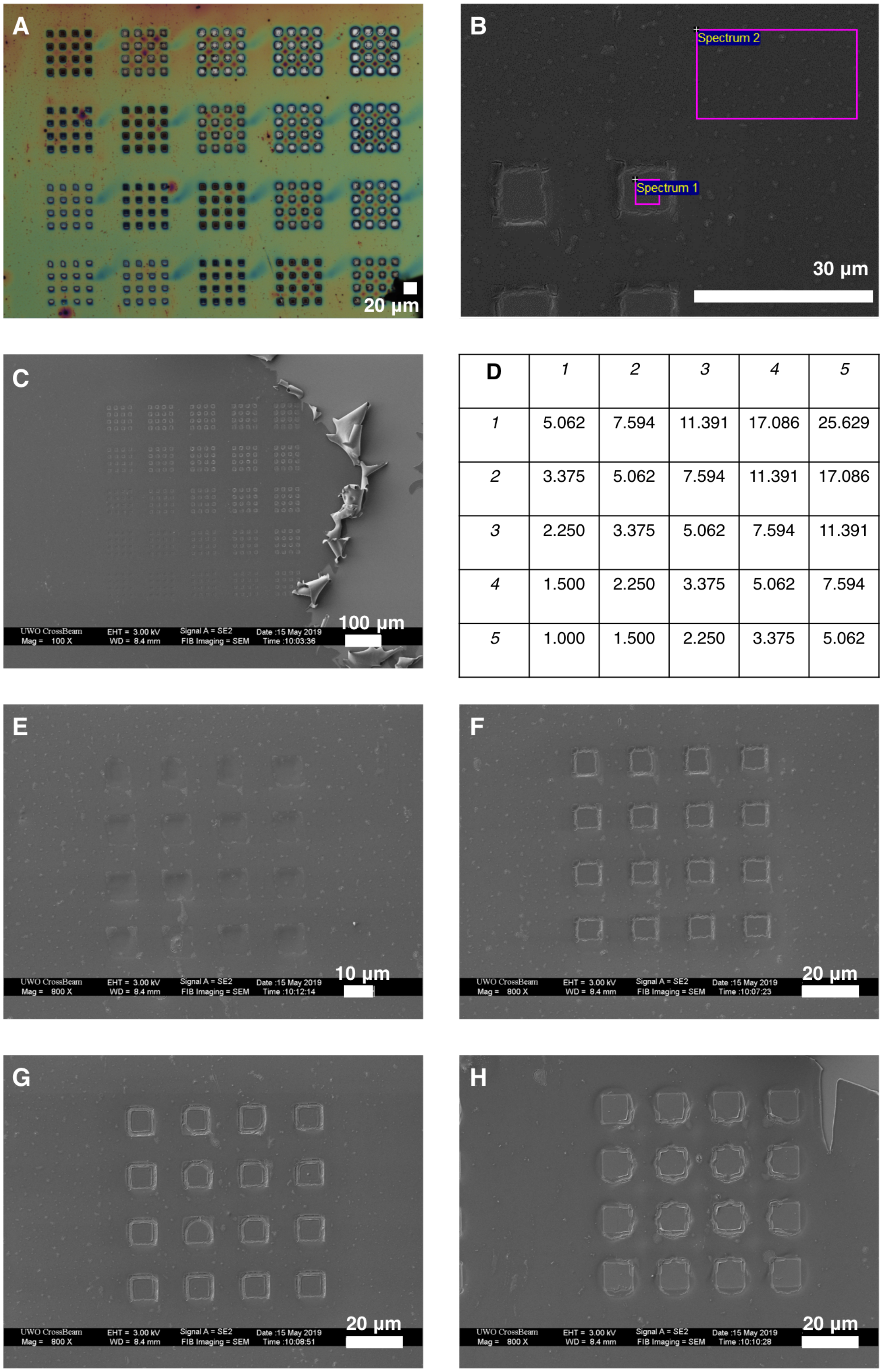

D	1	2	3	4	5
1	5.062	7.594	11.391	17.086	25.629
2	3.375	5.062	7.594	11.391	17.086
3	2.250	3.375	5.062	7.594	11.391
4	1.500	2.250	3.375	5.062	7.594
5	1.000	1.500	2.250	3.375	5.062

Figure 4.9: Network **4.1$^{\mathbf{thin}}$** after being patterned by EBL, functionalized with $AlMe_3$ and pyrolyzed. A) Optical microscope image of bottom four rows; B) SEM image with highlighted EDX spectrum 1: 32.07 % (C); 19.21 % (O); 5.67 % (Al); 42.44 % (Si), 0.61 % (P). EDX spectrum 2: 23.72 % (C); 53.63 % (O); 21.30 % (Al); 1.36 % (Si). C) SEM image; D) list of doses used for the 5x5 array of 4x4 squares. Zoom SEM images of 4x4 square arrays written at different doses: E) 1.000 $\mu C/cm^2$; F) 3.375 $\mu C/cm^2$; G) 5.062 $\mu C/cm^2$; H) 25.629 $\mu C/cm^2$.

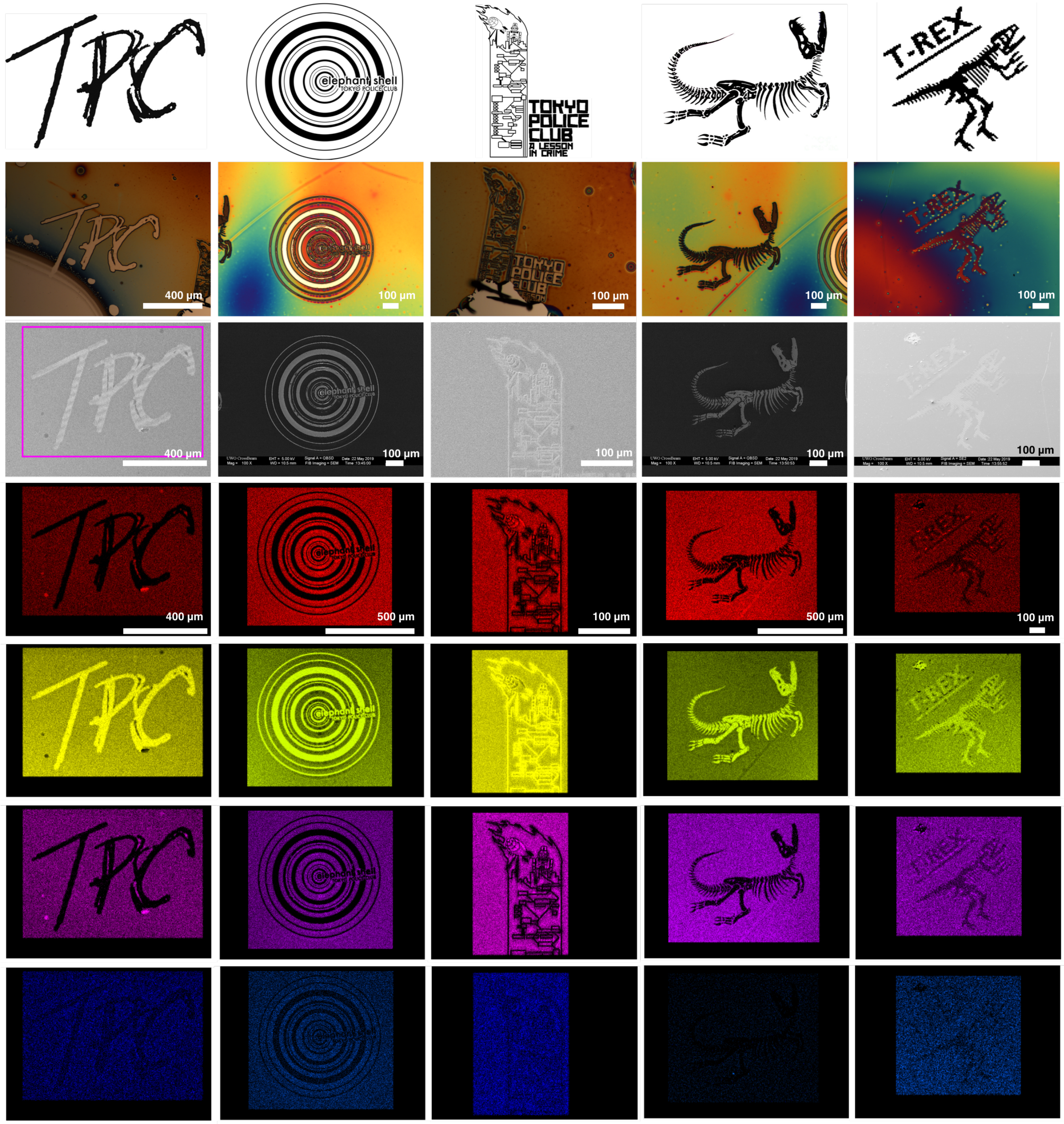

Figure 4.10: Patterned, metallized and pyrolyzed **4.1**$^{\mathbf{thin}}$. From left to right: "TPC," "A Lesson in Crime" and "Elephant Shell" (5.00 µC/cm^2) album covers, raptor fossil and T-rex (3.75 µC/cm^2). From top to bottom: Patterns used for EBL, confocal microscope pictures, SEM images, EDX maps of Al (red), Si (yellow), O (pink) and C (blue).

Once patterned, the film was functionalized as described above. After pyrolysis, the films were imaged, and aside from some areas of delamination, the inscribed shapes survived the solution chemistry modification and subsequent pyrolysis showing remarkable resilience. The confocal microscope images in Figure 4.10 reveal that the thin ceramic films reflected a wide spectrum of colours, indicative of small variations in film thickness, which were present in the films before pyrolysis (1.41 ± 0.43 μm). This phenomenon was particularly exaggerated for the “TPC” album cover and primitive T-rex image. Overall the SEM images demonstrated good resolution of shape retention across all images. In particular, it is possible to read the fine text that is embedded in the circles on the “Elephant Shell” album cover and the raptor fossil is very nicely articulated. Figure 4.10 shows delamination of part of the “A Lesson in Crime” album cover, but otherwise good articulation of the wording, burning building, robot and blimp features!

4.8 Conclusion

We prepared stibino-phosphonium networks with varying stoichiometries by post polymerization functionalization of tertiary phosphane-ene photopolymer networks. The NMR and XANES spectroscopic data of the functionalized networks was compared to that of structurally characterized small molecules and was found to match closely to stibino-*mono*(phosphonium) and stibino-*bis*(phosphonium) environments. The thermal data not only corroborates these structures, but also demonstrates how the physical properties of the networks can be tuned by controlling the types and number of stibino-phosphonium environments in the network through simple coordination chemistry. Functionalized networks **4.1(Sb)$_{0.5}$**, **4.1(Sb)$_{0.75}$**, and **4.1Sb** contain increasing amounts of Sb, which is manifested in the post-pyrolysis materials, showing that the composition of the polymer precursor influences the composition of the char.

The phosphane-ene platform is a promising material to that allowed for diverse control over composition through coordination to low valent phosphorus-based cations as well as Al, Ge and Co Lewis acids and tested the suitability of the material as precursors to metal-containing ceramics. The resulting ceramics were found to be largely composed of carbon yet doped with the metals in question as well as N and P heteroatoms, which are attractive qualities of carbon in the field and battery and fuel cell development. It is noteworthy that the polymeric material used in this context can be made from neat, commercially available reagents and can be easily purified, putting phosphane-ene based ceramic precursors ahead of MOFs in terms of their scalability.

The material also displays phenomenal shape retention properties after patterning, metallization and pyrolysis. Given the ease of incorporating different elements into phosphane-ene polymer networks and the many ways in which photopolymers can be patterned,[70–72] this methodology could be useful to the IT industry’s search for new spintronic materials.

In the end we describe a polymeric material that can be easily shaped and functionalized through the rich coordination chemistry of alkyl phosphines. We are currently working on improving our control over ceramic composition through tuning of the polymer backbone in order to apply the methodology to a broader range of ceramics.

4.9 Instrumentation

Solution state nuclear magnetic resonance (NMR) spectroscopy was either conducted on a Varian INOVA 400 MHz spectrometer, or a Bruker AVANCEIII HD 400 spectrometer which utilizes an H/FX Bruker 5mm Smart Probe with automated tuning and matching (^{1}H 400.09 MHz, $^{11}B\{^{1}H\}$ 128.25 MHz, $^{13}C\{^{1}H\}$ 100.53 MHz, $^{19}F\{^{1}H\}$ 376.32 MHz, $^{31}P\{^{1}H\}$ 161.82 MHz). All ^{1}H and $^{13}C\{^{1}H\}$ spectra were referenced relative to residual solvent signal. The chemical shifts for $^{19}F\{^{1}H\}$ and $^{31}P\{^{1}H\}$ spectra were referenced using external standards; α,α,α–trifluorotoluene (δ_F = -63.9 ppm) and 85% H_3PO_4 (δ = 0 ppm), respectively. Solid state NMR experiments were conducted on a Varian Infinity Plus 400 MHz spectrometer (^{11}B 128.00 MHz, ^{31}P 160.73 MHz). ATR-IR experiments were conducted using a Perkin Elmer UATR Two spectrometer. A high intensity single arc mercury lamp (23.3 mW) was used as the light source for photopolymerization. A SDT Q600 thermogravimetric analyzer (TGA) was used to determine char yields. A TA Q20 differential scanning calorimeter (DSC) was used to determine glass transition temperatures (T_g) with a ramp rate of 40 °C per minute. All T_g values are reported using the onset temperature from the last heating cycle. P K-edge and Sb L-edge X-ray absorption near edge structure (XANES) experiments were performed at the soft X-ray microcharacterization beamline (SXRMB) at the Canadian Light Source (CLS) in Saskatoon, Canada. For XANES, two scans were recorded and averaged for each sample. A Hitachi 3400n SEM instrument was used to collect scanning electron microscopy (SEM) images and energy dispersive X-ray (EDX) spectra. X-ray photoelectron spectroscopy (XPS) was performed using a Kratos AXIS Nova Spectrometer. An Intel CPS Powder Diffractometer was used with Cu K-α radiation to collect powder X-ray diffraction (PXRD) data. The diffraction patterns were assigned using the ICSD database and Match! software. Network **4.1$^{\textbf{thin}}$** was patterned using a Zeiss 1530 e-beam Lithography instrument with a 5-axis stage. Pyrolyzed thin films were coated with Os using a STS PECVD instrument equipped with OsO_4 before imaging by SEM.

4.10 Reagents and Synthesis

All manipulations were performed in a nitrogen filled MBraun Labmaster dp glovebox or by using standard Schlenk techniques. All solvents were purchased from Caledon and dried using an MBraun controlled atmosphere solvent purification system and stored in Straus flasks under an N_2 atmosphere or over 4 Å molecular sieves. Monoisobutylphosphine and phosphine gas were donated by Solvay and cyclopentadienylcobalt dicarbonyl ($CpCo(CO)_2$) was donated by Digital Specialty Chemicals and were used as recieved. Irgacure 819 (Ciba Chemicals), 1,3,5-triallyl-1,3,5-triazine-2,4,6(1*H*,3*H*,5*H*)-trione (TTT) (Sigma Aldrich), trimethylsilyl trifluoromethanesulfonate ($Me_3SiOSO_2CF_3$) (Sigma Aldrich), chloro(dimethyl)phosphine (Alfa Aesar), germanium(II) chloride dioxane complex (1:1) ($GeCl_2$(diox)) (Gelest), 2.0 M trimethylaluminum ($AlMe_3$) solution in toluene (Sigma Aldrich), 1.0 M chlorodimethylaluminum ($AlMe_2Cl$) solution in hexanes (Sigma Aldrich), 1,7-octadiene (Sigma Aldrich) and 1-hexene (Alfa Aesar) were used as received. Azobisisobutyronitrile (AIBN, DuPont) was recrystallized from methanol before use. $SbClPh_2$, $[Ph_2Sb(PMe_3)][OTf]$, $[Ph_2Sb(PMe_3)_2][OTf]$, $[(Ph_2P)(PPh_3)][OTf]$ and [P(dppe)]$[BPh_4]$ were prepared by following literature procedures.[48,57,59,73] $[Ph_2SbPPh_3][OTf]$ and $[Ph_2Sb(PPh_3)_2][OTf]$ were prepared by a modification from the literature.[49] The preparation of $[Ph_2Sb(PPh_3)][OTf]$ and $[Ph_2Sb(PPh_3)_2][OTf]$ was modified from the literature to give a $[OTf]^-$ instead of a $[PF_6]^-$ anion.[49]

4.1: Monoisobutylphosphine (2.3521 g, 26.12 mmol) was combined with TTT (8.6803 g, 34.82 mmol) neat in a vial. Irgacure 819 (0.0552 g, 0.5 wt%) was dissolved into the mixture to give a pale yellow liquid (**4.1u**). The vial was sealed and irradiated with ultraviolet light for ten minutes and cycled back into the glovebox. The vial was broken apart to release one solid piece of polymer network **4.1** in the shape of the inside of the vial. Polymer network **4.1** was a transparent pale yellow brittle solid that could be broken down using a mortar and pestle (**4.1c**). The ground polymer was leached overnight using dichloromethane (20 mL). The supernatant was decanted and the leaching process was repeated twice before the solids were dried *in vacuo* to give a colourless transparent solid. The $^{31}P\{^1H\}$ NMR (161.8 MHz): $\delta = -34.4$ ppm; FT-IR (ranked intensity): $\nu = 733.3$ (8), 763.0 (3), 930.3 (7), 992.3 (10), 1054.0 (15), 1101.5 (13), 1165.7 (14), 1318.0 (5), 1368.3 (6), 1451.8 (2), 1678.0 (1), 2868.5 (12), 2953.7 (4), 3596.4 (9), 3726.1 (11) cm^{-1}; Char yield = 9.16 %; Decomposition onset = 316 °C; T_g onset = 48 °C.

Stibino-phosphonium photopolymer network general procedure:

Trimethylsilyl trifluoromethanesulfonate was added to a dichloromethane solution of $SbClPh_2$. This solution was added to **4.1** and allowed to stand for seven days in the dark. The supernatant was decanted and unreacted material was leached overnight using dichloromethane (20 mL). The supernatant was decanted and the leaching process was repeated twice followed by drying the solids *in vacuo*. Dried solids were stored in the dark.

4.1(Sb)$_{0.5}$: A dichloromethane solution (20 mL) of $SbClPh_2$ (0.1713 g, 0.55 mmol, 1.0 equiv.) and $Me_3SiOSO_2CF_3$ (0.157 mL, 0.87 mmol, 1.5 equiv.) was added to **4.1** (0.4867 g, ca. 1.15 mmol, ca. 2.0 equiv.). After work up the network was transparent and yellow. $^{31}P\{^1H\}$ NMR (161.8 MHz): δ = -3.5, -34.4 ppm; $^{19}F\{^1H\}$ NMR (376.3 MHz): δ = -78.8 ppm; FT-IR (ranked intensity): ν = 635.9 (2), 695.6 (10), 732.4 (8), 764.6 (6), 925.4 (12), 1028.6 (4), 1151.6 (7), 1223.1 (9), 1255.4 (5), 1321.9 (11), 1375.0 (14), 1454.1 (3), 1551.1 (15), 1675.4 (1), 2963.9 (13) cm^{-1}; Char yield at 800 °C, t = 0 = 21.46 %; Char yield at 800 °C, t = 3 hours = 13.70 %; Decomposition onset = 180 °C; T_g onset = 73 °C.

4.1(Sb)$_{0.75}$: A dichloromethane solution (20 mL) of $SbClPh_2$ (1.5573 g, 5.00 mmol, 2.0 equiv.) and $Me_3SiOSO_2CF_3$ (1.3 mL, 7.4 mmol, 3.0 equiv.) was added to **4.1** (1.0378 g, ca. 2.46 mmol, ca. 1.0 equiv.). After work up the network was transparent and colourless. $^{31}P\{^1H\}$ NMR (161.8 MHz): δ = 10.9, -2.2 ppm; $^{19}F\{^1H\}$ NMR (376.3 MHz): δ = -78.8 ppm; FT-IR (ranked intensity): ν = 635.2 (2), 693.9 (8), 736.4 (9), 764.5 (5), 925.6 (11), 1028.1 (4), 1154.5 (7), 1222.9 (13), 1252.4 (6), 1323.0 (15), 1373.0 (12), 1457.4 (3), 1672.4 (10), 1676.1 (1), 2963.1 (14) cm^{-1}; Char yield at 800 °C at t = 0 = 22.55 %; Char yield at 800 °C, at t = 3 hours = 15.78 %; Decomposition onset = 176 °C; T_g onset = 43 °C.

4.1Sb: A dichloromethane solution (20 mL) of $SbClPh_2$ (2.5320 g, 8.13 mmol, 5.0 equiv.) and $Me_3SiOSO_2CF_3$ (2.2 mL, 12 mmol, 7.5 equiv.) was added to **4.1** (0.6826 g, ca. 1.62 mmol, ca. 1.0 equiv.). After work up the network was transparent and colourless. $^{31}P\{^1H\}$ NMR (161.8 MHz): δ = 10.1 ppm; $^{19}F\{^1H\}$ NMR (376.3 MHz): δ = -78.6 ppm; FT-IR (ranked intensity): ν = 636.0 (2), 694.9 (9), 733.0 (8), 764.4 (5), 1028.3 (4), 1152.4 (7), 1223.4 (14), 1254.9 (6), 1320.5 (13), 1455.8 (3), 1457.6 (11), 1670.3 (15), 1674.0 (10), 1676.3 (1), 1685.8 (12) cm^{-1}; Char yield at 800 °C at t = 0 = 22.29 %; Char yield at 800 °C, at t = 3 hours = 17.30 %; Decomposition onset = 178 °C; T_g onset = 34 °C.

$[Ph_2SbPPh_3][OTf]$: Yield: 65%. Mp = 148.9-154.5 °C. ^1H NMR (400 MHz, $CDCl_3$): δ = 7.40-7.59 (m, 3H), 7.38-7.39 (m, 12H), 7.27-7.30 (m, 4H), 6.99-7.03 (m, 6H) ppm; $^{13}C\{^1H\}$ NMR (100.6 MHz): δ = 137.0 (s), 133.7 (d, $^2J_{CP}$ = 10.1 Hz), 132.7 (s), 132.6 (s), 130.5 (s), 129.9 (d, $^2J_{CP}$ = 10.1 Hz), 129.6 (s), 125.0 (d, $^1J_{CP}$ = 40.2 Hz), ppm; $^{19}F\{^1H\}$ NMR (376.3 MHz): δ = -78.4 ppm; $^{31}P\{^1H\}$ NMR (161.8 MHz): δ = -4.2 ppm; FT-IR (ranked intensity): ν = 636.3 (2), 691.1 (3), 713.6 (12), 729.2 (5), 736.9 (13), 745.5 (9), 996.1 (11), 1016.9 (1), 1093.5 (10), 1156.0 (8), 1188.9 (15), 1215.9 (4), 1288.8 (7), 1432.8 (6), 1479.4 (14); ESI-MS: m/z 537.1 $[C_{30}H_{25}PSb]^+$ ($[M]^+$), m/z 149.0 $[CO_3F_3S]^-$ ($[M]^-$). Elemental analysis found (calculated) for $C_{31}H_{25}O_3F_3PSSb$: C 53.78 (54.17), H 3.53 (3.67), S 4.80 (4.67) %.

$[Ph_2Sb(PPh_3)_2][OTf]$: Yield: 57%. Mp = 134.5-140.6 °C. ^1H NMR (400 MHz, $CDCl_3$): δ = 7.35-7.49 (m, 24H), 7.26-7.30 (m, 4H), 7.10-7.15 (m, 12H) ppm; $^{13}C\{^1H\}$ NMR (100.6 MHz): δ = 136.9, 133.9, 133.8, 130.8, 130.6, 129.6, 129.3, 129.2 ppm; $^{19}F\{^1H\}$ NMR (376.3 MHz): δ = -78.4 ppm; $^{31}P\{^1H\}$ NMR (161.8 MHz): δ = -5.8 ppm; FT-IR (ranked intensity): ν = 634.2 (1), 691.6 (2), 727.1 (5), 741.4 (9), 746.9 (14), 996.7 (13), 1032.5 (3), 1095.4 (10), 1134.5 (15), 1153.4 (7), 1224.2 (12), 1257.5 (4), 1284.9 (8), 1434.3 (6), 1479.2 (11); ESI-MS: m/z 537.1 $[C_{30}H_{25}PSb]^+$ ($[M\text{-}C_{18}H_{15}P]^+$), m/z 148.9 $[CO_3F_3S]^-$ ($[M]^-$). Elemental analysis found (calculated) for $C_{43}H_{30}O_3F_3P_2SSb$: C 61.03 (61.82), H 4.06 (3.62), S 3.85 (3.84) %.

4.1ox: A 579 mg sample of **4.1** was immersed in a 30% solution of hydrogen peroxide (10 mL) for 18 hours. The supernatant was decanted and the remaining white solid was dried *in vacuo*. $^{31}P\{^1H\}$ NMR (161.8 MHz): δ = 55.5 ppm; FT-IR (ranked intensity): ν = 730.9 (10), 763.5 (3), 1153.6 (4), 1243.1 (8), 1318.1 (5), 1373.1 (7), 1393.9 (12), 1436.4 (11), 1451.6 (2), 1652.6 (14), 1674.9 (1), 1686.6 (13), 1718.0 (15), 2959.9 (6) cm^{-1}; Char yield at 800 °C at t = 0 = 13.85 %; Char yield at 800 °C at t = 3 hours = 10.67 %; Decomposition onset = 252 °C; T_g onset = 82 °C.

4.1PMe$_2$: Network **4.1** (0.4907 g) was combined with a dichloromethane solution of $P(CH_3)_2Cl$ (46 microlitres) and trimethylsilyl trifluoromethanesulfonate (10x158 microlitres) and allowed to stand for seven days. The solution was decanted and the polymer was leached with dichloromethane (20 mL) over the course of 3 days. The solution was decanted and the functionalized network was dried *in vacuo*. $^{19}F\{^1H\}$ NMR (376.3 MHz): δ = -78.6 ppm; $^{31}P\{^1H\}$ NMR (161.8 MHz): δ = 26.0 (d, $^1J_{PP}$ = 307.4 Hz), -58.4 (d, $^1J_{PP}$ = 307.4 Hz) ppm; FT-IR (ranked intensity): ν = 1674.8 (4), 1456.2 (5), 1252.8 (7), 1224.2 (10), 1148.8 (9), 1028.2 (2), 765.0 (6) 635.2 (1), 572.5 (8), 515.75 (3) cm^{-1}; decomposition onset = 145.2 °C; Char yield at 800 °C at t = 0 = 12.39 %; Char yield at 800 °C, at t = 3 hours = 9.17 %; T_g onset = 82.7 °C.

4.1PPh$_2$: Network **4.1** (0.3397 g), diphenylphosphino tripehnylphosphonium triflate (0.5040 g, 0.84 mmol), dichloromethane (20 mL). $^{19}F\{^1H\}$ NMR (376.3 MHz): δ = -78.6 ppm; $^{31}P\{^1H\}$ NMR (161.8 MHz): δ = 24.3 (d, $^1J_{PP}$ = 324.6 Hz), -27.1 (d, $^1J_{PP}$ = 324.6 Hz) ppm; FT-IR (ranked intensity): ν = 1677.5 (2), 1454.8 (4), 1255.8 (5), 1222.2 (9), 1150.0 (8), 1028.2 (3), 764.2 (7), 635.8 (1), 573.0 (10), 516.2 (6) cm^{-1}; decomposition onset = 238.6 °C; Char yield at 800 °C at t = 0 = 14.28 %; Char yield at 800 °C, at t = 3 hours = 11.07 %; T_g onset = 96.7 °C.

4.1AlMe$_3$: Dichloromethane (17 mL) and trimethylaluminum solution (1.1 mL, 2.0M in toluene) were added to **4.1** (0.9633 g). After one week, the supernatant was decanted, and volatiles were removed *in* *vacuo* to give a transparent colourless solid. $^{13}C\{^1H\}$ NMR (100.6 MHz): δ = 149.2 (carbonyl, $(R_2N)_2\underline{C}$=O), 131.1 (olefin, $\underline{C}$H), 118.3 (olefin, $\underline{C}H_2$), 44.8 (alkyl), 34.9 (alkyl), 24.3 (alkyl), -7.9 ppm ($R_3PAl(\underline{C}H_3)_3$); $^{31}P\{^1H\}$ NMR (161.8 MHz): δ = -26.0 ppm; FT-IR (ranked intensity): ν = 5954 (8), 2867 (9), 2368 (6), 2326 (7), 1676 (1), 1457 (2), 1362 (3), 1320 (5), 1165 (10), 765 (4) cm^{-1}; elemental composition by EDX: C, 58.85 %; O, 36.19 %; Al, 3.05 %; P, 1.91 %; decomposition onset = 206 °C; Char yield at 800 °C at t = 0 = 42.1 %; Char yield at 800 °C, at t = 3 hours = 41.0 %; T_g onset = 70 °C.

4.1AlMe$_2$Cl: Dichloromethane (17 mL) and chlorodimethylaluminum solution (5.8 mL, 1.0M in hexanes) were added to **4.1** (0.4912 g). After one week, the supernatant was decanted and volatiles were removed *in vacuo* to give a transparent colourless solid. $^{13}C\{^1H\}$ NMR (100.6 MHz): δ = 149.1 (carbonyl, $(R_2N)_2\underline{C}$=O), 128.7 (olefin, $\underline{C}$H), 120.4 (olefin, $\underline{C}H_2$), 46.1 (alkyl), 24.6 (alkyl), -6.4 ($R_3PAl(\underline{C}H_3)_2Cl$) ppm; $^{31}P\{^1H\}$ NMR (161.8 MHz): δ = -26.1 ppm; FT-IR (ranked intensity): ν = 2957 (3), 1676 (1), 1460 (2), 1375 (5), 1319 (6), 1251 (9), 1080 (10), 986 (8), 932 (7), 764 (4) cm^{-1}; elemental composition by EDX: O, 42.93 %; C, 52.88 %; Al, 2.53 %; Cl, 1.08 %; P, 0.58 %; decomposition onset = 198 °C; Char yield at 800 °C at t = 0 = 55.5 %; Char yield at 800 °C, at t = 3 hours = 52.8 %; T_g onset is not observed below the decomposition temperature.

4.1GeCl$_2$: $GeCl_2$(dioxane) (0.310 g, 1.3 mmol) was dissolved in acetonitrile (20 mL), the solution was filtered and added to network **4.1** (0.558 g). After one week, the supernatant was decanted and the solid polymer gel was leached with acetonitrile overnight (3x20 mL), decanted and dried *in vacuo* to give a transparent colourless brittle solid. $^{13}C\{^1H\}$ NMR (100.6 MHz): δ = 150.0 (carbonyl, $(R_2N)_2\underline{C}$=O), 132.7 (olefin, $\underline{C}$H), 44.4 (alkyl), 25.0 (alkyl) ppm; $^{31}P\{^1H\}$ NMR (161.8 MHz): δ = -4.0 ppm; FT-IR (ranked intensity): ν = 2961 (10), 1674 (1), 1455 (2), 1373 (4), 1321 (5), 992 (7), 926 (8), 807 (9), 762 (3), 531 (6) cm^{-1}; elemental composition by EDX: C, 68.10 %; O, 29.67 %; Ge, 1.50 %; Cl, 0.40 %; P, 0.32 %; decomposition onset = 227 °C; Char yield at 800 °C at t = 0 = 32.0 %; Char yield at 800 °C, at t = 3 hours = 26.2 %; T_g onset = 91 °C.

4.1CpCoCO: A THF solution (20 mL) of cyclopentadienylcobalt dicarbonyl (0.507 g, 2.8 mmol) was added to **4.1** (0.555 g) in a pressure tube and refluxed for seven days. The supernatant was decanted and the insoluble red material was leached three times with tetrahydrofuran, or until the supernatant was completely colourless, decanted and dried *in vacuo* resulting in a brittle red solid. $^{13}C\{^1H\}$ NMR (100.6 MHz): δ = 208.4 (Co$\underline{C}$O), 148.9 (carbonyl, $(R_2N)_2\underline{C}$=O), 132.0 (olefin, $\underline{C}$H), 117.5 (olefin, $\underline{C}H_2$), 81.1 ($\underline{C}_5H_5$), 44.8 (alkyl), 38.0 (alkyl) ppm; $^{31}P\{^1H\}$ NMR (161.8 MHz): δ = 51.0 ppm; FT-IR (ranked intensity): ν = 2956 (10), 1906 (7; ν_{CoCO}), 1676 (1), 1449 (2), 1364 (4), 1317 (5), 1162 (9), 1062 (6), 763 (3), 563 (8) cm^{-1}; elemental composition by EDX: C, 70.09 %; O, 28.23 %; P, 1.58 %; Co, 0.11 %;

decomposition onset = 119 °C; Char yield at 800 °C at t = 0 = 36.6 %; Char yield at 800 °C, at t = 3 hours = 33.2 %; T_g onset = 27 °C.

4.1(CpCoCO)$_{0.5}$: A THF solution (15 mL) of cyclopentadienylcobalt dicarbonyl (0.488 g, 2.7 mmol) was added to **4.1** (2.289 g) in a pressure tube and refluxed for seven days. The supernatant was decanted and the insoluble red material was leached three times with tetrahydrofuran, or until the supernatant was completely colourless, decanted and dried *in vacuo* resulting in a brittle red solid. $^{13}C\{^1H\}$ NMR (100.6 MHz): δ = 207.3 (Co$\underline{C}$O), 148.7 (carbonyl, $(R_2N)_2\underline{C}$=O), 131.8 (olefin, $\underline{C}$H), 117.4 (olefin, $\underline{C}H_2$), 81.0 ($\underline{C}_5H_5$), 44.3 (alkyl), 38.1 (alkyl) ppm; $^{31}P\{^1H\}$ NMR (161.8 MHz): δ = 50.8 (R_3PCoCpCO), -34.9 (**4.1**) ppm; FT-IR (ranked intensity): ν = 2956 (7), 2869 (8), 1908 (10; ν_{CoCO}), 1675 (1), 1456 (2), 1366 (4), 1320 (5), 1167 (9), 1064 (6), 764 (3) cm^{-1}; elemental composition by EDX: C, 68.05 %; O, 31.07 %; P, 0.86 %; Co, 0.03 %; decomposition onset = 123 °C; Char yield at 800 °C at t = 0 = 32.9 %; Char yield at 800 °C, at t = 3 hours = 26.2 %; T_g onset = 30 °C.

4.2H: A toluene solution (40 mL) of 1,7-octadiene (6 mL) and AIBN (40 mg) was charged into a stainless-steel pressure reactor which was flushed with N_2, charged with PH_3 (80 psi) and heated to 60 °C for 18 hours. After controllably burning off the excess PH_3, volatiles were removed *in vacuo* to give a colourless oil. A small sample was set aside for analysis and the remainder of the oil was used to synthesize network **4.2**. $^{13}C\{^1H\}$ NMR (100.6 MHz): δ = 33.3, 33.2, 32.0, 31.5, 30.9, 30.8, 29.8, 29.6, 29.5, 29.4, 28.9, 28.4, 28.3, 26.8, 26.6, 21.1, 21.0, 14.0, 13.9 ppm; ^{31}P NMR (161.8 MHz): δ = -137.7 (t, $^1J_{PH}$ = 186.1 Hz; RPH_2), -68.7 (d, $^1J_{PH}$ = 194.2 Hz; R_2PH), -31.5 (s; PR_3) ppm; FT-IR (ranked intensity): ν = 2918 (1), 2850 (2), 2280 (3; ν_{PH}), 1464 (4), 1418 (7), 1349 (12), 1342 (13), 1296 (15), 1197 (14), 1079 (6), 992 (10), 836 (8), 812 (9), 720 (5), 634 (11) cm^{-1}; decomposition onset = 160 °C; Char yield = 0 %; T_m onset = -37 °C (broad and amorphous, see SI).

4.2: Network **4.2H** was redissolved in toluene (50 mL) and combined with 1-hexene (10 mL) and AIBN (44 mg). The reaction mixture was heated to 60 °C in a stainless-steel pressure reactor for 18 hours followed by removal of volatiles *in vacuo* to give a colourless oil. $^{13}C\{^1H\}$ NMR (100.6 MHz): δ = 31.9, 31.6, 31.5, 29.8, 28.2, 28.0, 26.4, 22.9, 14.1 ppm; $^{31}P\{^1H\}$ NMR (161.8 MHz): δ = -31.6 ppm; FT-IR (ranked intensity): ν = 2955 (5), 2921 (1), 2851 (2), 1464 (4), 1416 (6), 1378 (7), 1348 (10), 1010 (9), 972 (8), 728 (3) cm^{-1}; decomposition onset = 165 °C; Char yield at 800 °C at t = 0 = 1. 1 %; T_g onset = -90 °C. Network **4.2** was oxidized using excess hydrogen peroxide (20 wt% in water), extracted with CH_2Cl_2 and dried *in vacuo* to give a colourless oil that was analyzed by GPC and MALDI, using trans-2-[3-(4-tert-Butylphenyl)-2-methyl-2-propenylidene]malononitrile (DCTB) as the matrix.

4.2P: A methylene chloride solution of [Pdppe][BPh_4] (0.573 g, 0.768 mmol in 8 mL) was added to a methylene chloride solution of network **2** (0.299 g in 2 mL). Upon addition, the solution became viscous and an aliquot of the reaction mixture revealed the consumption of the PR_3 network and appearance of dppe as well as a new doublet. Hexanes (3 mL) was added to the reaction mixture and a precipitate formed. The precipitate was separated by centrifugation and washed with tetrahydrofuran (3x10 mL). The pale yellow insoluble solids were dried *in vacuo*. ^{11}B SS NMR (128.00 MHz, 12.8 kHz spinning rate): δ = -6.7 (spinning side bands at 12.8 kHz) ppm; ^{31}P{^{1}H} SS NMR (160.73 MHz, 14 kHz spinning rate): δ = 32.7 (br, $[P(\underline{\mathbf{2}})]^+$, spinning side bands at 14 kHz), -241.7 (br, $[\underline{P}(\mathbf{2})]^+$) ppm; FT-IR (ranked intensity): ν = 3054 (15), 2926 (4), 2852 (5), 1479 (12), 1458 (7), 1426 (8), 1404 (10), 1066 (13), 1032 (9), 998 (11), 843 (14), 730 (2), 700 (1), 612 (3), 516 (6) cm^{-1}; decomposition onset = 118.9 °C; Char yield at 800 °C at t = 0 = 9.45 %; T_g onset = -114 °C.

[$P(POct_3)_2$][BPh_4]: Trioctylphosphine (540 μL, 1.21 mmol) was added neat to a dichloromethane (4 mL) solution of [Pdppe][BPh_4] (0.454 g, 0.61 mmol). The volatiles were removed *in vacuo*, the solids were extracted with hexanes and filtered. The hexanes solution was extracted three times with acetonitrile (3 mL). The acetonitrile extracts were combined, reduced to 2.5 mL *in vacuo* and cooled to -35 °C overnight to precipitate the product. Yield: 26 %. T_m by DSC = 48 °C; ^{11}B NMR (128.25 MHz): δ = -6.6 ppm; ^{1}H NMR (599.15 MHz): δ = 7.32-7.35 (m, 8H, *ortho*), 7.02-7.05 (m, 8H, *meta*), 6.87-6.90 (m, 4H, *para*), 1.83-1.84 (m, 12H, CH_2), 1.50-1.53 (m, 12H, CH_2), 1.41-1.43 (m, 12H, CH_2), 1.27-1.34 (m, 12H, CH_2), 0.91 (t, $^{3}J_{HH}$ = 6 Hz, 18H, CH_3) ppm; ^{11}B NMR (128.25 MHz): δ = -6.6 ppm; ^{13}C{^{1}H} NMR (100.53 MHz): δ = 164.4 (q, $^{1}J_{CB}$ = 50 Hz, *ipso*), 136.3 (s, *ortho*), 126.0 (s, *meta*), 122.1 (s, *para*), 32.2 (CH_2), 31.2 (CH_2), 31.1 (CH_2), 29.5 (CH_2), 27.4 (ddd, $^{1}J_{CP}$ = 22 Hz, $^{2}J_{CP}$ = 21 Hz, $^{3}J_{CP}$ = 9 Hz, CH_2), 23.0 (CH_2), 14.3 (CH_3) ppm; ^{31}P{^{1}H} NMR (161.82 MHz): δ = 33.2 (d, $^{1}J_{PP}$ = 469.2 Hz), -230.2 (t, $^{1}J_{PP}$ = 477.3 Hz) ppm; FT-IR (ranked intensity): ν = 2938 (10), 2922 (3), 2854 (5), 1472 (15), 1468 (7), 1429 (11), 1032 (12), 848 (13), 738 (8), 734 (2), 712 (6), 704 (1), 617 (14), 612 (4), 518 (9) cm^{-1}; ESI-MS: m/z 771.7 $[C_{48}H_{102}P_3]^+$ ($[M]^+$), m/z 319.2 $[C_{24}H_{20}B]^-$ ($[M]^-$); Elemental analysis found (calculated) for $C_{72}H_{122}BP_3$: C 78.57 (79.23), H 11.27 (11.27) %; Decomposition onset by TGA = 175 °C.

4.2CpCoCO: Network **4.2** (0.444 g) was dissolved in a tetrahydrofuran solution of cyclopentadienylcobalt dicarbonyl (0.411 g, 2.28 mmol). The solution was transferred to a pressure tube and refluxed for two weeks. The solvent was removed under reduced pressure and the resulting residue was triturated with hexanes (10 mL) three times, or until the removed supernatant came off colourless. The resulting material was dried *in vacuo* to give a dark red tacky gel. ^{13}C{^{1}H} NMR (100.6 MHz): δ =

207.3 (CO, d, $^2J_{PC}$ = 40.2 Hz), 80.5 (Cp), 31.4, 29.2, 24.0, 22.5, 13.5 (alkyl) ppm; $^{31}P\{^1H\}$ NMR (161.8 MHz): δ = 49.9 ppm; FT-IR (ranked intensity): ν = 2926 (3), 2852 (5), 1903 (1; ν_{CoCO}), 1456 (8), 1418 (11), 1378 (14), 1352 (15), 1110 (13), 1014 (10), 985 (12), 791 (2), 720 (6), 592 (7), 561 (4), 493 (9) cm^{-1}; elemental composition by EDX: C, 71.48 %; O, 22.94 %; Co, 2.16 %; P, 3.42 %; decomposition onset = 222 °C; Char yield at 800 °C at t = 0 = 29.7 %; Char yield at 800 °C, at t = 3 hours = 27.6 %; T_g onset = -19 °C.

4.1^{thin}: Piranha treated Si wafers were coated with uncured formulation **4.1u** and spun at 2000 rpm for 30 seconds, then ramped to 3000 rpm for 5 seconds in a N_2 filled glovebox. The samples were transferred into a glass-covered vessel that was sealed, exported from the glovebox, subjected to UV irradiation (UVA: 331.794 mJ/cm^2, 148.953 mW/cm^2; UVV: 380.704 mJ/cm^2, 175.336 mW/cm^2 x5) and imported back into the glovebox. The resulting films were iridescent. $^{31}P\{^1H\}$ NMR (161.8 MHz): δ = -35.7 ppm; FT-IR (ranked intensity): ν = 1675 (1), 1645 (6), 1448 (2), 1411 (3), 1367 (8), 1345 (9), 1317 (5), 992 (10), 930 (7), 764 (4) cm^{-1}. Thickness measured by SEM = 1.41 ± 0.43 μm.

$4.1^{thin}AlMe_3$: In a petri dish, **4.1^{thin}** was rinsed with a 2.0 M $AlMe_3$ solution in toluene. The film was rinsed with dichloromethane (3x2mL) and left to stand and dry. $^{31}P\{^1H\}$ NMR (161.8 MHz): δ = -25.9 ppm; FT-IR (ranked intensity): ν = 2928 (12), 2870 (14), 1676 (1), 1448 (2), 1324 (7), 1318 (6), 1192 (13), 1168 (15), 941 (10), 930 (9), 762 (3), 697 (4), 676 (5), 540 (8), 498 (11) cm^{-1}.

Pyrolysis: Samples were loaded into a quartz boat and tube, purged with 5% H_2 (balanced with N_2) for 20 minutes and then ramped at 10 °C per minute to either 800, 900 or 1000 °C. The furnace was held at the prescribed temperature for either 3 or 4 hours before the tube furnace was turned off and allowed to cool to room temperature. Ceramics from the boat were analyzed using EDX, XPS and XRD.

4.11 References

(1) Waldrop, M. M. *Nature* **2016**, *530*, 144.

(2) Awschalom, D. D.; Flatté, M. E.; Samarth, N. *Sci. Am.* **2002**, *286* (6), 66.

(3) Bader, S. D.; Parkin, S. S. P. *Annu. Rev. Condens. Matter Phys.* **2010**, *1*, 71.

(4) Bader, S. D. *Rev. Mod. Phys.* **2006**, *78*, 1.

(5) Ando, K. *Science.* **2006**, *312*, 1883.

(6) Zou, X.; Zhang, Y. *Chem. Soc. Rev.* **2015**, *44* (15), 5148.

(7) Chang, Z. R.; Lv, H. J.; Tang, H.; Yuan, X. Z.; Wang, H. *J. Alloys Compd.* **2010**, *501* (1), 14.

(8) Fan, C. L.; Lin, C. R.; Han, S. C.; Chen, J.; Li, L. F.; Bai, Y. M.; Zhang, K. H.; Zhang, X. *New J. Chem.* **2014**, *38* (2), 795.

(9) Li, Y.; Dai, H. *Chem. Soc. Rev.* **2014**, *43* (15), 5257.

(10) Li, Y.; Lu, J. *ACS Energy Lett.* **2017**, *2*, 1370.

(11) Masa, J.; Xia, W.; Sinev, I.; Zhao, A.; Sun, Z.; Grützke, S.; Weide, P.; Muhler, M.; Schuhmann, W. *Angew. Chem. Int. Ed.* **2014**, *53* (32), 8508.

(12) Serov, A.; Andersen, N. I.; Roy, A. J.; Matanovic, I.; Artyushkova, K.; Atanassov, P. *J. Electrochem. Soc.* **2015**, *162* (4), F449.

(13) Shi, Y.; Zhang, B. *Chem. Soc. Rev.* **2016**, *45* (6), 1529.

(14) Li, X.; Zheng, S.; Jin, L.; Li, Y.; Geng, P.; Xue, H.; Pang, H.; Xu, Q. *Adv. Energy Mater.* **2018**, *8* (23), 1800716.

(15) Pan, Y.; Lin, Y.; Chen, Y.; Liu, Y.; Liu, C. *J. Mater. Chem. A* **2016**, *4* (13), 4745.

(16) Mi, Y.; Yang, C.; Zuo, Z.; Qi, L.; Tang, C.; Zhang, W.; Zhou, H. *Electrochim. Acta* **2015**, *176*, 642.

(17) Tang, H.; Cai, S.; Xie, S.; Wang, Z.; Tong, Y.; Pan, M.; Lu, X. *Adv. Sci.* **2015**, *3*, 1500265.

(18) Julien, P. A.; Mottillo, C.; Friščić, T. *Green Chem.* **2017**, *19* (12), 2729.

(19) She, L.; Li, J.; Wan, Y.; Yao, X.; Tu, B.; Zhao, D. *J. Mater. Chem.* **2011**, *21* (3), 795.

(20) Rider, D. A.; Liu, K.; Eloi, J.; Vanderark, L.; Yang, L.; Wang, J.; Grozea, D.; Lu, Z.; Russell, T. P.; Manners, I. *ACS Nano* **2008**, *2* (2), 263.

(21) Cheng, J. Y.; Ross, C. A.; Chan, V. Z. H.; Thomas, E. L.; Lammertink, R. G. H.; Vancso, G. J. *Adv. Mater.* **2001**, *13* (15), 1174.

(22) Hadadpour, M.; Ragogna, P. J. *J. Polym. Sci. Part A Polym. Chem.* **2015**, *53* (23), 2747.

(23) Clendenning, S. B.; Han, S.; Coombs, N.; Paquet, C.; Rayat, M. S.; Grozea, D.; Brodersen, P. M.; Sodhi, R. N. S.; Yip, C. M.; Lu, Z.-H.; Manners, I. *Adv. Mater.* **2004**, *16* (4), 291.

(24) Chan, W. Y.; Clendenning, S. B.; Berenbaum, A.; Lough, A. J.; Aouba, S.; Ruda, H. E.; Manners, I. *J. Am. Chem. Soc.* **2005**, *127* (6), 1765.

(25) Dong, Q.; Li, G.; Ho, C. L.; Faisal, M.; Leung, C. W.; Pong, P. W. T.; Liu, K.; Tang, B. Z.; Manners, I.; Wong, W. Y. *Adv. Mater.* **2012**, *24* (8), 1034.

(26) Béland, V. A.; Ross, M. A. S.; Coady, M. J.; Guterman, R.; Ragogna, P. J. *Chem. Mater.* **2017**, *29* (20), 8884.

(27) Strehmel, B. *Nachr. Chem.* **2014**, *62* (2), 128.

(28) Guterman, R.; Gillies, E. R.; Ragogna, P. J. *Can. J. Chem.* **2016**, *94* (5), 476.

(29) Guterman, R.; Hesari, M.; Ragogna, P. J.; Workentin, M. S. *Langmuir.* **2013**, *29* (21), 6460.

(30) Guterman, R.; Gillies, E. R.; Ragogna, P. J. *Langmuir.* **2015**, *31* (18), 5181.

(31) Cuthbert, T. J.; Evoy, E.; Bow, J. P. J.; Guterman, R.; Stubbs, J. M.; Gillies, E. R.; Ragogna, P. J.; Blacquiere, J. M. *Catal. Sci. Technol.* **2017**, *7* (13), 2685.

(32) Tang, J.; Wang, K. L. *Nanoscale* **2015**, *7* (10), 4325.

(33) Weihrich, R.; Pöttgen, R.; Pielnhofer, F. *Angew. Chem. Int. Ed.* **2018**, *57* (48), 15642.

(34) Bujak, P.; Kulszewicz-Bajer, I.; Zagorska, M.; Maurel, V.; Wielgus, I.; Pron, A. *Chem. Soc. Rev.* **2013**, *42* (23), 8895.

(35) Bhattacharyya, G.; Choudhuri, I.; Pathak, B. *Phys. Chem. Chem. Phys.* **2018**, *20* (35), 22877.

(36) Bhattacharyya, G.; Choudhuri, I.; Bhauriyal, P.; Garg, P.; Pathak, B. *Nanoscale* **2018**, *10* (47), 22280.

(37) Du, J.; Dong, S.; Zhou, B.; Zhao, H.; Feng, L. *Appl. Phys. A Mater.* **2017**, *123* (4), 1.

(38) Bahramy, M. S.; Ogawa, N. *Adv. Mater.* **2017**, *29* (25).

(39) Babu, S. H.; Kaleemulla, S.; Rao, N. M.; Krishnamoorthi, C. *J. Magn. Magn. Mater.* **2016**, *416*, 66.

(40) Zhou, C.; Ghods, A.; Saravade, V. G.; Patel, P. V.; Yunghans, K. L.; Ferguson, C.; Feng, Y.; Jiang, X.; Kucukgok, B.; Lu, N. (Luna); Ferguson, I. *ECS Trans.* **2017**, *77* (6), 3.

(41) Canfield, P. C.; Thompson, J. D.; Beyermann, W. P.; Lacerda, A.; Hundley, M. F.; Peterson, E.; Fisk, Z.; Ott, H. R. *J. Appl. Phys.* **1991**, *70* (10), 5800.

(42) Fisk, Z.; Canfield, P. C.; Beyermann, W. P.; Thompson, J. D.; Hundley, M. F.; Ott, H. R.; Felder, E.; Maple, M. B.; Lopez De La Torre, M. A.; Visani, P.; Seaman, C. L. *Phys. Rev. Lett.* **1991**, *67* (23), 3310.

(43) Karla, I.; Pierre, J.; Skolozdra, R. V. *J. Alloys Compd.* **1998**, *265* (1–2), 42.

(44) Casper, F.; Felser, C. *Solid State Commun.* **2008**, *148* (5–6), 175.

(45) Bende, D.; Wagner, F. R.; Grin, Y. *Inorg. Chem.* **2015**, *54* (8), 3970.

(46) Béland, V. A.; Wang, Z.; Sham, T. K.; Ragogna, P. J. *Angew. Chem. Int. Ed.* **2018**, *57*, 13252.

(47) Chitnis, S. S.; Burford, N. *Dalton Trans.* **2015**, *44* (1), 17.

(48) Chitnis, S. S.; Burford, N.; McDonald, R.; Ferguson, M. J. *Inorg. Chem.* **2014**, *53* (10), 5359.

(49) Kilah, N. L.; Petrie, S.; Stranger, R.; Wielandt, J. W.; Willis, A. C.; Wild, S. B. *Organometallics.* **2007**, *26* (25), 6106.

(50) Guterman, R.; Rabiee Kenaree, A.; Gilroy, J. B.; Gillies, E. R.; Ragogna, P. J. *Chem. Mater.*

2015, *27* (4), 1412.

(51) Mathur, A. M.; Scranton, A. B. *Biomaterials* **1996**, *17* (6), 547.

(52) Capitani, D.; Segre, A. L.; Sparapani, R.; Giustini, M.; Scartazzini, R.; Luisi, P. L. *Langmuir* **1991**, *7* (2), 250.

(53) Li, J. Q.; Feng, X. W.; Sun, W. A.; Ao, W. Q.; Liu, F. S.; Du, Y. *Mater. Chem. Phys.* **2008**, *112* (1), 57.

(54) Hu, E.; Hu, X.; Liu, T.; Liu, Y.; Song, R.; Chen, Y. *Appl. Surf. Sci.* **2013**, *270*, 596.

(55) Engemann, C.; Franke, R.; Hormes, J.; Lauterbach, C.; Hartmann, E.; Clade, J.; Jansen, M. *Chem. Phys.* **1999**, *243* (1–2), 61.

(56) Burford, N.; Dyker, C. A.; Decken, A. *Angew. Chem. Int. Ed.* **2005**, *44*, 2364.

(57) Burford, N.; Ragogna, P. J.; McDonald, R.; Ferguson, M. J. *J. Am. Chem. Soc.* **2003**, *125* (47), 14404.

(58) Gray, P. A.; Carpenter, Y. Y.; Burford, N.; McDonald, R. *Dalton Trans.* **2016**, *45* (5), 2124.

(59) Norton, E. L.; Szekely, K. L. S.; Dube, J. W.; Bomben, P. G.; Macdonald, C. L. B. *Inorg. Chem.* **2008**, *47* (3), 1196.

(60) Ellis, B. D.; Carlesimo, M.; Macdonald, C. L. B. *Chem. Commun.* **2003**, *64* (15), 1946.

(61) Dube, J. W.; MacDonald, C. L. B.; Ragogna, P. J. *Angew. Chem. Int. Ed.* **2012**, *51* (52), 13026.

(62) Kosnik, S. C.; Farrar, G. J.; Norton, E. L.; Cooper, B. F. T.; Ellis, B. D.; Macdonald, C. L. B. *Inorg. Chem.* **2014**, *53* (24), 13061.

(63) Binder, J. F.; Swidan, A.; Tang, M.; Nguyen, J. H.; Macdonald, C. L. B. *Chem. Commun.* **2015**, *51* (36), 7741.

(64) Kosnik, S. C.; Macdonald, C. L. B. *Dalton Trans.* **2016**, No. 14, 6251.

(65) Binder, J. F.; Corrente, A. M.; Macdonald, C. L. B. *Dalton Trans.* **2016**, *45* (5), 2138.

(66) Barron, A. R. *J. Chem. Soc. Dalton Trans.* **1988**, No. 2, 3047.

(67) Leigh, G. J.; Bremser, W. *Dalton Trans.* **1972**, 1216.

(68) Furlani, A.; Polzonetti, G.; Russo, M. V.; Mattogno, G. *Inorg. Chim. Acta* **1978**, *26*, 39.

(69) Ross, C. A. *Annu. Rev. Mater. Res.* **2001**, *31*, 203.

(70) Inoue, S.; Amano, T.; Itani, T.; Watanabe, H.; Mori, I.; Watanabe, T.; Kinoshita, H.; Miyai, H.; Hatakeyama, M. *Adv. Opt. Technol.* **2012**, *1* (4), 269.

(71) Sturzebecher, L.; Fuchs, F.; Zeitner, U. D.; Tuennermann, A. *Microelectron. Eng.* **2015**, *132*, 120.

(72) Rühe, J. *ACS Nano* **2017**, *11* (9), 8537.

(73) Nunn, M.; Sowerby, D. B.; Wesolek, D. M. *J. Organomet. Chem.* **1983**, *251* (3), 45.

Chapter 5

5 Orthogonally Bi-Metallized Photopolymer Networks

5.1 Introduction

In a quest to lower the carbon footprint of vehicles, chemists are striving to improve battery performance, and develop efficient hydrogen evolution reaction (HER) catalysts for the clean generation of H_2 as an alternative to fossil fuels.[1–3] Metal containing ceramics have recently been investigated for an array of applications in the above capacities. The ceramics that currently show promise in battery development are transition metal doped $LiFePO_4$ cathode materials and metal oxide electrocatalysts.[2–7] Combinations of electrocatalysts, or bifunctional electrocatalysts are desired for rechargeable batteries,[4] where, several types of materials have emerged as promising low-cost HER electrocatalysts. Phosphides of Fe, Co, Ni, Cu, Mo, W and especially mixed metal phosphides have been found to be particularly active.[1,8–10]

Despite their desired electrochemical properties, a major drawback of the above-mentioned ceramics in the context of batteries or fuel cells is that they lack conductivity. In either field there has been an effort to improve the electrochemical activity of these materials by incorporating them into a carbon support. Carbon has the advantage of being conductive, and it is a substrate that can be doped with heteroatoms to further enhance conductivity.[1,11,12] A remaining challenge is finding a way to uniformly dope the active materials throughout the carbon support.[13] Recent work to address this issue has been in the pyrolysis of metal organic frameworks (MOFs) to form carbon that is uniformly doped with metals, however the scalability of the MOF design remains a challenge.[11,14,15]

Metallopolymers are structurally diverse and have found a role in numerous applications,[16] one of particular interest is their role as precursors for the preparation of polymer derived ceramics.[17–20] Upon pyrolysis, the composition of the resulting ceramics are dictated by that of the polymer precursor. We have recently shown that metal functionalized photopolymer networks can be used as precursors to metal-doped carbon.[21,22] Depending on the functionality within the photopolymer network, they can be chemically modified by simple salt metathesis or metal coordination, giving them the potential to impart varied composition of the resulting ceramic after pyrolysis.[21,23–26] While polymer networks have been synthesized by hydrometallation,[27] they have yet to be functionalized in this way post polymerization. Hydrides of Sc, Zr, B, Al, Si, P, S, Ge, Se, Sn, Pb and Te are able to undergo hydrometallation reactions with olefins.[28–36]

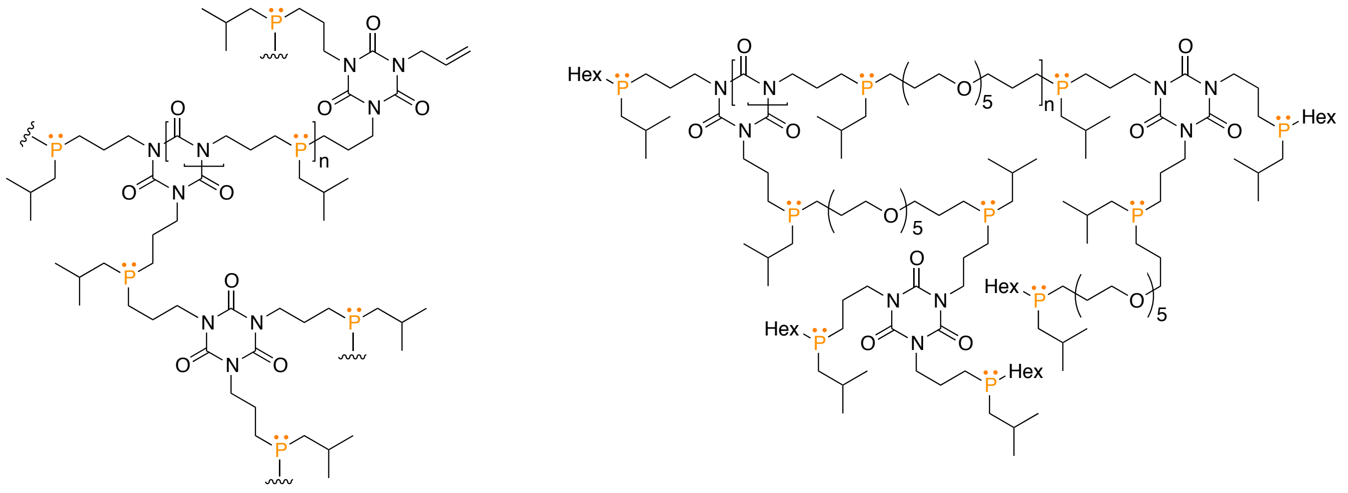

5.1 **5.2**

Figure 5.1: Photopolymer networks **5.1** and **5.2**.

To date, it has been feasible to controllably functionalize polymer networks with one metal at a time. In this work we present a method for functionalizing the network with two metals using orthogonal chemistries. In converting the phosphines in phosphane-ene polymer networks (Figure 5.1) to phosphonium salts by quaternization using allyl bromide, the allyl group can be further functionalized by hydrogermylation, while the bromide anion can subsequently coordinate transition metal halides to make complex counteranions (Scheme 5.1). In this way, bi-metallic ceramic precursors could be developed, which were comprehensively characterized. This new methodology for tailoring elemental composition in ceramic precursors is a fundamental step towards making diverse metal-doped carbon materials.

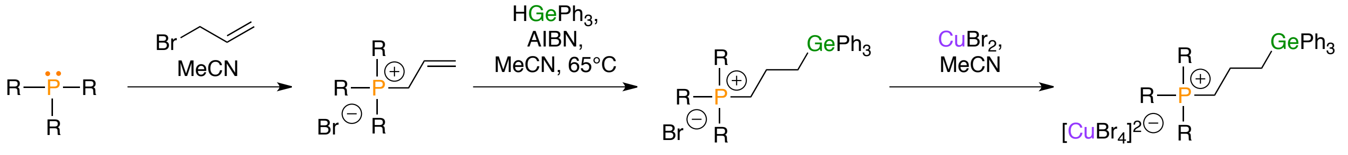

5.2 **5.2[Br]** **5.2[Br]Ge** **5.2[Cu]Ge**

Scheme 5.1: Synthetic scheme to make **5.2[Br]**, **5.2[Br]Ge** and **5.2[Cu]Ge**.

5.2 Photopolymer Network Synthesis

We have previously reported the synthesis of phosphane-ene polymer network (**5.1**) by combination of monoisobutyl phosphine ($^{i}BuPH_2$) with 1,3,5-triallyl-1,3,5-triazine-2,4,6(1*H*,3*H*,5*H*)-trione (TTT) in a 3:4 ratio and irradiation in the presence of the photoinitiator Irgacure 819.[22] Network **5.1** is a macromolecular tertiary phosphine, that is insoluble, yet solvent swellable, which allowed for the acquisition of solution-like ^{31}P NMR spectra, enabling easy assessment of the material.[22,37,38]

Network **5.1** was quaternized using vinyl benzyl chloride and allyl bromide in stoichiometric reactions over the course of three days (Scheme 5.2). Samples from both reactions demonstrated the consumption of 3° phosphine (δ_P = -34.4 ppm) and appearance of phosphonium cation ($\delta_P \approx 32$ ppm) by $^{31}P\{^1H\}$ NMR spectroscopy. However, based on the broadness of the signals in any given solvent, the materials were deemed to have low swellability and the starting phosphine network was redesigned to be more amenable to swelling and solution chemistry. To accomplish this, tetraethyleneglycol diallylether (TEGDAE) was incorporated as an additive in the photopolymerizable formulation to increase the flexibility of the polymer chains and to create sufficient interstitial space for subsequent reactions.

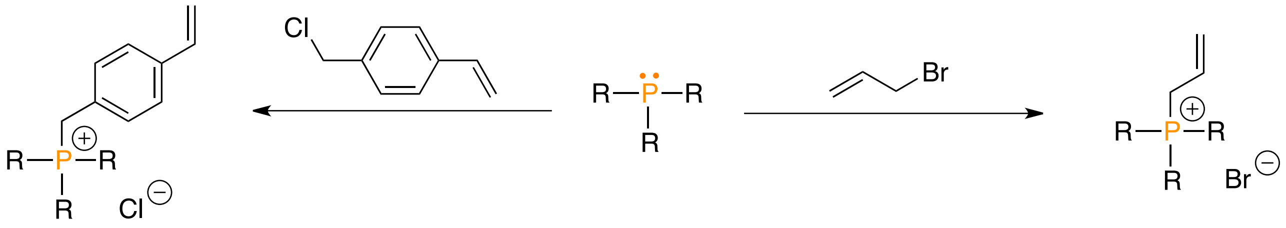

5.1[Cl] **5.1** **5.1[Br]**

Scheme 5.2: Quaternization reactions of **5.1** with vinyl benzyl chloride and allyl bromide.

The new formulation was composed of a slight excess of $^iBuPH_2$, TTT crosslinker, TEGDAE linear additive in a 35:56:168 molar ratio, with Irgacure 819 as the photoinitiator (0.5 wt%; Scheme 5.3). Upon irradiation, the formulation changed from yellow to colourless – an indication of the photoinitiator being consumed. In the ^{31}P NMR spectrum of the reaction mixture, unreacted $^iBuPH_2$ could be observed with new 2° and 3° phosphine signals (δ_P = -150.6; $^1J_{PH}$ = 202.2 Hz, -75.6; $^1J_{PH}$ = 194.2, -34.3, respectively; Figure 5.2), while the $^{13}C\{^1H\}$ NMR spectrum revealed the complete consumption of all olefin signals (δ_C = TTT: 131.0, 119.0; TEGDAE: 134.6, 116.8 ppm). The excess 1° phosphine was removed under reduced pressure to yield a tacky elastic material, **5.2H**. Network **5.2H** contains a mixture of 2° and 3° phosphines as confirmed by ^{31}P NMR and IR spectroscopies (ν_{PH} = 2270 cm^{-1}; Figure 5.2). In order to create a material with solely 3° phosphines, PH bonds in **5.2H** were capped via hydrophosphination using 1-hexene to give network **5.2** (Scheme 5.3). The two materials, **5.2H** and **5.2** exhibit similar glass transition profiles, but the onset temperature of **5.2H** (T_g = -83 °C) is low and broad because of the mixed composition, relative to **5.2** (T_g = -65 °C), which is solely composed of 3° phosphines (Figure 5.2).

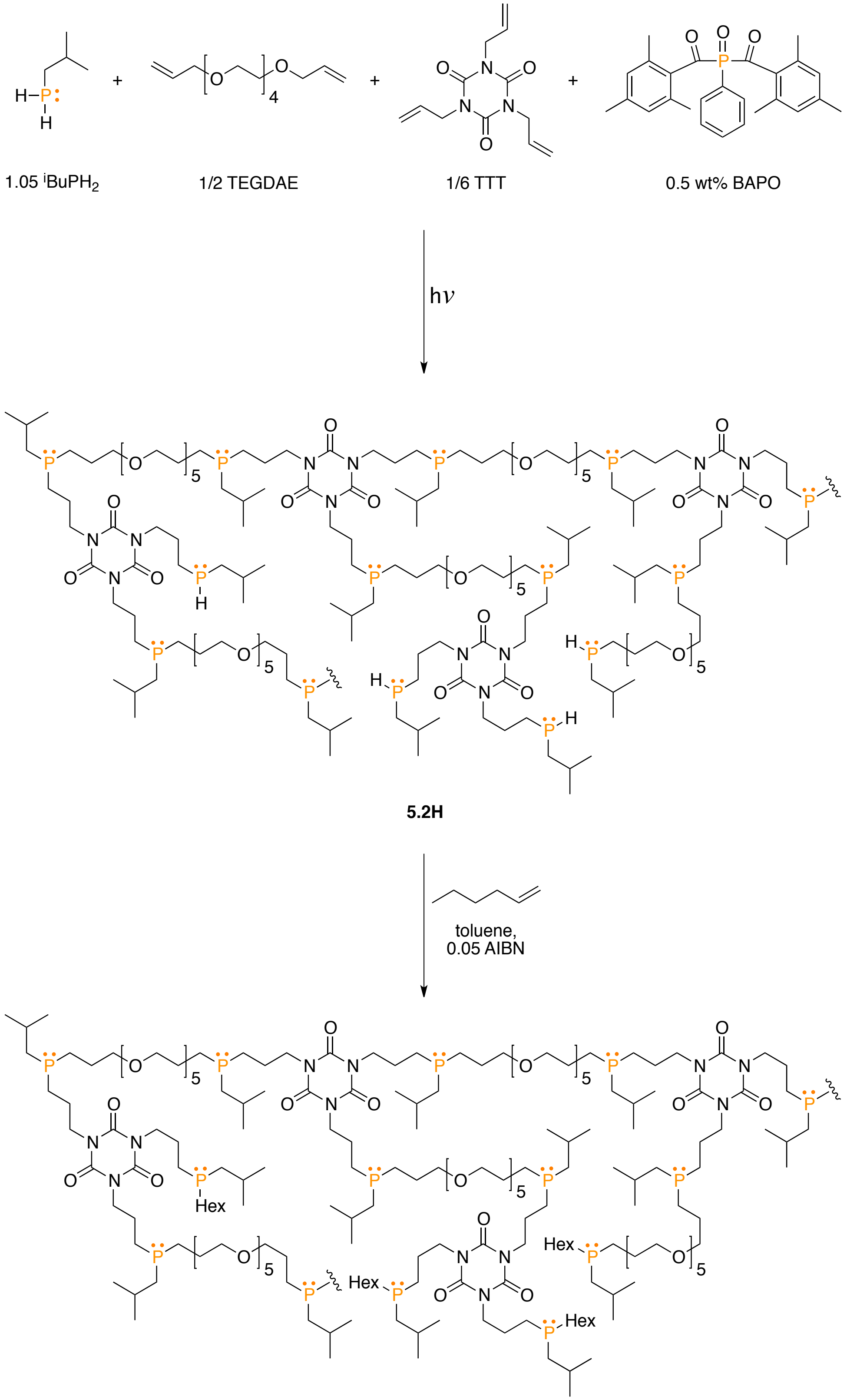

Scheme 5.3: Synthetic scheme to make networks **5.2H** and **5.2**.

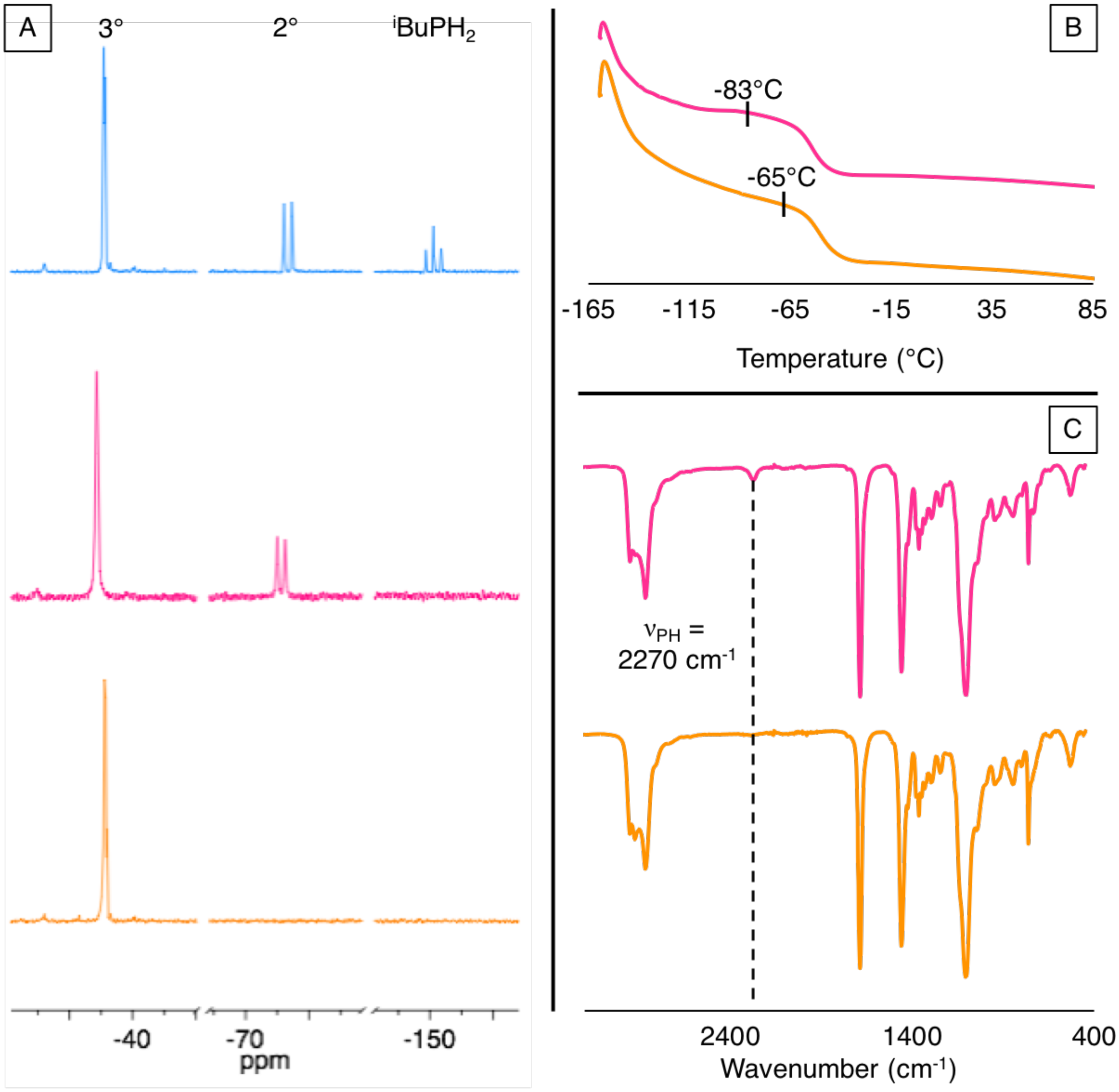

Figure 5.2: A) ^{31}P NMR spectra from top to bottom for the reaction mixture of **5.2H** (blue), purified **5.2H** (pink) and **5.2** (orange); B) DSC plots of **5.2H** (pink) and **5.2** (orange); C) IR spectra of **5.2H** (pink) and **5.2** (orange).

5.3 Metal Functionalization of Polymer Networks

The phosphines in **5.2** were quaternized using allyl bromide to create the corresponding allyl phosphonium cation centers (Scheme 5.1), the production of which was confirmed by the appearance of olefin signals in the ^{13}C NMR spectrum (δ_C = 125.8, 124.2 ppm). The quaternized network, **5.2[Br]** exhibits a cluster of three $^{31}P\{^1H\}$ NMR signals (δ_P = 34.1, 33.3, 32.6 ppm; Figure 5.3) which correspond to phosphorus bound to both or only TTT and TEGDAE. The glass transition temperature of **5.2[Br]** (T_g = -28 °C) is high relative to **5.2** because of the added ionic component.

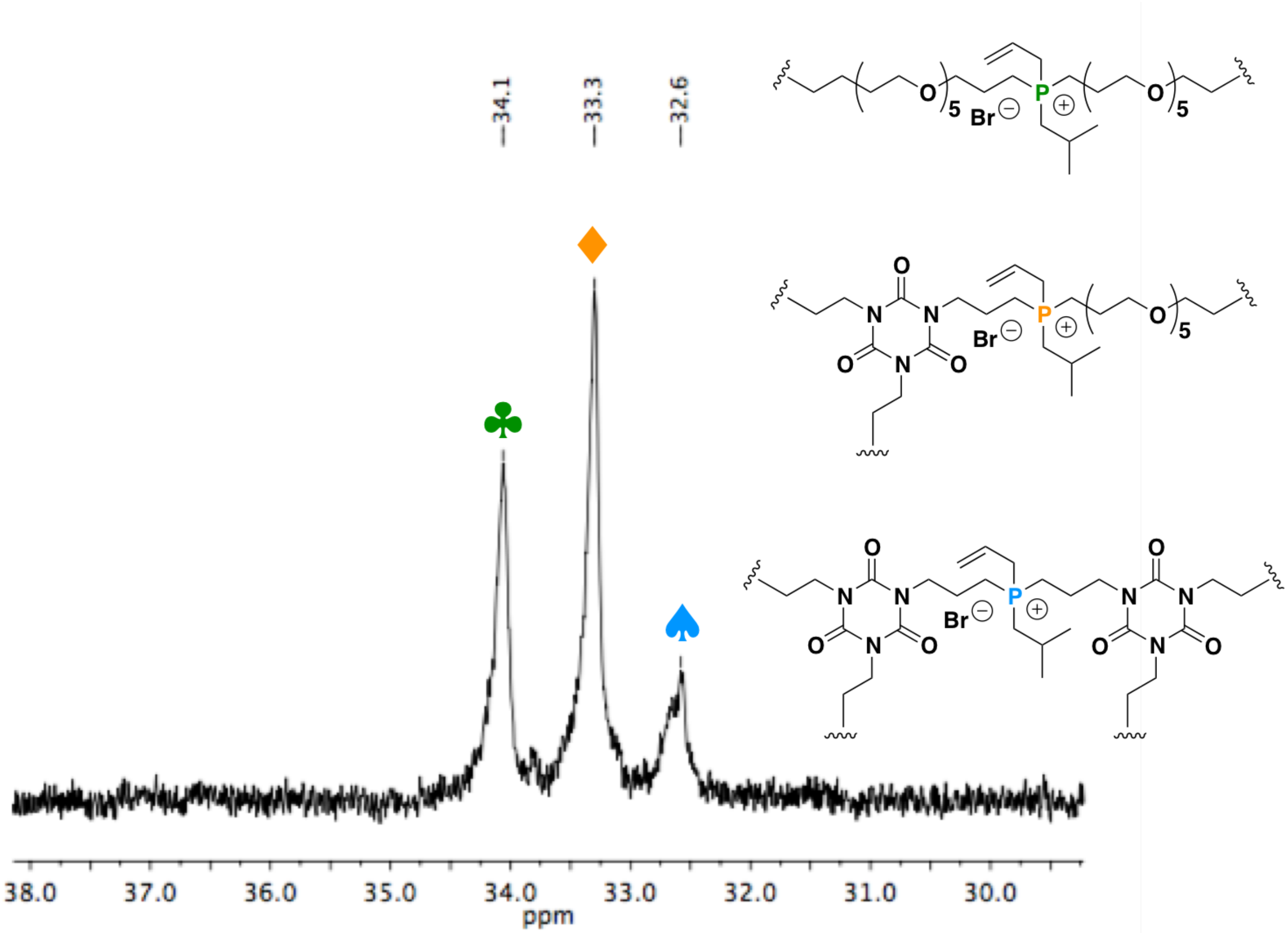

Figure 5.3: Labeled $^{31}P\{^1H\}$ NMR spectrum of **5.2[Br]**.

Network **5.2[Br]** was functionalized by hydrogermylation of the olefin functionality with a slight excess of triphenylgermanium hydride (Scheme 5.1). The new polymer gel, **5.2[Br]Ge** was purified by Soxhlet extraction to remove excess triphenylgermanium hydride. Network **5.2[Br]Ge** is distinguished by the absence of olefin signals (δ_C = 125.8, 124.2 ppm) and the appearance of aromatic carbon signals (δ_C = 137.5, 135.7, 130.1, 129.5 ppm; $\nu_{Ge\text{-}aryl}$ = 1430 cm^{-1}) in the ^{13}C NMR and IR spectra (Figure 5.4). The presence of germanium in the purified gel was confirmed by EDX spectroscopy and the ratio of germanium to phosphorus was found to be approximately 1:1 (Table 5.1).

Table 5.1: EDX data recorded from different areas of **5.2[Br]Ge**.

Atomic %				
C	*O*	*Br*	*Ge*	*P*
74.90	22.56	0.94	0.82	0.77
73.33	24.43	0.87	0.70	0.67
54.91	41.42	1.56	0.88	1.23

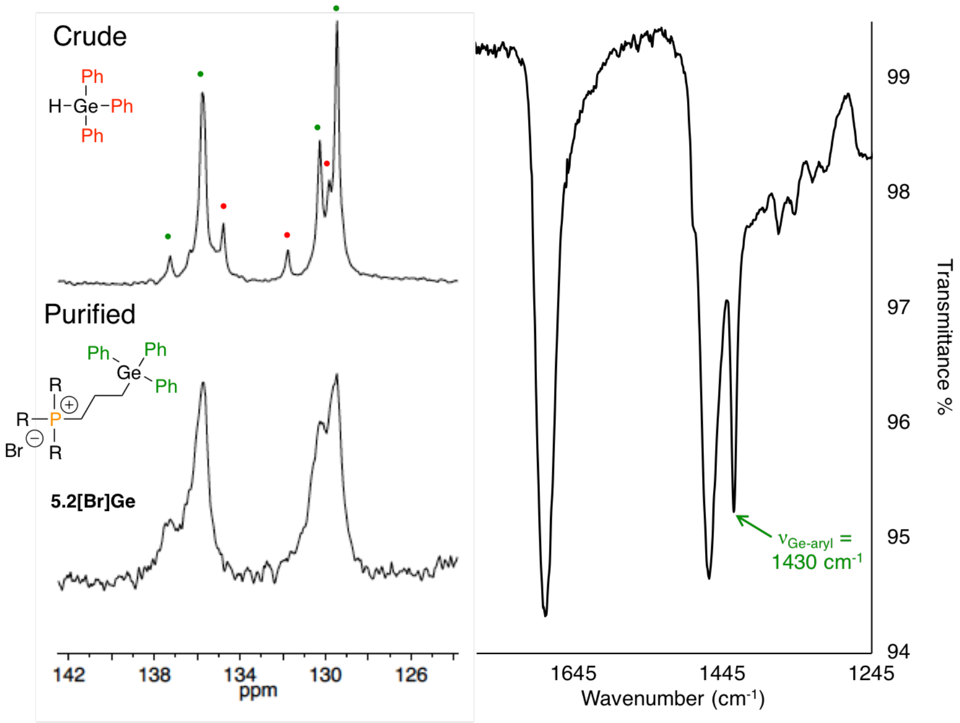

Figure 5.4: Left: Aromatic region of the $^{13}C\{^1H\}$ NMR spectrum of crude (top) and purified (bottom) **5.2[Br]Ge**. Right: IR spectrum of **5.2[Br]Ge**.

The bromide anion in **5.2[Br]Ge** can be utilized to functionalize the material with a second metal either by metathesis or ion coordination. Network **5.2[Br]Ge** was swelled in 250 mL of a 5.0x10^{-5} M solution of copper (II) bromide in acetonitrile (Scheme 5.1). After one week, the green solution was decanted from the purple gel, **5.2[Cu]Ge**, that was purified by Soxhlet extraction. After three days, a sample of the supernatant was removed from the Soxhlet apparatus and passed through a 0.22 μm PTFE syringe filter. Based on the flat line in the UV-vis absorption spectrum of the supernatant, all of the uncomplexed $CuBr_2$ had been leached from the gel (Figure 5.5). The solvent was removed to give a dark purple solid. Network **5.2[Cu]Ge** was swelled with acetonitrile in a cuvette to form a gel which could be analyzed by UV-vis spectroscopy. The spectrum for the purple gel revealed a yellow maximum absorption wavelength (λ_{max} = 549 nm), which corresponded to the purple $[CuBr_4]^{2-}$ anion and a red shoulder (λ = 628 nm), that corresponded to the green $[CuBr_3(MeCN)]^-$ anion (Figure 5.5).[39,40] Despite the paramagnetic anions, the ^{31}P NMR chemical shift did not change from **5.2[Br]Ge** and the IR spectrum confirmed that the aryl groups on germanium were still present. The presence of germanium and copper was confirmed by EDX spectroscopy and show a ration of approximately 6:6:1 for P:Cu:Ge (Table 5.2). The glass transition temperature of **5.2[Cu]Ge** (T_g = 2 °C) decreased from **5.2[Br]Ge** likely due to lower lattice energy of the complexed versus free bromide anions.

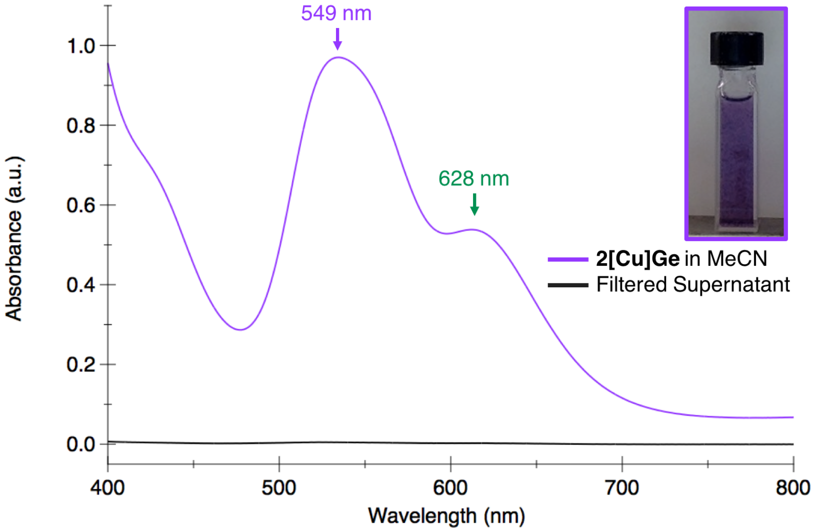

Figure 5.5: UV-vis spectrum for **5.2[Cu]Ge** swelled in MeCN.

Table 5.2: Atomic % by EDX from different areas of ceramics derived from **5.2[Cu]Ge** by pyrolysis at 800 °C for 4 hours.

C	*O*	*Cu*	*P*	*Ge*	*Br*
77.41	15.85	2.99	2.81	0.65	0.29
74.46	19.51	2.12	3.12	0.37	0.41
78.58	14.89	2.90	2.79	0.55	0.30

5.4 Pyrolysis of Metal Functionalized Polymer Networks

Network **5.2[Cu]Ge** was pyrolyzed at 800°C for 4 hours and the resulting grey char was found to be amorphous and speckled with metallic particles by SEM (Figure 5.6). The XPS reveal a material primarily composed of carbon and doped with copper (1.0%), germanium (0.8%) and phosphorus (2.1%). Copper was found the be in the mixed oxidation state form of Cu_4O_3 by the two binding energies at 934.0 and 933.0 eV.[41] The char contains a mixture of metallic germanium (29.5 eV, Ge3/2) and germanium (II) oxide (32.0 eV).[42] The majority of the phosphorus is phosphate (134.08 eV, 97.7%), with a small amount of P(III) (131.8 eV, 2.3%), which is likely incorporated covalently in the carbon black.[43,44]

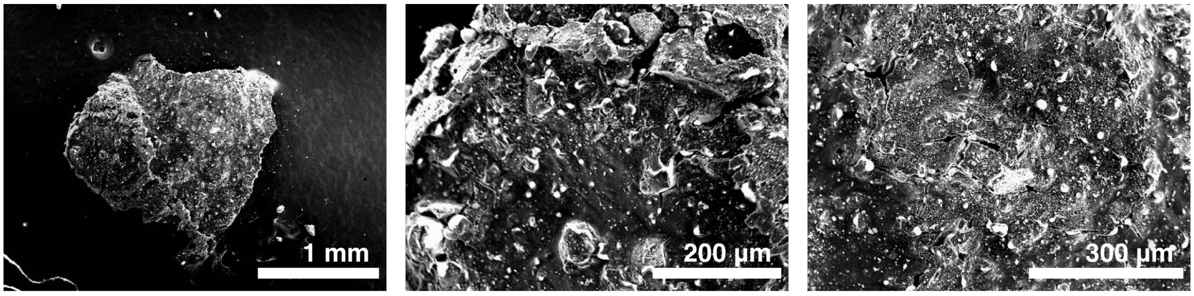

Figure 5.6: SEM images of ceramics derived from **5.2[Cu]Ge**. Char formed at 800 °C for 4 hours.

5.5 Conclusion

In this work we bi-metallized phosphane-ene polymer networks by quaternization with allyl bromide and subsequent metal functionalization by orthogonal mechanisms. The new material was tested for suitability as a precursor to metal-containing ceramics. The resulting ceramics were found to be largely composed of carbon yet doped with the metals in question as well as P heteroatoms. It is noteworthy that the polymeric material used in this context can be made from neat, commercially available reagents and can be easily purified, putting phosphane-ene based ceramic precursors ahead of MOFs in terms of their scalability.

In the end we describe a polymeric material that can be easily bi-metallized through hydrometallation, ion complexation or even ion exchange. Although this work focuses on functionalization with Ge and Cu, we are exploring functionalization with other elements to showcase the versatility of the material and access a broader range of ceramics.

5.6 Instrumentation

Solution state nuclear magnetic resonance (NMR) spectroscopy was either conducted on a Varian INOVA 400 MHz spectrometer, or a Bruker AVANCEIII HD 400 spectrometer which utilizes an H/FX Bruker 5mm Smart Probe with automated tuning and matching (^{1}H 400.09 MHz, ^{11}B{^{1}H} 128.25 MHz, ^{13}C{^{1}H} 100.53 MHz, ^{19}F{^{1}H} 376.32 MHz, ^{31}P{^{1}H} 161.82 MHz). All ^{13}C{^{1}H} spectra were referenced relative to residual solvent signal. The chemical shifts for ^{19}F{^{1}H} and ^{31}P{^{1}H} spectra were referenced using external standards; α,α,α–trifluorotoluene (δ_F = -63.9 ppm) and 85% H_3PO_4 (δ = 0 ppm), respectively. The chemical shifts for ^{31}P{^{1}H} spectroscopy were referenced using an external standard of 85% H_3PO_4; δ_P = 0. ATR-IR experiments were conducted using a Perkin Elmer UATR Two spectrometer. A UV-box from UV Process Supply Inc. (Chicago, IL, USA) equipped with a Mercury Bulb with an energy density of UVA (0.031 mJ cm^{-2}) and UVV (164 mJ cm^{-2}) was used for photopolymerization. These dose values were determined using a PP2-H-U Power Puck II purchased from EIT Instrument Markets (Sterling, VA, USA). UV-vis experiments were conducted using an Agilent Technologies Cary Series UV-vis-NIR Spectrophotometer. A SDT Q600 thermogravimetric analyzer (TGA) was used to determine char yields. A TA Q20 differential scanning calorimeter (DSC) was used to determine glass transition temperatures (T_g) with a ramp rate of 40 °C per minute. All T_g values are reported using the onset temperature from the last heating cycle. Pyrolysis was performed under 5 % H_2 (balance N_2) in a Lindberg furnace equipped with a quartz tube. A Hitachi 3400s SEM instrument was used to collect scanning electron microscopy (SEM) images and energy dispersive X-ray (EDX) spectra. Samples were osmium coated before SEM and EDX analysis. X-ray photoelectron spectroscopy (XPS) was performed using a Kratos AXIS Nova Spectrometer.

5.7 Reagents and Synthesis

All manipulations were performed in a nitrogen filled MBraun Labmaster dp glovebox or by using standard Schlenk techniques. All solvents were purchased from Caledon and dried using an MBraun controlled atmosphere solvent purification system and stored in Straus flasks under an N_2 atmosphere or over 4 Å molecular sieves. Monoisobutylphosphine ($^iBuPH_2$) was donated by Solvay and used as received. Irgacure 819 (Ciba Chemicals), 1,3,5-triallyl-1,3,5-triazine-2,4,6(1*H*,3*H*,5*H*)-trione (TTT) (Sigma Aldrich), vinyl benzyl chloride (Aldrich), allyl bromide (Alfa Aesar), triphenylgermanium hydride (Aldrich) and copper (II) bromide (Aldrich) were used as received. The thermal initiator, 2,2'-azobis(2-methylpropionitrile) (AIBN) (DuPont) was recrystallized from methanol before use. Tetraethyleneglycol diallylether (TEGDAE) was prepared by scaling a literature procedure to yield 100 g.[37] Briefly, polymer network **5.1** was synthesized as previously reported by combining and irradiating $^iBuPH_2$ (2.352 g, 26.1 mmol), TTT (8.680 g, 34.8 mmol) and BAPO (55 mg, 0.5 wt%).[22]

5.1[Br]: An acetonitrile solution (20 mL) of allyl bromide (0.3 mL, 3.5 mmol) as added to **1** (1.122 g) in a pressure tube and heated to 65 °C for two days. The supernatant was decanted, the colourless gel was leached with acetonitrile overnight (3 x 20 mL), decanted and dried *in vacuo*. $^{13}C\{^1H\}$ NMR (100.6 MHz): δ = 149.4 (carbonyl, $(R_2N)_2\underline{C}{=}O$), 131.9 (allyl, $\underline{C}H$), 125.1 (olefin, $\underline{C}H_2$), 117.5 (olefin, $\underline{C}H_2$), 44.9 (alkyl), 24.5 (alkyl), 2.0 ppm (alkyl); $^{31}P\{^1H\}$ NMR (161.8 MHz): δ = 32.4 ppm; FT-IR (ranked intensity): ν = 1676.0 (1), 1457.2 (2), 1372.5 (5), 1320.0 (4), 993.5 (9), 931.2 (6), 849.5 (10), 762.0 (3), 598.2 (8), 530.8 (7) cm^{-1}; decomposition onset (2% mass loss) = 239.9 °C; Char yield at 800 °C at t = 0 = 11.58 %; Char yield at 800 °C, at t = 3 hours = 8.72 %; T_g onset = 135.0 °C.

5.1[Cl]: Network **1** (0.524 g), 4-vinylbenzylchloride (0.382 g, 2.5 mmol) was dissolved in acetonitrile (5 mL) and refluxed in a pressure tube for seven days. The supernatant was decanted and the polymer network was leached three times with dichloromethane (3 x 15 mL) over the course of three days. After decanting the leaching solvent, the network was dried *in vacuo*. $^{13}C\{^1H\}$ NMR (100.6 MHz): δ = 149.1 (carbonyl, $(R_2N)_2\underline{C}{=}O$), 136.3 (aryl), 131.6 (olefin, $\underline{C}H$), 128.4 (aryl), 118.2 (olefin, $\underline{C}H_2$), 44.6 (alkyl), 24.7 (alkyl); $^{31}P\{^1H\}$ NMR (161.8 MHz): δ = 32.3 ppm; FT-IR (ranked intensity): ν = 1676.0 (1), 1511.5 (9), 1457.5 (2), 1373.0 (5), 1319.8 (4), 1265.5 (8), 909.5 (10), 858.0 (7), 762.8 (3), 729.0 (6) cm^{-1}; decomposition onset (2% mass loss) = 169.5 °C; Char yield at 800 °C at t = 0 = 16.83 %; Char yield at 800 °C, at t = 3 hours = 14.82 %; T_g onset = 97.0 °C.

5.2H: TEGDAE (4.621 g, 16.8 mmol), TTT (1.401 g, 5.6 mmol) and $^iBuPH_2$ (3.160 g, 3.5 mmol) were combined neat. The photoinitiator, Irgacure 819 (46 mg, 0.5 wt%) was added, the pale yellow mixture was sealed and irradiated with ultraviolet light for 30 minutes. Unreacted monomers were removed *in vacuo* from the resulting transparent, colourless, tacky, elastic gel. $^{13}C\{^{1}H\}$ NMR (100.6 MHz): δ = 149.9 (carbonyl, $(R_2N)_2\underline{C}$=O), 73.2, 73.1, 72.7, 72.6, 71.5, 71.1 (ethereal, $\underline{C}H_2$), 45.0, 39.2, 27.4, 27.3, 27.1, 27.0, 25.9, 25.8, 25.1, 24.5, 18.3, 18.2 (alkyl, $\underline{C}H_2$) ppm; ^{31}P NMR (161.8 MHz): δ = -34.3 (3° PR_3, s), -75.6 (2° PHR_2, d; $^{1}J_{PH}$ = 194.2 Hz) ppm; FT-IR (ranked intensity): ν = 2950 (6), 2866 (4), 2270 (ν_{PH}), 1687 (1), 1460 (3), 1427 (8), 1365 (7), 1350 (9), 1333 (10), 1107 (2), 763 (5) cm^{-1}; decomposition onset (2% mass loss) = 227 °C; Char yield = 1.349 %; T_g onset = -83.3 °C.

5.2: AIBN (0.182 g, 1.1 mmol) was dissolved in toluene (75 mL) added to swell network **5.2H** (5.975 g). 1-Hexene (11 mL, 8.8 mmol) was added and the mixture was heated to 80°C on a sand bath in a pressure reactor for two days. After confirming the disappearance of P-H signals by ^{31}P NMR spectroscopy, the material was decanted and dried *in vacuo*. $^{13}C\{^{1}H\}$ NMR (100.6 MHz): δ = 148.9 (carbonyl, $(R_2N)_2\underline{C}$=O), 72.2, 70.5, 70.1 (ethereal, $\underline{C}H_2$), 44.0, 38.2, 38.1, 31.6, 26.5, 26.4, 26.3, 26.0, 25.0, 24.8, 24.1, 22.6, 22.3, 13.9 (alkyl, $\underline{C}H_2$) ppm; $^{31}P\{^{1}H\}$ NMR (161.8 MHz): δ = -35.6 ppm; FT-IR (ranked intensity): ν = 2952 (7), 2922 (6), 2866 (4), 1688 (2), 1461 (3), 1364 (9), 1350 (10), 1104 (1), 1046 (8), 764 (5) cm^{-1}; decomposition onset (2% mass loss) = 234 °C; Char yield = 4.59 %; T_g onset = -65.4 °C.

5.2[Br]: Network **5.2** (5.4963 g), was combined with allyl bromide (3.6 mL, 42 mmol) in acetonitrile (60 mL) and left to swell overnight. Any free solvent was decanted from the swollen polymer network and the rest of the volatiles were removed *in vacuo* to give a tacky, colourless, transparent material. $^{13}C\{^{1}H\}$ NMR (100.6 MHz): δ = 150.5 (carbonyl, $(R_2N)_2\underline{C}$=O), 125.8 (allyl, $\underline{C}H$), 124.2 (allyl, $\underline{C}H_2$), 70.7 (ethereal, $\underline{C}H_2$), 43.5, 31.2, 30.6, 27.6, 27.2, 25.8, 25.3, 24.5, 24.4, 23.6, 22.3, 20.9, 19.7, 18.7, 18.2, 17.1, 16.6, 13.9, 10.2 (alkyl, $\underline{C}H_2$) ppm; $^{31}P\{^{1}H\}$ NMR (161.8 MHz): δ = 34.1, 33.3, 32.6 ppm; FT-IR (ranked intensity): ν = 2956 (10), 2924 (8), 2869 (4), 1682 (2), 1464 (3) 1107 (1), 998 (9), 934 (6), 858 (7), 762 (5) cm^{-1}; decomposition onset (2% mass loss) = 213 °C; Char yield at 800 °C at t = 0 = 2.45 %; T_g onset = -28 °C.

5.2[Br]Ge: An acetonitrile (20 mL) solution of triphenylgermanium hydride (0.332 g, 3.3 mmol) and AIBN (0.018 g, 0.1 mmol) was added to network **5.2[Br]** (0.419 g) and heated at 65°C for six days. The resulting colourless, tacky network was purified by Soxhlet extraction with acetonitrile and then dried *in vacuo*. $^{13}C\{^{1}H\}$ NMR (100.6 MHz): δ = 137.5, 135.7, 130.1, 129.5 (Ge-aryl), 71.1 (ethereal, $\underline{C}H_2$), 28.1, 24.9, 18.8, 9.4 (alkyl, $\underline{C}H_2$) ppm; $^{31}P\{^{1}H\}$ NMR (161.8 MHz): δ = 34.5, 33.9 ppm; FT-IR (ranked intensity): ν = 2958 (14), 2868 (9), 1682 (3), 1464 (4), 1430 (6; $\nu_{Ge\text{-}aryl}$), 1370 (13), 1090 (1), 1026 (7), 998 (8), 940 (11), 856 (15), 751 (12), 736 (5), 699 (2), 467 (10) cm^{-1}; decomposition onset (2% mass loss) = 318.2 °C; Char yield at 800 °C at t = 0 = 22.53 %; Char yield at 800 °C, at t = 3 hours = 18.98 %; T_g onset = 35 °C.

5.2[Cu]Ge: $CuBr_2$ (0.108 g, 0.482 mmol) was dissolved in 250 mL acetonitrile volumetrically. An aliquot of this solution was measured by UV-vis spectroscopy, recombined with the bulk solution, added to network **5.2[Br]Ge** (0.324 g) in a 500 mL jar and sealed. After one week, the green solution was decanted from the violet gel and an aliquot of the reaction mixture solution was sampled by UV-vis spectroscopy. The gel was purified by Soxhlet extraction with acetonitrile and dried *in vacuo* to yield a dark purple brittle solid. $^{31}P\{^1H\}$ NMR (161.8 MHz): δ = 33.8 ppm; FT-IR (ranked intensity): ν = 2930 (12), 2872 (9), 1683 (3), 1464 (4), 1430 (7; $\nu_{Ge\text{-}aryl}$), 1403 (15), 1108 (6), 1090 (2), 1026 (10), 998 (13), 762 (14), 737 (5), 700 (1), 674 (11), 466 (8) cm^{-1}; λ_{max} = 549; decomposition onset (2% mass loss) = 213.40 °C; Char yield at 800 °C at t = 0 = 19.44 %; Char yield at 800 °C, at t = 3 hours = 8.576 %; T_g onset = 2 °C.

5.8 References

(1) Zou, X.; Zhang, Y. *Chem. Soc. Rev.* **2015**, *44* (15), 5148.

(2) Chang, Z. R.; Lv, H. J.; Tang, H.; Yuan, X. Z.; Wang, H. *J. Alloys Compd.* **2010**, *501* (1), 14.

(3) Fan, C. L.; Lin, C. R.; Han, S. C.; Chen, J.; Li, L. F.; Bai, Y. M.; Zhang, K. H.; Zhang, X. *New J. Chem.* **2014**, *38* (2), 795.

(4) Li, Y.; Dai, H. *Chem. Soc. Rev.* **2014**, *43* (15), 5257.

(5) Li, Y.; Lu, J. *ACS Energy Lett.* **2017**, *2*, 1370.

(6) Masa, J.; Xia, W.; Sinev, I.; Zhao, A.; Sun, Z.; Grützke, S.; Weide, P.; Muhler, M.; Schuhmann, W. *Angew. Chem. Int. Ed.* **2014**, *53* (32), 8508.

(7) Serov, A.; Andersen, N. I.; Roy, A. J.; Matanovic, I.; Artyushkova, K.; Atanassov, P. *J. Electrochem. Soc.* **2015**, *162* (4), F449.

(8) Shi, Y.; Zhang, B. *Chem. Soc. Rev.* **2016**, *45* (6), 1529.

(9) Yu, J.; Li, Q.; Li, Y.; Xu, C.; Zhen, L.; Dravid, V. P.; Wu, J. *Adv. Funct. Mater.* **2016**, *26*, 7644.

(10) Tan, Y.; Wang, H.; Liu, P.; Shen, Y.; Cheng, C.; Hirata, A.; Fujita, T.; Tang, Z.; Chen, M. *Energy Environ. Sci.* **2016**, *9* (7), 2257.

(11) Li, X.; Zheng, S.; Jin, L.; Li, Y.; Geng, P.; Xue, H.; Pang, H.; Xu, Q. *Adv. Energy Mater.* **2018**, *8* (23), 1800716.

(12) Pan, Y.; Lin, Y.; Chen, Y.; Liu, Y.; Liu, C. *J. Mater. Chem. A* **2016**, *4* (13), 4745.

(13) Mi, Y.; Yang, C.; Zuo, Z.; Qi, L.; Tang, C.; Zhang, W.; Zhou, H. *Electrochim. Acta* **2015**, *176*,

642.

(14) Tang, H.; Cai, S.; Xie, S.; Wang, Z.; Tong, Y.; Pan, M.; Lu, X. *Adv. Sci.* **2015**, *3*, 1500265.

(15) Julien, P. A.; Mottillo, C.; Friščić, T. *Green Chem.* **2017**, *19* (12), 2729.

(16) Whittell, G. R.; Hager, M. D.; Schubert, U. S.; Manners, I. *Nat. Mater.* **2011**, *10* (3), 176.

(17) Kenaree, A. R.; Gilroy, J. B. *Dalton Trans.* **2016**, *45* (45), 18229.

(18) Liu, K.; Clendenning, S. B.; Friebe, L.; Chan, W. Y.; Zhu, X.; Freeman, M. R.; Yang, G. C.; Yip, C. M.; Grozea, D.; Lu, Z.; Manners, I. *Chem. Mater.* **2006**, *18* (10), 2591.

(19) Zhang, J.; Yan, Y.; Chen, J.; Chance, W. M.; Gai, Z.; Tang, C. *Chem. Mater.* **2014**, *26* (10), 3185.

(20) Paquette, J. A.; Gilroy, J. B. *J. Polym. Sci. A* **2016**, *54*, 3257.

(21) Béland, V. A.; Ross, M. A. S.; Coady, M. J.; Guterman, R.; Ragogna, P. J. *Chem. Mater.* **2017**, *29* (20), 8884.

(22) Béland, V. A.; Wang, Z.; Sham, T. K.; Ragogna, P. J. *Angew. Chem. Int. Ed.* **2018**, *57*, 13252.

(23) Guterman, R.; Gillies, E. R.; Ragogna, P. J. *Can. J. Chem.* **2016**, *94* (5), 476.

(24) Guterman, R.; Hesari, M.; Ragogna, P. J.; Workentin, M. S. *Langmuir.* **2013**, *29* (21), 6460.

(25) Guterman, R.; Gillies, E. R.; Ragogna, P. J. *Langmuir.* **2015**, *31* (18), 5181.

(26) Cuthbert, T. J.; Evoy, E.; Bow, J. P. J.; Guterman, R.; Stubbs, J. M.; Gillies, E. R.; Ragogna, P. J.; Blacquiere, J. M. *Catal. Sci. Technol.* **2017**, *7* (13), 2685.

(27) Guterman, R.; Harrison, T. D.; Gillies, E. R.; Ragogna, P. J. *Polym. Chem.* **2017**, No. 8, 3425.

(28) Labinger, J. A. In *Comprehensive Organic Synthesis*; Trost, B. M., Fleming, I., Eds.; Pergamon Press: Elmsford, New York, USA, 1991; pp 667–702.

(29) Smith, K.; Pelter, A. In *Comprehensive Organic Synthesis*; Trost, B. M., Fleming, I., Eds.; Pergamon Press: Elmsford, New York, USA, 1991; pp 703–731.

(30) Eisch, J. J. In *Comprehensive Organic Synthesis*; Trost, B. M., Fleming, I., Eds.; Pergamon Press: Elmsford, New York, USA, 1991; pp 733–761.

(31) Trost, B. M.; Ball, Z. T. *Synthesis* **2005**, (6), 853.

(32) Dobbs, A. P.; Chio, F. K. I. *Hydrometallation Group 4 (Si, Sn, Ge, and Pb)*; Elsevier Ltd., 2014; Vol. 8.

(33) Jambor, R.; Lyčka, A. *Eur. J. Inorg. Chem.* **2017**, *2017* (42), 4887.

(34) Kavanagh, Y.; Ford, L.; Schiesser, C. H. *Organometallics.* **2011**, *30* (16), 4387.

(35) Braia, N.; Saihi, Y.; Azzouzi, A. E.; Ferkous, F. *Asian J. Chem.* **2009**, *21* (6), 4628.

(36) Comasseto, J. V; Cunha, R. L. O. R.; Clososki, G. C. In *Comprehensive Organometallic Chemistry III*; Knochel, P., Ed.; Elsevier Ltd.: Kidlington, Oxford, UK, 2007; pp 587–648.

(37) Guterman, R.; Rabiee Kenaree, A.; Gilroy, J. B.; Gillies, E. R.; Ragogna, P. J. *Chem. Mater.* **2015**, *27* (4), 1412.

(38) Mathur, A. M.; Scranton, A. B. *Biomaterials* **1996**, *17* (6), 547.

(39) Willett, R. D.; Pon, G.; Nagy, C. *Inorg. Chem.* **2001**, *40*, 4342.

(40) Hasselgren, C.; Jagner, S.; Dance, I. *Chem. Eur. J.* **2002**, No. 6, 1269.

(41) Das, S.; Alford, T. L. *Appl. Phys. Lett.* **2013**, *103*, 094104.

(42) Hernández, A. G.; Escobosa-Echavarría, A. E.; Kudriavtsev, Y. *Appl. Surf. Sci.* **2018**, *428*, 1098.

(43) Leigh, G. J.; Bremser, W. *Dalton Trans.* **1972**, 1216.

(44) Furlani, A.; Polzonetti, G.; Russo, M. V.; Mattogno, G. *Inorganica Chim. Acta* **1978**, *26*, 39.

Chapter 6

6 Conclusions and Future Work

6.1 Tailored Ceramic Precursors – "Alkyl in Chains"

The target of this work was to generate metallized polymers that can be used as precursors for metal-containing ceramics. Three general methods of incorporating elemental diversity into polymers were demonstrated by leveraging phosphonium cations, alkyl phosphines or olefins in metathesis, coordination, or hydrometallation reactions, respectively. It was demonstrated that these methods of deriving ceramics from photopolymer networks are effective ways of producing carbon doped with metal oxides. It was found that tuning the amount of metal in the polymer precursor has the effect of controlling the amount of metal in the ceramics after pyrolysis and that the composition of the ceramics can be tuned by altering the composition of the polymer backbone. With these findings in mind, it can be concluded that these general methodologies for creating polymer derived ceramics may be well-suited for targeting materials for electrochemical applications. As mentions in Chapter 1, electrochemically active ceramics have shown an increase in activity when incorporated into carbon. On the other hand, due to the high carbon content of these materials, they may not be well-suited for applications in the IT industry as ceramics in the field generally require a high purity. The following proposals will outline possible routes towards tuning the carbon content of resulting ceramics, incorporating more metals into the materials and how the polymers themselves may become useful.

The next steps in developing these methodologies will be to gain control over the ratio of metal to carbon in the ceramics, as well as targeting different types of ceramics, specifically metal phosphides. The issue in achieving these has been the high oxygen content in the polymer backbone, where on pyrolysis, reacts with the oxophilic phosphorus and metals. Using an alkyl backbone improves the amount of cobalt phosphide in the ceramic. In order to increase the amount of metal in the resulting ceramics, polymer precursors should be designed with minimal carbon and oxygen. A proposed way of doing this is by hydrophosphinating triallylphosphine with PH_3 to make a crosslinked network (Scheme 6.1). The 3° phosphine sites could be metallized by coordination chemistry and pyrolyzed to give metal containing ceramics.

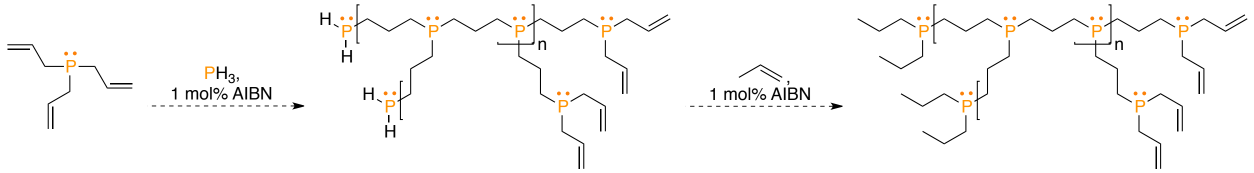

Scheme 6.1: Route to tripropylphosphine polymer networks.

Triallyl phosphine is synthesized by combination of PCl_3 with allyl Grignard.[1] In order to tune the amount of metal in the ceramics, it would be straight forward to generate tris(1-butene), tris(1-pentene) and tris(1-hexene) substituted phosphines from the corresponding bromoalkenes, which are commercially available. The resulting metallized networks with a high percentage of carbon will yield ceramics with high carbon content and vice versa.

The above method could be extended to the metallization by metathesis method in two different ways. The 3° phosphines in the final network of Scheme 1 could be quaternized to create phosphonium cations. Alternatively, by reacting a 1° phosphine with two stoichiometric equivalents of allyl bromide, the phosphine can hydrophosphinate and quaternize in one step to form a polyphosphonium cation network, where the phosphonium cations are linked by propyl groups (Scheme 6.2). The propyl linkers will give the material a relatively low carbon content compared to the networks described in this thesis. This could also be extended to other bromoalkenes to tune the carbon content of the polymer precursor as discussed above.

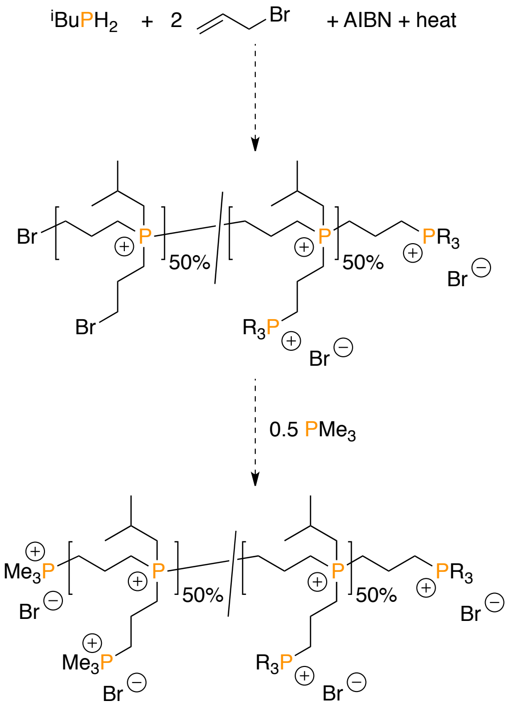

Scheme 6.2: Route to polyphosphonium cation networks liked by propyl groups.

6.2 Orthogonal Functionalization

Chapter 5 showcased a methodology to orthogonally functionalize polymer networks with two metals. The goal is to now build on this methodology by expanding the scope and number of metals that can be incorporated. Scheme 6.3 shows a route of orthogonally incorporating three metals by adding a 2° phosphine functional group into the cationic polyphosphonium allyl network. While this step would realistically produce a mixture of 2° and 3° phosphines, the remaining PH bonds could be used to hydrophosphinate a main group allyl compound, such as allyl cacodyl.[2,3] This would provide the first of three metals, the subsequent metals could be incorporated by metathesis, or coordination to the anion or 3° phosphine.

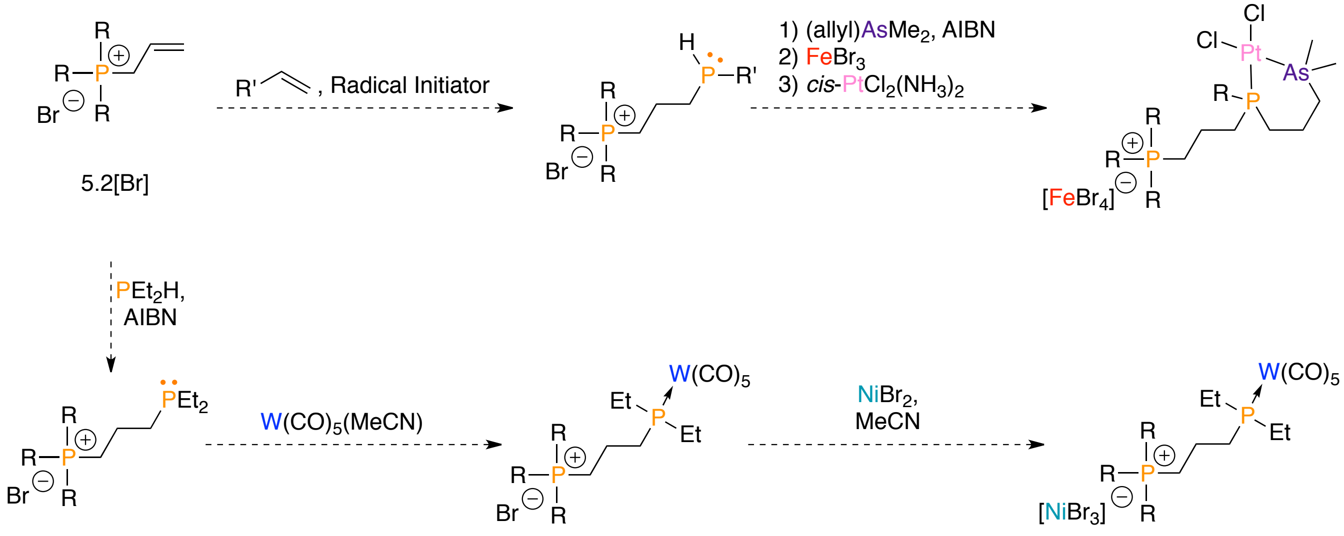

Scheme 6.3: Options for orthogonally including up to three metals into **2[Br].**

A less ambitious, yet still versatile method could be to hydrophosphinate the cationic phosphonium allyl network with a 2° phosphine and metallize by coordindination or ion exchange. While this method only metallizes twice, it expands the possible scope from what was presented in Chapter 5 because of the rich coordination chemistry of alkyl phosphines.[4–6]

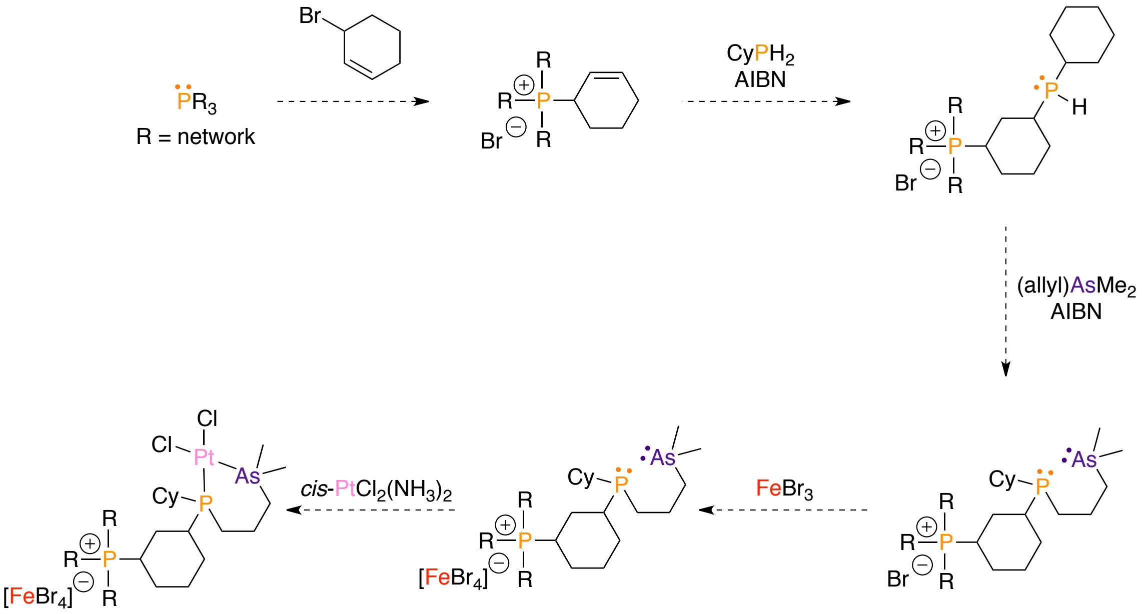

Scheme 6.4: Proposed route for selectively generating 2° cyclohexyl phosphine environments based on steric bulk.

In order to get around the potential selectivity issues with forming solely 2° phosphines in Scheme 6.3, an alternative method would be to quaternize the phosphine network with 3-bromocyclohexene to create a cationic cyclohexene polyphosphonium network (Scheme 6.4). This would provide enough bulk to solely form 2° phosphines in the material and provide a reliable way of orthogonally metallizing three times.[7]

6.3 "I'm the Only One"

Free radical hydrophosphination of olefins using PH_3 is the most economical way of making alkyl phosphines. While stoichiometry can be altered to favor 1° and 3° phosphines, 2° phosphines are difficult to access cleanly by this method as they are almost always formed in low abundance, mixed in with 1° and 3° phosphines and are isolated in low yields.[7] However, it is well-established that singly deprotonating phosphines can be done selectively.[8]

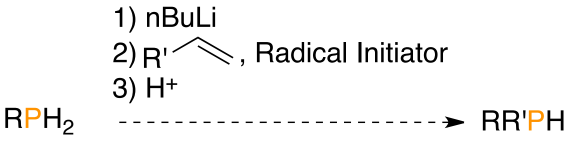

Scheme 6.5: Deprotonation, followed by hydrophosphination of a 1° phosphine to selectively synthesize a 2° phosphine after workup.

Inspired by Melissa Etheridge's 1993 hit, "I'm the Only One," a proposed selective route 2° phosphines is to singly deprotonate a 1° phosphine, leaving only one PH bond to hydrophosphinate. The product could be protonated in the workup to give a 2° phosphine (Scheme 6.5). This method could be applied to make 2° phosphines with two different substituents or two of the same substituents if made from 1° phosphine, or PH_3, respectively.

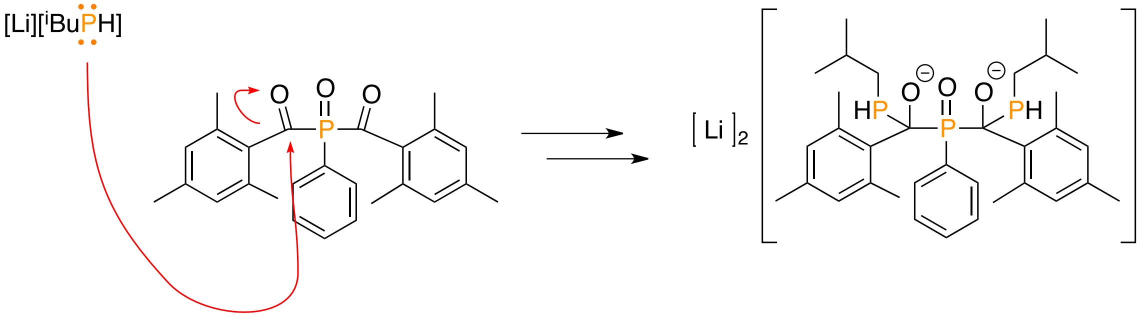

Scheme 6.6: Proposed nucleophilic attack of Irgacure 819 by the 1° alkyl phosphide species.

It should be noted that the hydrophosphination reaction in Scheme 6.5 has been attempted both thermally and photochemically, using AIBN and Irgacure 819 as radical initiators, respectively. In both cases the yellow lithium phosphide solution turned momentarily red on addition of the radical initiator.

After triggering the reaction with either heat or light, no significant change was observed by NMR spectroscopy. It is postulated that the nucleophilic 1° alkyl phosphine reacts with the azo or nitrile and carbonyl groups of the initiators, respectively, thus deactivating them (Scheme 6.6). With no radical initiator present, the hydrophosphination step cannot proceed.

The majority of radical initiators contain either carbonyl, or azo functionality that will react unfavorably with the 1° alkyl phosphide species (Scheme 6.6).[9] Irgacure 784 is an alkyl titanocene visible initiator (λ_{max} = 473 nm), which should be robust to nucleophilic attack (Figure 6.1).[9,10] If successful this route could provide a general "spot-to-spot" conversion of PH_3 or 1° phosphines to 2° phosphines without the use of a catalyst.[11,12]

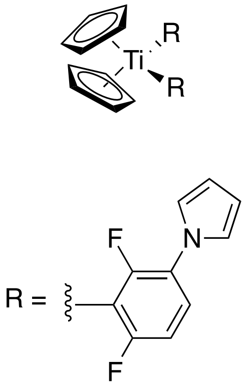

Figure 6.1: Structure of Irgacure 784 also known as bis-(η^5-2,3,-cyclopentadien-1-yl)-bis[2,6-difluoro-3-(1H-pyrrol-1-yl)phenyl]titanium.

6.4 Tuning Electronic Structure & Physical Properties

In Chapter 4, the electronic structure and physical properties of the native phosphane-ene polymer network could be modified by crosslinking with Sb cations. We hypothesize that the change in electronic structure of the phosphines arises from an increased inductive effect that results from the relatively longer crosslinked chains.

The gel property of phosphane-ene networks could be advantageous in the context of heterogeneous catalysis. This would allow substrates access to catalytic sites via swelling, but the catalyst would remain insoluble and could easily be removed from the reaction mixture. This, combined with the potential to tune electronic structure by crosslinking makes heterogeneous phosphane-ene supported catalysts attractive materials to pursue.

We are in the process of probing for this phenomenon in molecular versus macromolecular triphosphenium cations. The question is whether or not the inductive effect of the crosslinking has a significant impact on the electronic structure of the phosphorus atoms. Pending these results, we are interested in comparing the donation ability of molecular versus macromolecular phosphanide-type centers on coordination to Lewis acids (Scheme 6.7). Triphosphenium cations are interesting because of their two lone pairs of electrons that can bind to one, or sometimes two metals in cases where the supporting phosphine ligands are sufficiently electron rich.[13–18] Although they have never been used as ligands in catalysis, in learning to tune their electronic structure by crosslinking might be the first step towards their development as heterogeneous catalysts.

On top of triphosphenium cations, transition metal based catalysts that use chelating alkyl phosphine ligands can be used as inspiration for catalyst design within phosphane-ene networks. The network can be used, not only as a heterogeneous platform for catalysis, but also a means of tuning electron-richness at the metal center.

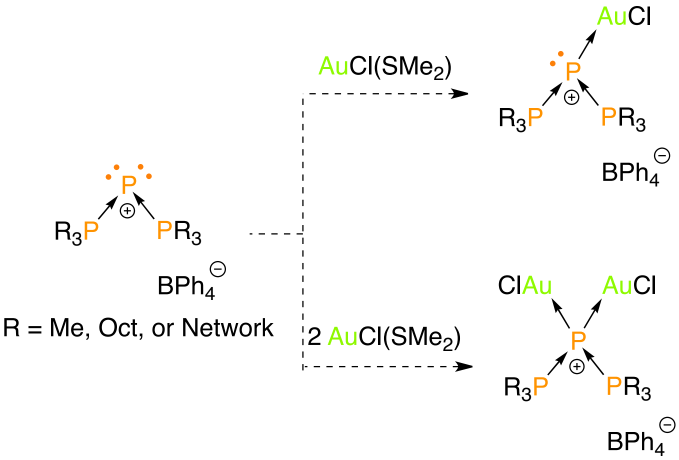

Scheme 6.7: Proposed coordination chemistry of alkyl phosphine supported phosphanide-type centers, analogous to what is reported in the literature.[15]

If successful, it would be interesting to delve into a study on the effect of different polymer chain lengths. If crosslinking results in longer chain lengths and ultimately a stronger inductive effect, increasing chain lengths from the beginning should result in an even stronger inductive effect after crosslinking. This could be tested by crosslinking different chain lengths of phosphane-ene polymers and comparing their electronic structure. Although there is no established method of controlling radical phosphane-ene polymerizations, control over chain length could be achieved by hydrophosphinating the unreacted olefins in prescribed chain lengths of polyisoprene.[19,20] The phosphine-functionalized polyisoprene could then be crosslinked by metals, or main group centers and the different chain length samples could be probed for differences in electronic structure (Scheme 6.8).

The hydrophosphination of polyisoprene could be extended to rubber with a low degree of vulcanization, like the rubber in a balloon for example. By crosslinking, or "knitting," the functionalized rubber using low valent main group centers, the material should become more rigid, perhaps like the rigid plastic in a chair (Scheme 6.8). The advantage of using low valent main group centers as crosslinkers is that they are sensitive to degradation, unlike the irreversible industrial method of vulcanization.[21] While phosphines are sensitive to O_2, they are otherwise robust compounds. If the low valent main group center could be degraded with acid for example, it should leave the phosphine functionality intact and reusable. The ultimate goal would be to make a plastic chair from a balloon, and then once we no longer require the chair, degrade it back into a balloon, which can now be used as a feedstock material to make the different types of plastic that we use every day. Although this may not be feasible using air sensitive plastic, the idea may inspire similar work that could work more practically, underscoring the importance of this fundamental research.

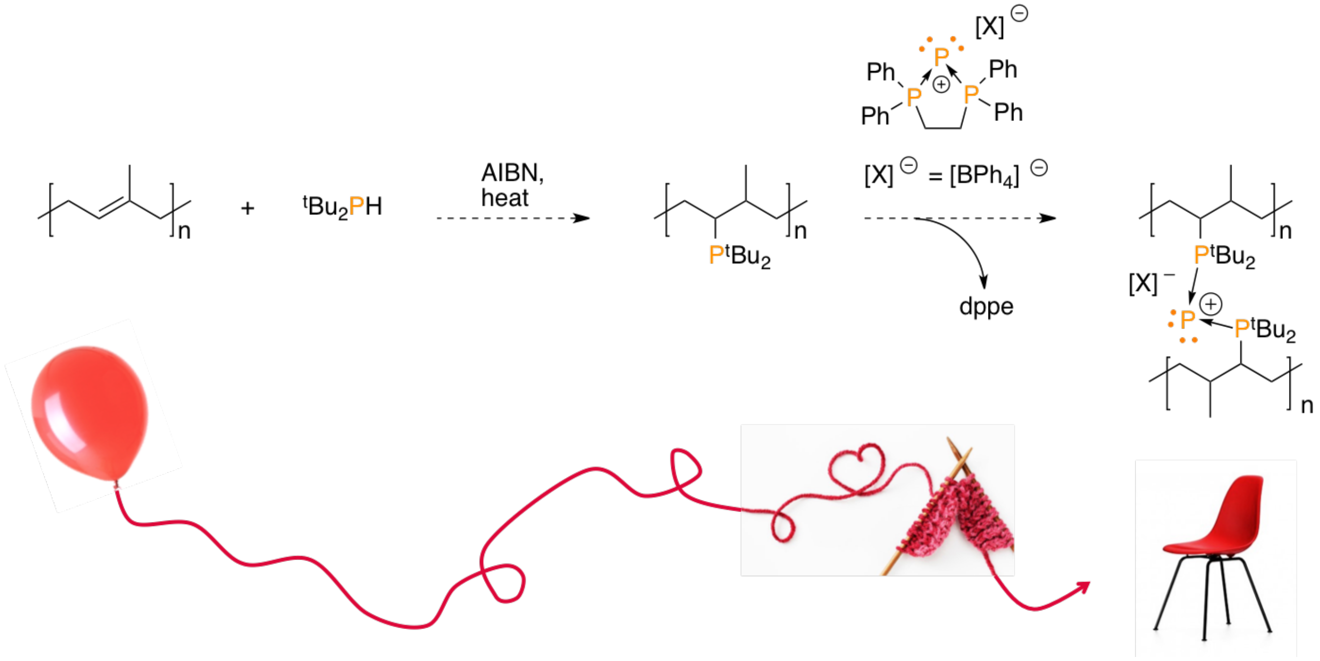

Scheme 6.8: Route towards triphosphenium-functionalized rubber.

6.5 References

(1) Jones, W. J.; Davies, W. C.; Bowden, S. T.; Edwards, C.; Davis, V. E.; Thomas, L. H. *J. Chem. Soc.* **1947**, 1446.

(2) Mödritzer, K. *Chem. Ber.* **1959**, *92*, 2637.

(3) Steinkopf, W.; Mieg, W. *Chem. Ber.* **1920**, *53B*, 1013.

(4) McAuliffe, C. A.; Levason, W. *Phosphine, Arsine and Stibine Complexes of the Transition Elements*; Elsevier Scientific Publishing Company: Oxford, UK, 1979.

(5) Norman, N. C.; Pickett, N. L. *Coord. Chem. Rev.* **1995**, *145* (C), 27.

(6) Chitnis, S. S.; Burford, N. *Dalton Trans.* **2015**, *44* (1), 17.

(7) *Organic Phosphorus Compounds*; Kosolapoff, G. M., Maier, L., Eds.; New York, NY, USA,

1972.

(8) Schäfer, H.; Fritz, G.; Hölderich, W. *Zeitschrift fuer Anorg. und Allg. Chemie* **1977**, *428* (1), 222.

(9) Decker, C. *Prog. Polym. Sci.* **1996**, *21* (4), 593.

(10) Fouassier, J. P.; Lalevée, J. *Photoinitiators for Polymer Synthesis*; Wiley-VCH: Weinheim, Germany, 2012.

(11) Douglass, M. R.; Marks, T. J. *J. Am. Chem. Soc.* **2000**, *122* (8), 1824.

(12) Basalov, I. V.; Roşca, S. C.; Lyubov, D. M.; Selikhov, A. N.; Fukin, G. K.; Sarazin, Y.; Carpentier, J. F.; Trifonov, A. A. *Inorg. Chem.* **2014**, *53* (3), 1654.

(13) Coffer, P. K.; Deng, R. M. K.; Dillon, K. B.; Fox, M. A.; Olivey, R. J. *Inorg. Chem.* **2012**, *51* (18), 9799.

(14) Kosnik, S. C.; Binder, J. F.; Nascimento, M. C.; Swidan, A.; Macdonald, C. L. B. *Chem. Eur. J.* **2019**, *25* (5), 1208.

(15) Dube, J. W.; MacDonald, C. L. B.; Ragogna, P. J. *Angew. Chem. Int. Ed.* **2012**, *51* (52), 13026.

(16) Kosnik, S. C.; Nascimento, M. C.; Binder, J. F.; MacDonald, C. L. B. *Dalton Trans.* **2017**, *46* (48), 17080.

(17) Dube, J. W.; Macdonald, C. L. B.; Ellis, B. D.; Ragogna, P. J. *Inorg. Chem.* **2013**, *52* (19), 11438.

(18) Dube, J. W.; Béland, V. A.; Boyle, P. D.; Ragogna, P. J. *Can. J. Chem.* **2014**, *93* (2), 253.

(19) Chen, H.; Pan, W.; Huang, K. W.; Zhang, X.; Gong, D. *Polym. Chem.* **2017**, *8* (11), 1805.

(20) Gao, F.; Zhang, L.; Yu, C.; Yan, X.; Zhang, S.; Li, X. *Macromol. Rapid Commun.* **2018**, *39* (8), 1.

(21) *Chemistry, Manufacture and Applications of Natural Rubber*; Kohjiya, S., Ikeda, Y., Eds.; Woodhead Publishing: Cambridge, UK, 2014.

Chapter 7

7 Appendix

7.1 Copyrights and Permissions

7.1.1 American Chemical Society Permission

Title: Patterned Phosphonium-Functionalized Photopolymer Networks as Ceramic Precursors

Author: Vanessa A. Béland, Matthew A. S. Ross, Matthew J. Coady, et al

Publication: Chemistry of Materials

Publisher: American Chemical Society

Date: Oct 1, 2017

Copyright © 2017, American Chemical Society

Logged in as:
Vanessa Beland
The University of Western Ontario

PERMISSION/LICENSE IS GRANTED FOR YOUR ORDER AT NO CHARGE

This type of permission/license, instead of the standard Terms & Conditions, is sent to you because no fee is being charged for your order. Please note the following:

- Permission is granted for your request in both print and electronic formats, and translations.
- If figures and/or tables were requested, they may be adapted or used in part.
- Please print this page for your records and send a copy of it to your publisher/graduate school.
- Appropriate credit for the requested material should be given as follows: "Reprinted (adapted) with permission from (COMPLETE REFERENCE CITATION). Copyright (YEAR) American Chemical Society." Insert appropriate information in place of the capitalized words.
- One-time permission is granted only for the use specified in your request. No additional uses are granted (such as derivative works or other editions). For any other uses, please submit a new request.

7.1.2 John Wiley and Sons License Terms and Conditions

This Agreement between The University of Western Ontario -- Vanessa Beland ("You") and John Wiley and Sons ("John Wiley and Sons") consists of your license details and the terms and conditions provided by John Wiley and Sons and Copyright Clearance Center.

License Number: 4503811327611

License date: Jan 07, 2019

Licensed Content Publisher: John Wiley and Sons

Licensed Content Publication: Angewandte Chemie International Edition

Licensed Content Title: Antimony-Functionalized Phosphine-Based Photopolymer Networks

Licensed Content Date: Sep 4, 2018

Licensed Content: Pages 5

Type of use: Dissertation/Thesis

Requestor type: Author of this Wiley article

Format: Print and electronic

Portion: Full article

Will you be translating? No

Title of your thesis/dissertation: Methodologies for Metal Functionalization of Photopolymer Networks

Expected completion date: Apr 2019

Expected size (number of pages): 230

Requestor Location: The University of Western Ontario, 1151 Richmond Street, London, ON N6A 3K7

Canada

Attn: Vanessa Béland

Publisher Tax ID: EU826007151

Total: 0.00 CAD

TERMS AND CONDITIONS

This copyrighted material is owned by or exclusively licensed to John Wiley & Sons, Inc. or one of its group companies (each a"Wiley Company") or handled on behalf of a society with which a Wiley Company has exclusive publishing rights in relation to a particular work (collectively "WILEY"). By clicking "accept" in connection with completing this licensing transaction, you agree that the following terms and conditions apply to this transaction (along with the billing and payment terms and conditions established by the Copyright Clearance Center Inc., ("CCC's Billing and Payment terms and conditions"), at the time that you opened your RightsLink account (these are available at any time at http://myaccount.copyright.com).

Terms and Conditions

The materials you have requested permission to reproduce or reuse (the "Wiley

Materials") are protected by copyright. You are hereby granted a personal, non-exclusive, non-sub licensable (on a standalone basis), non-transferable, worldwide, limited license to reproduce the Wiley Materials for the purpose specified in the licensing process. This license, and any CONTENT (PDF or image file) purchased as part of your order, is for a one-time use only and limited to any maximum distribution number specified in the license. The first instance of republication or reuse granted by this license must be completed within two years of the date of the grant of this license (although copies prepared before the end date may be distributed thereafter). The Wiley Materials shall not be used in any other manner or for any other purpose, beyond what is granted in the license. Permission is granted subject to an appropriate acknowledgement given to the author, title of the material/book/journal and the publisher. You shall also duplicate the copyright notice that appears in the Wiley publication in your use of the Wiley Material. Permission is also granted on the understanding that nowhere in the text is a previously published source acknowledged for all or part of this Wiley Material. Any third party content is expressly excluded from this permission.

With respect to the Wiley Materials, all rights are reserved. Except as expressly granted by the terms of the license, no part of the Wiley Materials may be copied, modified, adapted (except for minor reformatting required by the new Publication), translated, reproduced, transferred or distributed, in any form or by any means, and no derivative works may be made based on the Wiley Materials without the prior permission of the respective copyright owner. For STM Signatory Publishers clearing permission under the terms of the STM Permissions Guidelines only, the terms of the license are extended to include subsequent editions and for editions in other languages, provided such editions are for the work as a whole in situ and does not involve the separate exploitation of the permitted figures or extracts, You may not alter, remove or suppress in any manner any copyright, trademark or other notices displayed by the Wiley Materials. You may not license, rent, sell, loan, lease, pledge, offer as security, transfer or assign the Wiley Materials on a stand-alone basis, or any of the rights granted to you hereunder to any other person.

The Wiley Materials and all of the intellectual property rights therein shall at all times remain the exclusive property of John Wiley & Sons Inc, the Wiley Companies, or their respective licensors, and your interest therein is only that of having possession of and the right to reproduce the Wiley Materials pursuant to Section 2 herein during the continuance of this Agreement. You agree that you own no right, title or interest in or to the Wiley Materials or any of the intellectual property rights therein. You shall have no rights hereunder other than the license as provided for above in Section 2. No right, license or interest to any trademark, trade name, service mark or other branding ("Marks") of WILEY or its licensors is granted hereunder, and you agree that you shall not assert any such right, license or interest with respect thereto

NEITHER WILEY NOR ITS LICENSORS MAKES ANY WARRANTY OR REPRESENTATION OF ANY KIND TO YOU OR ANY THIRD PARTY, EXPRESS, IMPLIED OR STATUTORY, WITH RESPECT TO THE MATERIALS OR THE ACCURACY OF ANY INFORMATION CONTAINED IN THE MATERIALS, INCLUDING, WITHOUT LIMITATION, ANY IMPLIED WARRANTY OF MERCHANTABILITY, ACCURACY, SATISFACTORY QUALITY, FITNESS FOR A PARTICULAR PURPOSE, USABILITY, INTEGRATION OR NON-INFRINGEMENT AND ALL SUCH WARRANTIES ARE HEREBY EXCLUDED BY WILEY AND ITS LICENSORS AND WAIVED BY YOU.

WILEY shall have the right to terminate this Agreement immediately upon breach of this Agreement by you. You shall indemnify, defend and hold harmless WILEY, its Licensors and their respective directors, officers, agents and employees, from and against any actual or threatened claims, demands, causes of action or proceedings arising from any breach of this Agreement by you.

IN NO EVENT SHALL WILEY OR ITS LICENSORS BE LIABLE TO YOU OR ANY OTHER PARTY OR ANY OTHER PERSON OR ENTITY FOR ANY SPECIAL, CONSEQUENTIAL, INCIDENTAL, INDIRECT, EXEMPLARY OR PUNITIVE DAMAGES, HOWEVER CAUSED, ARISING OUT OF OR IN CONNECTION WITH THE DOWNLOADING, PROVISIONING,

VIEWING OR USE OF THE MATERIALS REGARDLESS OF THE FORM OF ACTION, WHETHER FOR BREACH OF CONTRACT, BREACH OF WARRANTY, TORT, NEGLIGENCE, INFRINGEMENT OR OTHERWISE (INCLUDING, WITHOUT LIMITATION, DAMAGES BASED ON LOSS OF PROFITS, DATA, FILES, USE, BUSINESS OPPORTUNITY OR CLAIMS OF THIRD PARTIES), AND WHETHER OR NOT THE PARTY HAS BEEN ADVISED OF THE POSSIBILITY OF SUCH DAMAGES. THIS LIMITATION SHALL APPLY NOTWITHSTANDING ANY FAILURE OF ESSENTIAL PURPOSE OF ANY LIMITED REMEDY PROVIDED HEREIN.

Should any provision of this Agreement be held by a court of competent jurisdiction to be illegal, invalid, or unenforceable, that provision shall be deemed amended to achieve as nearly as possible the same economic effect as the original provision, and the legality, validity and enforceability of the remaining provisions of this Agreement shall not be affected or impaired thereby.

The failure of either party to enforce any term or condition of this Agreement shall not constitute a waiver of either party's right to enforce each and every term and condition of this Agreement. No breach under this agreement shall be deemed waived or excused by either party unless such waiver or consent is in writing signed by the party granting such waiver or consent. The waiver by or consent of a party to a breach of any provision of this Agreement shall not operate or be construed as a waiver of or consent to any other or subsequent breach by such other party.

This Agreement may not be assigned (including by operation of law or otherwise) by you without WILEY's prior written consent.

Any fee required for this permission shall be non-refundable after thirty (30) days from receipt by the CCC.

These terms and conditions together with CCC's Billing and Payment terms and conditions (which are incorporated herein) form the entire agreement between you and WILEY concerning this licensing transaction and (in the absence of fraud) supersedes all prior agreements and representations of the parties, oral or written. This Agreement may not be amended except in writing signed by both parties. This Agreement shall be binding upon and inure to the benefit of the parties' successors, legal representatives, and authorized assigns.

In the event of any conflict between your obligations established by these terms and conditions and those established by CCC's Billing and Payment terms and conditions, these terms and conditions shall prevail.

WILEY expressly reserves all rights not specifically granted in the combination of (i) the license details provided by you and accepted in the course of this licensing transaction, (ii) these terms and conditions and (iii) CCC's Billing and Payment terms and conditions.

This Agreement will be void if the Type of Use, Format, Circulation, or Requestor Type was misrepresented during the licensing process.

This Agreement shall be governed by and construed in accordance with the laws of the State of New York, USA, without regards to such state's conflict of law rules. Any legal action, suit or proceeding arising out of or relating to these Terms and Conditions or the breach thereof shall be instituted in a court of competent jurisdiction in New York County in the State of New York in the United States of America and each party hereby consents and submits to the personal jurisdiction of such court, waives any objection to venue in such court and consents to service of process by registered or certified mail, return receipt requested, at the last known address of such party.

WILEY OPEN ACCESS TERMS AND CONDITIONS

Wiley Publishes Open Access Articles in fully Open Access Journals and in Subscription journals offering Online Open. Although most of the fully Open Access journals publish open access articles under the terms of the Creative Commons Attribution (CC BY) License only, the subscription journals and a few of the Open Access Journals offer a choice of Creative Commons Licenses. The license type is clearly identified on the article.

The Creative Commons Attribution License

The Creative Commons Attribution License (CC-BY) allows users to copy, distribute and transmit an article, adapt the article and make commercial use of the article. The CC-BY license permits commercial and non-

Creative Commons Attribution Non-Commercial License

The Creative Commons Attribution Non-Commercial (CC-BY-NC)License permits use, distribution and reproduction in any medium, provided the original work is properly cited and is not used for commercial purposes.(see below)

Creative Commons Attribution-Non-Commercial-NoDerivs License

7.2 Appendix to Chapter 2

Table 7.1: Important structural data for compound **2.2Mo**.

Formula	$C_{56}H_{66}BLiMoN_2O_6P_2$
Formula Weight (*g/mol*)	1038.73
Crystal Dimensions (*mm*)	0.108 x 0.112x 0.380
Crystal Colour and Habit	Colourless prism
Crystal System	Monoclinic
Space Group	$P2_1/n$
Temperature, K	150
a, Å	17.18(2)
b, Å	19.51(2)
c, Å	18.25(2)
α,°	90
β,°	117.88(2)
Γ,°	90
V (Å^3)	5411(11)
Z	4
F(000)	2176
ρ (*g/cm^3*)	1.275
λ, Å, (MoKα)	0.71073
μ, (*cm^{-1}*)	0.351
Max 2θ for data collection, °	52.85
Measured fraction of data	0.996
Number of reflections measured	87747
Unique reflections measured	11090
R_{merge}	0.0454
Number of reflections included in refinement	11090
Number of parameters in least-squares	759
R_1, wR_2	0.0465, 0.1076
R_1 (all data), wR_2 (all data)	0.0812, 0.1281
GOF	1.023
Min & Max peak heights on final ΔF Map (e^-Å^{-3})	-0.663, 0.631

WHERE: $R_1 = \Sigma(|F_O| - |F_C|)/\Sigma F_O$, $WR_2 = [\Sigma(W(F_O^2 - F_C^2)^2)/\Sigma(WF_O^4)]^{½}$, GOF = $[\Sigma(W(F_O^2 - F_C^2)^2)/(\text{NO. OF REFLNS. - NO. OF PARAMS.})]^{½}$

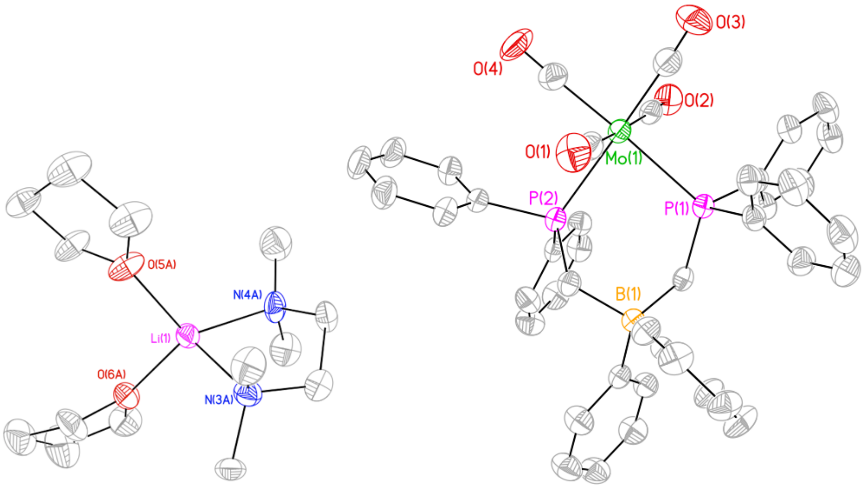

Figure 7.1: Solid State structure of **2.2Mo**. The unit cell is $P2_1/n$, monoclinic. The anion is a distorted twist boat. The cation is disordered and was given an 80:20 fit for the occupation of the highly disordered THF molecule.

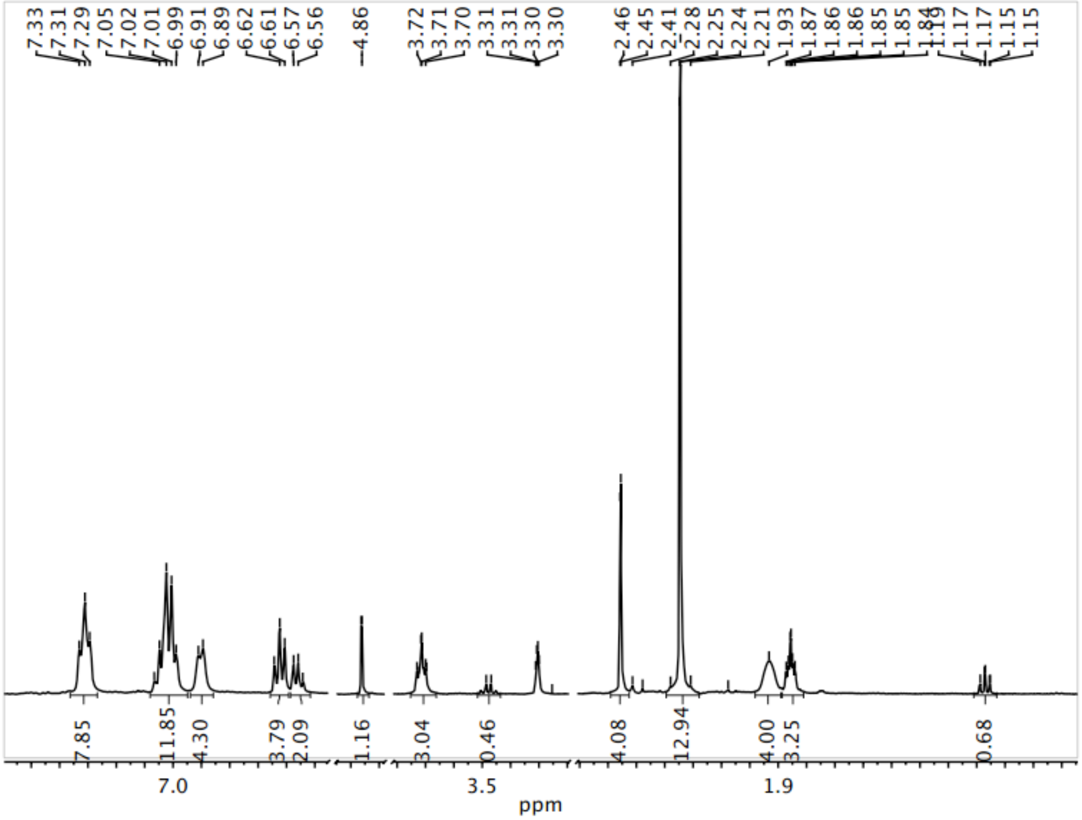

Figure 7.2: ^{1}H NMR spectrum of dissolved crystals of **2.2Mo**, This spectrum reinforces the evidence for the solid state structure that the cation is not well-defined. Based on the integration of the THF protons, there is no well-defined number of THF protons for this spectrum to match the solid state structure. As the cation is disordered in the solid state and had to be modeled as described above, it is possible that there are more components to the disorder than were selected to be fit during the structure solving process. As it is the cation, and not the anion, that exhibits the disorder, this result does not affect the onward chemistry with this compound in the context of this work.

7.3 Appendix to Chapter 3

7.3.1 Instrumentation.

Nuclear magnetic resonance (NMR) spectroscopy was conducted on a Varian INOVA 400 MHz spectrometer (^{1}H 400.09 MHz, ^{11}B{^{1}H} 128.25 MHz, ^{13}C{^{1}H} 100.53 MHz, ^{19}F{^{1}H} 376.32 MHz, ^{31}P{^{1}H} 161.82 MHz). All ^{1}H and ^{13}C{^{1}H} spectra were referenced relative to residual solvent signal. The chemical shifts for ^{19}F{^{1}H} and ^{31}P{^{1}H} spectra were referenced using external standards; α,α,α–trifluorotoluene (δ_F = -63.9 ppm) and 85% H_3PO_4 (δ = 0 ppm), respectively. FT-IR spectra were recorded using a Bruker Tensor 27 spectrometer. P K-edge X-ray absorption near edge structure (XANES) experiments were performed at the soft X-ray microcharacterization beamline (SXRMB) at the Canadian Light Source (CLS) in Saskatoon, Canada. Ge K-edge XANES experiments were performed at beamline 20-BM-B at the Advance Photon Source (APS) in Lemont, Illinois, USA. For XANES, 3 scans were used to acquire each spectrum except for the Ge K-edge of **1Ge** where only one scan was used due to evident decomposition in the post-edge features of subsequent scans, presumably from decomposition by X-ray exposure. Elemental analysis was performed at the Université de Montréal in Montreal, Canada.

7.3.2 Reagents.

The synthesis of all compounds was performed in a nitrogen filled MBraun Labmaster dp glovebox or by using standard Schlenk techniques. All solvents were purchased from Caledon, dried using an MBraun controlled atmosphere solvent purification system. Toluene, tetrahydrofuran and diethylether were stored in Straus flasks over a potassium mirror. **1GeCl**, **3Mg**, **1P** and **4P** were synthesized following literature procedures.[1–4] $GeCl_2$(dioxane) (Sigma Aldrich), 1,3-bis(diphenylphosphino)propane (dppp) (Sigma Aldrich), trimethylsilyl trifluoromethanesulfonate ($Me_3SiOSO_2CF_3$) (Alfa Aesar) were used as received.

7.3.3 X-ray Crystallography.

Single crystal diffraction studies were performed at the Western University X-ray facility. Single crystals for X-ray diffraction studies were grown by vapor diffusion or cooling of a saturated solution at -30 °C. Crystals were selected under Paratone-N oil using a MiTeGen polyimide micromount and immediately placed under a stream of cold nitrogen gas (110 K). All X-ray measurements were made on a Bruker Kappa Axis Apex II diffractometer using Mo-Kα radiation (λ = 0.71073 angstroms operating a SMART and COLLECT software. For **1Ge**, **2GeCl** and **2OTf** the unit cell dimensions were determined from a symmetry constrained fit of 8097, 9455 and 9893 reflections with 4.7° < 2q < 51.84°, 4.9° < 2q <

76.54° and 4.8° < 2q < 58.16°, respectively. The data collection strategy was a number of w and j scans which collected data up to 59.27° (2q), 80.894° (2q) and 59.152° (2q), respectively. The frame integration was performed using SAINT.[5] The resulting raw data was scaled and absorption corrected using a multi-scan averaging of symmetry equivalent data using SADABS.[6] The SHELXTL program was used to solve the structure by direct methods. Subsequent difference Fourier synthesis allowed the remaining atoms to be located while hydrogen atoms were placed in the calculated positions and allowed to ride on the parent atom. The structural model was fit to the data using full matrix least-squares based on F^2. The calculated structure factors included corrections for anomalous dispersion from the usual tabulation. The structure was refined using the SHELXL-2014 program from the SHELXTL suite of crystallographic software.[7]

7.3.4 Computational Calculations.

All of the computational investigations were performed using the **Compute Canada** *Shared Hierarchical Academic Research Computing Network* (SHARCNET) facilities (www.sharcnet.ca) with the Gaussian09 program suites.[8] Geometry optimizations have been calculated using density functional theory (DFT), specifically implementing the M062X method[9] ENREF 60 in conjunction with the TZVP basis set[10] for all atoms. The geometry optimizations were not subjected to any symmetry restrictions and each stationary point was confirmed to be a minimum having zero imaginary vibrational frequencies. Single point calculations were conducted at the same level using on models in which the heavy atom positions were those observed in the solid state structures and hydrogen atoms were placed in appropriate geometrically-calculated positions (with C-H bond lengths set to 1.07 Å) using Gaussview 3.0.[11] Population analyses were conducted using the Natural Bond Orbital 6.0 (NBO6)[12] implementation included with the Gaussian package. MO energies, Voronoi charges, and plots of molecular orbitals were obtained using the geometry optimized structures generated at the M062X/TZ2P level of theory and examined using ADF2017.[13–15] QT-AIM analyses were performed on the geometry optimized structures using the AIMAll suite of software.[16]

The geometrical features for model compounds of [LGeCl], $[(dHpe)GeCl]^{1+}$ and [LGeGeL], in which all substituents were modeled with hydrogen atoms for clarity, were fully optimized in the absence of any symmetry constraints. Both twist-boat and chair conformations for the 6-membered rings were computed and the chair conformations were determined to be the lowest energy conformations in each instance. The metrical parameters for the optimized geometries are consistent with those of the experimental observations and justify the use of the model compounds. Similar calculations were conducted on models of the related triphosphenium species [LP] and [(dHpe)P]$^{1+}$ for further comparison.

Calculations on the geometry-optimized models EL$_n$ (E = [GeCl]$^+$, n = 1, L = $(PH_2CH_2)_2BH_2$; E = [GeCl]$^+$, n = 1, L = **2**; E = [Ge-Ge]$^{2+}$, n = 2, L = **1**) were used to obtain information regarding the composition and energy of the highest occupied molecular orbital (HOMO) and the lowest unoccupied molecular orbital (LUMO) for each system. The HOMO and LUMO energies for the Kohn-Sham (K-S) orbitals are presented in Table 3.

7.3.5 Summary of Model **[LGeCl]**

```
1\1\GINC-ORC315\FOpt\RM062X\TZVP\C2H10B1Cl1Ge1P2\CMACD\03-Apr-2017\0\\
 # M062x/TZVP scf=tight opt freq pop=(full,nbo6read) test\\Optimization of ClGe(PH2CH2)2BH2
chair\\0, 1\P, -0.166403121, -0.0600554649, 0.0256046084\P, 2.2335301293, 2.343179879,-
0.0174293401\C, 1.2055856031, 2.9291650829, 1.3447784791\B, -0.3816253538, 2.5733332122,
1.0054251689\C, -0.7284762913, 0.99192732, 1.3795180125\H, 1.5629314936, 2.4363220049,
2.252105485\H, 1.3717724497, 4.0027524887, 1.4444873339\H, -0.6035808823, 2.7737138243, -
0.1858084369\H, -1.0855604459, 3.2881194241, 1.6794361553\H, -1.7997076481, 0.8261694217,
1.5025327461\H, -0.2181164212, 0.6516064828, 2.2837043741\H, -0.9336123498, 0.2792581617, -
1.1019242138\H, -0.5205080846, -1.4179790453, 0.1888442952\H, 1.8711600502, 3.0880982871, -
1.1527317776\H, 3.5934890278, 2.7030345642, 0.1130628497\Cl, 2.6851899246, -0.4795311828,
1.6947184551\Ge, 2.2428295195, -0.0751712305, -0.5022763247\\Version=EM64L-G09RevD.01\
 State=1-A\HF=-3326.9677471\RMSD=4.663e-09\RMSF=1.386e-05\Dipole=0.34774, -0.3683366, -
1.2042563\Quadrupole=-0.3668743, -0.358306, 0.7251803, 11.7340358, 0.3433675, -
0.5299165\PG=C01 [X(C2H10B1Cl1Ge1P2)]\\@
Zero-point correction=                       0.118494 (Hartree/Particle)
Thermal correction to Energy=                  0.129190
Thermal correction to Enthalpy=                0.130134
Thermal correction to Gibbs Free Energy=         0.081525
Sum of electronic and zero-point Energies=         -3326.849253
Sum of electronic and thermal Energies=            -3326.838557
Sum of electronic and thermal Enthalpies=          -3326.837613
Sum of electronic and thermal Free Energies=        -3326.886222
```

7.3.6 Summary of model **[(dppp)GeCl]$^+$**

```
1\1\GINC-ORC39\FOpt\RM062X\TZVP\C3H10Cl1Ge1P2(1+)\CMACD\11-Apr-2017\0\
 \# M062x/TZVP scf=tight opt freq pop=(full,nbo6read) test\\Optimization of ClGe(PH2CH2)2CH2
cation chair\\1, 1\P, -0.1139630876, -0.0581919461, -0.0675445852\P, 2.2339494291, 2.2892950845, -
0.1016935191\C, 1.1498676445,2.8755876895, 1.2681769886\C, -0.3305520284, 2.5232515621,
1.0813326974\C, -0.6791378409, 1.0456235351, 1.2954700983\H, 1.5417694239, 2.4292877964,
2.1844929499\H, 1.2773198472, 3.9558169272, 1.340439943\H, -0.6896184158, 2.8676615481,
0.1067242447\H, -0.8909806674, 3.0945357852, 1.8227117289\H, -1.7580083453, 0.9189361932,
1.3867578743\H, -0.2181060775, 0.6673481493, 2.2102100934\H, -0.8894698015, 0.3062488741, -
1.1848149868\H, -0.6349935931, -1.3265210893, 0.241293387\H, 1.8528860464, 3.0468126127, -
1.2257497161\H, 3.5063968518, 2.81551678, 0.1801969289\Cl, 2.5774626819, -0.374570197,
1.8252295397\Ge, 2.3940755325, -0.222696075, -0.409185797\\Version=EM64L-G09RevD.01\
```

```
State=1-A\HF=-3340.0066271\RMSD=4.174e-09\RMSF=1.082e-05\Dipole= -1.4827604, 1.4717195, -
0.8426421\Quadrupole=2.8730053, 2.9424956, -5.8155009, 3.2158851, -2.5233236,
2.3498217\PG=C01 [X(C3H10Cl1Ge1P2)]\\@
Zero-point correction=                           0.126064 (Hartree/Particle)
Thermal correction to Energy=                    0.136651
Thermal correction to Enthalpy=                  0.137596
Thermal correction to Gibbs Free Energy=         0.088873
Sum of electronic and zero-point Energies=          -3339.880563
Sum of electronic and thermal Energies=             -3339.869976
Sum of electronic and thermal Enthalpies=           -3339.869032
Sum of electronic and thermal Free Energies=        -3339.917754
```

7.3.7 Summary of model **[LGeGeL]**

```
1\1\GINC-ORC39\FOpt\RM062X\TZVP\C4H20B2Ge2P4\CMACD\11-Apr-2017\0\\# M062x/TZVP
scf=tight opt freq pop=(full,nbo6read) test\\Optimization of [Ge(PH2CH2)2BH2] dimer from xrd\\0,
1\Ge, 11.3121602114, 13.4484196096, 11.7859014368\Ge, 10.1068416684, 11.6839305642,
13.2768299701\P, 10.3628639171, 15.2350754299, 13.1529189362\P, 9.2510927616, 13.6956812788,
10.4852112203\P, 11.7709675078, 12.0430860818, 15.0271832607\P, 11.686267955, 9.9908261197,
12.4769895015\C, 9.5596530288, 16.4537869773, 12.0873413597\C, 7.8410305155, 14.3175836526,
11.4278667441\C, 12.4507800439, 10.4538261113, 15.5544022347\C, 13.4110226786,
10.3136137035, 12.9067131898\B, 8.0073201853, 15.9550144564, 11.707720318\B, 13.6789363994,
9.9795318291, 14.5203314168\H, 9.516721968, 17.4185745789, 12.5916438428\H, 10.2159219416,
16.5567352629, 11.2178430235\H, 6.9182020624, 14.1363896737, 10.8768378787\H, 7.8076428542,
13.715649322, 12.341183131\H, 12.8418388639, 10.5339846476, 16.5681213929\H, 11.5997886283,
9.7662831402, 15.574678385\H, 14.0672470143, 9.6944869259, 12.2950528352\H, 13.5920197118,
11.3586840741, 12.6371725575\H, 13.800645541, 8.7797430532, 14.6529020749\H, 11.1658555802,
12.764090838, 16.0789674307\H, 12.8744180144, 12.8780585803, 14.7483904417\H, 11.3952413852,
8.6914568804, 12.9318146272\H, 11.4845962408, 9.8240754214, 11.0888727294\H, 14.6882917988,
10.5750812896, 14.8352264246\H, 8.9873107204, 12.4652326398, 9.8435252601\H, 9.390017506,
14.5383861826, 9.3669656474\H, 11.3913935992, 15.7851624737, 13.9477687754\H, 9.4243232373,
14.8952539387, 14.1510012233\H, 7.2852883615, 16.2219682537, 12.645825305\H, 7.6857111182,
16.5546879192, 10.7033096449\\Version=EM64L-G09RevD.01\State=1-A\HF=-
5733.4573447\RMSD=8.415e-09\RMSF=1.836e-06\Dipole=-0.0978366, -0.2936577, -
0.426578\Quadrupole=-14.5300351, -1.7185057, 16.2485407, 19.9582282,-4.8256439,
13.3583284\PG=C01 [X(C4H20B2Ge2P4)]\\@
Zero-point correction=                           0.234636 (Hartree/Particle)
Thermal correction to Energy=                    0.254178
Thermal correction to Enthalpy=                  0.255122
Thermal correction to Gibbs Free Energy=         0.185673
Sum of electronic and zero-point Energies=          -5733.222708
Sum of electronic and thermal Energies=             -5733.203167
Sum of electronic and thermal Enthalpies=           -5733.202223
Sum of electronic and thermal Free Energies=        -5733.271672
```

7.3.8 Summary of model **[LP]**

```
1\1\GINC-ORC312\FOpt\RM062X\TZVP\C2H10B1P3\CMACD\26-Apr-2017\0\\# M062x/TZVP
scf=tight opt freq pop=(full,nbo6read) test\\Optimization of P(PH2CH2)2BH2 chair\\0,1\P,-
0.0121009776, -0.0074291929, 0.0940457227\P, 2.1289402408, 0.0639495118, -0.1219731029\P,
2.1793914141, 2.2097278337, 0.0484919635\C, 1.1823431754, 2.9586796555, 1.3380255942\B, -
```

```
0.4144558384, 2.6018051686, 1.0380423697\C, -0.7466646546, 1.007791143, 1.3777194455\H,
1.533697632, 2.5777004229, 2.2993203682\H, 1.3519573131, 4.0368113148, 1.2988973124\H, -
0.6605871591, 2.8210758226, -0.1425705979\H, -1.1055950611, 3.2996539666, 1.7415323131\H, -
1.8233374544, 0.8253664794, 1.3634060295\H, -0.3429844791, 0.6805553555, 2.3382533401\H, -
0.7401155495, 0.2902322872, -1.0744061913\H, -0.2645535329, -1.3871313065, 0.2343288978\H,
1.8488290133, 2.9098857161, -1.1280960973\H, 3.558654088, 2.4807251417,
0.1544280928\\Version=EM64L-G09RevD.01\State=1-A\HF=-1131.0299359\RMSD=8.705e-
09\RMSF=9.775e-06\Dipole=0.5531335, -0.5539065, -0.3396508\Quadrupole=0.2010898, 0.3653927,
-0.5664825, 10.2789332, 1.6761916, -1.8863104\PG=C01 [X(C2H10B1P3)]\\@
Zero-point correction=                           0.119018 (Hartree/Particle)
Thermal correction to Energy=                    0.127056
Thermal correction to Enthalpy=                  0.128000
Thermal correction to Gibbs Free Energy=         0.086626
Sum of electronic and zero-point Energies=       -1130.910918
Sum of electronic and thermal Energies=          -1130.902880
Sum of electronic and thermal Enthalpies=        -1130.901936
Sum of electronic and thermal Free Energies=     -1130.943310
```

7.3.9 Summary of model **[dpppP]$^+$**

```
1\1\GINC-ORC312\FOpt\RM062X\TZVP\C3H10P3(1+)\CMACD\26-Apr-2017\0\\# M062x/TZVP
scf=tight opt freq pop=(full,nbo6read) test\\Optimization of P(PH2CH2)2CH2 cat chair\\1, 1\P,
0.0417789742, -0.0037674513,0.0437517405\P, 2.1876487061, 0.005564141, -0.0699967111\P,
2.1778500262, 2.1532329154, 0.0049430557\C, 1.1037366394, 2.9170493985, 1.2789951354\C, -
0.3768013003, 2.5664581647, 1.0839364295\C, -0.7104598816, 1.0865268387, 1.3110494862\H,
1.4657019806, 2.5689111135, 2.2482003263\H, 1.2503011903, 3.997167488, 1.2253006413\H, -
0.7146111739, 2.8838991837, 0.0926468411\H, -0.9551879643, 3.1520790687, 1.798937578\H, -
1.7899036482, 0.9292695922, 1.2781413159\H, -0.3428378417, 0.7450722303, 2.2805173267\H, -
0.6740718839, 0.2871067542, -1.1361139185\H, -0.3438099473, -1.321281302, 0.3355884062\H,
1.8574899285, 2.845217865, -1.1815424043\H, 3.4965943659, 2.5568933193,
0.2650902109\\Version=EM64L-G09RevD.01\State=1-A\HF=-1144.0641605\RMSD=4.725e-
09\RMSF=4.855e-05\Dipole=-0.7754738, 0.7707902,0.1537867\Quadrupole=2.3587286, 2.5110077, -
4.8697363, 6.0277442, -1.1415339, 0.8903101\PG=C01 [X(C3H10P3)]\\@
Zero-point correction=                           0.127377 (Hartree/Particle)
Thermal correction to Energy=                    0.134995
Thermal correction to Enthalpy=                  0.135939
Thermal correction to Gibbs Free Energy=         0.095258
Sum of electronic and zero-point Energies=       -1143.936784
Sum of electronic and thermal Energies=          -1143.929165
Sum of electronic and thermal Enthalpies=        -1143.928221
Sum of electronic and thermal Free Energies=     -1143.968902
```

7.3.10 Supplemental Crystallographic Data

Table 7.2: Important structural data for compounds **3.1Ge**, **3.2GeCl$_3$**, and **3.2OTf**.

Compound	**1Ge**	**2GeCl$_3$**	**2OTf**
Formula	$C_{90}H_{84}B_2Ge_2P_4$	$C_{27}H_{27}C_{14}Ge_2P_2$	$C_{68}H_{52}F_6Ge_2O_6P_4S_2$
Formula Weight (g/mol)	1456.25	700.40	1339.05
Crystal Dimensions (mm)	0.147 x 0.137 x 0.089	0.325 x 0.315 x 0.256	0.179 x 0.157 x 0.134
Crystal Color and Habit	Yellow Prism	Colourless Prism	Colourless Prism
Crystal System	Triclinic	Monoclinic	Monoclinic
Space Group	P-1	$P2_1/n$	$P2_1/c$
Temperature (K)	110	110	110
a (Å)	12.532(3)	9.712(2)	17.730(6)
b (Å)	17.119(6)	16.596(6)	15.761(4)
c (Å)	18.328(7)	18.414(6)	21.414(6)
α (°)	87.937(11)	90	90
β (°)	71.093(10)	101.170(9)	106.819(12)
γ (°)	83.926(9)	90	90
V (Å^3)	3699(2)	2911.7(15)	5728(3)
Z	2	4	4
F(000)	1516	1404	2720
ρ (g/cm^3)	1.307	1.598	1.553
λ (Å) MoKα	0.71073	0.71073	0.71073
μ (cm^{-1})	0.946	2.558	1.397
Max 2θ for data collection (°)	25.92	38.27	29.08
Measured fraction of data	0.998	0.998	0.998
Number of reflections measured	20633	18426	16008
Number of reflections included in refinement	12370	13964	12749
Number of parameters in least-squares	883	335	703
R_1, wR_2	0.0580, 0.1275	0.0333, 0.0737	0.0301, 0.0617
R_1 (all data), wR_2 (all data)	0.1164, 0.1506	0.0538, 0.0806	0.0463, 0.0663
GOF	1.032	0.997	1.036

7.4 Appendix to Chapter 4

7.4.1 Swelling Experiments

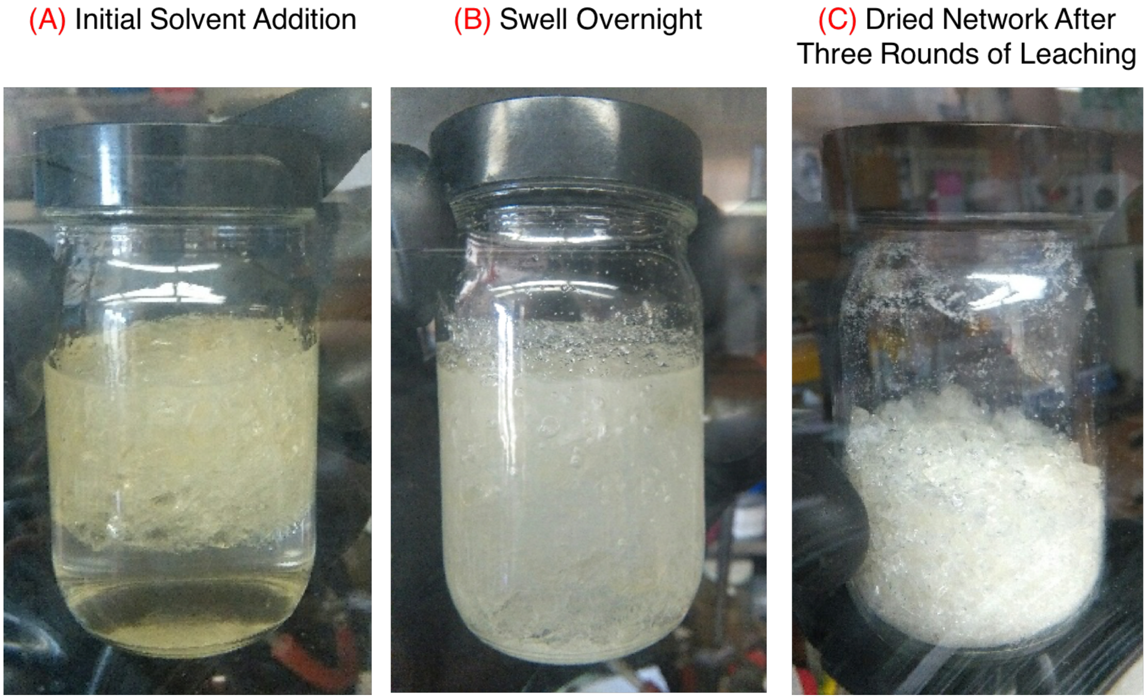

Figure 7.3: Demonstration of swellability for network **4.1** in CH_2Cl_2 during the leaching process. Notice how the slight yellow colour the crude material disappears after leaching. (A) Initial addition of CH_2Cl_2; (B) swelled overnight; (C) Dried material after three rounds of leaching.

Swelling experiments were performed in triplicate on ca. 100 mg samples of **4.1c**, **4.1(Sb)$_{0.5}$** and **4.1Sb**. The samples were vacuum dried overnight *in vacuo* at 95 °C and weighed (m_1). The samples were swelled in solvent overnight and the solvent decanted three times and weighed (m_2). They were dried *in vacuo* for four nights at 80 °C and weighed (m_3). Sb-containing samples were kept in the dark for the entire process.

Equation 7.1: Equation to determine % swelling.

$$\%\ \text{Swelling} = \left(\frac{m_2}{m_1} \times 100\%\right) - 100$$

Equation 7.2: Equation to determine swelling (mL/g). Note: $\rho_{solvent}$ = solvent density.

$$\text{Swelling} = \left(\frac{\left(m_2 / \rho_{solvent}\right)}{m_1}\right)$$

$$\text{Units} = \frac{\left(g / \frac{g}{mL}\right)}{g}$$

$$\text{Units} = \left(\frac{mL}{g}\right)$$

Equation 7.3: Equation to determine swelling (mol/g). Note: $MW_{solvent}$ = $\boxed{\boldsymbol{MW_{solvent}} =}$ solvent molecular weight.

$$\text{Swelling} = \left(\frac{\left(m_2 / MW_{solvent}\right)}{m_1}\right)$$

$$\text{Units} = \frac{\left(g / \frac{g}{mol}\right)}{g}$$

$$\text{Units} = \left(\frac{mol}{g}\right)$$

Equation 7.4: Equation to determine gel content.

$$\text{Gel \%} = \frac{m_3}{m_1} \times 100\%$$

Table 7.3: Swelling and Gel content data for **4.1** different solvents.

Solvent	Swell % by mass	Swelling (mL/g)	Swelling (mol/g)	Gel Content (%)
CH_2Cl_2	205.5 ± 13.9	2.30 ± 0.10	$3.60 \times 10^{-2} \pm 1.6 \times 10^{-3}$	73.5 ± 3.2
Toluene	81.9 ± 3.5	2.10 ± 0.04	$1.97 \times 10^{-2} \pm 4 \times 10^{-3}$	78.8 ± 1.8
THF	88.2 ± 3.7	2.12 ± 0.04	$2.61 \times 10^{-2} \pm 5 \times 10^{-4}$	78.6 ± 5.2
MeCN	47.9 ± 8.1	1.88 ± 0.10	$3.60 \times 10^{-2} \pm 2.0 \times 10^{-3}$	82.5 ± 2.3
H_2O	10.0 ± 1.6	1.12 ± 0.05	$6.24 \times 10^{-2} \pm 2.8 \times 10^{-3}$	96.8 ± 0.7
Et_2O	24.8 ± 5.2	1.75 ± 0.07	$1.68 \times 10^{-2} \pm 7 \times 10^{-4}$	90.9 ± 2.8
Pentane	15.8 ± 1.0	1.85 ± 0.02	$1.60 \times 10^{-2} \pm 1 \times 10^{-4}$	97.8 ± 1.4

Table 7.4: Swelling data for **4.1(Sb)$_{0.5}$** in different solvents.

Solvent	Swell % by mass	Swelling (mL/g)	Swelling (mol/g)
MeCN	86.0 ± 3.1	3.01 ± 0.05	$5.77\text{x}10^{-2} \pm 1.0\text{x}10^{-3}$
CH_2Cl_2	148.0 ± 8.5	1.40 ± 0.05	$2.20\text{x}10^{-2} \pm 8\text{x}10^{-4}$
THF	65.3 ± 6.1	2.09 ± 0.08	$2.58\text{x}10^{-2} \pm 1.0\text{x}10^{-3}$
Toluene	44.2 ± 7.0	1.92 ± 0.09	$1.80\text{x}10^{-2} \pm 9\text{x}10^{-4}$
Et_2O	34.8 ± 4.0	2.65 ± 0.08	$2.55\text{x}10^{-2} \pm 8\text{x}10^{-4}$
Pentane	24.0 ± 5.9	3.16 ± 0.15	$2.74\text{x}10^{-2} \pm 1.3\text{x}10^{-3}$

Table 7.5: Swelling data for **4.1Sb** in different solvents.

Solvent	Swell % by mass	Swelling (mL/g)	Swelling (mol/g)
MeCN	113.7 ± 6.5	3.46 ± 0.10	$2.95\text{x}10^{-2} \pm 9\text{x}10^{-4}$
CH_2Cl_2	97.4 ± 5.9	1.12 ± 0.03	$1.61\text{x}10^{-2} \pm 5\text{x}10^{-4}$
THF	56.5 ± 6.9	1.98 ± 0.09	$1.91\text{x}10^{-2} \pm 8\text{x}10^{-4}$
Toluene	31.1 ± 5.4	1.74 ± 0.07	$1.64\text{x}10^{-2} \pm 7\text{x}10^{-4}$
Pentane	12.6 ± 5.4	2.87 ± 0.14	$1.95\text{x}10^{-2} \pm 9\text{x}10^{-4}$
Et_2O	23.9 ± 3.0	2.44 ± 0.06	$1.89\text{x}10^{-2} \pm 4\text{x}10^{-4}$

7.4.2 XANES Spectra

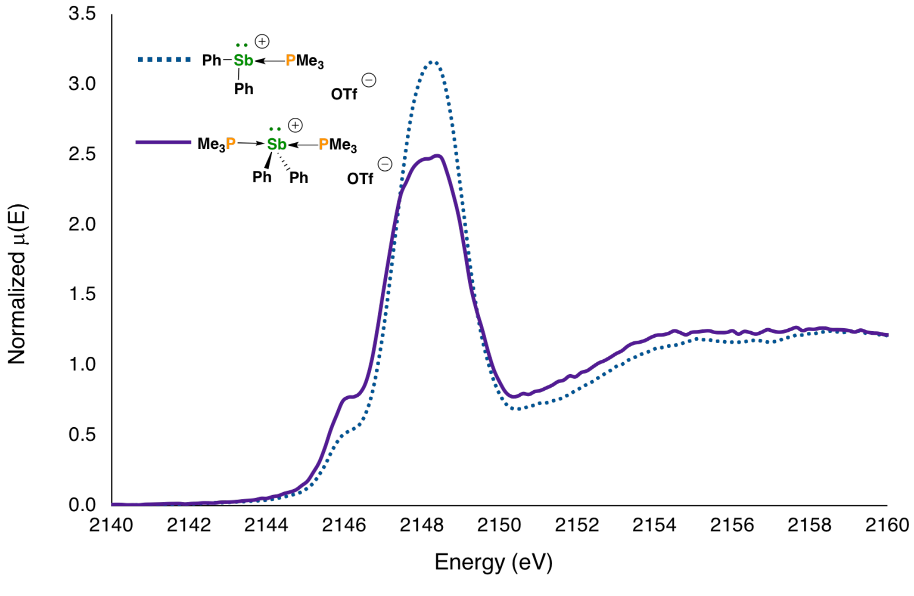

Figure 7.4: P K-edge XANES spectra of $[Ph_2Sb(PMe_3)_2][OTf]$ and $[Ph_2Sb(PMe_3)][OTf]$. The shoulder at low energy is attributed to adventitious PMe_3.

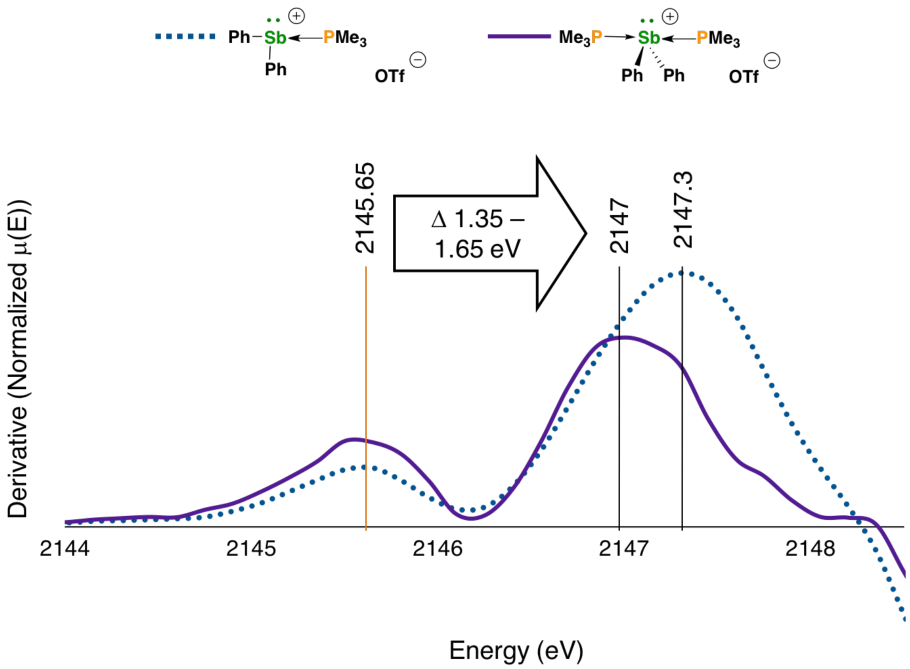

Figure 7.5: First derivative P K-edge XANES spectra of [$Ph_2Sb(PMe_3)_2$][OTf] and [$Ph_2Sb(PMe_3)$][OTf]. These signals from adventitious PMe_3 in each spectrum provide an internal standard with which to compare the coordination compounds.

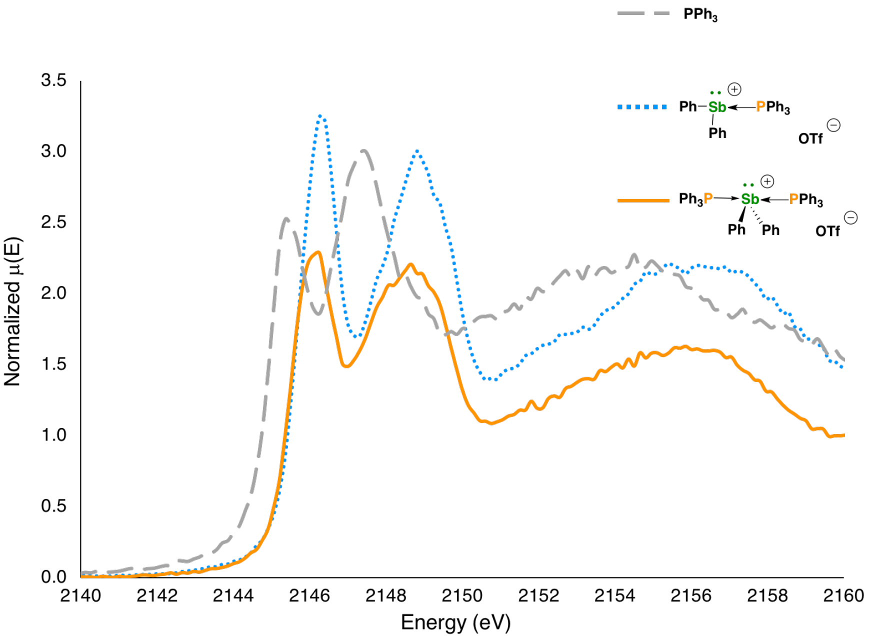

Figure 7.6: P K-edge XANES spectra of PPh_3, [$Ph_2Sb(PPh_3)_2$][OTf] and [$Ph_2Sb(PPh_3)$][OTf].

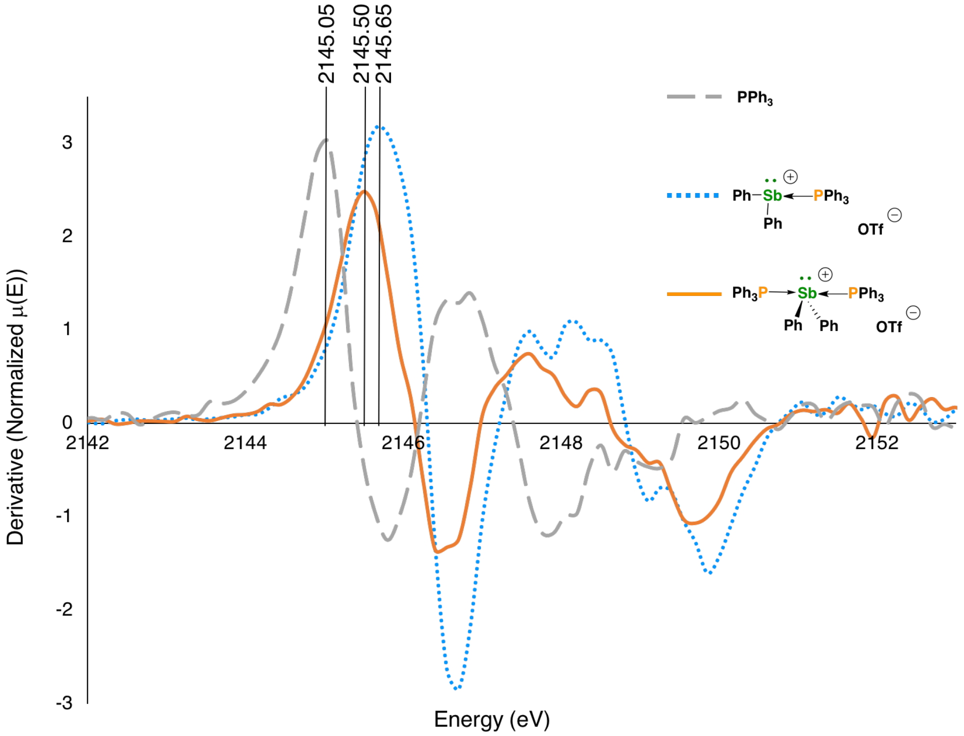

Figure 7.7: First derivative P K-edge XANES spectra of PPh_3, $[Ph_2Sb(PPh_3)_2][OTf]$ and $[Ph_2Sb(PPh_3)][OTf]$. These residual signals provide an internal standard with which to compare the coordination compounds.

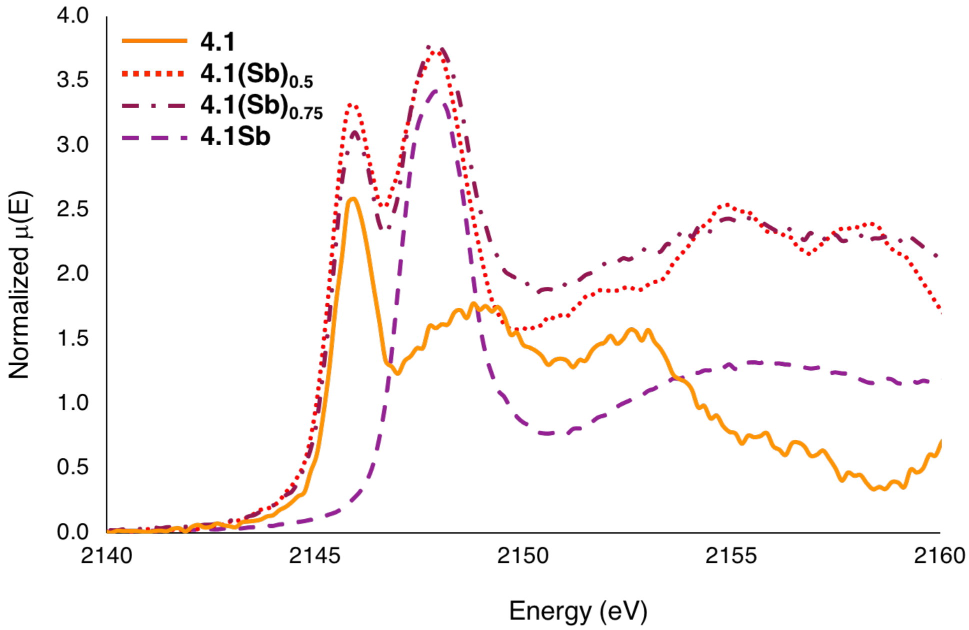

Figure 7.8: P K-edge XANES spectra for **4.1**, **4.1(Sb)$_{0.5}$**, **4.1(Sb)$_{0.75}$** and **4.1Sb**.

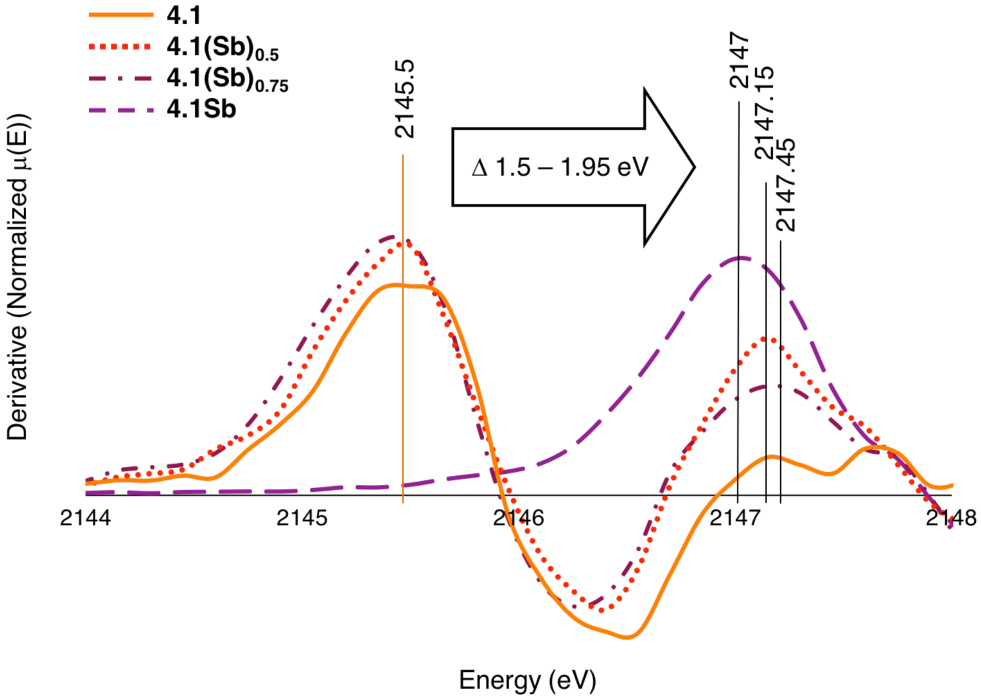

Figure 7.9: First derivative P K-edge XANES spectra for **4.1**, **4.1(Sb)$_{0.5}$**, **4.1(Sb)$_{0.75}$** and **4.1Sb**. The ^{31}P{^{1}H} NMR spectra for **4.1(Sb)$_{0.5}$** and **4.1(Sb)$_{0.75}$** reveal that they contain a small amount of unreacted **4.1**. This is also apparent in the XANES spectra, which exhibit two edges. The first edge at 2145.50 eV corresponds to **4.1**.

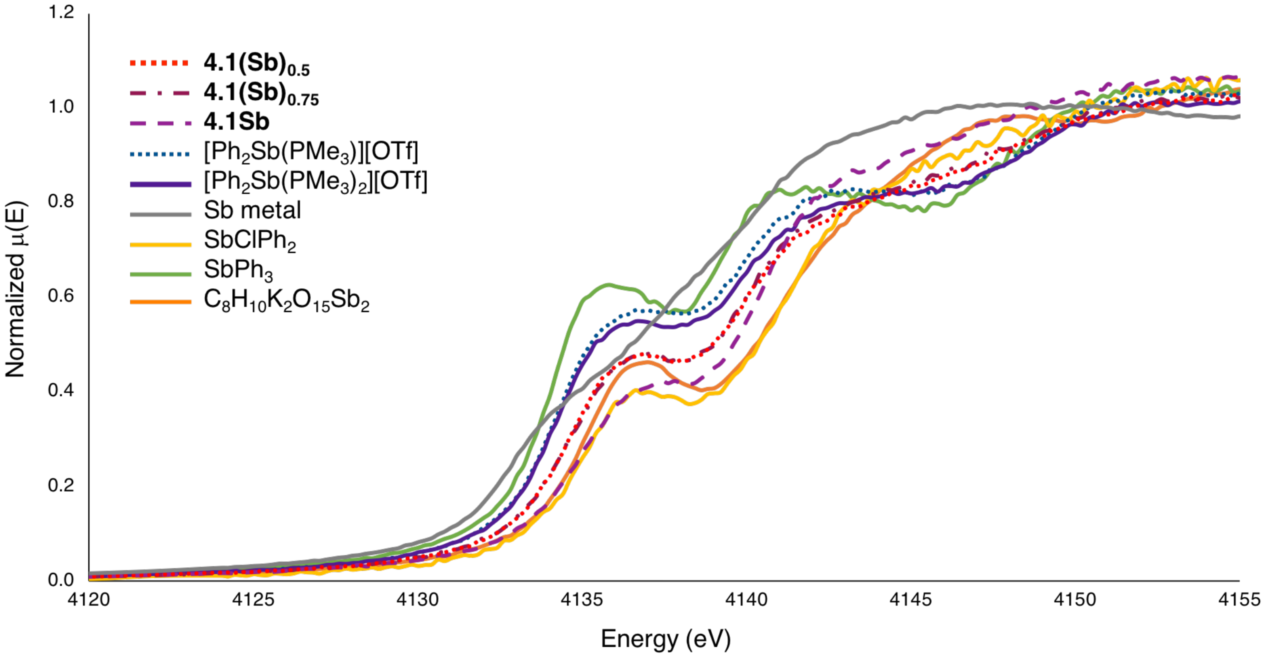

Figure 7.10: Sb L$_3$-edge XANES spectra.

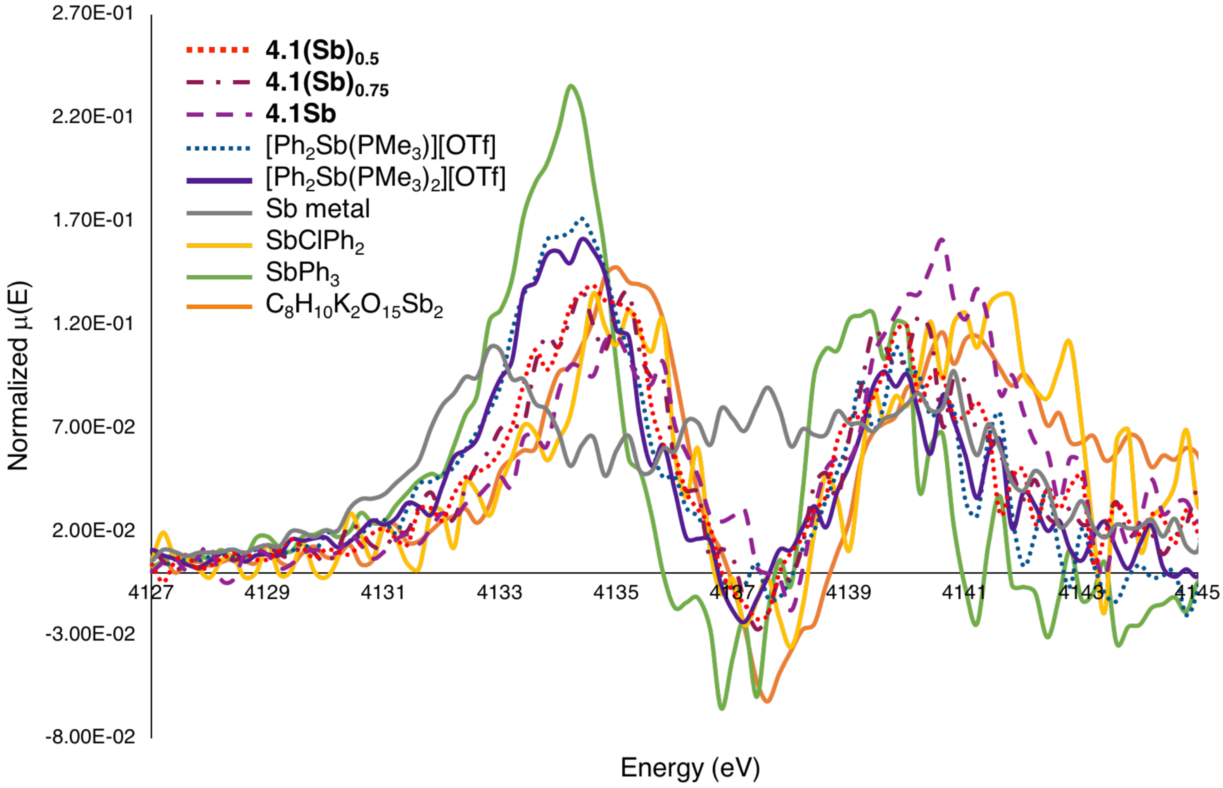

Figure 7.11: First derivative Sb L_3-edge XANES spectra.

7.4.3 XPS Data

Table 7.6: Summarized XPS data for atomic % of char derived from polymer networks **4.1(Sb)$_{0.5}$**, **4.1(Sb)$_{0.75}$** and **4.1Sb**.

	Atomic %		
Photoelectron Peaks	**Ceramics 4.1(Sb)$_{0.5}$**	**Ceramics 4.1(Sb)$_{0.75}$**	**Ceramics 4.1Sb**
Sb 3d3/2	1.3	2.3	2.6
O 1s	7.1	10.1	7.7
N 1s	4.6	3.6	4.3
C 1s	86.1	83.0	84.9
P 2p	1.0	0.7	0.4

Table 7.7: Summarized XPS data for the oxidation states of Sb, C and P of char derived from polymer networks **4.1(Sb)$_{0.5}$**, **4.1(Sb)$_{0.75}$** and **4.1Sb**.

		% Area		
Element	*Photoelectron Peaks*	**Ceramics 4.1(Sb)$_{0.5}$**	**Ceramics 4.1(Sb)$_{0.75}$**	**Ceramics 4.1Sb**
Sb	*3d3/2* Sb_2O_3	0.0	0.0	0.0
	3d3/2 Sb(0)	0.0	0.0	0.0
	3d5/2 Sb_2O_3	88.8	93.8	89.7
	3d5/2 Sb(0)	11.2	6.2	10.3
C	π-π*	0.0	0.0	0.0
	O-C=O	2.3	3.6	2.3
	C=O	2.9	2.5	3.4
	C-OH, C-O-	9.3	13.3	10.3
	C-C, C-H	34.4	42.2	47.9
	C=C	51.1	38.4	36.2
P	*2p1/2 Phosphate*	0.0	0.0	0.0
	2p3/2 Phosphate	100.0	100.0	100.0

Table 7.8: Summarized XPS data for atomic % of ceramics derived from **4.1AlMe$_3$** by pyrolysis at 800, 900 and 1000 °C for 3 or 4 hours.

	Atomic %					
	800°C		**900°C**		**1000°C**	
Photoelectron Peaks	**3 h**	**4 h**	**3 h**	**4 h**	**3 h**	**4 h**
Al 2p	18.3	18.7	8.0	20.3	20.3	20.8
O 1s	37.0	39.5	16.4	41.4	37.6	36.7
N 1s	3.6	2.4	2.8	1.2	1.7	2.9
C 1s	39.6	37.9	72.4	36.2	40.0	39.4
P 2p	0.9	1.3	0.4	0.8	0.2	0.1
Cl 2p	0.6	0.2	-	-	0.1	-

Table 7.9: Summarized XPS data for the oxidation states of Al, C and P of ceramics derived from **4.1AlMe$_3$** by pyrolysis at 800, 900 and 1000 °C for 3 hours.

		% Area					
		800°		**900°C**		**1000°C**	
Element	*Photoelectron Peaks*	**3 h**	**4 h**	**3 h**	**4 h**	**3 h**	**4 h**
Al	*2p – Al(III)*	100.0	100.0	100.0	100.0	100.0	100.0
C	*π-π**	0.0	0.0	0.0	0.0	0.0	0.0
	O-C=O	4.3	4.0	2.9	4.4	3.8	3.5
	C=O	5.3	4.8	4.0	4.5	4.5	4.0
	C-OH, C-O-C	14.8	13.4	11.5	12.5	11.8	11.2
	C-C, C-H	63.5	60.5	32.5	51.6	38.7	39.8
	C=C	12.0	17.3	49.1	27.1	41.2	41.4
P	*2p1/2 Phosphate*	0.0	0.0	0.0	0.0	0.0	0.0
	2p3/2 Phosphate	100.0	100.0	100.0	100.0	100.0	100.0

Table 7.10: Summarized XPS data for atomic % of ceramics derived from **4.1CpCoCO** by pyrolysis at 800, 900 and 1000 °C for 3 or 4 hours. Optimized amount of P and Co seems to be 800°C for 4 hours.

	Atomic %					
	800°C		**900°C**		**1000°C**	
Photoelectron Peaks	**3 h**	**4 h**	**3 h**	**4 h**	**3 h**	**4 h**
Co	2.0	2.5	2.7	2.4	2.3	1.7
O 1s	12.3	12.9	10.4	10.1	10.2	8.8
N 1s	1.7	1.8	1.3	1.3	0.7	1.0
C 1s	80.7	79.1	82.9	83.4	84.4	86.3
P 2p	2.9	3.0	2.8	2.8	2.3	2.2
Si 2s	0.4	0.7	-	-	-	-

Table 7.11: Summarized XPS data for the oxidation states of Sb, C and P of ceramics derived from **4.1CpCoCO** by pyrolysis at 800, 900 and 1000 °C for 3 hours.

		% Area					
		800°		**900°C**		**1000°C**	
Element	*Photoelectron Peaks*	**3 h**	**4 h**	**3 h**	**4 h**	**3 h**	**4 h**
Co	*$Co_3(PO_4)_2$ - 2*	47.9	49.1	47.3	48.0	47.6	47.3
	CoP – 3	0.8	0.6	0.9	0.8	0.9	0.9
	$Co_3(PO_4)_2$ - 3	28.8	29.6	28.5	28.9	28.6	28.5
	$Co_3(PO_4)_2$ - 1	14.9	15.3	14.7	14.9	14.8	14.7
	CoP – 2	0.6	0.4	0.7	0.6	0.6	0.7
	CoP – 1	7.0	5.1	7.9	6.9	7.5	8.0
	$Co_3(PO_4)_2$ - total	91.6	94.0	90.5	91.8	91.0	90.5
	CoP - total	8.4	6.1	9.5	8.3	9.0	9.6
C	*π-π**	0.0	0.0	0.0	0.0	0.0	0.0
	O-C=O	3.9	3.4	3.7	4.1	3.6	4.0
	C=O	4.9	4.6	4.2	4.1	3.8	3.6
	C-OH, C-O-C	14.0	13.7	12.3	12.3	11.4	11.5
	C-C, C-H	38.3	40.6	29.4	29.1	22.6	21.1
	C=C	38.9	37.7	50.4	50.4	58.6	59.8
P	*2p1/2 Phosphate*	0.0	0.0	0.0	0.0	0.0	0.0
	2p3/2 Phosphate	38.9	47.3	40.2	45.1	43.3	42.7
	2p1/2 Intermediate	0.0	0.0	0.0	0.0	0.0	0.0
	2p3/2 Intermediate	33.9	27.2	25.4	21.6	19.9	19.4
	2p1/2 Phosphide	0.0	0.0	0.0	0.0	0.0	0.0
	2p3/2 Phosphide	27.2	25.5	34.4	33.2	36.8	38.0
	Phosphate total	38.9	47.3	40.2	45.1	43.3	42.7
	Intermediate total	33.9	27.2	25.4	21.6	19.9	19.4
	Phosphide total	27.2	25.5	34.4	33.2	36.8	38.0

Table 7.12: Summarized XPS data for atomic % of ceramics derived from **4.2CpCoCO** by pyrolysis at 800 °C 4 hours.

Photoelectron Peaks	*Atomic %*
Co 2p	6.9
O 1s	14.5
N 1s	3.0
C 1s	68.5
P 2p	6.7
Zn 2p 3/2	0.4

Table 7.13: Summarized XPS data for the oxidation states of Sb, C and P of ceramics derived from **4.2CpCoCO** by pyrolysis at 800 °C for 4 hours.

Element	*Photoelectron Peaks*	*Area %*
Co	*$Co_3(PO_4)_2$ - 2*	38.7
	CoP – 3	2.5
	$Co_3(PO_4)_2$ - 3	23.3
	$Co_3(PO_4)_2$ - 1	12.0
	CoP – 2	1.8
	CoP – 1	21.6
	$Co_3(PO_4)_2$ - total	74.0
	CoP - total	25.9
C	π-π*	0.0
	O-C=O	4.2
	C=O	4.9
	C-OH, C-O-C	10.0
	C-C, C-H	21.8
	C=C	59.3
P	*2p1/2 Phosphate*	0.0
	2p3/2 Phosphate	35.3
	2p1/2 Intermediate	0.0
	2p3/2 Intermediate	10.2
	2p1/2 Phosphide	0.0
	2p3/2 Phosphide	54.5
	Phosphate total	35.3
	Intermediate total	10.2
	Phosphide total	54.5

7.4.4 SEM Images

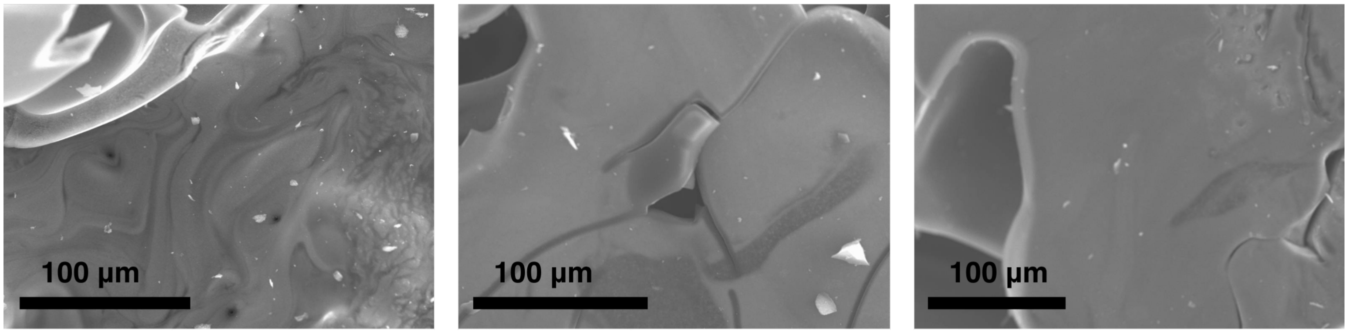

Figure 7.12: SEM images of ceramics derived from **4.1(Sb)$_{0.75}$**. Char formed at 800 °C for 4 hours.

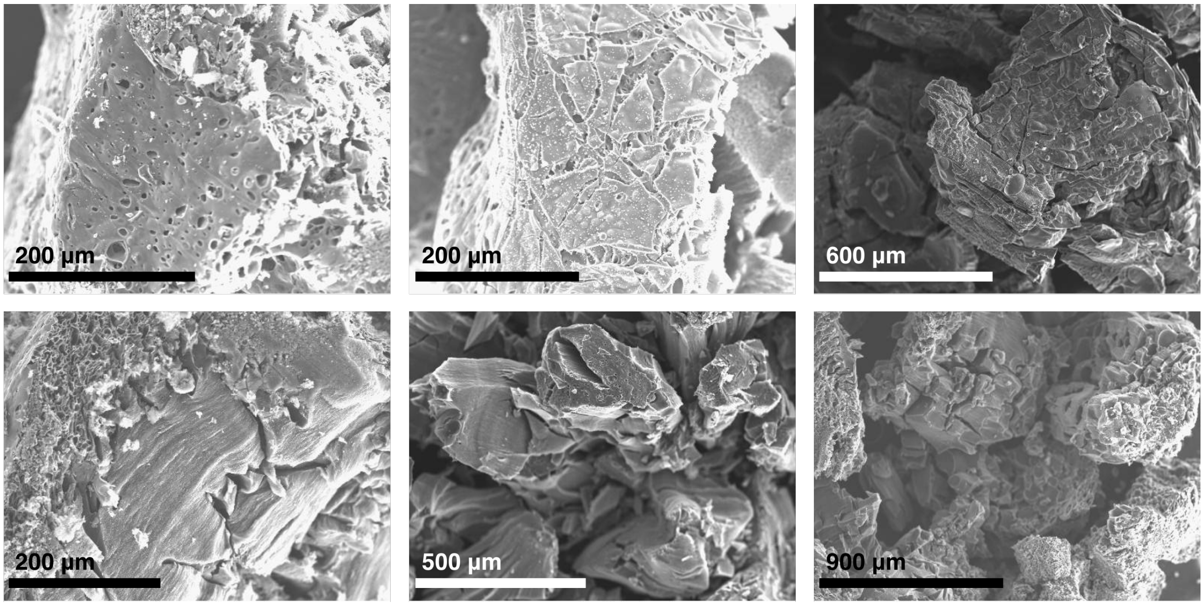

Figure 7.13: SEM images of ceramics derived from **4.1AlMe$_3$**. Char formed at 800, 900 and 1000 °C (left to right); char pyrolyzed for 3 hours (top); char pyrolyzed for 4 hours (bottom).

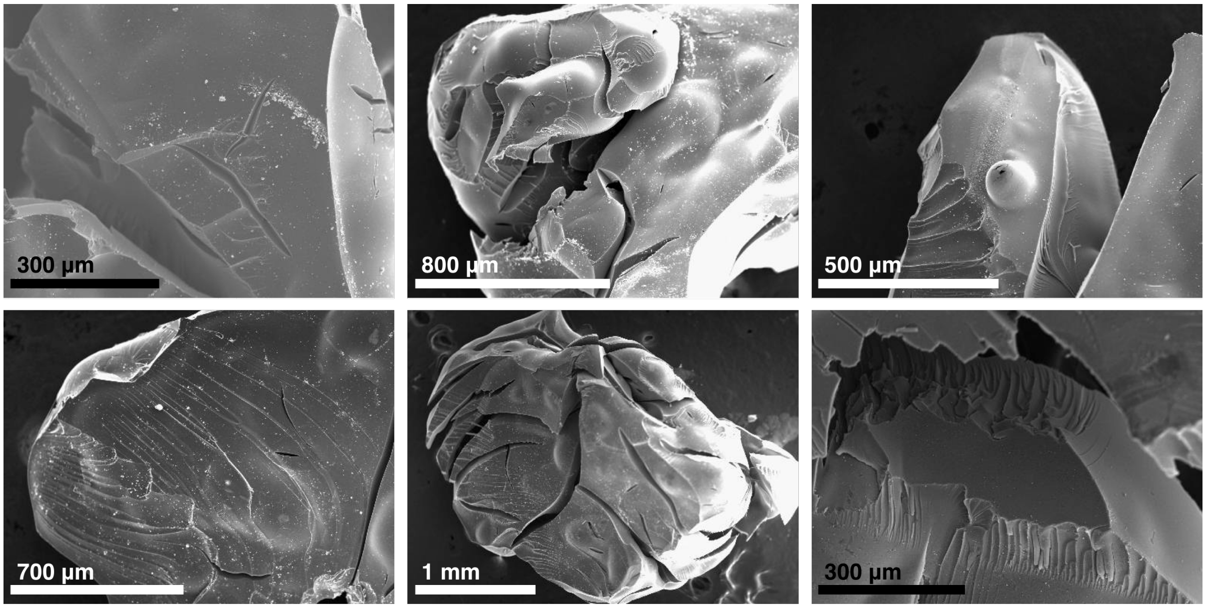

Figure 7.14: SEM images of ceramics derived from **4.1CpCoCO**. Char formed at 800, 900 and 1000 °C (left to right); char pyrolyzed for 3 hours (top); char pyrolyzed for 4 hours (bottom).

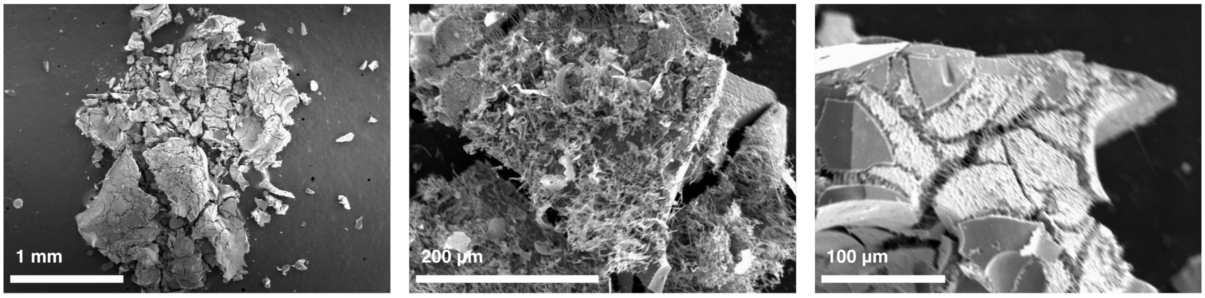

Figure 7.15: SEM images of ceramics derived from **4.2CpCoCO**. Char formed at 800 °C for 4 hours.

7.4.5 PXRD Data

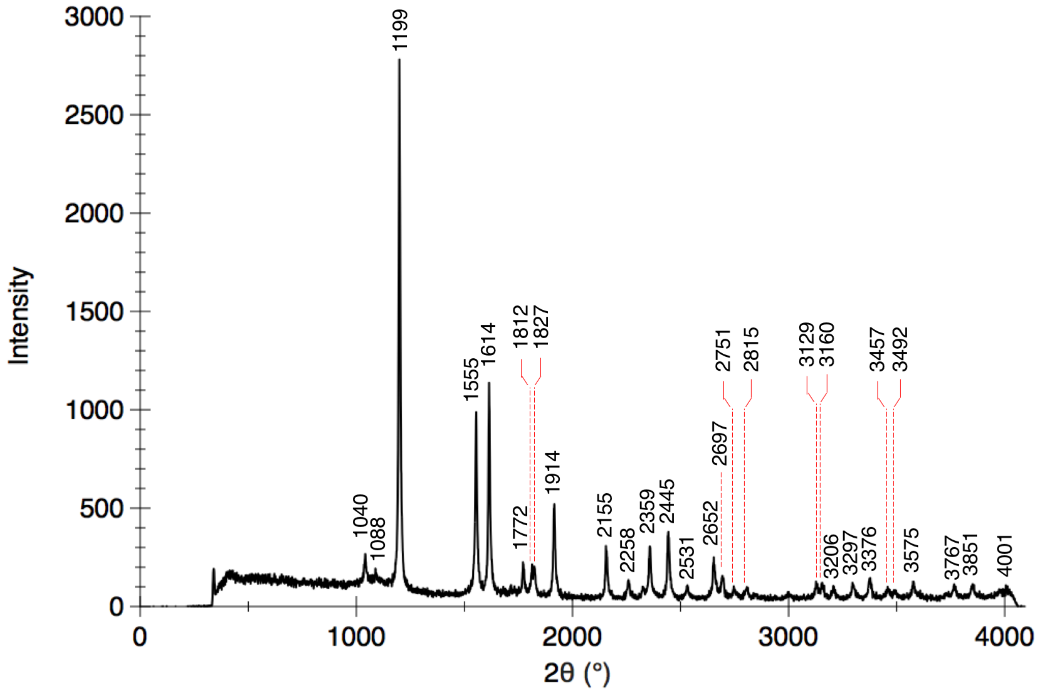

Figure 7.16: XRD data **for 4.1(Sb)$_{0.5}$** pyrolyzed at 800 °C for 4 h. Matches with powder pattern for Sb metal.[17]

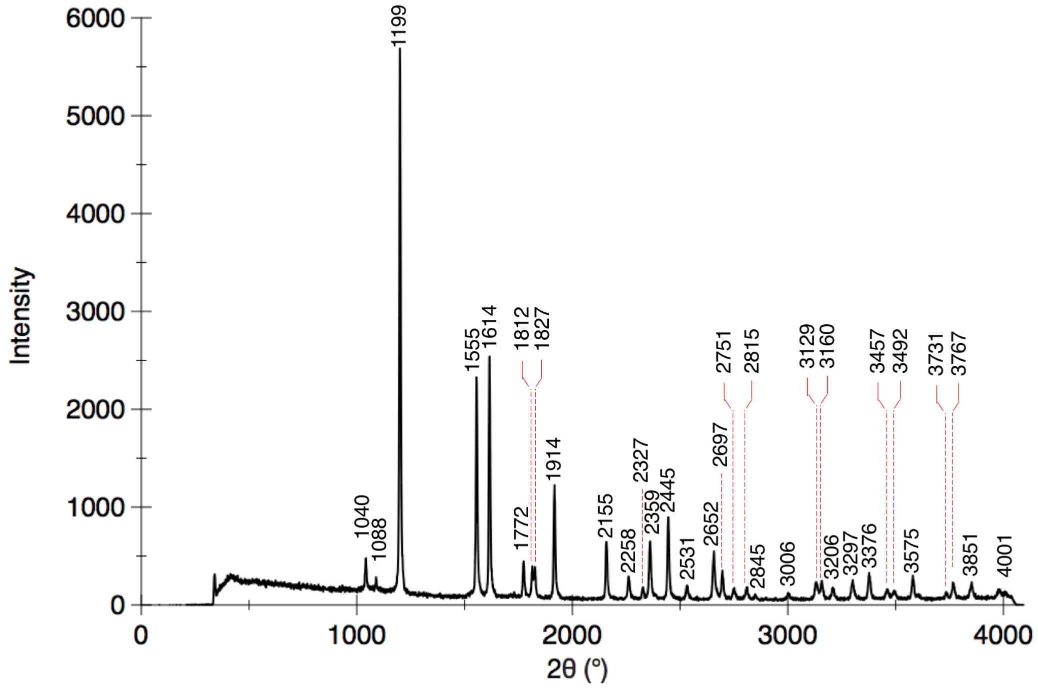

Figure 7.17: XRD data for **4.1(Sb)$_{0.75}$** pyrolyzed at 800 °C for 4 h. Matches with powder pattern for Sb metal.[17]

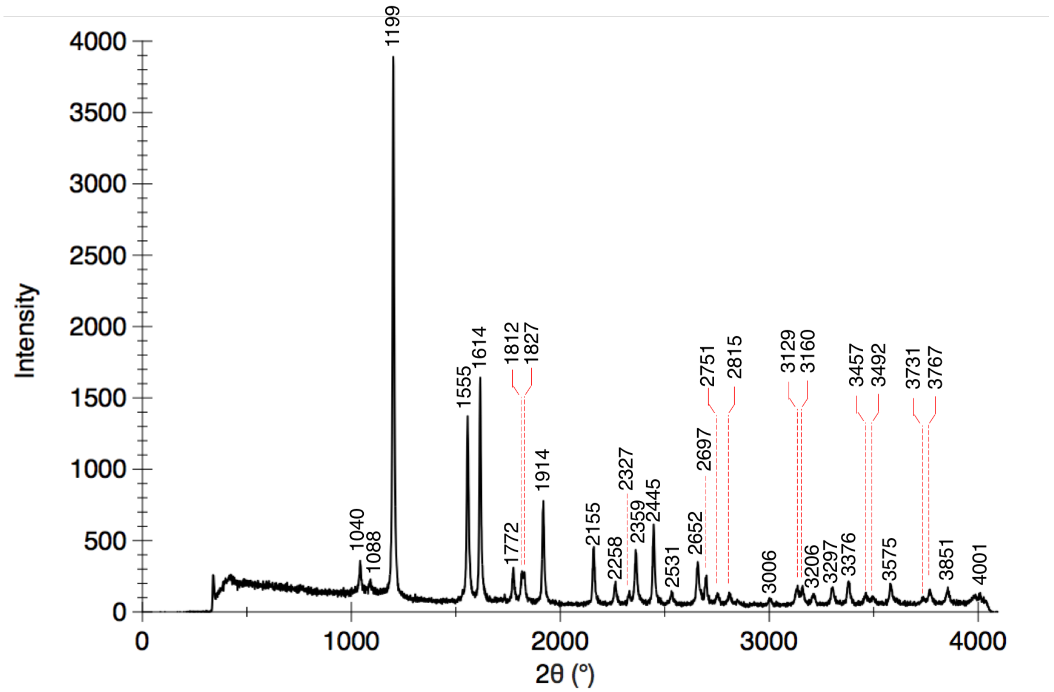

Figure 7.18: XRD data for **4.1Sb** pyrolyzed at 800 °C for 4 h. Matches with powder pattern for Sb metal.[17]

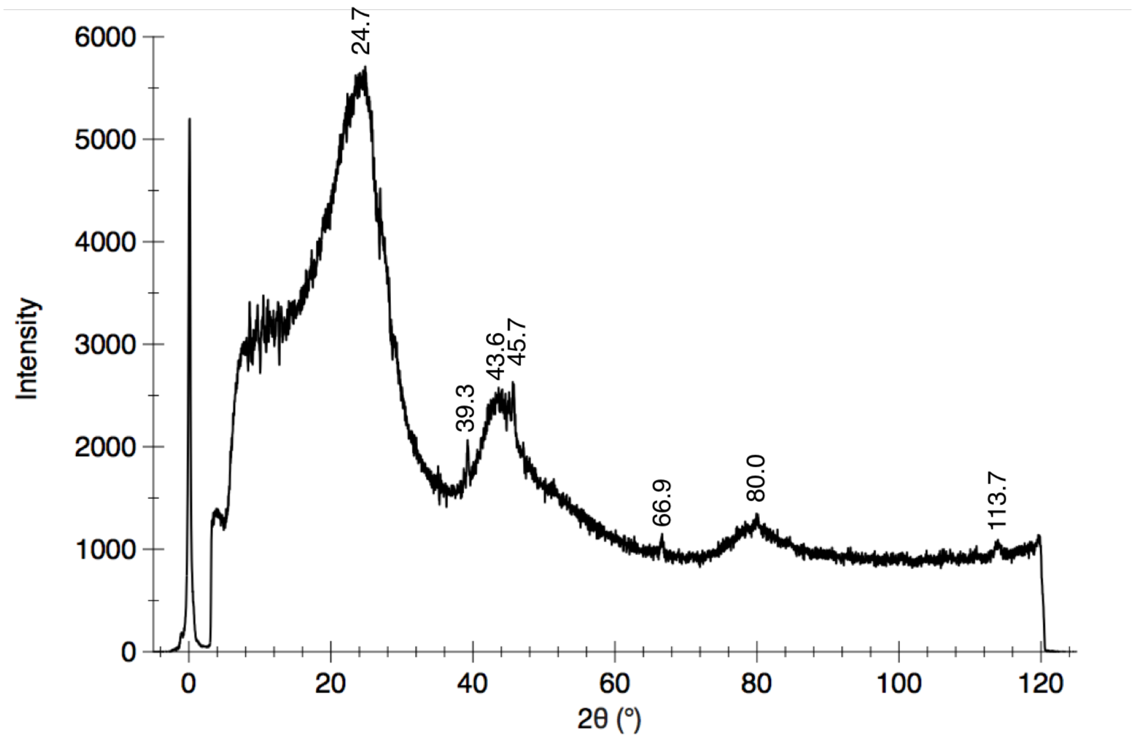

Figure 7.19: Low angle PXRD data for **4.1** pyrolyzed at 800 °C for 4 hours.

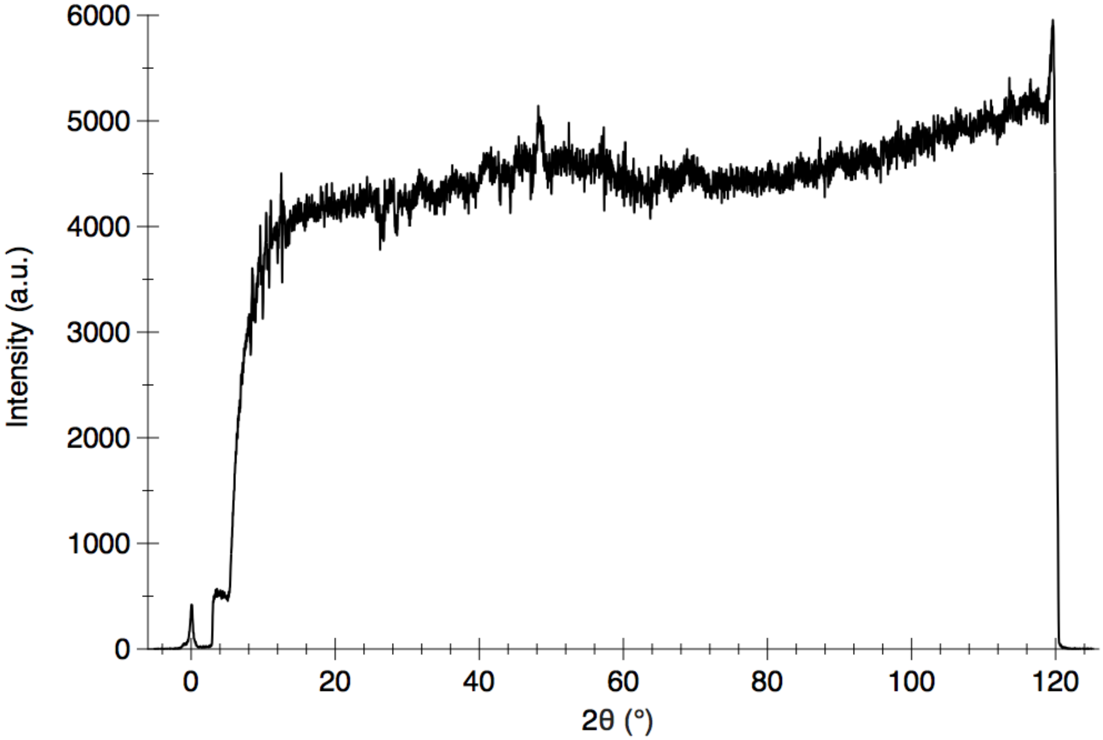

Figure 7.20: XRD diffractogram for **4.1AlMe$_3$** pyrolyzed at 800 °C for 3 h.

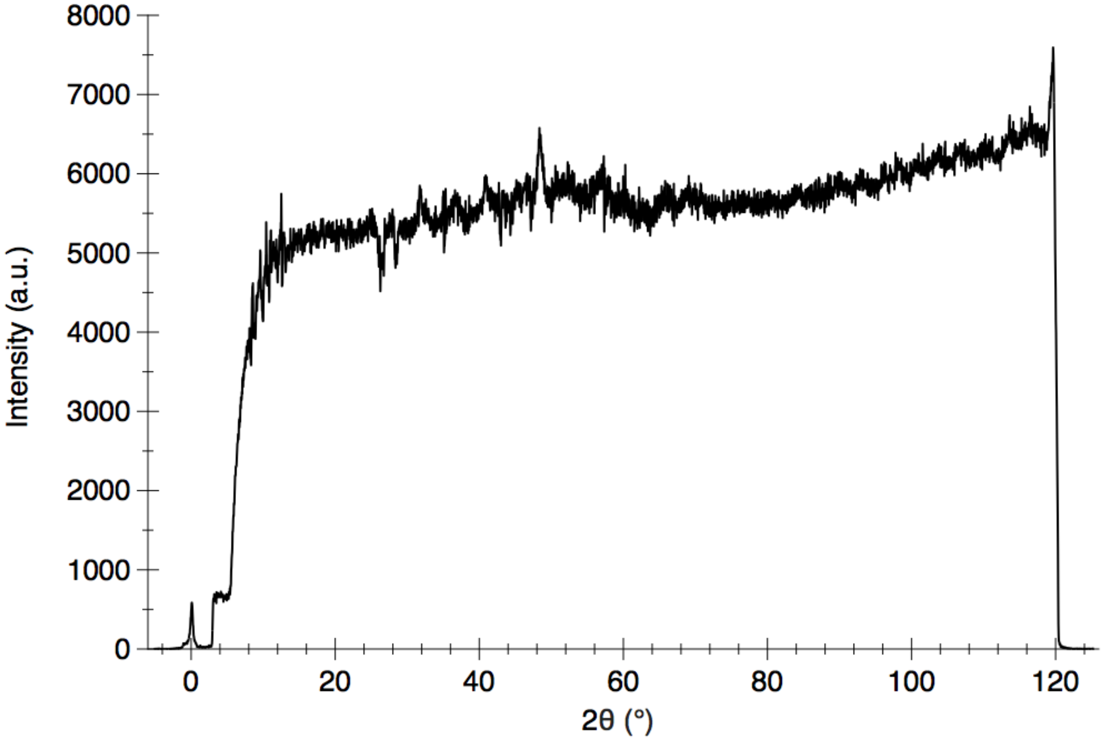

Figure 7.21: XRD diffractogram for **4.1AlMe$_3$** pyrolyzed at 900 °C for 3 h.

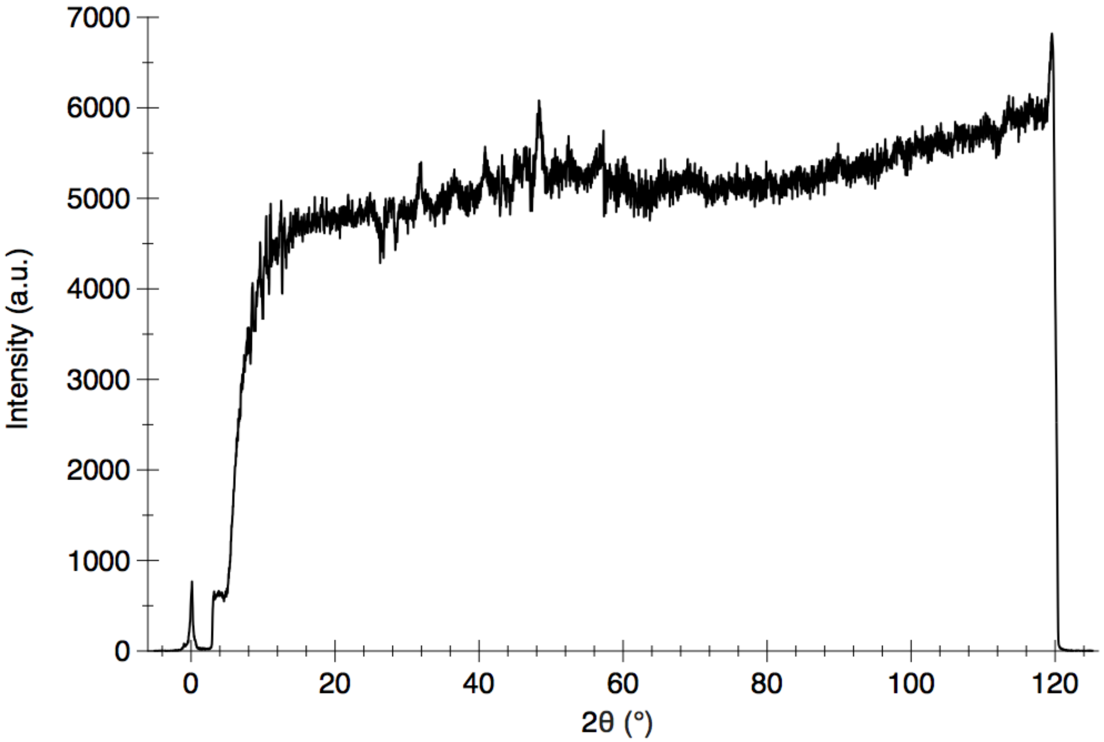

Figure 7.22: XRD diffractogram for **4.1AlMe$_3$** pyrolyzed at 1000 °C for 3 h.

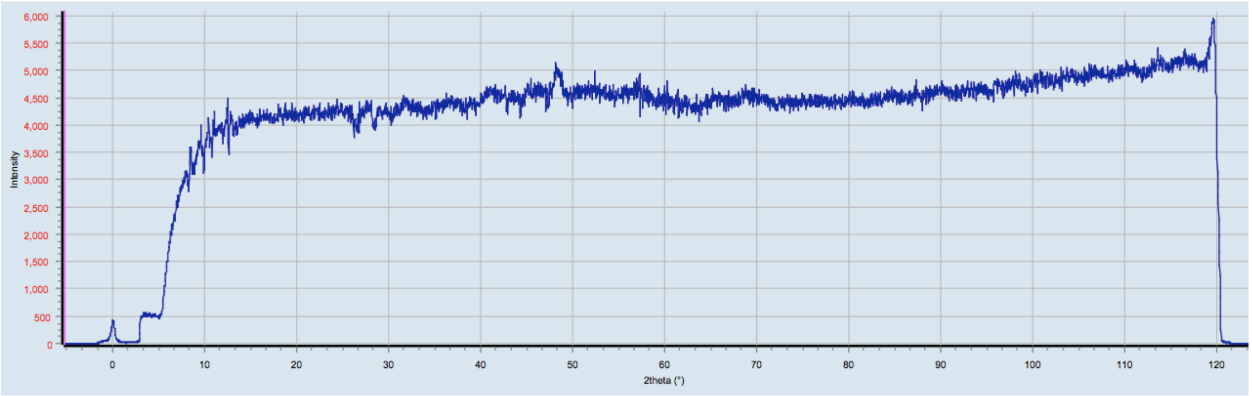

Figure 7.23: XRD diffractogram for **4.1AlMe$_3$** pyrolyzed at 800 °C for 4 h.

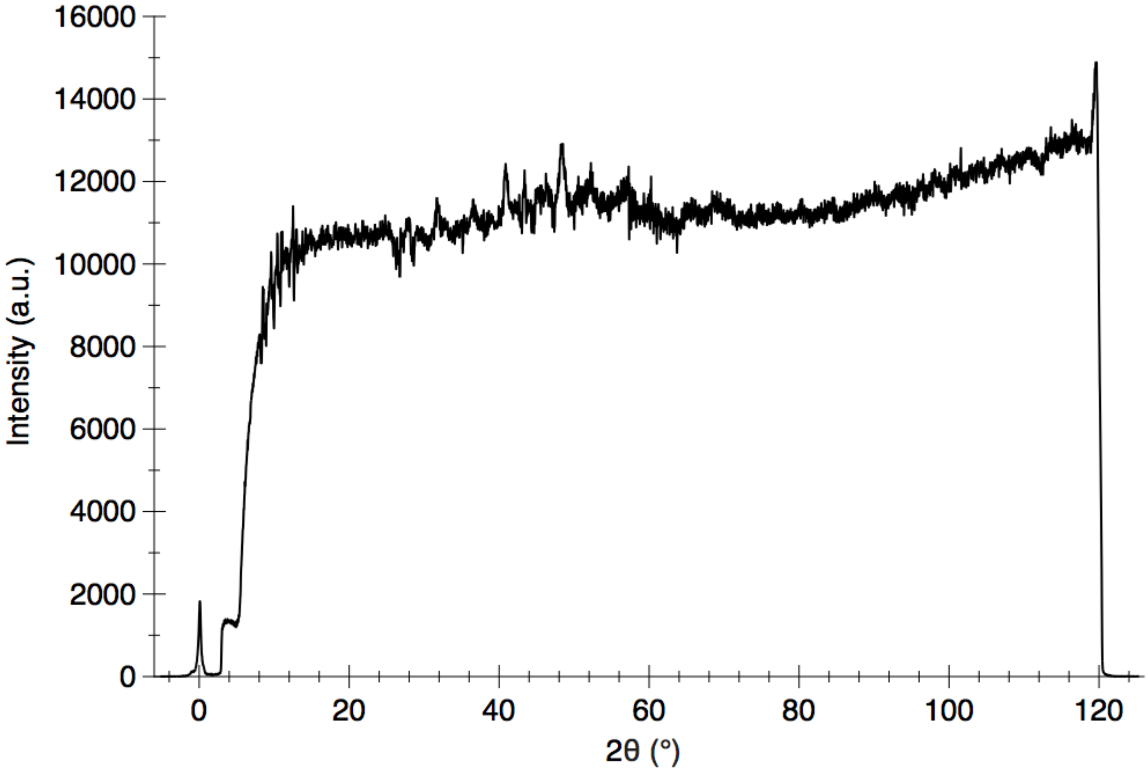

Figure 7.24: XRD diffractogram for **4.1AlMe$_3$** pyrolyzed at 900 °C for 4 h.

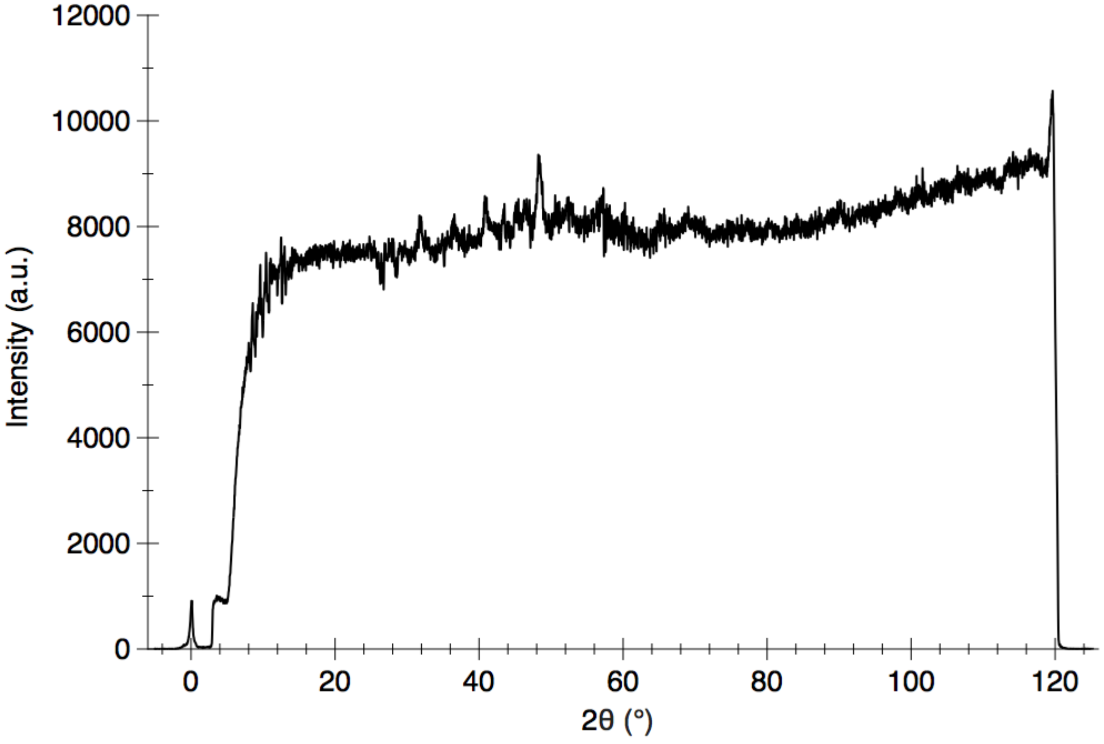

Figure 7.25: XRD diffractogram for **4.1AlMe$_3$** pyrolyzed at 1000 °C for 4 h.

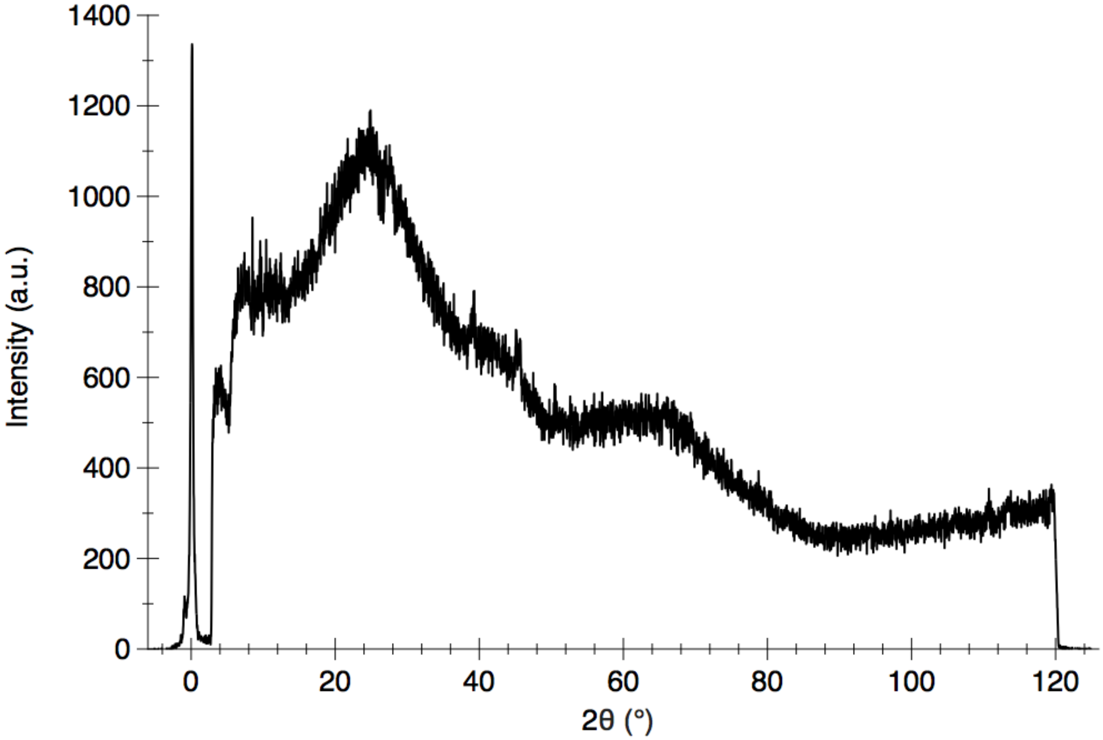

Figure 7.26: XRD diffractogram for **4.1CpCoCO** pyrolyzed at 800 °C for 3 h.

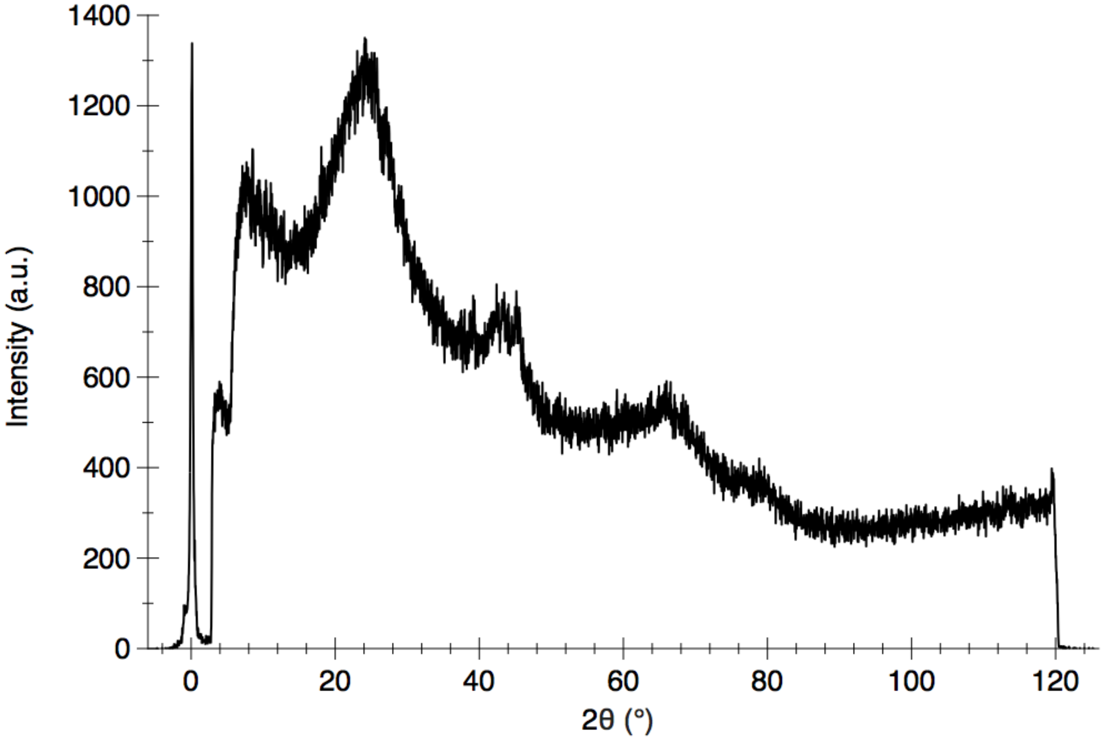

Figure 7.27: XRD diffractogram for **4.1CpCoCO** pyrolyzed at 900 °C for 3 h.

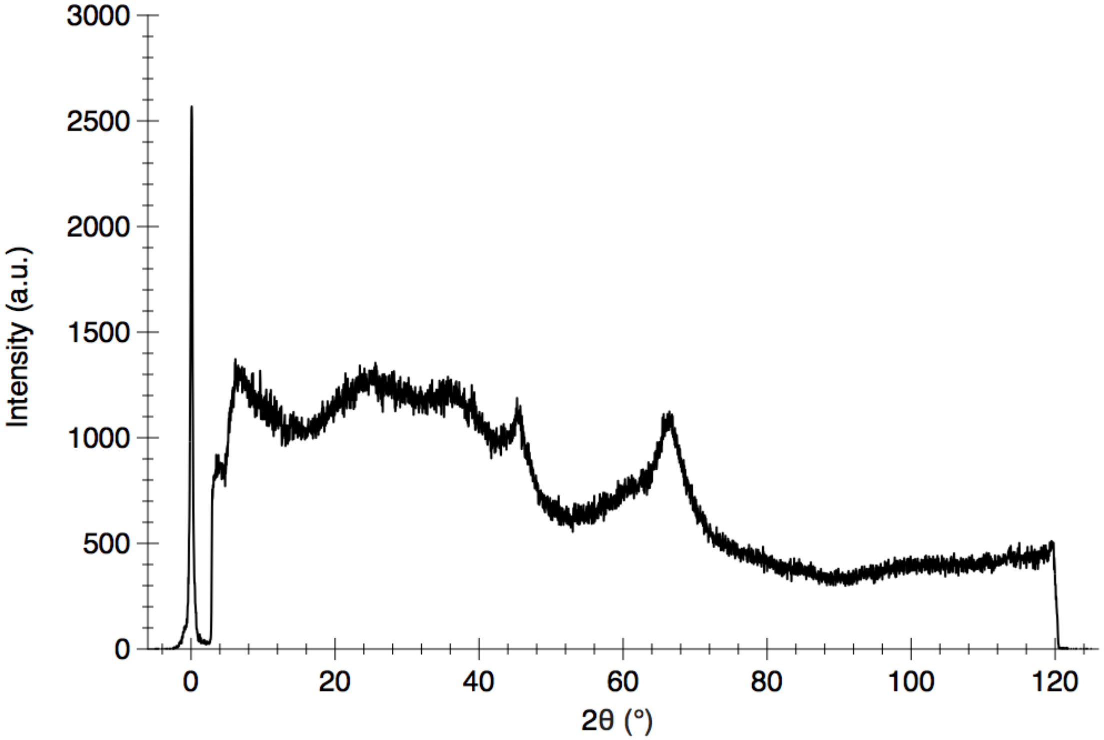

Figure 7.28: XRD diffractogram for **4.1CpCoCO** pyrolyzed at 1000 °C for 3 h.

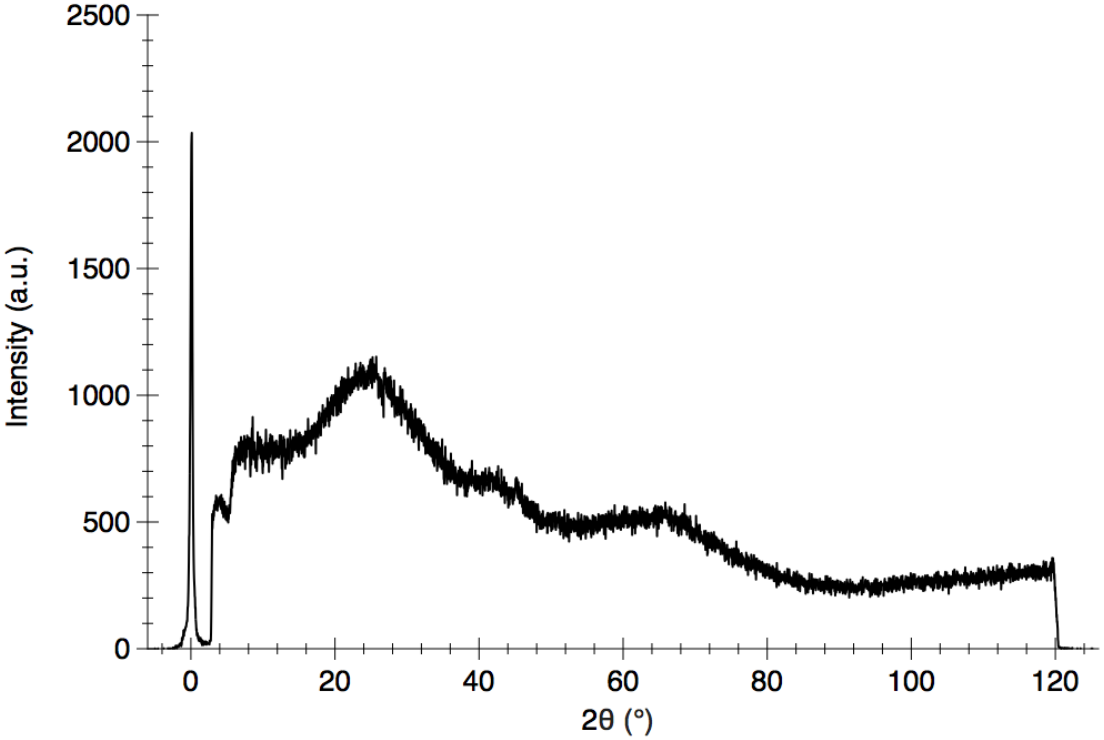

Figure 7.29: XRD diffractogram for **4.1CpCoCO** pyrolyzed at 800 °C for 4 h.

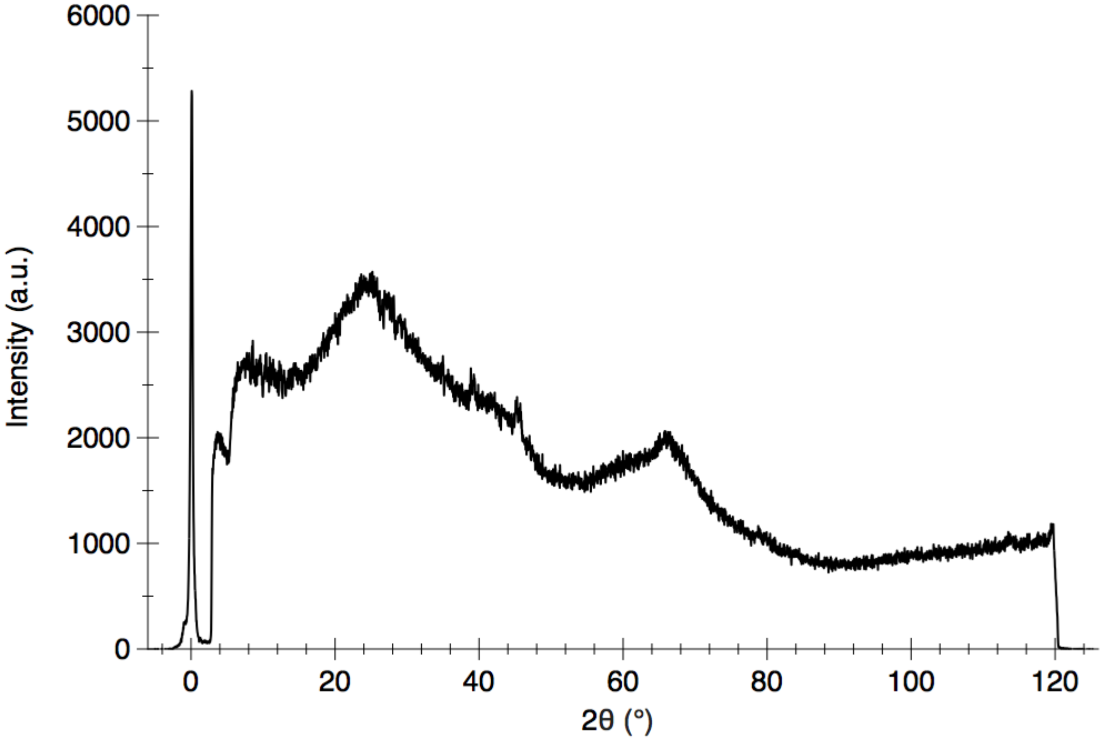

Figure 7.30: XRD diffractogram for **4.1CpCoCO** pyrolyzed at 900 °C for 4 h.

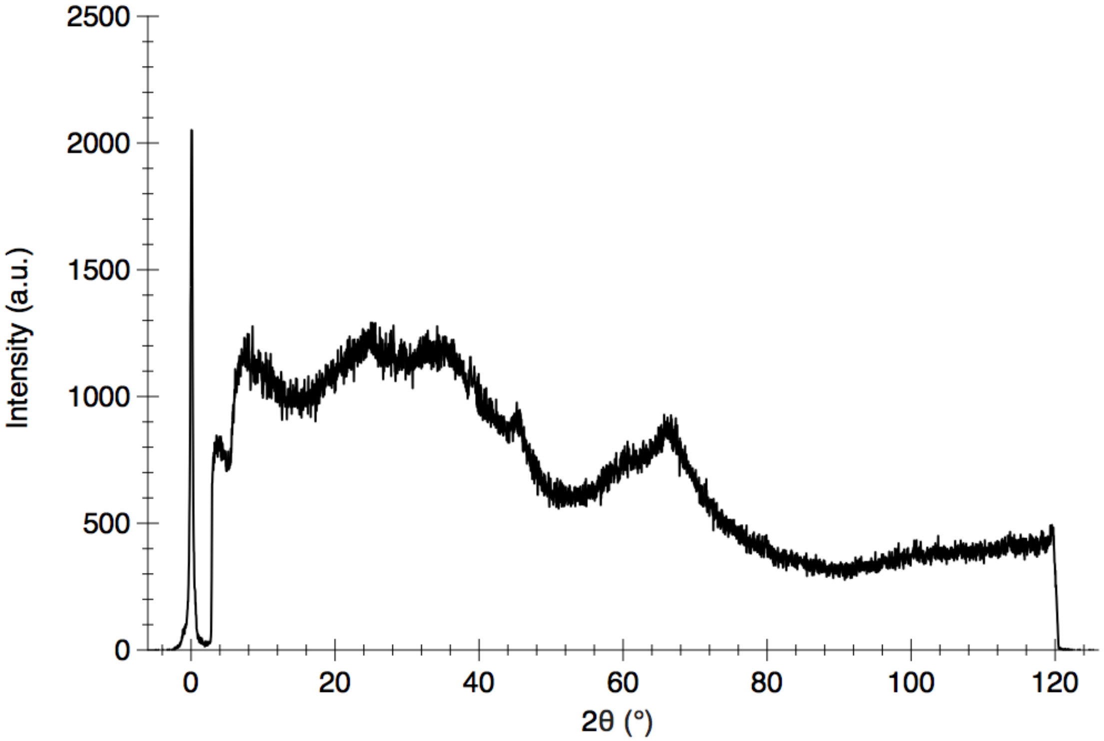

Figure 7.31: XRD diffractogram for **4.1CpCoCO** pyrolyzed at 1000 °C for 4 h.

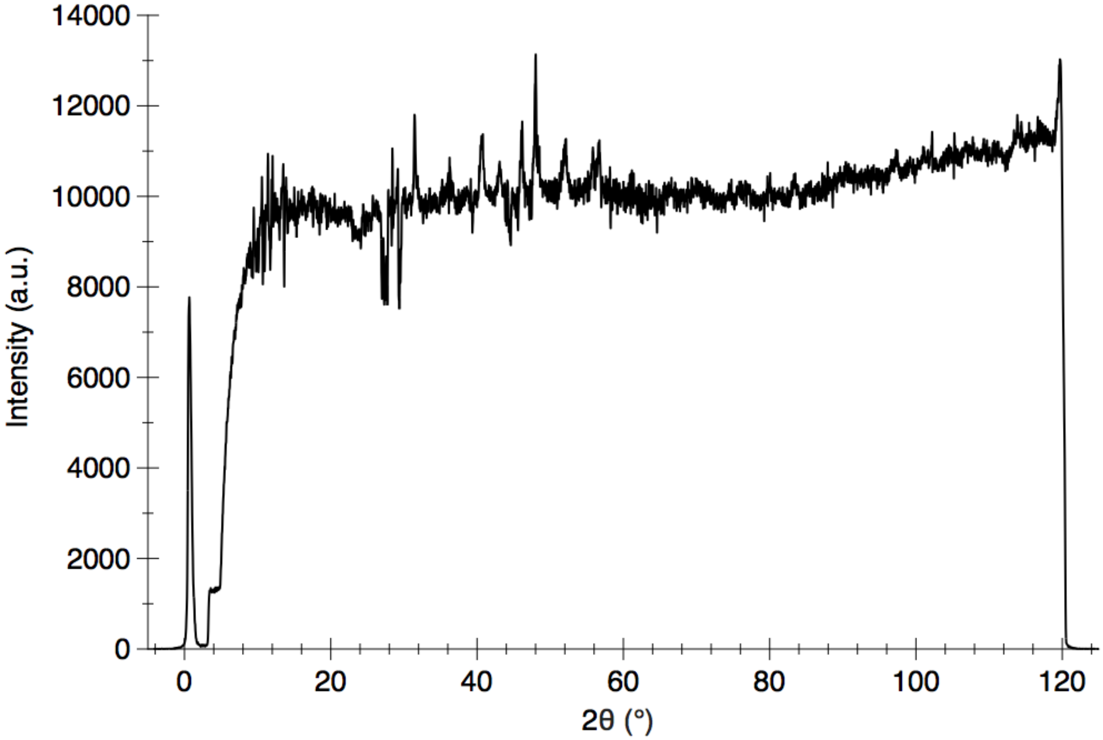

Figure 7.32: XRD diffractogram for **4.2CpCoCO** pyrolyzed at 800 °C for 4 h.

7.5 References

(1) Weicker, S. A.; Dube, J. W.; Ragogna, P. J. *Organometallics.* **2013**, *32* (22), 6681.

(2) Green, S. P.; Jones, C.; Stasch, A. *Science.* **2007**, *318*, 1754.

(3) Dube, J. W.; MacDonald, C. L. B.; Ragogna, P. J. *Angew. Chem. Int. Ed.* **2012**, *51* (52), 13026.

(4) Norton, E. L.; Szekely, K. L. S.; Dube, J. W.; Bomben, P. G.; Macdonald, C. L. B. *Inorg. Chem.* **2008**, *47* (3), 1196.

(5) SAINT. Bruker-AXS: Madison, WI 2013,.

(6) *SADABS*; Bruker AXS Inc.: Madison, WI, 2001.

(7) Sheldrick, G. M. *Acta. Cryst.* **2008**, *A64*, 112.

(8) Frisch, M. J.; Trucks, G. W.; Schlegel, H. B.; Scuseria, G. E.; Robb, M. A.; Cheeseman, J. R.; Scalmani, G.; Barone, V.; Mennucci, B.; Petersson, G. A.; Nakatusuji, H.; Caricato, M.; Li, X.; Hratchian, H. P.; Izmaylov, A. F.; Bloino, J.; Zheng, G.; Sonnenberg, J. L.; Hada, M.; Ehara, M.; Toyota, K.; Fukuda, R.; Hasegawa, J.; Ishida, M.; Nakajima, T.; Honda, Y.; Kitao, O.; Hakai, H.; Vreven, T.; Montgomery, J.; Peralta, J. E.; Ogliaro, F.; Bearpark, M.; Heyd, J. J.; Brothers, E.; Kudin, K. N.; Staroverov, V. N.; Kobayashi, R.; Normand, J.; Raghavachari, K.; Rendell, A.; Burant, J. C.; Iyengar, S. S.; Tomasi, J.; Cossi, M.; Rega, N.; Millam, N. J.; Klene, M.; Knox, J. E.; Cross, J. B.; Bakken, V.; Adamo, C.; Jaramillo, J.; Gomperts, R.; Stratmann, R. E.; Yazyev, O.; Austin, A. J.; Cammi, R.; Pomelli, C.; Ochterski, J. W.; Martin, R. L.; Morokuma, K.; Zakrzewski, V. G.; Voth, G. A.; Salvador, P.; Dannenberg, J. J.; Dapprich, S.; Daniels, A. D.;

Farkas, Ö.; Foresman, J. B.; Oritz, J. V.; Cioslowski, J.; Fox, D. J. *Gaussian09, Revision D01*; Gaussian Inc.: Wallingford, CT, USA, 2009.

(9) Zhao, Y.; Truhlar, D. G. *Theor. Chem. Acc.* **2008**, *120*, 215.

(10) Ansgar Schäfer, Christian Huber, R. A. *J. Chem. Phys.* **1994**, *100* (8), 5829.

(11) *Gaussview 3.0*; Gaussian Inc.: Pittsburgh, PA, USA, 2003.

(12) Glendening, E. D.; Badenhoop, J. K.; Reed, A. E.; Carpenter, J. E.; Bohmann, J. A.; Morales, C. M.; Landis, C. R.; Weinhold, F. *NBO Version 6.0*; Theoretical Chemistry Institute, University of Wisconsin: Madison, WI, USA, 2013.

(13) G. te Velde, F. M. Bickelhaupt, E. J. Baerends, C. Fonseca Guerra, S. J. A. van Gisbergen, J. G. Snijders, T. Z. *J. Comput. Chem.* **2001**, *22* (9), 931.

(14) C. F. Guerra, J. G. Snijders, G. te Velde, E. J. B. *Theor. Chem. Acc.* **1998**, *99*, 391.

(15) *ADF 2016 SCM, Theoretical Chemistry*; Vrije Universiteit: Amsterdam, The Netherlands, 2016.

(16) *AIMAII 17.11.14, Keith, T. A.*; TK Gristmill Software: Overland Park, KS, USA, 2017.

(17) Li, J. Q.; Feng, X. W.; Sun, W. A.; Ao, W. Q.; Liu, F. S.; Du, Y. *Mater. Chem. Phys.* **2008**, *112* (1), 57.

Curriculum Vitae

Name:	Vanessa Ann Béland
Post-secondary Education and Degrees:	University of Western Ontario London, Ontario, Canada 2010-2014 B.Sc. Honors Specialization Chemistry & Minor General English
	The University of Western Ontario London, Ontario, Canada 2014-2019 Ph.D. Synthetic Chemistry
Honours and Awards:	Faculty of Science Teaching Assistant Award 2019
Related Work Experience	Teaching Assistant The University of Western Ontario 2014-2019
	Mitacs Accelerate Intern Digital Specialty Chemicals 2017

Publications:

4. V.A. Béland, Z. Wang, C.L.B. Macdonald, T.K. Sham, P.J. Ragogna. A comprehensive investigation of a zwitterionic Ge(I) dimer with a 1,2-dicationic core. *Chem. Eur. J.* **2019**, Accepted.

3. V.A. Béland, Z. Wang, T.K. Sham, P.J. Ragogna. Antimony-functionalized phosphine-based photopolymer network. *Angew. Chem. Int. Ed.* **2018**, 57, 13252-13256.

2. V.A. Béland, M.A.S. Ross, M.J. Cody, R. Guterman, P.J. Ragogna. Patterned Phosphonium-Functionalized Photopolymer Networks as Ceramic Precursors. *Chem. Mater.* **2017**, *29*, 8884-8891.

1. J.W. Dube, V.A. Béland, P.D. Boyle, P.J. Ragogna. Utilizing a zwitterionic approach for the synthesis of late transition metal-triphosphenium ion coordination compounds. *Can. J. Chem.* **2015**, 93, 1-12. (Full Paper).

Technical Presentations:

1. V.A. Béland, P.J. Ragogna "Methodologies for Metal Functionalization of Photopolymer Networks" Skype presentation to Dr. Floryan De Campo from Solvay, between London, Ontario, Canada and Milan, Italy, November 15, 2018. (Oral)

Conference Oral Presentations:

8. V.A. Béland, P.J. Ragogna "Metallized Phosphane-ene Polymer Networks as Ceramic Precursors" at the 102nd Canadian Chemistry Conference & Exhibition, Québec City, QC, June 4, 2019. (Oral)

7. V.A. Béland, Z. Wang, T.K. Sham, P.J. Ragogna "Plastic Alchemy With Phosphorus & Antimony" at the 22nd International Conference on Phosphorus Chemistry, Budapest, Hungary, July 10, 2018. (Oral)

6. V.A. Béland, Z. Wang, T.K. Sham, P.J. Ragogna "Stibino-Phosphonium Photopolymer Networks" at the 50th Inorganic Discussion Weekend, Toronto, ON, November 4, 2017. (Oral)

5. V.A. Béland, P.J. Ragogna "Pnictenium Functionalized Phosphane-ene Polymer Networks" at the 100th Canadian Chemistry Conference & Exhibition, Toronto, ON, May 29, 2017. (Oral)

4. V.A. Béland, Z. Wang, T.K. Sham, P.J. Ragogna “Reductions of a Phosphino(borate) Germanium Zwitterion” at the 99th Canadian Chemistry Conference & Exhibition, Halifax, NS, June 9, 2016. (Oral)

3. V.A. Béland, M.A.S. Ross, R. Guterman, J.W. Dube, P.J. Ragogna “Metal-Containing Micro-/Nano-Structures from the Pyrolysis of Ion Exchanged Phosphonium Polymer Blend Films” at the 47th Inorganic Discussion Weekend, Montreal, QC, November 15, 2014. (Oral)

2. V. A. Béland, J. W. Dube, R. Guterman, P. J. Ragogna “Incorporating Metals onto a UV-Cured Phosphonium Polymer Blend Film via Ion Exchange” at the 1st Annual Undergraduate Three-Minute Thesis Competition, London, ON, April 4, 2014. (Oral)

1. V. A. Béland, J. W. Dube, R. Guterman, P. J. Ragogna “Incorporating Metals onto a UV-Cured Phosphonium Polymer Blend Film via Ion Exchange” at the 42nd Southern Ontario Undergraduate Student Chemistry Conference, Windsor, ON, March 29 2014. (Oral) *Recipient of 1st place Materials Chemistry Award* http://www.uwo.ca/sci/news/souscc_2014.html

Conference Poster Presentations:

6. V.A. Béland, P.J. Ragogna “Orthogonally Metallized Phosphane-ene Photopolymer Networks” at the 102nd Canadian Chemistry Conference & Exhibition, Québec City, QC, June 4, 2019. (Poster)

5. V.A. Béland, Z. Wang, C.L.B Macdonald, T.K. Sham, P.J. Ragogna “A XANES Investigation on a Ge 1,2-Dication” at the 22nd International Conference on Phosphorus Chemistry, Budapest, Hungary, July 10, 2018. (Poster)

4. V.A. Béland, P.J. Ragogna “Main Group Polymers As Patterned Ceramic Precursors” for RSC Twitter Poster Conference March 20, 2017. (Twitter Poster)

3. V.A. Béland, M.A.S. Ross, R. Guterman, J.W. Dube, P.J. Ragogna “Surface Functionalization Via Main Group Chemistry” at the Interdisciplinary Research Showcase, London, ON, December 5, 2014. (Poster)

2. T. J. Cuthbert, R. Guterman, V. A. Béland, E. R. Gilles, P. J. Ragogna “UV Curing for Phosphorus-Containing Polymers” at the Sustainability and the Environment Research Showcase, London, ON, March 6, 2014. (Poster)

1. V.A. Béland, M.A.S. Ross, R. Guterman, J.W. Dube, P.J. Ragogna “Surface Functionalization Via Main Group Chemistry” at the CAMBR Materials and Biomaterials Research Day, London, ON, April 27, 2015. (Poster)